



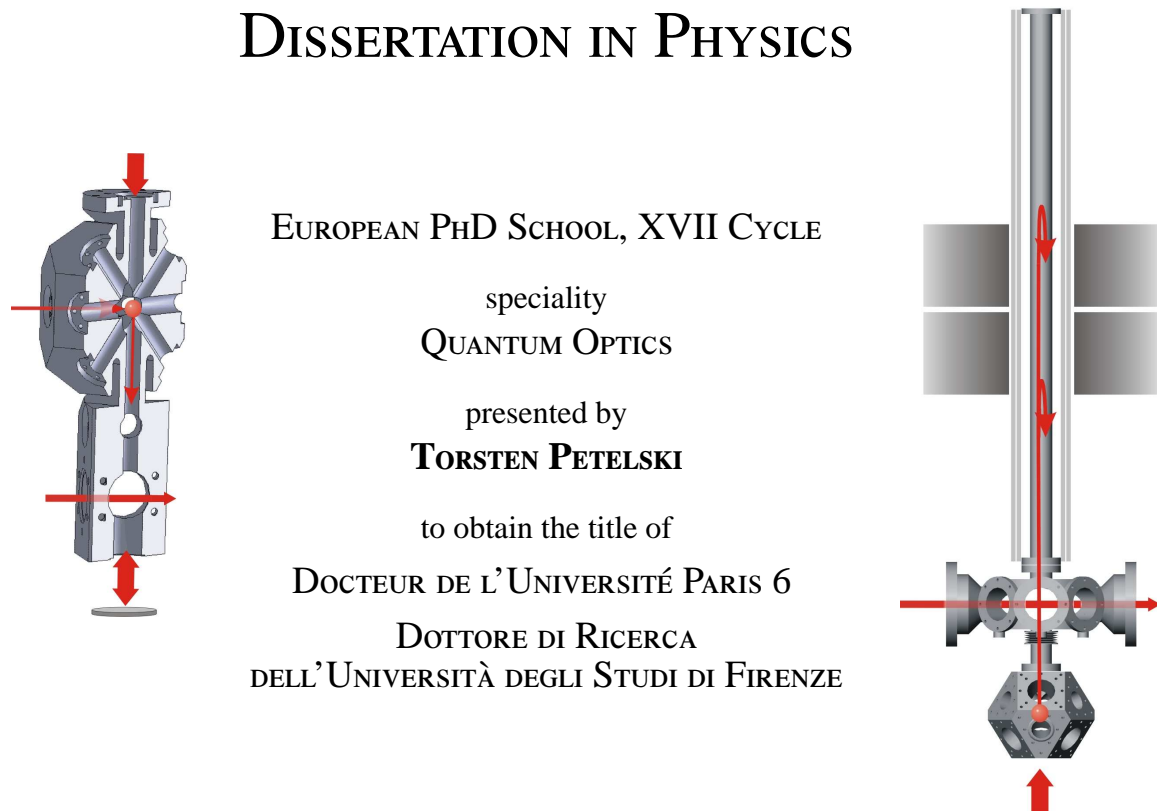
European
Laboratory for
Nonlinear
Spectroscopy



Università
degli Studi
di Firenze

l'Observatoire de Paris SYRTE
Systèmes de Référence Temps-Espace

UNIVERSITE PIERRE & MARIE CURIE
LA SCIENCE A PARIS



ATOM INTERFEROMETERS FOR PRECISION GRAVITY MEASUREMENTS

Submitted the 4th February 2005

Guglielmo Tino	Italian principle adviser
Christophe Salomon	French principle adviser
Robert Pick	Examiner
Vincenzo Schettino	Examiner
Tilman Pfau	Referee
Ernst Rasel	Referee

European Laboratory for Non-linear Spectroscopy (LENS)
&
Università degli studi di Firenze, Dipartimento di Fisica
Polo Scientifico di Sesto Fiorentino
Via Sansone 1, 50019 Sesto Fiorentino - Firenze, Italy

Bureau Nationale de Métrologie - Systèmes de Référence Temps - Espace
(BNM-SYRTE), Observatoire de Paris
61, avenue de l'Observatoire, 75014 Paris, France

Université Pierre et Marie Curie
4 place Jussieu, 75252 Paris Cedex 05, France

**ATOM INTERFEROMETERS FOR PRECISION
GRAVITY MEASUREMENTS**

**INTERFÉROMÈTRES ATOMIQUES POUR DES MÉSURES
DE PRÉCISION DE LA GRAVITATION**

**INTERFEROMETRI ATOMICI PER MISURE DI PRECISIONE
DI GRAVITAZIONE**

Abstract

The subject of this work is two separate atom-interferometry experiments. The first is a gravimeter in the frame of a new Watt-balance to measure the Earth acceleration g with an absolute precision of 10^{-9} , whereas the emphasis is placed on the second experiment, a gradiometer for the determination of the gravitational constant G with a precision of 10^{-4} . Both experiments perform interferometry on a freely falling sample of cold ^{87}Rb atoms by the application of a sequence of three Raman light-pulses. We describe the idea of the two experiments and report on the details of the apparatus, including a source of an intense flux of cold atoms, frequency and phase stabilization of the lasers and problems related to the source masses that we use for a double-differential measurement of G . Here again, the main weight lies on the gradiometer experiment, where we observed first interference fringes recently with a resolution of the order of 10^{-5} m/s^2 per shot.

Key-words: Atom Interferometer, Atomic fountain, Gravity, Gravitational Constant

Résumé

Nous décrivons dans cette thèse deux expériences d'interférométrie atomique. La première est un gravimètre qui mesurera l'accélération de la pesanteur terrestre g avec une exactitude relative de 10^{-9} , et qui est développé dans le cadre d'un projet de réalisation d'une Balance du Watt. La deuxième, sur laquelle l'essentiel du travail de cette thèse a porté, est un gradiomètre pour la détermination de la constante de la gravitation universelle G avec une exactitude relative de 10^{-4} . Dans ces deux expériences, des atomes froids de ^{87}Rb en chute libre sont soumis à une séquence de trois impulsions laser Raman, afin de réaliser un interféromètre atomique. Nous décrivons d'abord le principe de ces expériences, puis le dispositif expérimental que nous avons mis au point. Nous présenterons notamment la réalisation d'une source intense d'atomes froids, les méthodes de stabilisation en fréquence et en phase des lasers ainsi que les problèmes liés aux masses sources utilisées pour la mesure doublement différentielle de G . On porte ici l'accent sur le gradiomètre, avec lequel nous avons observé des premières franges d'interférence récemment, avec une résolution sur la mesure de l'accélération de l'ordre de 10^{-5} m/s^2 par coup.

Mots-clés : Interférométrie Atomique, Fontaine Atomique, Pésanteur terrestre, Constante de la Gravitation

Riassunto

Nella presente tesi viene illustrato il lavoro effettuato su due distinti esperimenti di interferometria atomica. Il primo è un gravimetro inserito nel contesto di una nuova bilancia di Watt per misurare l'accelerazione di gravità terrestre g con una precisione assoluta di 10^{-9} , ma maggiore enfasi viene riservata per il secondo esperimento, un gradiometro per la determinazione della costante di gravitazione universale G con una precisione di 10^{-4} . Entrambe gli esperimenti si basano su tecniche interferometriche su un campione di atomi freddi di ^{87}Rb in caduta libera mediante l'interazione con una sequenza di tre impulsi Raman. Viene descritta l'idea alla base di tali esperimenti e vengono riportati i dettagli dei singoli apparati, con particolare riferimento alla sorgente di un flusso intenso di atomi freddi, al sistema per la stabilizzazione in fase e frequenza dei laser ed ai problemi relativi alle masse sorgenti utilizzate per una misura doppio-differenziale di G . Ribadisco che nel lavoro di tesi viene data maggior rilevanza al gradiometro, con il quale si sono di recente osservate le prime frange di interferenza con una risoluzione sull'accelerazione dell'ordine di 10^{-5}m/s^2 per lancio.

Parole chiave: Interferometria Atomica, Fontana Atomica, Gravità terrestre, Costante di Gravitazione

Contents

Abstract, Résumé, Riassunto	i
Introduction	1
Organization of thesis	4
1 The Paris gravimeter and Florence gradiometer	5
1.1 Atom interferometry	5
1.1.1 Past and present devices	6
1.1.2 Future developments and applications	7
1.2 A gravimeter for a new Watt Balance	10
1.2.1 New definition of the Kilogram	10
1.2.2 Watt balance	11
1.2.3 Atom interferometer or falling corner cube	13
1.2.4 Experimental Realization	14
1.3 A gradiometer for the determination of G	15
1.3.1 Significance of the Gravitational Constant G	15
1.3.2 Past G -measurements	16
1.3.3 G measurement with atom interferometry	18
1.3.4 Experimental realization	19
1.4 Intuitive explanation of gravimeter and gradiometer	20
2 Theory of Raman light pulse interferometry	27
2.1 Atoms and Light	27
2.1.1 Two level atom in a light-field	27
2.1.2 External degrees of freedom	30
2.1.3 Raman transitions	31
2.1.4 Velocity selection	37
2.1.5 Comments on plane-wave approximation	38
2.2 Raman light pulse interferometer	40
2.2.1 Principle	40
2.2.2 Phase contribution of Raman pulses	41
2.2.3 Free evolution	43
2.2.4 The <i>Bordé method</i>	46
2.2.5 Interferometer phase shift for certain potentials	50
2.3 Sensitivity to noise	51
2.3.1 Definitions	51

2.3.2	Weighting function	53
2.3.3	Exact calculation of the weighting function	55
2.3.4	Comparison of rough and exact result for the weighting function	58
2.3.5	Dick effect	61
3	Experimental setup	65
3.1	Vacuum System	65
3.1.1	Description of MAGIA apparatus	67
3.1.2	Pressure estimation	71
3.1.3	Sealing with lead and glue	73
3.2	Magnetic fields	76
3.2.1	Coils	76
3.2.2	Magnetic shielding	77
3.3	Laser System	80
3.3.1	Extended cavity diode lasers	81
3.3.2	Laser setup of gradiometer	83
3.3.3	Laser setup of gravimeter	86
3.3.4	Summary and new laser system gradiometer:	88
3.3.5	Fiber system	89
3.4	Masses	92
3.4.1	Double differential measurement	93
3.4.2	Gravity gradient	94
3.4.3	Best Trajectories	96
3.4.4	Characteristics of Masses	98
4	Laser frequency and phase control	103
4.1	Frequency stabilization	103
4.1.1	Frequency modulation spectroscopy	104
4.1.2	DAVLL	107
4.1.3	Doppler free DAVLL lock	107
4.1.4	Further modulation-free locking techniques	111
4.1.5	Frequency Lock with f-to-V converter	113
4.2	Phase Stabilization	113
4.2.1	Phase-locked-loop	114
4.2.2	Analog Phase Detector	115
4.2.3	Digital Phase and Frequency Detector	116
4.2.4	Digital Phase Difference Counter	116
4.2.5	Locking bandwidth and capture range	117
4.3	Frequency control for gravimeter	118
4.3.1	Lock Reference Laser on rubidium transition	118
4.3.2	Lock Repumper on Reference	120
4.3.3	Lock Cooling Laser on Repumper	121
4.4	Frequency control for gradiometer	124
4.4.1	Lock Repumper on rubidium transition	124
4.4.2	Lock Reference Laser on rubidium transition	124
4.4.3	Lock Master Raman laser	125
4.4.4	Phase-Lock Slave Raman laser	125

4.4.5	Noise on phase-lock	127
5	Experimental procedure and first results	133
5.1	2D-MOT	133
5.1.1	Experimental setup	135
5.1.2	Tools to describe a 2D-MOT	136
5.1.3	Characterization of 2D-MOT	140
5.1.4	2D-MOT for gradiometer	145
5.2	Sample preparation and analysis gradiometer	146
5.2.1	3D MOT	146
5.2.2	Launch	147
5.2.3	Juggling	150
5.2.4	Velocity selection	151
5.2.5	State preparation	155
5.2.6	Detection	157
5.3	Interferometry	159
5.3.1	Velocity insensitive Interferometer	159
5.3.2	Velocity selective Interferometer	160
6	Conclusion	165
6.1	Summary of work on gravimeter experiment	165
6.2	Summary of work on gradiometer experiment	166
6.3	Milestones of gravimeter	167
6.4	Milestones of gradiometer	168
A	Rubidium Data	171
A.1	Rubidium spectroscopy signals	171
A.2	Transition probabilities	175
A.3	Temperature dependence of pressure	176
A.4	Further useful numbers on ^{87}Rb	177
B	Geophysical determination of gravity	179
B.1	Predicted value of g	179
B.2	Predicted value of γ , γ' and γ''	181
Bibliography		183
Men and machine		193

Introduction



"Gravity is a contributing factor in nearly 73 percent of all accidents involving falling objects." Dave Barry. The photo shows a rather unusual example of an accident; but also here the contribution of gravity can hardly be denied.

One of the most obvious things in the world is that if you hold a stone in your hand and release it, then the stone falls. Around 350 B.C., Aristotle concludes in his book '*on the heavens*' [1] that a stone falls, because it is driven to its natural place, which is the center of the Earth:

...It (a moving body) could not move infinitely; for to traverse an infinite is impossible, and impossibilities do not happen. So the moving thing must stop somewhere, and there rest not by constraint but naturally. But a natural rest proves a natural movement to the place of rest. ... For if the natural motion is upward, it will be fire or air, and if downward, water or earth. Hence air and water each have both lightness and weight, and water sinks to the bottom of all things except earth, while air rises to the surface of all things except fire.

Natural motion of the heavenly bodies, according to Aristotle, is circular. The ideas of Aristotle imply further that heavy objects fall faster than light things, because their consistence determines the degree of their desire to return to their natural position, the center of the Earth¹. Since this 'natural desire' of objects to fall is the only manifestation of gravitation in daily life, we understand that the ideas of Aristotle – although completely wrong – survived for almost 2000 years.

In 1632 Galileo published his text '*Dialogo dei massimi sistemi*' [3] and proved those ideas to be wrong. His experiments together with the celestial mechanics of Kepler [2] delivered a stunningly new description of the motion of objects on Earth as well as of planets, but could not deliver a philosophical description of the origin of the forces that determine this motion.

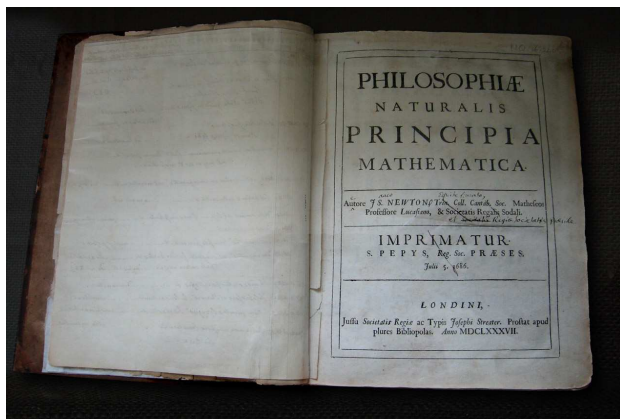


Figure 1: In the so-called 'Principia' of 1687 [5], Newton published his studies about the gravitational force that he developed during the plague in 1665/66 at the age of 23.

This hole was filled for a certain time by the ether theory of Descartes [4] until Newton in his '*Philosophiae naturalis principia mathematica*' delivered strong arguments against the ether. Newton proposed universal gravitation and the inverse square law of attraction between any two bodies even separated in a vacuum [5]:

... all matter attracts all other matter with a force proportional to the product of their masses and inversely proportional to the square of the distance between them.

Newton's law of gravitation received its definitive analytic form from Euler and is expressed as

$$F = G \frac{Mm}{r^2} ,$$

¹Aristotle concluded a reasoning about the question about the form of the Earth: *Its shape must necessarily be spherical.*

where F is the absolute value of the force between two bodies of masses m and M at a distance r . G is the universal gravitational constant. The Earth acceleration g can be written as $G \cdot M_{\text{Earth}} / r_{\text{Earth}}^2$. Newton realized that it is precisely the same force that keeps planets on its orbit that make a stone fall to Earth. Despite the enormous potential of his theory to explain effects of gravitation, it nevertheless did not explain the origin of this attractive force; worse, it is based on some 'magic power' that attract objects to each other.

In the following decades, Newton's theory became commonly accepted and is fully valid until nowadays, except in the presence of very large gravitational fields, in which case Einstein's general relativity theory must be applied – that nowadays also fills the philosophical gap by delivering an explanation for the nature of gravity.

Within the past 300 years, Earth gravity acceleration g and the gravitational constant G have been measured to always higher precision. The up-to-date most precise instruments for the determination of g use the powerful technique of *laser-interferometry* to read out changes in the position of a freely falling test mass that are provoked by the Earth acceleration g . The identical technique has been applied for the determination of G , but could not compete with the more precise angular measurements on suspended test masses.

Interference of matter waves can offer a much higher sensitivity in the detection of accelerations and the past decade has seen impressive progress in the field of *atom interferometry*, whose range of applications changed from pure fundamental physics to precision measurements and metrology. Atom interferometers have already proved their superiority on a g -measurement and they could compete when used to determine G .

In my lab, we've surpassed the sensitivity of the best absolute-measurement gravimeter, which measures the acceleration due to gravity. So you think that's kind of crazy, that by dropping atoms you can make the most sensitive measurement of gravity, but it's true. Steven Chu in [6]

This thesis contains work on two recently started atom-interferometry experiments for an accurate measurement of g and G , respectively.

Organization of thesis

The first **chapter 1** of this thesis '*The Paris gravimeter and Florence gradiometer*' will give an introduction to atom interferometry, its potentials and future applications. Then we will describe the idea of the two experiments, which are topics of this thesis: a gravimeter in the frame of a Watt-balance to measure the Earth's acceleration g with an absolute precision of 10^{-9} and a gradiometer for the determination of the Gravitational constant G to a precision of 10^{-4} .

Both experiments perform interferometry on a freely falling sample of cold ^{87}Rb atoms, on which we apply a sequence of three Raman light-pulses. After the intuitive explanation of atom interferometry at the end of chapter 1, we will provide a detailed theoretical description of the phase shift of a Raman light-pulse interferometer in **chapter 2**: '*Theory of Raman light pulse interferometry*'. In addition, chapter 2 will discuss the problem of laser phase-noise and its transmission onto the interferometer signal.

We constructed an ultra-high vacuum system by applying new sealing techniques and set up a laser system, such that we are able to prepare in a reliable way samples of about 10^9 atoms, cooled to a few micro-Kelvin by laser-cooling techniques. **Chapter 3**, '*Experimental setup*', will satisfy eventual curiosity about the apparatus of mainly the gradiometer and will include the multifaceted problem of the design and characterization of the source masses for the measurement of G , as well as a study of an optimized double-differential measurement.

Different strategies have been chosen for the gravimeter and gradiometer to realize the frequency- and phase control of the lasers, that is required for the manipulation of the atoms. Both approaches partly rely on newly developed methods like a powerful frequency sweep control at the gravimeter and a new frequency stabilization and phase-lock scheme at the gradiometer; the latter able to stabilize the relative phase of the interferometer lasers to about one milliradian. We dedicate a separate **chapter 4**, '*Frequency and phase control*', to the description of all stabilization systems.

A two-dimensional magneto-optical trap (2D-MOT) with push beam has been assembled and delivers a sufficiently high flux of up to 10^{10} transversely cooled atoms per second to ensure the desired repetition rate of the gravimeter. At the gradiometer, we could recently observe interference fringes resulting from a 40 millisecond long interferometer sequenced. The present interferometer has a relative resolution on the order of 10^{-5} m/s^2 per single measurement. These preliminary results and a description of the experimental procedure are contained in **chapter 5**, '*Experimental procedure and first results*'.

Finally, the last **chapter 6**, '*Conclusion*', will summarize the main results of the work and give an outlook on the milestones of the gravimeter and gradiometer.

Chapter 1

The Paris gravimeter and Florence gradiometer

The development of the gradiometer experiment at University of Florence and the Watt-balance-gravimeter at Observatoire de Paris have to be seen within the context of the stunning progress in atom interferometry to get an idea of where to direct the efforts of further research. Some of the main research topics will be mentioned in the first part of this chapter as well as possible applications of atom interferometry. In the second and third section, we will explain the significance and goals of the two recently started experiments, which are subject to thesis. Finally, the last section will give an intuitive explanation of atom interferometry in general and of the gravimeter and gradiometer in particular.

1.1 Atom interferometry

Performance of optical interferometers is basically limited by the wavelength of the light or, in some applications, by the size of the experimental apparatus. It has long been a tempting idea to use matter waves in interferometry. Such interferometers can be by far better than optical interferometers of same size and flux: the Sagnac effect¹ measured with an atom interferometer with the same area and flux as a laser interferometer could for example deliver a signal to noise ratio, which is almost 10^{11}

¹An interferometer, whose two arms enclose a certain area A will be sensitive on rotations of the reference frame with angular velocity Ω and will show a phase shift

$$\Delta\phi = 4\pi\Omega \cdot A / \lambda v \quad (1.1)$$

for both light and massive particles. Here v is the particle velocity and λ its wavelength (de-Broglie wavelength in the case of massive particles). This effect, called *Sagnac effect*, was first described in 1913 by G. Sagnac, who split a light beam into two parts that were travelling around the circumference of an area in opposite directions, and observed that the interference fringes are a function of the rotation velocity.

times higher than in an optical interferometer, assuming a shot-noise limited detection for both. Although there are more severe restrictions to size and flux of atom interferometers, an improvement factor of several orders of magnitude remains. Unlike their photon counterparts, atom interferometers can be sensitive to electric and magnetic fields, which makes these instruments particularly suited for a larger set of sensor applications, though by the same token, they are sensitive to a larger variety of detrimental noise sources. The first matter wave interferometers with neutrons appeared in the 70s [7] and were already sensitive to the Earth's gravitational acceleration g [47].

1.1.1 Past and present devices

To describe the history of neutral atom interferometry, we do not have to go very far into the past: the first realization of atom interferometers were reported in 1991 by various groups. They used different approaches to realize beam-splitters and mirrors: some were using slits [13] or diffraction gratings [12] similar to the optical interferometers, others light, either as periodic fields acting like physical diffraction gratings [11, 16] or as pulses, coupling various internal states of the atoms and thus couple internal and external degrees of freedom [14], [15]. Meanwhile, a great variety of beam-splitters for interferometers has been demonstrated, ranging from pure evanescent light fields [17, 18] over combinations like magneto-optical gratings [19] to purely magnetic (Stern-Gerlach effect [20]) and electric fields (field of a charged wire [21]).

The method of using light pulses as beam splitters and mirrors proved to be advantageous and the second generation of atom interferometers mainly made use of this principle. Measurements of astonishing precision and with comparable – if not better – performance than state of the art classical instruments have been made; namely by the two groups of Steven Chu and Mark Kasevich. Using atom interferometry, they were able to measure Earth gravity g with a precision of $2 \cdot 10^{-9} \text{ m/s}^2/\sqrt{\text{Hz}}$ [46], Earth gravity gradient γ with a precision of $4 \cdot 10^{-9} \text{ 1/s}^2/\sqrt{\text{Hz}}$ [43, 42] and rotations with an angular resolution better than $10^{-9} \text{ rad/s}/\sqrt{\text{Hz}}$ [44]. Also \hbar/m has been determined with an accuracy of 10^{-7} with a similar method [45] as well as the fine structure constant α to $7.4 \cdot 10^{-9}$ [35].

Inspired by these achievements, a third generation of atom interferometers, designed for new applications, is under development. Under construction are amongst others: a gyroscope at the IQ in Hannover [22] and at BNM-SYRTE in Paris [23], a gravimeter in the frame of the Watt balance at BNM-SYRTE in Paris (this thesis), a gradiometer for the measurement of the Newtonian gravitational constant G in Florence (this thesis) [96, 105], a robust gradiometer for Earth and space science applications in Pasadena [97] and a transportable acceleration sensor in Stanford [98]. In addition, instruments for a new accurate measurement of \hbar/m are set up at LKB in Paris [36, 37] and in Stanford.

1.1.2 Future developments and applications

Present state-of-the-art accelerometers, gravimeters (like the FG5, described later on) or gradiometers – as well as laser gyroscopes – seem to be close to their physical limits of resolution. Matter wave interferometers already reach or even outreach the performance of these instruments and thus promise far more precise instruments in future. Their ultimate limit of resolution is not yet clear and this topic is therefore in itself interesting for investigation. We will mention some of the most important or interesting developments.

Portable acceleration sensors: Information about gravity or gravity gradients and their temporal monitoring is of big geophysical interest, for example in vulcanology, plate tectonics, mapping of natural resources or earth composition. Especially in Italy with its big seismic activity exists a big interest in portable gravimeters and gradiometers for volcano supervision. Gravity data deliver important information about underground structures and the possible faster measurement time and higher accuracy of atom interferometers makes them superior to mechanical instruments. The idea of constructing a portable gravi- or gradiometer as in the United States [97, 98] is already in discussion but funding still open. A further application of portable devices would be ultra-precise inertial sensors that would allow a stand-alone navigation of planes, ships or submarines.

Atom interferometry with Bose-Einstein Condensates: Two of the key elements in the sensitivity of atom interferometers and atom clocks are the free evolution time and the collisional shift. Cooling atoms down to a Bose-Einstein condensates would lower their temperature and thus spatial spread, what principally would allow longer interferometer times. But since dense BECs (in traps) underlie the mean field shift, interferometry is here again done on a freely falling cloud [31] which is expanded to reduce density and interaction-time gets limited by the size of the apparatus. The signal of such an interferometer is shown in Fig. 1.1. Despite of the disturbing shifts, many experiments with BECs on micro-chips [39] are set up for – amongst others – guided matter wave interferometry experiments (for a summary see [10]). A big advantage of the chip technology besides far longer interaction times is the significant reduction of the size of possible interferometers. Systematic effects in these kind of interferometers are still not studied in detail.

Atom interferometry with Fermions: The absence of interactions between fermions may allow bright atomic sources for interferometry without disturbing collisional shifts² [24]. The superiority of interferometry with trapped cold fermions over a BEC has already been demonstrated [41] by the far slower decay of Bloch-oscillations of trapped

²In the presence of Feshbach-resonances, interactions between Bosons can also be eliminated; but often this requires the application of 'high' magnetic fields.

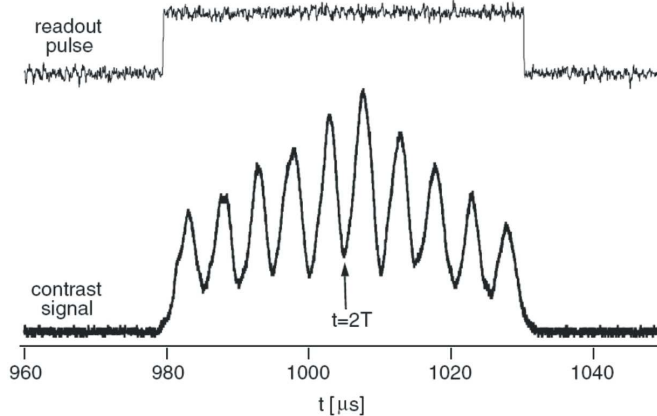


Figure 1.1: *Interferometer signal taken with ‘contrast interferometry’ on a freely falling BEC [31]. The information about the photon recoil, transmitted to the atoms during the interferometer, is encoded in the contrast of the interferometer. This technique could offer enough precision for a measurement of h/m on the ppm-level.*

fermions in a lattice.

Test of Newton’s law at small distances: Deviations from the inverse square law of gravitation 1.8 are predicted by string theory [25] and have recently received a lot of attention. In general, deviations are parameterized by the parameters α and λ , which correspond to strength and range of the interaction, respectively. The gravitational potential energy between two masses m and M is such written as

$$V(r) = -G \frac{mM}{r} (1 + \alpha e^{-r/\lambda}), \quad (1.2)$$

where r is the distance between the masses. Of special interest are distances between the mm- and μm - regime. A compilation of the limits to α and γ of present laboratory experiments are given in [26]. At small distances, atoms show the advantage that systematic effects are well understood or at least offer the possibility of analyzing them well, such that the high sensitivity of atom interferometry makes it a possible candidate for revealing non-Newtonian potentials. The signal of a wire or plate at around 100 μm distance from the arm of a spatially separated atom interferometer would be sufficiently large to reveal eventual violations of the $1/r^2$ dependence. An interferometer of such kind has been studied in [27] for a slowed Cs beam; whereas the method proposed in [28] relies on the interference of two ^{87}Rb condensates at different distances from a surface. Both approaches seem to be promising; however, the effect of systematic errors due to Van-der-Waals forces and other surface effects (Rb deposition) must be carefully studied.

Atom interferometers in space: In space no gravity accelerates the atoms, what

would permit long measurement times of the interferometer and lead to higher sensitivity on small forces. A further possible application is the gravity or gravity gradient

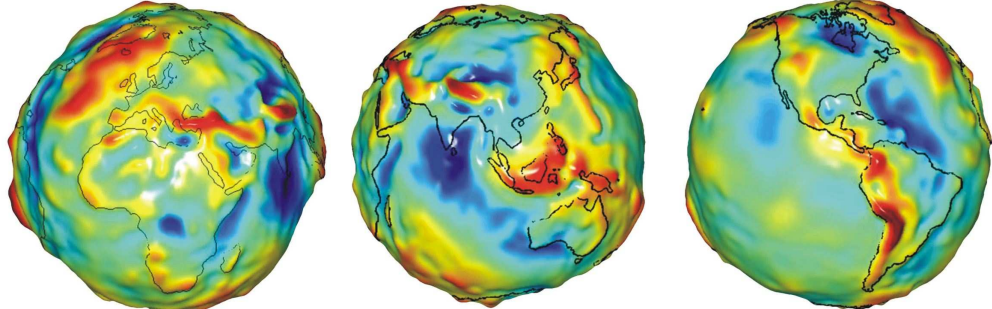
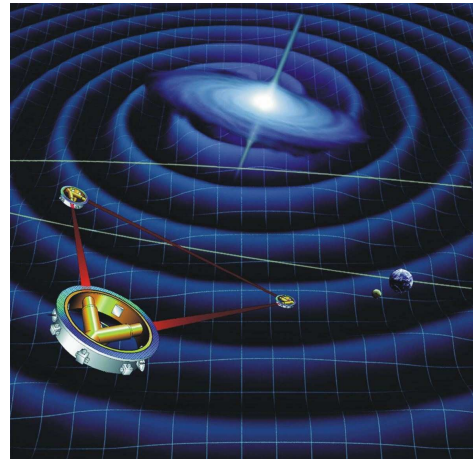


Figure 1.2: Gravity map of the Earth, taken by the satellite GRACE in 2003. Regions of big gravity are emerging. Pictures taken from GRACE homepage [91].

mapping of the Earth, as it is already done today with the existing satellite GRACE (Fig. 1.2, [91]) or the planned GOCE mission [90]. An atom interferometric measurement of the geoid height could improve the accuracy of the GRACE mission by several orders of magnitude [97].

Gravitational wave detection: There is a vivid debate going on presently, arguing about the question if gravitational wave detectors based on matter wave interferometers (MIGO) can compete with the sensitivity of the large scale laser interferometers [40] like Virgo in Pisa or LIGO in the States, and – in case they can – if relativistic atoms or slow atoms should be used. Some arguments of the debate can be found in [29], who claim that indeed, cold atom interferometry can actually reach sensitivities on gravitational waves over a higher bandwidth, and in far smaller devices than laser interferometers. Be that as it may, the amplitudes of strong gravitational waves in terms of distortion of space $\Delta L/L$ are smaller than 10^{-20} and the necessary resolution for their detection requires new interferometer schemes, preferable in space, where the interferometer length and interaction time can be extended. An equivalent system based on a laser interferometer with arms of 5 million km, *LISA* (Laser Interferometer Space Antenna, see picture above and [30]) is in development and planned to be launched in 2011.



Also fundamental tests of physics are possible using atom interferometry, like a test of the equivalence principle by comparing acceleration of two different elements or isotopes. Such a measurement has recently been performed in the group of M. Weitz by comparing ^{85}Rb and ^{87}Rb [9]. New ideas still come up, like the proposal of multi-dimensional atom interferometers [95].

1.2 A gravimeter for a new Watt Balance

The Bureau National de Métrologie (BNM) has recently initialized a new Watt-balance experiment, aiming at a redefinition of the kilogram. A gravimeter with an absolute precision of 10^{-9} is one of the (many) crucial parts of the experiment and is presently mounted at the BNM–SYRTE (Systèmes de Référence Temps Espace) in Paris. A part of the work for this thesis has been dedicated to this gravimeter, to which we would like to give a motivation in the present section.

1.2.1 New definition of the Kilogram



Figure 1.3: *The international prototype of the kilogram. Picture taken from BIPM homepage [92].*

The kilogram is the last remaining international standard defined by a 'thing': a macroscopic object made of platinum-iridium, cast in England in 1889 and kept in Paris at the BIPM (Bureau International des Poids et Mesures) under conditions specified by the 1st CGPM (General Conference on Weights and Measures) in 1889 (see Fig. 1.3). No one knows why it is shedding weight ($1 \mu\text{g}/\text{kg}/\text{year}$ [57]), at least in comparison with other reference weights, but the phenomenon has spurred an international search to trace back the definition of the mass on more stable microscopic quantities and natural constants. If this efforts would succeed in tracing back the definition of the kilogram to constants

of nature, the amazingly long story of physical standards (in terms of 'things') would finish. The Egyptians already used an artefact length standard, a length of black granite rod, called the Royal Cubit (≈ 524 mm), from which were copied wood sticks of same length for use in daily life. The method proved to be of great effect in the construction of pyramids, the side lengths of which are equal at a 0.05% level. But let us stay in the present and have a look on the most promising methods which are presently in the race for the redefinition of the kg:

- *Ion accumulation:* A beam of ions hits a surface and each ion produces a well defined current. By the integration of the current and with the knowledge of the ion-mass, the mass of the deposited material can be deduced. The approach, developed at PTB (Physikalisch Technische Bundesanstalt) is not yet very far advanced [85].
- *Atom counting:* The mass of a single macroscopic crystal of silicon can be determined by its size, the lattice spacing and the atomic mass. Although fighting with many difficulties ³ mainly of lattice errors and isotopical purity, the results are encouraging, what means to reach competitive accuracies of 10^{-8} within the next decade(s). See e.g. [107]
- *Watt balance:* A comparison of electric and gravitational force on a test mass leads to the expression of the mass by fundamental constants and well measurable quantities [86]. At present, this approach seems to be the most advanced one: the accuracies of the NIST and NPL Watt balance are on the order of 10^{-7} .

1.2.2 Watt balance

B.P. Kibble of the NPL (National Physics Laboratory) first proposed the method of the Watt balance in 1975. We will just explain its principle, the real experimental procedure will be slightly little different.

One measurement cycle includes two steps [60]: The first step is a static comparison of the gravitational and electrical force. Fig. 1.4 shows a balance with a mass m and a coil suspended on one side and a small mass to counterbalance the weight of the coil on the other side. The mass m is attracted by the Earth's gravity g with the force

$$F_{\text{mec}} = -mg. \quad (1.3)$$

A current I is sent through the coil that is located in a magnetic flux gradient $\partial\Phi/\partial z$ to provoke a force, which exactly compensates the gravitational force and brings the balance to equilibrium:

$$F_{\text{el}} \stackrel{!}{=} F_{\text{mec}} \iff -I \frac{\partial\Phi}{\partial z} \stackrel{!}{=} -mg. \quad (1.4)$$

In the second part of the experiment the mass is taken off the holder and the constant current source removed. The balance is again in equilibrium and by giving it a kick, it will move with constant velocity. The velocity $v = \partial z/\partial t$ is monitored with an interferometer. The current of the coil, which is induced by the movement through the

³M. Glaeser of PTB in Science, desperate: "If one could only measure the density of holes!", R. Deslattes of BIPM commenting the search for errors: "It was torturous"; but also people of the Watt balance don't have a better time: B. Kibble of NPL also in Science about his last 15 years of Watt balance: "The work is very slow and painstaking."

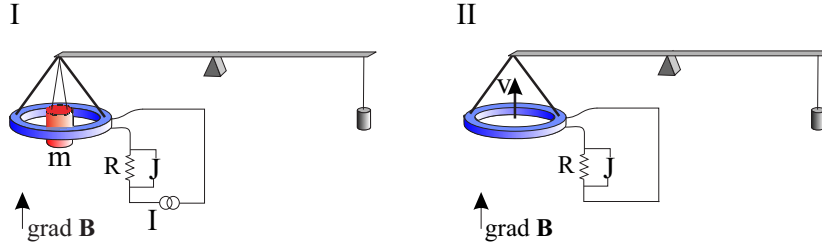


Figure 1.4: Watt balance in static mode I: The gravitational force is counter-balanced with an electromechanical force. This force is provoked by a coil with regulable current in a magnetic field gradient along the vertical axis (I). Voltages are measured on a Josephson junction. Dynamic mode II: The movement of the coil through the magnetic gradient with constant velocity v induces a current through the resistance R .

gradient, is measured over the resistance R creating the voltage \bar{U} :

$$\bar{U} = \frac{\partial \Phi}{\partial t} = \frac{\partial \Phi}{\partial z} \frac{\partial z}{\partial t} = v \frac{\partial \Phi}{\partial z}. \quad (1.5)$$

Inserting equation (1.5) into (1.4) will exclude the common flux gradient and a relationship between the electrical and mechanical realization of the Watt is found:

$$\bar{U}I = mgv. \quad (1.6)$$

The current I creates a voltage U over the resistance R and both voltages U and \bar{U} are measured against a Josephson voltage standard ($U \sim h/2e$), whereas the value of the resistance is determined with the quantum Hall effect ($R \sim h/ne^2$), such that we can finally express (1.6) as

$$m = \frac{U\bar{U}}{gvR} = A \frac{h}{gv}. \quad (1.7)$$

Here A contains some calibration parameters and depends on the Josephson constant and the von Klitzing constant. The Watt balance thus allows us to express the test mass in terms of the meter, the second and the Planck constant. One of the major advantages of the experiment is that neither the geometry of the coil nor the magnetic flux has to be known. The goal of the Paris Watt balance is a determination of the kilogram with a relative accuracy of 10^{-8} , which means that each parameter should be determined with some parts in 10^{-9} . The demand on the gravimeter therefore is to measure g with an accuracy of $\Delta g/g = 10^{-9}$.

1.2.3 Atom interferometer or falling corner cube

The g -measurement for the new Watt balance in Paris aims at an accuracy of $10^{-9} g$, or, using the unit Gal ($1 \text{ Gal} = 10^{-2} \text{ m/s}^2 = 10^{-3} g$), $1 \mu\text{Gal}$. The only two absolute gravimeters, which are able to reach such an accuracy are, until now, the atom gravimeter of Steve Chu in Stanford [46] and the commercial falling corner-cube gravimeter FG5 from Micro-g Solutions [58, 59]. Let us compare both gravimeters:

FG5	Steven Chu gravimeter
<ul style="list-style-type: none"> • <i>Setup</i> [93, 94] 	
<ul style="list-style-type: none"> • <i>Method</i> 	<p>Laser interferometer between two corner cubes, one of them in free fall. During a time T of free fall, the number of fringes N is counted to deduce the free fall distance L. The acceleration is derived as $a = 2L/T^2$.</p>
<ul style="list-style-type: none"> • <i>Repetition rate</i> 	<p>0.1 Hz repetition rate and 200 ms measurement time</p>
<ul style="list-style-type: none"> • <i>Short term resolution</i> 	<p>4-15 μGal/ 15 min</p>
<ul style="list-style-type: none"> • <i>Long term resolution</i> 	<p>1 μGal/ 3-10h</p>
<ul style="list-style-type: none"> • <i>Accuracy</i> 	<p>2 μGal</p>
<ul style="list-style-type: none"> • <i>Comments</i> 	<p>Low repetition rate increases sensitivity on low frequency noise</p>
	<p>Atom interferometer, whose signal is proportional to the difference in position covered during time 0 and T and during T and $2T$. This difference is proportional to the acceleration g.</p>
	<p>3 Hz repetition rate with 200 ms measurement time</p>
	<p>3 μGal/ 1 min</p>
	<p>0,1 μGal/ 48h</p>
	<p>3 μGal</p>
	<p>High repetition rate allows faster averaging</p>

The higher repetition rate and the possible improvements in sensitivity turned the balance towards the decision for an atom interferometer.

1.2.4 Experimental Realization

The scope of the gravimeter is not to be the limiting factor in the Watt-balance, what means a determination of g to a few times 10^{-9} . A second emphasis is put on the *compactness* and transportability of the apparatus, given evidence in the small number of lasers and a tight optical setup (see sections 3.3.3 and 4.3).

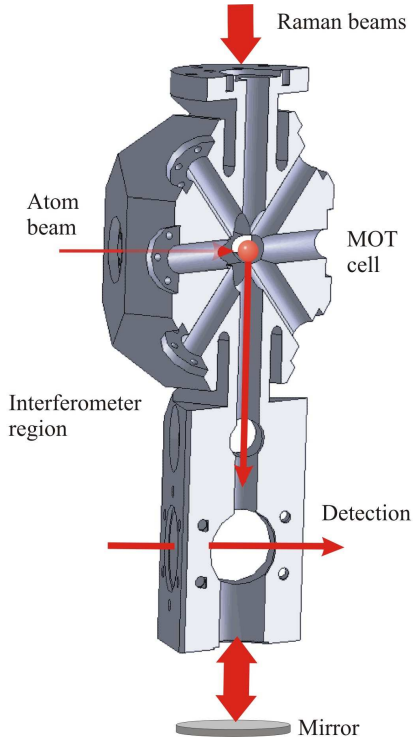


Figure 1.5: Schematic view of the gravimeter for the Watt balance. A flux of cold ^{87}Rb atoms from a 2D-MOT loads a 3D-MOT, where the atoms get trapped and further cooled in a molasses until they are released for a free fall along the vertical axis. During the free fall, an interferometer sequence is applied to the atoms by pulses of two Raman lasers and the acceleration of the atoms is read out in terms of state population in the detection region. The whole experiment is shielded from magnetic fields by a double-layer of mu-metal.

For a fast integration of the signal, a repetition rate of 3 Hz is aspired, what seems to be easily feasible with the *high loading rate* obtained with the 2D-MOT (section 5.1).

For a high precision acceleration-measurement, it is of fundamental importance to exclude all spurious accelerations other than the Earth acceleration g . The measurement platform will be *sound and vibration-isolated* and the *interferometer lasers* – whose phase noise acts exactly as acceleration noise – are *phase-stabilized* to about 1 mrad.

During the interferometer, atoms will spatially split, and for a cloud with a non-zero horizontal velocity component the interferometer will enclose a physical area. Any rotation will thus create a bothering phase-shift in the interferometer signal, which can become extremely annoying. A simple release of the atom cloud from an optical trap (molasses or dipole-trap) will avoid any disturbances during the release.

The hole experiment-chamber is inclosed in a *magnetic shield* and the light enters this closed region via *optical fibers*, whose out-couplers are rigidly fixed to the experiment chamber.

1.3 A gradiometer for the determination of G

The main part of this PhD work has been dedicated to the MAGIA (Misura Accurata di G mediante Interferometria Atomica) experiment at University of Florence. We will summarize the history and present state of G -measurements and explain the interest in a measurement with atom interferometry.

1.3.1 Significance of the Gravitational Constant G

Newton's law of gravitation expresses the force between two point masses m and M at a distance r

$$\mathbf{F} = G \frac{mM}{r^2} \cdot \frac{\mathbf{r}}{|\mathbf{r}|} \quad (1.8)$$

and represents the first discovery of one of the four fundamental forces. However, gravity is by far the weakest of all forces and the value of the Gravitational constant

$$G = (6.6742 \pm 0.0010) \cdot 10^{-11} \text{ m}^3 \text{ kg}^{-1} \text{ s}^{-2} \quad (\text{CODATA 2002}) \quad (1.9)$$

is known to only 150 ppm, which makes G one of the least known physical constants. The reasons for the *difficulties in the determination* of G can be found in the completely different nature of the gravitational force from the other forces: gravity cannot be shielded or compensated for. This very special property makes it the dominating force in the regimes of big masses and large distances but the very same characteristic makes it very hard to measure in laboratory experiments. Its weakness allows other forces to contribute with big systematic effects in laboratory experiments (a 1 kg mass is accelerated by another 1 kg mass at 10 cm distance with only $6 \cdot 10^{-9} \text{ m s}^{-2} \approx 6 \cdot 10^{-10} \text{ g}$!). Furthermore, there exists no known dependence on other physical constants for indirect determination. We will give some reasons why a more precise determination of G is important, besides the purely metrological interest:

- *Astronomy*: The factor $G M$ of astronomical objects can be determined extremely well. A better knowledge of G leads to a better knowledge of M , which in turn leads to a better physical understanding of celestial bodies. The luminosity of a star increases approximately as G^7 , which in turn caused discussions about the possibility of using the luminosity to determine temporal changes of G .
- *Geophysics*: Uncertainties of density and elastic parameters of the Earth are directly related to the uncertainties on G . The calibration of gradiometers, used for geophysical prospecting, is limited by the precision to with which G is known.
- *Modern physics*: The strong -, electromagnetic- and weak interaction exist embedded in space-time, whereas gravity itself is a deformation of space-time.

When trying to unify quantum theory and gravitation, the characteristic agitation of the quantum world (Heisenberg uncertainty) translates as a fluctuation of space-time on small (Planck) scales. In String theory, gravity can be seen as the string tension on this Planck scale and therefore enters the theory in a fundamental way [81]. It must be stated that as current theoretical understanding is incomplete, one cannot make yet full use of any precise value of G .

- *Predictions of G :* Using both, classical physics based on the 'standard model' and 'new' physics like string theory, some physicists tried to make theoretical predictions of G . An accurate knowledge would at least exclude some of these theories although at the moment many predictions from String theory provide a value, which is 100 times too big. References for all these topics can be found in [82].
- *Variations of G :* For completeness, we should mention the search for variations of G , as predicted by some theories: *Temporal variations* of G is of astrophysical interest, but the expected variations of 10^{-11} per year are not yet accessible by laboratory experiments. *Spatial variations* of G are predicted by the String theory, which assumes additional dimensions rolled up at small distances, causing a breakdown of the inverse square law of gravity. Experiments, searching for a *dependence of G on temperature, physical or chemical properties* of the masses, *magnetization* of the material and many other things are summarized in [82]. An eventual coupling between gravitation and electromagnetism can be described with the Kaluza-Klein theory and predicts a variation of G depending on the value of the Earth's electromagnetic field, thus on the latitude and longitude of the place of measurement. A fit of the best 44 measurements taken in past, yields a significantly lower χ^2 if G is not assumed constant [87].

A look at the latest G measurements in Fig. 1.6 reveals a discrepancy between the experimental values of several standard deviations – although the very last measurements seem to converge.

1.3.2 Past G -measurements

Fig. 1.6 shows the evolution of measurements over the last century and it is clearly visible that only modest improvements in accuracy could be made. Almost all methods rely on the torsion pendulum, designed by John Mitchell in 1790 and used by Cavendish to determine the density of the Earth in 1798 [84]⁴. Since then, the principle of the apparatus remained practically the same, whereas big efforts were taken on

⁴One typically finds the Cavendish-value for the density of the Earth of 5.48 times the density of water. The accepted value nowadays is 5.518. Actually, Cavendish made an error in the evaluation of his in detail reported measurement data, which lead to a relative density of 5.45 ± 0.22 . Assuming very accurate values for the Earth radius r_E and acceleration g this correctly calculated density yields a 1.3% overestimated G -value of $(6.76 \pm 0.27) \cdot 10^{-11} \text{ m}^3 \text{ kg}^{-1} \text{ s}^{-2}$ [83].

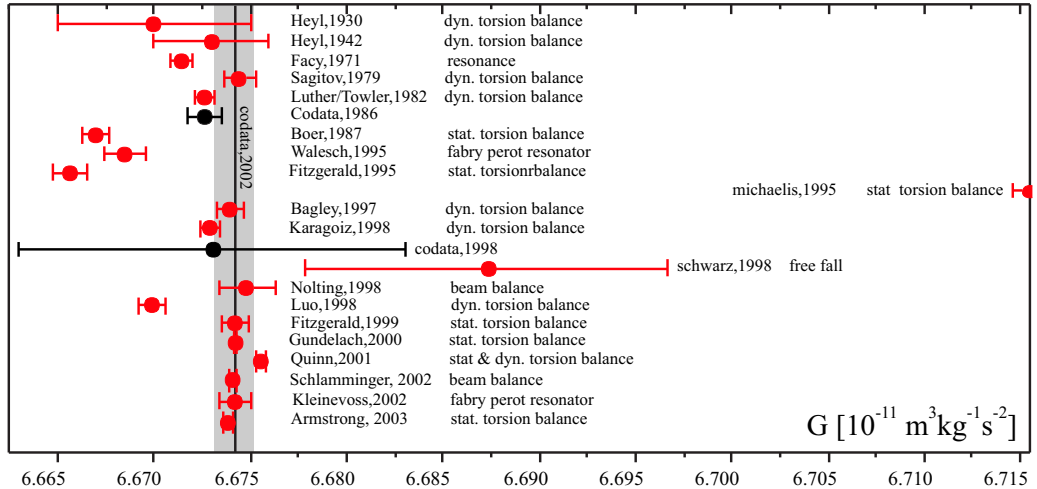


Figure 1.6: A selection of modern G -measurements and the method used. The latest 2002 CODATA value is plotted as a line with the uncertainty as a shadow. The only free-fall measurement is the one of Schwarz. References are from top to bottom [61, 62, 63, 64, 65, 66, 67, 68, 69, 70, 71, 72, 73, 74, 75, 76, 77, 78, 79, 80].

the improvement of experimental details. There are only few methods, which do not rely on a torsion pendulum and there has been only one free fall experiment without any suspension [72], based on the FG5 apparatus (see section 1.2.3). The last boom of experiments was provoked by the measurement of Michaelis et al. [69], which was about 50 standard deviations apart from previous measurements. Reasons are still not totally understood, but as a consequence the 1998 CODATA value for G was corrected and its uncertainty significantly increased to 1500 ppm with respect to the previous value of 1986 with 128 ppm uncertainty. This fact motivated many groups to start new experiments, which resulted in a more precise definition of the CODATA value in 2002 (see (1.9)) with an uncertainty of 150 ppm. The value is mainly based on the Gundlach experiment at University of Washington [76], up to date the most precise experiment: $G = (6.674215 \pm 0.000092) \cdot 10^{-11} \text{m}^3 \text{kg}^{-1} \text{s}^{-2}$, corresponding to an uncertainty of 14 ppm. In this experiment, 8 source masses were rotating around a suspended test mass. The rotation of the source masses induces a swinging of the suspended test mass, which tries to follow the source masses. The swinging can be counterbalanced by a servo on the suspension platform of the test mass, such that the suspending fiber does not tilt. Possible systematic effects arising from mass distribution could be minimized by choosing a plate as a test mass, which can be assumed as two-dimensional so that mass distribution gets insignificant. Permanent rotation of the system additionally reduces background noise. Fig. 1.7 shows a schematic view of the apparatus with the rectangular shaped test mass in the center and the spherical source masses on a rotating platform.

It is of course an appealing idea to perform a G measurement in space, where one

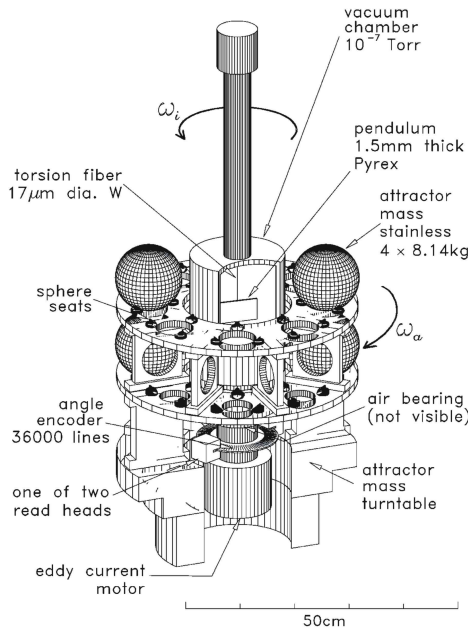


Figure 1.7: The torsion pendulum apparatus of the Washington group. A plate as a test mass is accelerated by rotating source masses and its swinging is balanced by a servo [76].

could get rid of the big gravitational offset and noise floor down on Earth. Several proposals have been made: SEE [89], GRAVCON, NEWTON, Galileo Galilei, (all [88]); but without any definite decision.

1.3.3 G measurement with atom interferometry

The disagreement among the past G measurements implies either *new physics* or *unknown sources of systematic errors* in these experiments.

New theoretical models could explain the discrepancies, as for example the above mentioned possible coupling between the electromagnetic field of the Earth and gravity [87]. Every new measurement of G could therefore be important to check the validity of such theories. If, in contrast, unknown sources of systematic errors would be the reason for the discrepancies, a new measurement technique, which implies totally different systematic effects, would be very important. During past, mainly all experiments relied on the torsion pendulum, or at least on suspended source masses, while the only free-fall experiment performed until now [72] has not reached high enough accuracy.

These arguments justify a new *free fall* experiment with cold atoms, even if the targeted accuracy of 100 ppm will not reach the value of the latest measurements. The big mass difference between the microscopic source masses ($^{87}\text{Rubidium}$ atoms) and the very heavy source masses (around 500 kg of tungsten), could also be of possible interest for theory. Atom interferometry will include different systematic errors and might exclude errors common to all suspended-mass experiments. Furthermore, the design

of the MAGIA experiment will cancel out many of the expected systematic errors and those remaining are mostly the same as in atomic clocks, where techniques for their precise characterization are well known. In contrary to the torsion pendulum, the limiting factor is expected to be the resolution rather than any systematic effect. A further experiment for the determination of G to a precision of 10^{-3} with the existing gravity gradiometer of M. Kasevich is in progress at Stanford University [43].

1.3.4 Experimental realization

The aim of the MAGIA experiment is the measurement of G with an *accuracy* of $\Delta G/G = 10^{-4}$. A hollow disk of 500 kg ton of tungsten creates a vertical acceleration of about $1 \cdot 10^{-7} g$, which should be measured with an accuracy of 10^{-4} on the huge background of the Earth acceleration. A *double differential measurement* with two clouds and two positions of the source masses (section 3.4.1) eliminates systematic effect such that an accuracy of $10^{-11} g$ on the source mass induced acceleration comes into reach.

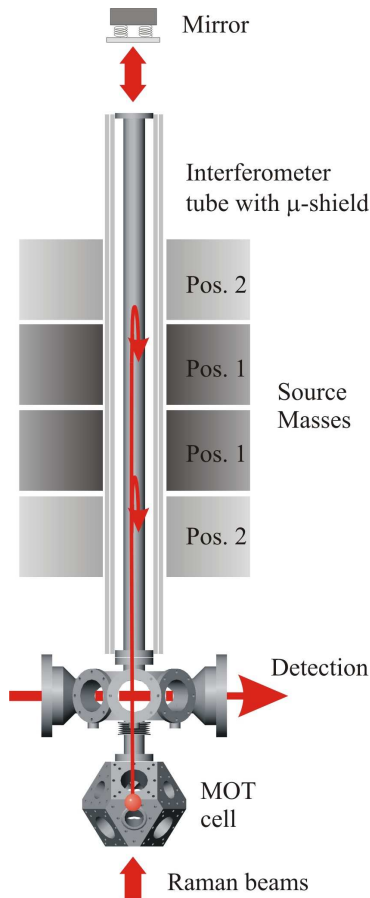


Figure 1.8: Schematic view of the experiment MAGIA (Italian for 'Accurate Measurement of G with Atom Interferometry'). Two clouds of ^{87}Rb atoms are collected in a 3D-MOT from either background gas or a 2D-MOT, cooled in moving molasses and launched up shortly after each other into the interferometer tube to different heights. The two clouds will be attracted in different manner by heavy source masses and their acceleration is measured with atom interferometry using counter-propagating Raman lasers as beam-splitters and mirror. After the return from the magnetically shielded interferometer tube, the interferometer signal is read out in the detection chamber and a double differential measurement between the two clouds and two source mass positions will lead to the determination of G .

The double difference suppresses all common mode accelerations, to which an accelerometer like the gravimeter is intrinsically sensitive. Nevertheless we put stringent

limits on vibrations and laser phase-noise (section 4.4), which are undistinguishable from acceleration noise, to keep the possibility of measuring g and to better characterize the apparatus; having in mind that the theoretical suppression might in practice not work as well as predicted.

An effect, which does not cancel out efficiently in this double difference is the *Sagnac effect*: a non-vertical launch implies the inclosure of an area in the atomic trajectories, making the apparatus sensitive on rotations. A careful alignment of verticality and eventual controlled rotations of the table are necessary.

The deleterious influence on the measurement signal of non-uniform *magnetic fields* is minimized first by the selection of magnetic unsensitive $m_F = 0$ states and second by a double layer magnetic shielding around the interferometer region.

A measurement with two clouds launched closely one after another requires a high loading rate of the atom-trap, and therefore we envisaged a *2D-MOT*, which is currently being set up. Meanwhile, one can accommodate with the *juggling* of two clouds to gain some loading time (section 5.2.3).

High demands are made on the source masses, which need to exhibit a *high enough density* for both a big signal and an efficient compensation of the gravity gradient, a necessity, which is described among other essential features of the masses in section 3.4. Since the distance between source and probe mass enters in Newton's law, efforts must be taken to provide an experiment-region of uniform potential as well as for accurate *position control* of the masses. It is this point of positioning, which also demands an environment with a *temperature*, stabilized to within 0.1 degrees.

Figure 1.8 shows the heart of the experimental setup: the vacuum chamber with MOT cell, detection chamber and the interferometer region (described in section 3.1). The laser beams to manipulate the atoms are all delivered to the experiment through optical fibers (section 3.3.5) to enhance the reliability of the apparatus. A short description of the apparatus is given in the caption of figure 1.8, whereas a detailed description of the various elements can be found elsewhere within this thesis.

1.4 Intuitive explanation of gravimeter and gradiometer

In this section, we will explain in an intuitive way the principle of atom interferometry in twelve steps, leading us via the gravimeter to the understanding of a gradiometer and our *G*-sensor.

Step One – Settings: A two level atom with ground state $|a\rangle$ and excited state $|b\rangle$ is initially found in state $|a\rangle$ with energy zero. A local oscillator (LO) provides a frequency ω_{LO} close to the resonance frequency ω_{ab} of the atomic transition $|a\rangle \rightarrow |b\rangle$.

Step Two – Excitation: A first pulse of radiation emitted by the local oscillator will put the atom into a superposition of state $|a\rangle$ and state $|b\rangle$:

$$|\psi\rangle = \frac{1}{\sqrt{2}}(|a\rangle + e^{i\omega_{ab}t}|b\rangle). \quad (1.10)$$

The internal dipole operator of the atom starts oscillating with frequency ω_{ab} . This kind of pulse is called $\pi/2$ -pulse; – see section 2.1.1 for a detailed explanation.

Step Three – Free evolution: While waiting for a time T without doing anything, the atomic wave-function evolves in time with a frequency ω_{ab} , which is not necessarily the same as ω_{LO} , thus introducing a phase difference

$$\Delta\phi = \int_0^T (\omega_{\text{LO}} - \omega_{ab})dt. \quad (1.11)$$

If during this time T the atoms move relative to the radiation field generated by the local oscillator by a distance Δz , an additional phase shift

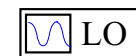
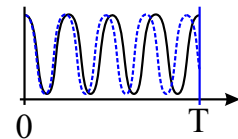
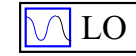
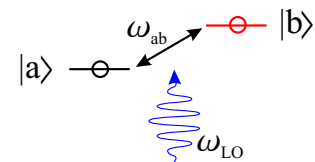
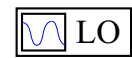
$$\Delta\phi = \mathbf{k}_{\text{LO}} \cdot \Delta\mathbf{z}. \quad (1.12)$$

has to be considered.

Step Four – Interferometer: Suppose now to apply a second $\pi/2$ -pulse to the atom. The final state of the atom will depend on the relative phase between the two oscillators. The atom will either be pushed into state $|b\rangle$ if the oscillators are still perfectly in phase, or back into state $|a\rangle$, if they are out of phase by π . The probability of finding the atom in state $|a\rangle$ or $|b\rangle$ after this pulse depends on the dephasing in the following way:

$$P_a = \frac{1}{2}(1 + \cos(\Delta\phi)). \quad (1.13)$$

As the result depends on the interference between two oscillators, we already built an *interferometer*.



Step Five – Clock: Let us have a closer look at the phase difference acquired during the time T of free evolution:

$$\Delta\phi = \mathbf{k}_{\text{LO}} \cdot \Delta\mathbf{z} + \int_0^T (\omega_{\text{LO}} - \omega_{\text{ab}}) dt. \quad (1.14)$$

Let us assume that the atom is falling downwards along the vertical z -axis, attracted by gravity. If the k -vector of the radiation is orthogonal to the direction of propagation, the scalar-product $\mathbf{k}_{\text{LO}} \cdot \Delta\mathbf{z}$ is zero and the phase difference only depends on how accurate our LO frequency matches the atomic resonance. With many atoms instead of one, the relative population of the two states can be used as a signal, to lock the LO frequency onto the atomic resonance; and in this case we have an *atomic clock*.



Step Six – Gravimeter: Now let us shine in the radiation along the vertical z -axis such that the scalar product becomes $\mathbf{k}_{\text{LO}} \cdot \Delta\mathbf{z} = k\Delta z \neq 0$. Let us furthermore assume that we exactly match the atomic resonance ω_{ab} and the LO frequency ω_{LO} . The interferometer phase signal in a gravity field

$$\Delta\phi = k \cdot \Delta z = \frac{1}{2}kgT^2 \quad (1.15)$$

is now proportional to the gravitational acceleration g . Since we know k and T very well, we can determine g . This is the basic principle of a *gravimeter*. We wonder, how easy this has been and continue some further.



Step Seven – Gradiometer: Now we introduce a second cloud of atoms (indicated as 2) below the first cloud (1), also falling in the gravity field parallel to the k -vector of the radiation. The difference signal between both interferometers

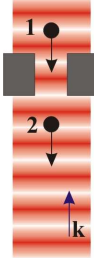
$$\Delta\phi_2 - \Delta\phi_1 = \frac{1}{2}k_{\text{LO}} (g_2 - g_1)T^2 \quad (1.16)$$

is proportional to the difference of gravity experienced by both clouds and we can claim to have a *gradiometer*.



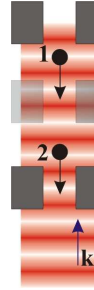
Step Eight – Mass: For curiosity, let us place a big mass between the two atom clouds and see, what effect it has: The upper cloud of atoms will be accelerated downwards towards the masses by Newton's law and the lower cloud upwards. The difference between the two signals contains the gravity gradient and in addition will include twice the signal produced by the acceleration of the source mass ϕ_{mass} :

$$\Delta\phi_2 - \Delta\phi_1 = \frac{1}{2}k_{\text{LO}}(g_2 - g_1)T^2 + 2\phi_{\text{mass}}. \quad (1.17)$$



Step Nine – G sensor: Now we remove the mass from its original position between the two clouds (I) and place it above the upper cloud. Then we place a second mass below the lower cloud. In this new configuration (II), the upper cloud is attracted upwards and vice versa. The difference between the signals in configuration I and II yields the following result:

$$(\Delta\phi_2^I - \Delta\phi_1^I) - (\Delta\phi_2^{II} - \Delta\phi_1^{II}) = 2\phi_{\text{mass}}^I + 2\phi_{\text{mass}}^{II}. \quad (1.18)$$

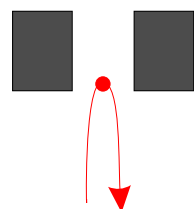


We expect this phase signal, provoked by the masses' acceleration, to be around 0.4 rad for the experimental conditions of the MAGIA experiment. The only signal remaining after the double differential measurement is proportional to the acceleration a induced on the atoms by the source masses. From a , it is possible to deduce G , presuming the knowledge of the density distribution ρ_{mass} of the source mass m_{mass} and the geometry of the experiment.

$$\mathbf{a}_{\text{mass}} = \int_{\text{mass}} G \frac{\rho_{\text{mass}}}{r^2} \frac{\mathbf{r}_{am}}{|\mathbf{r}_{am}|} d^3r \quad (1.19)$$

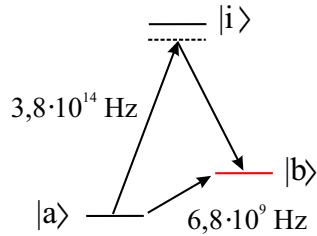
Here, r is the distance between mass and atoms and \mathbf{r}_{am} the vector pointing from the atoms to the mass. We herewith understood the idea of a *G sensor*. It is important to point out that besides gravity and the gravity gradient, all systematic effects cancel out during this double differential measurement, except of those which are different at both positions *and* change during the time between configuration I and II, typically 10 minutes.

Step Ten – Displacement Δz : By now we know how to get a signal, but what about the size of the signal? The gravitational force is very small, and the bigger the phase shift, the better it is. The signal of one interferometer is $k\Delta z$, where Δz is the displacement of the atoms in the gravitational field of the source masses; and as we have seen, all other terms cancel out. To realize a big displacement of the atom trajectories, the atoms need to be as long and as close as possible to the (heavy) source masses, which implies a low velocity of



the atoms. This can be achieved by launching the atoms up such that the maximum attraction is located around the turning point of the atomic trajectory. We therefore need an *atomic fountain*. If the goal of the experiment is to measure g and not G , a fountain can nevertheless be useful to increase the interferometer time T , which might be limited by the size of the apparatus.

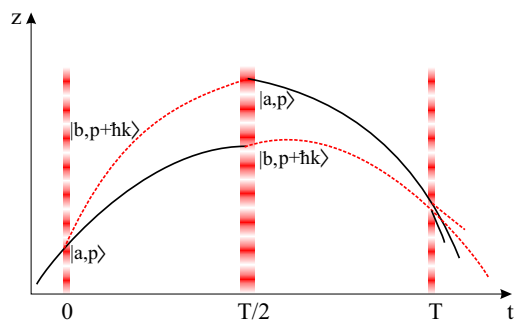
Step Eleven – Wave-vector k : In $^{87}\text{Rubidium}$, which is used in both experiments, the transition frequency between the two ground states is $6.8 \cdot 10^9 \text{ Hz}$. This microwave-frequency does not correspond to big wave-vector k . To increase the phase resolution, one can excite the atom with an optical two photon Raman transition via an intermediate state. For rubidium, the transition can be performed by two photons, each with a frequency of $f = 3.8 \cdot 10^{14} \text{ Hz}$.



Using *counter-propagating Raman beams*, the atom will absorb one photon coming from below (kick upwards) and do a stimulated emission downwards to get a further momentum kick upwards. With this configuration, the effective k -vector $k_{\text{eff}} \approx 2 \cdot 2\pi f/c$ is in the optical domain and we consequently gain a factor of 10^5 on the transferred momentum and in the final phase shift $\Delta\phi$.

Step Twelve – Three pulse interferometer:

As we explained before, the first Raman-pulse will transfer the population initially in state $|a\rangle$ in a coherent superposition of state $|a\rangle$ and $|b\rangle$. The big momentum transferred during the interaction with the light spatially separates the atoms in state $|b\rangle$ from the initial trajectory. After a time T , the wave-functions will no longer overlap and one needs to introduce an additional pulse in the middle of the interferometer to redirect the trajectories to a common point, acting like a mirror in an optical interferometer.



Simply speaking, the faster atoms will be decelerated and the slower ones accelerated. The momentum transfer is coupled with a total population transfer and this kind of population-inverting pulse is called π -pulse (see chapter 2.1.1)⁵. To stay with the convention, let us introduce this pulse at time T such that the total interferometer time becomes $2T$ (see image on right). Therefore, the separation accumulated during the first T is compensated exactly at time $2T$, the wave-functions will overlap again and

⁵In reality, the effect of the second pulse is not only the redirection of the trajectories, but also an echo-effect that increases the resolution of the interferometer.

the probability amplitudes related to the two interferometric paths will interfere. The total interferometer sequence such consists of a $\pi/2$, π and another $\pi/2$ pulse. The interferometer signal is now the difference between the dephasing during the first and the second half of the interferometer:

$$\begin{aligned}\Delta\phi &= (\Delta\phi(2T) - \Delta\phi(T)) - (\Delta\phi(T) - \Delta\phi(0)) \\ &= \frac{1}{2}k_{\text{eff}}g((2T)^2 - T^2 - T^2 + 0) = k_{\text{eff}}gT^2.\end{aligned}\quad (1.20)$$

This phase signal reaches $\Delta\phi \approx 3.6 \cdot 10^6$ rad for a typical interferometer spacing of $T=150$ ms.

Chapter 2

Theory of Raman light pulse interferometry

Both gravimeter and gradiometer make use of the identical type of atom-interferometer, which is based upon the interaction of Raman laser pulses with an atom at three distinct times, as was pointed out in the previous section 1.4.

The present chapter will provide some tools for the calculation of this phase shift. The first part will sketch the derivation of the temporal evolution of a two- and three-level atom in a light field and we will use the results to calculate a three-pulse Raman interferometer in the second part. The third and last part of this chapter will explain, how laser phase-noise will transmit onto the interferometer phase.

2.1 Atoms and Light

The scope of this section is to summarize the most important results of atom-light interaction and give an insight of how and under which assumptions they are derived. We will use these equations later as tools to describe and understand the interferometer. We will not enter the theory of laser cooling, which can be found in many textbooks. In our derivation, we will loosely follow [38]. Instead of atomic wave-packets, we will consider plane-waves to describe the interaction. We will make some remarks about this plane-wave approximation towards the end of this section.

2.1.1 Two level atom in a light-field

The time dependent Schrödinger equation for the atomic wave-function $|\psi(t)\rangle$ is

$$\mathcal{H}|\psi(t)\rangle = i\hbar \frac{|\mathrm{d}\psi(t)\rangle}{\mathrm{d}t} \quad (2.1)$$

with the total Hamiltonian

$$\mathcal{H}(t) = \mathcal{H}_0 + \mathcal{H}'(t), \quad (2.2)$$

where \mathcal{H}_0 is the internal Hamiltonian with eigenenergies $E_n = \hbar\omega_n$ and $\mathcal{H}'(t)$ is the interaction Hamiltonian of the atom with the light field field \mathbf{E} of constant intensity. We can expand the solution $|\psi(t)\rangle$ of (2.1) in terms of the eigenfunctions $|\varphi_n\rangle$ of \mathcal{H}_0 and factor out the rapid oscillating terms of frequency ω_k to remain with slowly oscillating coefficients c_k :

$$|\psi(t)\rangle = \sum_k c_k(t) |\varphi_k\rangle e^{-i\omega_k t} \quad (2.3)$$

Substituting (2.3) into (2.1) by using (2.2), multiplying from the left with $\langle\varphi_j^*|$ and integrating over d^3r yields

$$i\hbar \frac{dc_j(t)}{dt} = \sum_k c_k(t) \mathcal{H}'_{jk}(t) e^{i\omega_{jk} t} \quad (2.4)$$

with $\mathcal{H}'_{jk}(t) = \langle\varphi_j|\mathcal{H}'(t)|\varphi_k\rangle$ and $\omega_{jk} = (\omega_j - \omega_k)$. The interaction term \mathcal{H}' has only non-diagonal matrix elements.

Our first *approximation* is to assume a *two level atom* and to truncate the sum (2.4) after $k = 2$, naming the two remaining components a and b , respectively. This approximation is reasonable if we have two states with a long lifetime, and if the detuning of the coupling light field from the transition $|a\rangle \rightarrow |b\rangle$ is far less than the distance to another state. Equation (2.4) reduces to

$$\begin{aligned} i\hbar \frac{dc_a(t)}{dt} &= c_b(t) \mathcal{H}'_{ab}(t) e^{-i\omega_{ba} t} \\ i\hbar \frac{dc_b(t)}{dt} &= c_a(t) \mathcal{H}'_{ba}(t) e^{i\omega_{ba} t} \end{aligned} \quad (2.5)$$

with $\omega_{ba} = \omega_b - \omega_a$ the atomic resonance frequency. The wave-function in the base $\{|a\rangle, |b\rangle\}$ is

$$|\psi(t)\rangle = c_a(t) |a\rangle e^{-i\omega_a t} + c_b(t) |b\rangle e^{-i\omega_b t}, \quad (2.6)$$

and the Hamiltonian (2.2) of this system is

$$\begin{aligned} \mathcal{H}(t) &= \mathcal{H}_0 + \mathcal{H}'(t) \\ &= \hbar\omega_a |a\rangle\langle a| + \hbar\omega_b |b\rangle\langle b| - \mathbf{d} \cdot \mathbf{E}(t) \end{aligned} \quad (2.7)$$

with the interaction Hamiltonian \mathcal{H}' . For simplicity, we abbreviated the electric dipole operator of the transition $a \leftrightarrow b$ with

$$\mathbf{d} = \hat{\mathbf{d}}_{ab} + \hat{\mathbf{d}}_{ba}, \quad \text{where } \hat{\mathbf{d}}_{ij} = |i\rangle\langle j| \mathbf{d}_{ij}. \quad (2.8)$$

The solution of (2.5) furthermore requires two approximations: the first one is the *rotating wave approximation (RWA)*, which implies a detuning δ of the laser frequency ω_L from resonance much smaller than the transition frequency:

$$\delta = (\omega_L - \omega_{ba}) \ll \omega_{ba}. \quad (2.9)$$

In this case, one can neglect the rapid oscillating terms of the order $(\omega_{ba} + \omega_L)$ compared with slowly changing terms δ .

The second approximation, the *dipole approximation*, assumes a homogeneous E-field

$$\mathbf{E}(t) = \mathbf{E}_0 \cos(\omega_L t + \phi_{L,0}) \quad (2.10)$$

within the location of the atom and is used when evaluating the integral $\langle \varphi_j | \mathcal{H}'(t) | \varphi_k \rangle$. We define the Rabi frequency at resonance Ω and out of resonance Ω_r as follows:

$$\Omega = \frac{\langle b | \mathcal{H}' | a \rangle}{\hbar} = -\frac{\langle b | \mathbf{d} \cdot \mathbf{E}_0 | a \rangle}{\hbar} \quad (2.11)$$

$$\Omega_r = \sqrt{\delta^2 + \Omega^2}. \quad (2.12)$$

We can write $\mathbf{d} \cdot \mathbf{E}(t) = -\hbar\Omega \cos(\omega_L t + \phi_0)$. The time evolution of the slowly varying coefficients (2.5) becomes:

$$\begin{aligned} \dot{c}_a(t) &= -i\frac{\Omega}{2} e^{i(\delta t - \phi_{L,0})} c_b(t) \\ \dot{c}_b(t) &= -i\frac{\Omega^*}{2} e^{-i(\delta t + \phi_{L,0})} c_a(t). \end{aligned} \quad (2.13)$$

We write the new approximated Hamiltonian in the base of $\{|a\rangle, |b\rangle\}$ (where we already separated $e^{-i\omega_{a,b}}$):

$$\mathcal{H} = \frac{\hbar}{2} \begin{pmatrix} 0 & \Omega e^{-i(t\delta + \phi_{L,0})} \\ \Omega e^{i(t\delta + \phi_{L,0})} & 0 \end{pmatrix}. \quad (2.14)$$

The time dependence in (2.13) and therefore of the Hamiltonian can be eliminated by a transformation into a rotating frame, turning with frequency δ . In the new base $\{|\bar{a}\rangle, |\bar{b}\rangle\} = \{e^{-\delta t}|a\rangle, e^{\delta t}|b\rangle\}$, the Hamiltonian is

$$\hat{\mathcal{H}} = \frac{\hbar}{2} \begin{pmatrix} -\delta & \Omega e^{-i\phi_{L,0}} \\ \Omega e^{i\phi_{L,0}} & \delta \end{pmatrix}. \quad (2.15)$$

Light shift: The eigenvalues of the new Hamiltonian $\hat{\mathcal{H}}$, $\lambda_{\pm} = \pm \frac{\hbar\Omega_r}{2}$ are shifted from the eigenvalues of the unperturbed Hamiltonian ¹ $\mp \frac{\hbar\delta}{2}$ by

$$\begin{aligned} \Delta E_a &= \frac{\hbar}{2} (-\delta + \Omega_r) \quad \text{and} \\ \Delta E_b &= \frac{\hbar}{2} (\delta - \Omega_r). \end{aligned} \quad (2.16)$$

For big detuning $|\delta| \gg \Omega$, the shift due to the radiation can be developed in series of Ω/δ , which in second order gives

$$\left\| \Delta E_a = -\Delta E_b = \frac{\hbar}{2} (-\delta + \Omega_r) = \frac{\hbar}{2} \left(-\delta + \delta \sqrt{1 + \left(\frac{\Omega}{\delta} \right)^2} \right) \approx \frac{\hbar\Omega^2}{4\delta}. \right. \quad (2.17)$$

This shift, due to the radiation, is called *light shift*, or *AC-Stark shift*. If the light intensity is not homogeneous, the energy will be position dependent, what is the origin of the dipole force.

¹The unperturbed Hamiltonian is equal to (2.15) without the off-diagonal matrix elements

System evolution: To derive the solution for the time evolution of the coefficients $c_i(t)$ (2.13) one has to do the following (see [38]): Calculate the eigen-states of the new Hamiltonian $\hat{\mathcal{H}}$, transform $|\psi\rangle$ into the rotating frame and project it onto the new basis of eigen-states, write down the evolution during a time τ and perform a back-transformation. The solutions for the coefficients are the following:

$$\begin{aligned} c_a(t_0 + \tau) &= \\ &\left\{ c_a(t_0) \left[\cos\left(\frac{\Omega_r \tau}{2}\right) - i \frac{\delta}{\Omega_r} \sin\left(\frac{\Omega_r \tau}{2}\right) \right] + c_b(t_0) e^{i(\delta t_0 + \phi_{L,0})} \left[-i \frac{\Omega}{\Omega_r} \sin\left(\frac{\Omega_r \tau}{2}\right) \right] \right\} e^{i \frac{\delta \tau}{2}} \\ c_b(t_0 + \tau) &= \\ &\left\{ c_a(t_0) e^{-i(\delta t_0 + \phi_{L,0})} \left[-i \frac{\Omega}{\Omega_r} \sin\left(\frac{\Omega_r \tau}{2}\right) \right] + c_b(t_0) \left[\cos\left(\frac{\Omega_r \tau}{2}\right) + i \frac{\delta}{\Omega_r} \sin\left(\frac{\Omega_r \tau}{2}\right) \right] \right\} e^{-i \frac{\delta \tau}{2}}. \end{aligned} \quad (2.18)$$

For zero detuning $\delta = 0$, (2.18) simplify to

$$\begin{aligned} c_a(t_0 + \tau) &= c_a(t_0) \cos\left(\frac{\Omega \tau}{2}\right) + c_b(t_0) e^{-i(\frac{\pi}{2} - \phi_{L,0})} \sin\left(\frac{\Omega \tau}{2}\right) \\ c_b(t_0 + \tau) &= c_a(t_0) e^{-i(\frac{\pi}{2} + \phi_{L,0})} \sin\left(\frac{\Omega \tau}{2}\right) + c_b(t_0) \cos\left(\frac{\Omega \tau}{2}\right). \end{aligned} \quad (2.19)$$

Assuming $c_a(0) = 1$ and $c_b(0) = 0$, we let the atom interact with the light for a certain time τ . The probability P of the atom being in state a or b is the following:

$$\begin{aligned} P_a(\tau) = |c_a(\tau)|^2 &= \left(\frac{\Omega}{\Omega_r}\right)^2 \cos^2\left(\frac{\Omega_r \tau}{2}\right) = \left(\frac{\Omega}{\Omega_r}\right)^2 \frac{1 + \cos(\Omega_r \tau)}{2} \\ P_b(\tau) = |c_b(\tau)|^2 &= \left(\frac{\Omega}{\Omega_r}\right)^2 \sin^2\left(\frac{\Omega_r \tau}{2}\right) = \left(\frac{\Omega}{\Omega_r}\right)^2 \frac{1 - \cos(\Omega_r \tau)}{2}. \end{aligned} \quad (2.20)$$

The probability is oscillating with the Rabi frequency and the amplitude depends on detuning. For zero detuning, a pulse of length $\tau = \pi/\Omega$ (*Pi-pulse*) will invert the occupation probability (mirror) and a pulse of length $\tau = \pi/2\Omega$ (*Pi-half pulse*) will equally distribute the probability (beam-splitter).

2.1.2 External degrees of freedom

We now consider the external degrees of freedom of the atom and write the atomic wave-function as a travelling plane wave as

$$|\psi(\mathbf{r}, t)\rangle = a e^{-i(\omega t - \frac{\mathbf{p} \cdot \mathbf{r}}{\hbar})} |\psi_0\rangle \quad (2.21)$$

with an amplitude factor a and $|\psi_0\rangle \equiv |\psi(\mathbf{r} = 0, t = 0)\rangle$. Including the external degrees of freedom in our Hamiltonian (2.7) leads to:

$$\begin{aligned} \mathcal{H}(t) &= \hbar \omega_a |a\rangle \langle a| + \hbar \omega_b |b\rangle \langle b| + \frac{\mathbf{p}^2}{2m} - \mathbf{d} \cdot \mathbf{E}(\mathbf{r}, t) \\ &= \mathcal{H}_0 + \mathcal{H}_{mov} + \mathcal{H}'(t), \end{aligned} \quad (2.22)$$

where \mathcal{H}_{mov} is the Hamiltonian of the free movement of the atom. The atomic plane-wave is travelling in the light field

$$\mathbf{E}(\mathbf{r}, t) = \mathbf{E}_0 \cos(\omega_L t - \mathbf{k}\mathbf{r} + \phi_{L,0}). \quad (2.23)$$

The interaction term with the light can be written using the closure relation:

$$\mathbf{1} \cdot e^{\pm i\mathbf{k} \cdot \mathbf{r}} = \int d^3 p e^{\pm i\mathbf{k} \cdot \mathbf{r}} |\mathbf{p}\rangle \langle \mathbf{p}| = \int d^3 p |\mathbf{p} \pm \hbar\mathbf{k}\rangle \langle \mathbf{p}|. \quad (2.24)$$

The internal and external degrees of freedom in our two level system are coupled; the absorption and emission of a photon is correlated with a momentum change. The two possible eigenstates $|\varphi_{k,p_k}\rangle$ of this two level system are $|a, \mathbf{p}\rangle$ and $|b, \mathbf{p} + \hbar\mathbf{k}\rangle$, which correspond to a ground state $|a\rangle$ with momentum \mathbf{p} and an excited state $|b\rangle$ with an additional momentum $\hbar\mathbf{k}$, acquired during the absorption of a photon.

According to (2.6), we write the wave-function in our new base $|a, \mathbf{p}\rangle, |b, \mathbf{p} + \hbar\mathbf{k}\rangle$ with time dependent coefficients $c_{k,p_k}(t)$, which we decompose into

$$c_{a,p}(t) = c_a(t) e^{-i\frac{|\mathbf{p}|^2}{2m\hbar}t} \quad c_{b,p+\hbar k}(t) = c_b(t) e^{-i\frac{(|\mathbf{p}+\hbar\mathbf{k})^2}{2m\hbar}t}, \quad (2.25)$$

with the $c_{a,b}$ being the same coefficients as in section 2.1.1 with the evolution (2.13). The wave-function thus is:

$$|\psi(t)\rangle = c_a(t) |a, \mathbf{p}\rangle e^{-i(\omega_a + \frac{|\mathbf{p}|^2}{2m\hbar})t} + c_b(t) |b, \mathbf{p} + \hbar\mathbf{k}\rangle e^{-i(\omega_b + \frac{(|\mathbf{p}+\hbar\mathbf{k})^2}{2m\hbar})t}. \quad (2.26)$$

The eigenenergies of the system are now

$$\begin{aligned} E_{|a,p\rangle} &= \hbar\omega_a + \frac{\mathbf{p}^2}{2m} = \hbar\bar{\omega}_a \quad \text{and} \\ E_{|b,p+\hbar k\rangle} &= \hbar\omega_b + \frac{(\mathbf{p} + \hbar\mathbf{k})^2}{2m} = \hbar\bar{\omega}_b. \end{aligned} \quad (2.27)$$

$\bar{\omega}_{a,b}$ is shifted from the original $\omega_{a,b}$ (without motion) by the Doppler effect and the photon recoil. To know the time evolution of the system, we simply need to replace the laser detuning δ by the new detuning

$$\left\| \bar{\delta} = \omega_L - \left(\frac{E_{|b,p+\hbar k\rangle} - E_{|a,p\rangle}}{\hbar} \right) = \omega_L - \omega_{ab} + \frac{\mathbf{k} \cdot \mathbf{p}}{m} + \frac{\hbar\mathbf{k}^2}{2m} \right. \quad (2.28)$$

in the equations (2.18) and (2.19).

2.1.3 Raman transitions

We have seen in section 1.4 that Raman pulses are very suitable to drive transitions between two long living states and to transfer a big momentum to the atoms. Let us

assume an atom with two ground states $|a\rangle$ and $|b\rangle$ and an intermediate excited level $|i\rangle$, interacting with two lasers

$$\mathbf{E}_{L1}(\mathbf{r}, t) = \mathbf{E}_{L1,0} \cos(\omega_{L1}t - \mathbf{k}_{L1}\mathbf{r} + \phi_{L1,0}) \quad \text{and} \quad (2.29)$$

$$\mathbf{E}_{L2}(\mathbf{r}, t) = \mathbf{E}_{L2,0} \cos(\omega_{L2}t - \mathbf{k}_{L2}\mathbf{r} + \phi_{L2,0}) \quad (2.30)$$

with frequency ω_{L1} detuned by Δ_{ai1} from transition frequency ω_{ia} and frequency ω_{L2} as shown in Figure 2.1. Δ_{lmn} are the detunings of the laser frequency ω_{Ln} relative to the transition frequencies ω_{lm} .

Like in the previous section, the external degrees of freedom are closely coupled to the

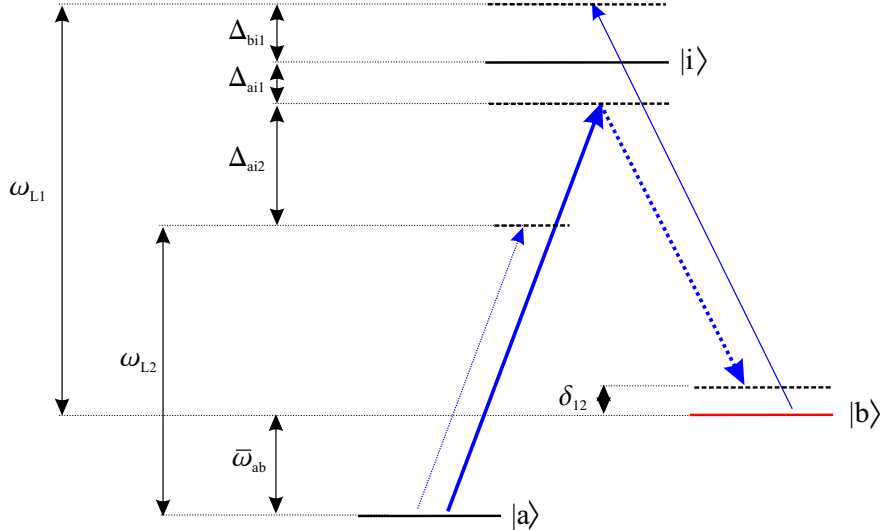


Figure 2.1: Four possible excitations of a three level system by two Raman lasers. For big detuning Δ_{ai1} of laser 1 (solid arrow) from transition $|a\rangle \rightarrow |i\rangle$, and small detuning δ_{12} , the only probable transition is the one indicated by thick arrows.

internal ones, because the atom can only change its state by absorption or stimulated emission of the laser photons. The atom in state $|a, \mathbf{p}\rangle$ can be exited to state $|i\rangle$ by laser 1 or laser 2, which implicates the following possible states: $|i, \mathbf{p} + \hbar\mathbf{k}_{L1}\rangle$ and $|i, \mathbf{p} + \hbar\mathbf{k}_{L2}\rangle$. By stimulated emission the atom can finally transfer to state $|b, \mathbf{p} + \hbar\mathbf{k}_{L1} - \hbar\mathbf{k}_{L2}\rangle$. (see Fig. 2.2). The energies of these states are shifted by the Doppler effect and the recoil energy:

$$\begin{aligned} E_{|a,\mathbf{p}\rangle} &= \hbar\omega_a + \frac{\mathbf{p}^2}{2m} \equiv \hbar\bar{\omega}_a \\ E_{|b,\mathbf{p}+\hbar\mathbf{k}_{L1}-\hbar\mathbf{k}_{L2}\rangle} &= \hbar\omega_b + \frac{(\mathbf{p} + \hbar(\mathbf{k}_{L1} - \mathbf{k}_{L2}))^2}{2m} \equiv \hbar\bar{\omega}_b \end{aligned} \quad (2.31)$$

and we define the detuning δ_{12} of the effective laser frequency ω_{eff} from the transition frequency $\bar{\omega}_{ba} = \bar{\omega}_b - \bar{\omega}_a$ as:

$$\delta_{12} = (\omega_{L1} - \omega_{L2}) - (\bar{\omega}_b - \bar{\omega}_a) = \omega_{\text{eff}} - \left(\omega_{ba} + \frac{\mathbf{p} \cdot \mathbf{k}_{\text{eff}}}{m} + \frac{\hbar\mathbf{k}_{\text{eff}}^2}{2m} \right). \quad (2.32)$$

We used the definition the effective frequency, wave-vector and offset phase of both lasers according to:

$$\begin{aligned}\phi_{L1}(t) - \phi_{L2}(t) &= (\omega_{L1} - \omega_{L2})t - (\mathbf{k}_{L1} - \mathbf{k}_{L2})\mathbf{r} + (\phi_{L1,0} - \phi_{L2,0}) \\ &= \omega_{\text{eff}}t - \mathbf{k}_{\text{eff}}\mathbf{r} + \phi_{\text{eff},0}.\end{aligned}\quad (2.33)$$

We will suppose first that the beams propagate along the axis of the motion of the atoms and second that the detuning Δ_{ai1} of laser 1 from transition $|a\rangle \rightarrow |i\rangle$ is much bigger than the detuning δ_{12} ; and that Δ_{ai1} is also much bigger than the natural linewidth Γ of level $|i\rangle$:

$$\Delta_{ai1} \gg \delta_{12}, \quad \Delta_{ai1} \gg \Gamma. \quad (2.34)$$

In this case, the probability of a transition $|a\rangle \rightarrow |i\rangle$ is very small and no spontaneous emission can occur. We will see that in this case of big detuning, the intermediate state can be eliminated and the system treated as a two-level system with resonance frequency $\bar{\omega}_{ba}$ and a momentum difference of $\hbar\mathbf{k}_{\text{eff}}$.

The total Hamiltonian of a three level system in the absence of spontaneous emission is given by

$$\mathcal{H}(t) = \underbrace{\hbar\omega_a|a\rangle\langle a| + \hbar\omega_b|b\rangle\langle b| + \hbar\omega_i|i\rangle\langle i|}_{\mathcal{H}_0} + \underbrace{\frac{\mathbf{p}^2}{2m} - \mathbf{d} \cdot (\mathbf{E}_{L1}(\mathbf{r}, t) + \mathbf{E}_{L2}(\mathbf{r}, t))}_{\mathcal{H}_{\text{mov}}}, \quad (2.35)$$

where \mathbf{d} is again an abbreviation for all four different dipole operators, corresponding to the four possible transitions $|a\rangle \leftrightarrow |i\rangle$ and $|b\rangle \leftrightarrow |i\rangle$ (see (2.8)). We define the Rabi frequencies, corresponding to the excitation of the two transitions by either laser:

$$\begin{aligned}\Omega_{ai1} &= -\frac{\langle i|\mathbf{d} \cdot \mathbf{E}_{0,L1}|a\rangle}{\hbar}, & \Omega_{bi1} &= -\frac{\langle i|\mathbf{d} \cdot \mathbf{E}_{0,L1}|b\rangle}{\hbar}, \\ \Omega_{ai2} &= -\frac{\langle i|\mathbf{d} \cdot \mathbf{E}_{0,L2}|a\rangle}{\hbar}, & \Omega_{bi2} &= -\frac{\langle i|\mathbf{d} \cdot \mathbf{E}_{0,L2}|b\rangle}{\hbar}.\end{aligned}\quad (2.36)$$

We write the atomic wave-function $|\psi\rangle$ as a linear superposition of these four states according to (2.26) and insert it in the Shrödinger equation (2.1) to get the time evolution of the coefficients $c_{a,p} \equiv \tilde{c}_a$, $c_{b,p+\hbar(\mathbf{k}_1-\mathbf{k}_2)} \equiv \tilde{c}_b$, $c_{i,p+\hbar\mathbf{k}_1} \equiv \tilde{c}_{i1}$ and $c_{i,\hbar+\hbar\mathbf{k}_2} \equiv \tilde{c}_{i2}$:

$$\begin{aligned}\dot{\tilde{c}}_a(t) &= -i\frac{\Omega_{ai1}^*}{2}e^{i\Delta_{ai1}t-i\phi_{L1,0}}\tilde{c}_{i1}(t) - i\frac{\Omega_{ai2}^*}{2}e^{i\Delta_{ai2}t-i\phi_{L2,0}}\tilde{c}_{i2}(t) \\ \dot{\tilde{c}}_b(t) &= -i\frac{\Omega_{bi1}^*}{2}e^{i\Delta_{bi1}t-i\phi_{L1,0}}\tilde{c}_{i1}(t) - i\frac{\Omega_{bi2}^*}{2}e^{i\Delta_{bi2}t-i\phi_{L2,0}}\tilde{c}_{i2}(t) \\ \dot{\tilde{c}}_{i1}(t) &= -i\frac{\Omega_{ai1}^*}{2}e^{i\Delta_{ai1}t-i\phi_{L1,0}}c_{a,p+\hbar\mathbf{k}_1}(t) - i\frac{\Omega_{bi1}^*}{2}e^{i\Delta_{bi1}t-i\phi_{L1,0}}c_{b,p+\hbar\mathbf{k}_1}(t) - \frac{\Gamma}{2}c_{i,p+\hbar\mathbf{k}_1} \\ \dot{\tilde{c}}_{i2}(t) &= -i\frac{\Omega_{ai2}^*}{2}e^{i\Delta_{ai2}t-i\phi_{L2,0}}c_{a,p+\hbar\mathbf{k}_2}(t) - i\frac{\Omega_{bi2}^*}{2}e^{i\Delta_{bi2}t-i\phi_{L2,0}}c_{b,p+\hbar\mathbf{k}_2}(t) - \frac{\Gamma}{2}c_{i,p+\hbar\mathbf{k}_2}.\end{aligned}\quad (2.37)$$

From the intermediate state $|i\rangle$, we added a small loss channel due to spontaneous emission to the coupling terms with the states $|a\rangle$ and $|b\rangle$, with Γ being the natural linewidth of the state. This term would be important for small detuning Δ_{ai1} .

In the limit of $\Delta_{ai1} \gg \Omega$, the coefficients $\tilde{c}_{i1,2}$ can be adiabatically removed ([8, 33]), reducing the four equations to only two equations similar to a two-level system (2.13):

$$\begin{aligned}\dot{\tilde{c}}_a(t) &= \\ -i\left(\frac{|\Omega_{ai1}|^2}{4\Delta_{ai1}+2i\Gamma} + \frac{|\Omega_{ai2}|^2}{4\Delta_{ai2}+2i\Gamma}\right)\tilde{c}_a(t) - i\frac{\Omega_{ai1}^*\Omega_{bi2}}{2\Delta_{ai2}+i\Gamma}e^{i\delta_{12}t+i(\phi_{L1,0}-\phi_{L2,0})}\tilde{c}_b(t) \\ \dot{\tilde{c}}_b(t) &= \\ -i\left(\frac{|\Omega_{bi1}|^2}{4\Delta_{bi1}+2i\Gamma} + \frac{|\Omega_{bi2}|^2}{4\Delta_{bi2}+2i\Gamma}\right)\tilde{c}_b(t) - i\frac{\Omega_{ai1}^*\Omega_{bi2}}{2\Delta_{ai1}+i\Gamma}e^{-i\delta_{12}t-i(\phi_{L1,0}-\phi_{L2,0})}\tilde{c}_a(t).\end{aligned}\quad (2.38)$$

We define the following parameters using $\Delta_{ai1} \equiv \Delta$:

$$\Omega_{\text{eff}} = \frac{\Omega_{ai1}^*\Omega_{bi2}}{2\Delta + i\Gamma} \quad (2.39)$$

$$\Omega_a^{AC} = \frac{|\Omega_{ai1}|^2}{4\Delta_{ai1}^2 + \Gamma^2}\Delta_{ai1} + \frac{|\Omega_{ai2}|^2}{4\Delta_{ai2}^2 + \Gamma^2}\Delta_{ai2} \quad (2.40)$$

$$\Omega_b^{AC} = \frac{|\Omega_{bi1}|^2}{4\Delta_{bi1}^2 + \Gamma^2}\Delta_{bi1} + \frac{|\Omega_{bi2}|^2}{4\Delta_{bi2}^2 + \Gamma^2}\Delta_{bi2} \quad (2.41)$$

$$\delta^{AC} = (\Omega_b^{AC} - \Omega_a^{AC}) \quad (2.42)$$

$$\Omega_R = \sqrt{\Omega_{\text{eff}}^2 + (\delta_{12} - \delta^{AC})^2}. \quad (2.43)$$

Ω_{eff} is the effective coupling frequency between the two ground states, $\hbar\Omega_{a,b}^{AC}$ are the light shifts of the two levels and $\hbar\delta^{AC}$ the shift of the two-photon Raman transition. In the following, we will forget about the loss due to spontaneous emission ($\Gamma \ll \Delta$). If we do a substitution of the following parameters

Two level transition	ω_L	$\phi_{L,0}$	\mathbf{k}_L	Ω	δ	Ω_r
Raman transition	ω_{eff}	$\phi_{\text{eff},0}$	\mathbf{k}_{eff}	Ω_{eff}	δ_{12}^*	Ω_R

*: δ is replaced in phase factors as δ_{12} , in amplitude factor as $(\delta_{12} - \delta^{AC})$; see (2.46).

we can use all equations derived before for a two level system, in particular (2.18), (2.19) and (2.20). One can such deduce the probability to perform a transition during a time τ from (2.20) as

$$P_b(\tau) = \frac{\Omega_{\text{eff}}^2}{\Omega_{\text{eff}}^2 + (\delta_{12} - \delta^{AC})^2} \sin^2\left(\sqrt{\Omega_{\text{eff}}^2 + (\delta_{12} - \delta^{AC})^2}\frac{\tau}{2}\right). \quad (2.44)$$

Additional phase factor: The diagonal elements of the Hamiltonian of this system are the AC-Stark shifts of the levels $|a\rangle$ and $|b\rangle$, equivalent to (2.14). This shift is not any more symmetric as in the two-level case. Before transforming the system to the rotating frame – according to (2.15) – to get a time-independent Hamiltonian $\hat{\mathcal{H}}$, we shift the energy scale by the average Stark-shift $\Delta E_{ab}^{AC} = -\frac{\hbar}{2}(\Omega_a^{AC} + \Omega_b^{AC})$ of both levels, which will re-symmetrize the problem. Once the system is shifted, one can find $\hat{\mathcal{H}}$ and

adopt the solutions (2.18). To account for the energy shift, we need to multiply the solution with the phase factor

$$e^{-i\frac{1}{2}(\Omega_a^{AC} + \Omega_b^{AC})\tau}. \quad (2.45)$$

We write the equations (2.18) with the additional phase factor using the substitutions from table 2.1.3, yielding

$$\begin{aligned} \tilde{c}_a(t_0 + \tau) &= \left\{ \tilde{c}_a(t_0) \left[\cos\left(\frac{\Omega_R\tau}{2}\right) - i\frac{(\delta_{12} - \delta_{AC})}{\Omega_R} \sin\left(\frac{\Omega_R\tau}{2}\right) \right] \right. \\ &\quad \left. + \tilde{c}_b(t_0) e^{i(\delta_{12}t_0 + \phi_{\text{eff},0})} \left[-i\frac{\Omega_{\text{eff}}}{\Omega_R} \sin\left(\frac{\Omega_R\tau}{2}\right) \right] \right\} e^{i(\delta_{12} - (\Omega_a^{AC} + \Omega_b^{AC}))\frac{\tau}{2}} \\ \tilde{c}_b(t_0 + \tau) &= \left\{ \tilde{c}_a(t_0) e^{-i(\delta_{12}t_0 + \phi_{\text{eff},0})} \left[-i\frac{\Omega_{\text{eff}}}{\Omega_R} \sin\left(\frac{\Omega_R\tau}{2}\right) \right] \right. \\ &\quad \left. + \tilde{c}_b(t_0) \left[\cos\left(\frac{\Omega_R\tau}{2}\right) + i\frac{(\delta_{12} - \delta_{AC})}{\Omega_R} \sin\left(\frac{\Omega_R\tau}{2}\right) \right] \right\} e^{-i(\delta_{12} + (\Omega_a^{AC} + \Omega_b^{AC}))\frac{\tau}{2}}. \end{aligned} \quad (2.46)$$

For a small detuning from the AC-Stark shifted resonance ($\delta_{12} - \delta_{AC} \ll \Omega_R$), we will find for a $\pi/2$ -pulse with $\tau = \frac{\pi}{2\Omega_R}$ and for a π -pulse with $\tau = \frac{\pi}{\Omega_R}$ the coefficients

$$\begin{array}{lcl} \left| \begin{array}{l} \tilde{c}_a^{\frac{\pi}{2}}(t_0 + \tau) = \frac{1}{\sqrt{2}} \left(\tilde{c}_a(t_0) + \tilde{c}_b(t_0) \frac{\Omega_{\text{eff}}}{\Omega_R} e^{i(\delta_{12}t_0 + \phi_{\text{eff},0} - \pi/2)} \right) e^{i(\delta_{12} - AC)\frac{\tau}{2}} \\ \tilde{c}_b^{\frac{\pi}{2}}(t_0 + \tau) = \frac{1}{\sqrt{2}} \left(\tilde{c}_b(t_0) + \tilde{c}_a(t_0) \frac{\Omega_{\text{eff}}}{\Omega_R} e^{-i(\delta_{12}t_0 + \phi_{\text{eff},0} + \pi/2)} \right) e^{-i(\delta_{12} + AC)\frac{\tau}{2}} \\ \tilde{c}_a^\pi(t_0 + \tau) = \tilde{c}_b(t_0) \frac{\Omega_{\text{eff}}}{\Omega_R} e^{i(\delta_{12}t_0 + \phi_{\text{eff},0} - \pi/2)} e^{i(\delta_{12} - AC)\frac{\tau}{2}} \\ \tilde{c}_b^\pi(t_0 + \tau) = \tilde{c}_a(t_0) \frac{\Omega_{\text{eff}}}{\Omega_R} e^{-i(\delta_{12}t_0 + \phi_{\text{eff},0} + \pi/2)} e^{-i(\delta_{12} + AC)\frac{\tau}{2}} \end{array} \right. \end{array} \quad (2.47)$$

with $AC \equiv \Omega_a^{AC} + \Omega_b^{AC}$.

In the following, we will use the equations (2.46) often for the special case of $\delta_{12} = \delta_{AC} = 0$ and $AC = 0$ and omit the tilde on the coefficients:

$$\begin{array}{lcl} \left| \begin{array}{l} c_a(t_0 + \tau) = c_a(t_0) \cos\left(\frac{\Omega_R\tau}{2}\right) - i c_b(t_0) e^{i\phi_{\text{eff},0}} \sin\left(\frac{\Omega_R\tau}{2}\right) \\ c_b(t_0 + \tau) = c_b(t_0) \cos\left(\frac{\Omega_R\tau}{2}\right) - i c_a(t_0) e^{-i\phi_{\text{eff},0}} \sin\left(\frac{\Omega_R\tau}{2}\right) \end{array} \right. \end{array} \quad (2.48)$$

Phase changes: A pulse of radiation starting at time $t = 0$ and of duration τ couples the two atomic states and adds a phase factor to the wave-function, which differs, depending on the initial state the atom. From equation (2.46) one can extract the phase factor for the different possible transitions:

Transition	Momentum	Phase factor
$ a\rangle \rightarrow a\rangle$	$p \rightarrow p$	$(-AC + \delta_{12}) \frac{\tau}{2}$
$ b\rangle \rightarrow b\rangle$	$p + \hbar k_{\text{eff}} \rightarrow p + \hbar k_{\text{eff}}$	$(-AC - \delta_{12}) \frac{\tau}{2}$
$ a\rangle \rightarrow b\rangle$	$p \rightarrow p + \hbar k_{\text{eff}}$	$(-AC - \delta_{12}) \frac{\tau}{2} - \frac{\pi}{2} - \delta_{12}t_0 - \phi_{\text{eff},0}$
$ b\rangle \rightarrow a\rangle$	$p + \hbar k_{\text{eff}} \rightarrow p$	$(-AC + \delta_{12}) \frac{\tau}{2} - \frac{\pi}{2} + \delta_{12}t_0 + \phi_{\text{eff},0}$

Let us have a closer look at the phase terms, which are added during a Raman pulse in regard to their importance for an interferometer. Therefore, we anticipate for a moment the three-pulse interferometer-signal, where the atom is initially in state $|a\rangle$ is split into a superposition of state $|a\rangle$ and $|b\rangle$ ($\pi/2$ -pulse of length $\tau/2$), reflected (π -pulse of length τ) and superimposed ($\pi/2$ -pulse of length $\tau/2$). On the first path I, the atoms perform the transition $|a\rangle \xrightarrow{\pi/2} |b\rangle \xrightarrow{\pi} |a\rangle \xrightarrow{\pi/2} |a\rangle$, on the second path II $|a\rangle \xrightarrow{\pi/2} |a\rangle \xrightarrow{\pi} |b\rangle \xrightarrow{\pi/2} |a\rangle$. The interferometer signal depends on the phase difference on both paths.

- $AC \frac{\tau}{2}$ -Term: This phase factor due to the asymmetric light shift is added always in the same way and such cancels out by the difference between two paths of an interferometer. Since the AC-Stark shift scales in the same way as the Rabi-frequency, this term does not even depend on the pulse length.
- $\delta_{12}t_0$ and $\delta_{12}\frac{\tau}{2}$ -Terms: These terms accounts for the phase evolution between the different momentum states until the middle of the pulse. We introduce the time t_c at the center of the pulse $t_c \equiv t_0 + \frac{\tau}{2}$ such that $\delta_{12}t_0 + \delta_{12}\frac{\tau}{2} = \delta_{12}t_c$. We separate the laser frequency ω_{eff} from δ_{12} defined in (2.32) to keep the phase term $\omega_{\text{eff}}t_0$, which considers an eventual frequency change of the laser. The remaining terms contributing to δ_{12} are considered constant and will thus cancel out in the interferometer. We can thus write $\delta_{12}t_c = \omega_{\text{eff}}t_c + \text{const.}$
- $\frac{\pi}{2}$ -Term: If both paths start and finish in the same state $|a\rangle$, the constant factor $\frac{\pi}{2}$ cancels out. In the final state $|b\rangle$ however, the $\frac{\pi}{2}$ add up to 2π .
- $\phi_{\text{eff},0}$ -Term: This term has the biggest importance, because it no longer stands for a constant phase offset at time zero, but indicates the phase of the Raman-laser at the position of the atomic wave-packet. We write

$$\phi_{\text{eff},z_c} = -\mathbf{k}_{\text{eff}}z_c + \phi_{\text{eff},0}. \quad (2.49)$$

It is here, where the plane-wave approximation of our calculation does not hold any more. The effective laser-phase can be assumed to change linearly with position during the (very short) pulse, so a good approximation is to use the phase offset at the position of the center of the wave-packet at the center of the pulse: $z_c \equiv z(t_c)$.

Conclusion: The important terms of the phase change during a pulse of length τ thus are:

$$\left. \Delta\phi = \omega_{\text{eff}} t_c - \mathbf{k}_{\text{eff}} z_c + \phi_{\text{eff},0} . \right\} \quad (2.50)$$

where t_c is the time at the center of the pulse.

Light-shift compensation: By choosing the proper intensities $\mathbf{E}_{0,L1}$ and $\mathbf{E}_{0,L2}$ of the Raman lasers, the light shifts $\Delta E^{AC} = \hbar\Omega^{AC}$ (2.40) and (2.41) can be matched to compensate the total shift δ^{AC} . We assume $\Omega_{ai1} \approx \Omega_{bi1}$ and $\Omega_{ai2} \approx \Omega_{bi2}$.

$$\begin{aligned} \delta^{AC} = 0 \Leftrightarrow \left(\frac{I_{L1}}{I_{L2}} \right) &= \left(\frac{|\mathbf{E}_{0,L1}|^2}{|\mathbf{E}_{0,L2}|^2} \right) = \left(\frac{|\Omega_{ai1}|^2}{|\Omega_{bi2}|^2} \right) = \frac{\Delta(\Delta + \omega_{ab})}{(\Delta - \delta_{12})(\omega_{ab} - \Delta + \delta_{12})} \\ &\approx \frac{(\omega_{ab} + \Delta)}{(\omega_{ab} - \Delta)} \quad \text{for } \delta_{12} \ll \Delta \end{aligned} \quad (2.51)$$

The usual parameters for our experiment are $\Delta = -2\pi \cdot 3.3$ GHz and $\omega_{ab} = 2\pi \cdot 6.8$ GHz, which makes a relation of $I_{L1}/I_{L2} \approx 1/3$ to cancel out the light shift.

2.1.4 Velocity selection

In a vertical experiment arrangement, with the k -vectors of the Raman lasers parallel to atomic motion (free fall), one can choose between a configuration with co-propagating or counter-propagating Raman lasers. We will discuss the effect of both arrangements that are sketched in Fig. 2.2.

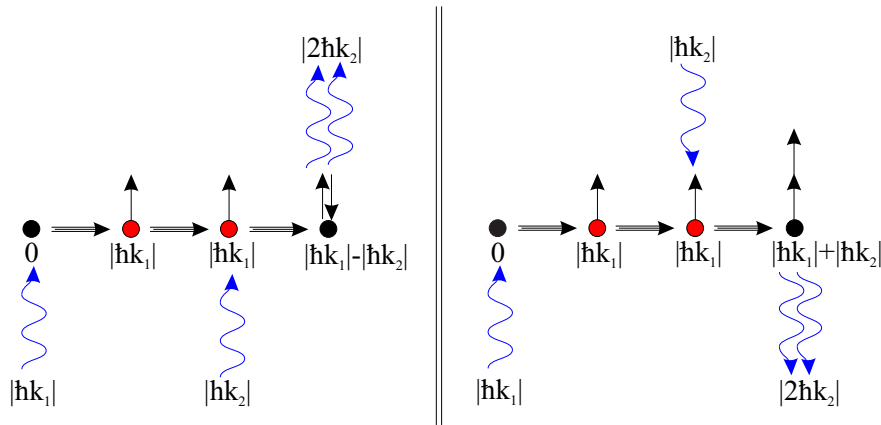


Figure 2.2: Recoil kicks for co- (left) and counter-(right) propagating Raman beams. Indicated are the momenta of photons and atoms (balls). From left to right: The atom first absorbs one photon of laser 1 and then emits a photon stimulated by laser 2. Co-propagating beams will transfer little momentum to the atoms, whereas counter-propagating beams transfer two recoil kicks.

Counter-propagating Raman-beams: Atoms with a certain velocity component parallel to the Raman beams (vertical z-axis) will be exactly in resonance when the Doppler shift compensates the detuning. Atoms with different velocities will be off-resonant and have a lower probability of performing the transition. According to (2.32), the Doppler shift of the transition frequency is $\delta = \mathbf{p} \cdot \mathbf{k}_{\text{eff}}/m = \mathbf{v} \cdot \mathbf{k}_{\text{eff}}$. A velocity spread Δv_z of the selected atoms is therewith related to the width of the Raman transition $\Delta\delta$ by:

$$\Delta v_z = \frac{\Delta\delta}{k_{\text{eff}}}. \quad (2.52)$$

The Raman linewidth can be very small, because both states involved have very long lifetimes and because the frequency difference ω_{L12} can be stabilized very accurately. In our experiment, the linewidth is mainly limited by the interaction time with the Raman light, typically $50 \mu\text{s}$, which is equivalent to $\Delta f = 1/\tau = 20 \text{ kHz}$. For $\lambda = 780 \text{ nm}$, formula (2.52) determines a velocity spread of $\Delta v = 2.6 \text{ mm/s}$. (The recoil velocity for rubidium is 5.8 mm/s .) For long interaction times, Raman transitions can be used for velocity selection on the order of one Hz [8].

The recoil kick acquired by one Raman transition is $\hbar(\mathbf{k}_{L1} - \mathbf{k}_{L2}) = \hbar k_{\text{eff}} \approx 2\hbar k_{L1}$. The velocity change $\Delta v = \hbar k_{\text{eff}}/m_{Rb}$ due to the stimulated absorption and emission is 11.6 mm/s in our case².

Co-propagating Raman-beams: If working with big detuning $\Delta \gg \delta_{12}$, then $k_{\text{eff}} \approx 2k_{L1} \approx 2k_{L2}$, the Doppler-shift of the two Raman lasers will always be the same, no matter how fast the atoms move and the transition will always be in resonance. (Of course, the transition probability will decrease, if the Doppler shift becomes comparable to the detuning Δ .)

The interferometer signal is proportional to the effective wave-vector $k_{\text{eff}} = |k_{L1}| - |k_{L2}|$, which, in the case of rubidium, is a factor of 10^5 smaller than the effective wave-vector $k_{\text{eff}} = |k_{L1}| + |k_{L2}|$ in the counter-propagating case. The co-propagating configuration is useful for testing the interferometer, since it will provide a big signal and small sensitivity to acceleration.

2.1.5 Comments on plane-wave approximation

The results of this chapter were obtained for atomic plane waves. Although we will see that this assumption is not realistic, it can nevertheless be justified, if the result are interpreted in the right way.

The plane-wave approximation implies a well defined laser phase ϕ of the light field during the interaction with the atomic wave-function. This is valid for wavelengths far bigger than the extension of the atomic wave-packets, but no longer in our case, where we deal with optical light fields of $\lambda = 780 \text{ nm}$:

² $m_{Rb} = 1.44 \cdot 10^{-25} \text{ kg}$, $\hbar = 1.05 \cdot 10^{-34} \text{ Js}$

A temperature of the atom cloud in the order of $1 \mu\text{K}$ corresponds to a velocity uncertainty of $\Delta v < 10^{-2} \text{ m/s}$. The position uncertainty ($\Delta x \Delta p = \hbar$) is therefore $\Delta x \lesssim 100 \text{ nm}$, which means that the wave-function experiences different phases of the laser at different positions. To account for velocity or momentum uncertainty, we can describe the atom by a Gaussian wave-packet as the integral over momentum plane-waves:

$$\psi(\mathbf{r}, t) = A e^{-i(\omega t - \frac{\mathbf{p}\mathbf{r}}{\hbar})} \leftrightarrow \psi(\mathbf{r}, t) = \int_{-\infty}^{\infty} a(\mathbf{p}) e^{-i(\omega t - \frac{\mathbf{p}\mathbf{r}}{\hbar})} d\mathbf{p}, \quad (2.53)$$

where $a(\mathbf{p})$ denotes the width of the momentum distribution; in our case a narrow Gauss centered at \mathbf{p}_0 .

Our previous treatment for one plane wave with \mathbf{p}_0 (see (2.46)) resulted in a phase shift (2.50), which is *independent* of \mathbf{p} , which means that all momentum plane-waves will contribute coherently to the phase-signal.

In all this treatment, we did not have the ambition yet to describe the total phase evolution of the atom in a light field in the presence of gravity plus gravity gradient, which becomes very difficult. This calculation has been performed by Ch. Bordé and leads to the conclusion that the plane-wave result is correct as a description of the pure interaction and that one can consider the evolution independently to sum both effects on the phase; as we will see in chapter 2.2.

2.2 Raman light pulse interferometer

Two main effects contribute to the output of a Raman interferometer: the interaction with the light during the Raman-pulses and the free evolution in a potential. The first parts of this section will evaluate these two contributions independently, according to the 'classical' approach used by Chu and Kasevich to describe an interferometer. The result from the previous section of the interaction of plane-waves with (only) the light field is used to describe the interaction with the short laser pulses. The free evolution will be treated separately. Towards the end of the chapter, a method introduced by Ch. Bordé will be sketched for comparison. This method solves the whole problem for Gaussian wave-packets in the presence of a light field and an external quadratic potential.

2.2.1 Principle

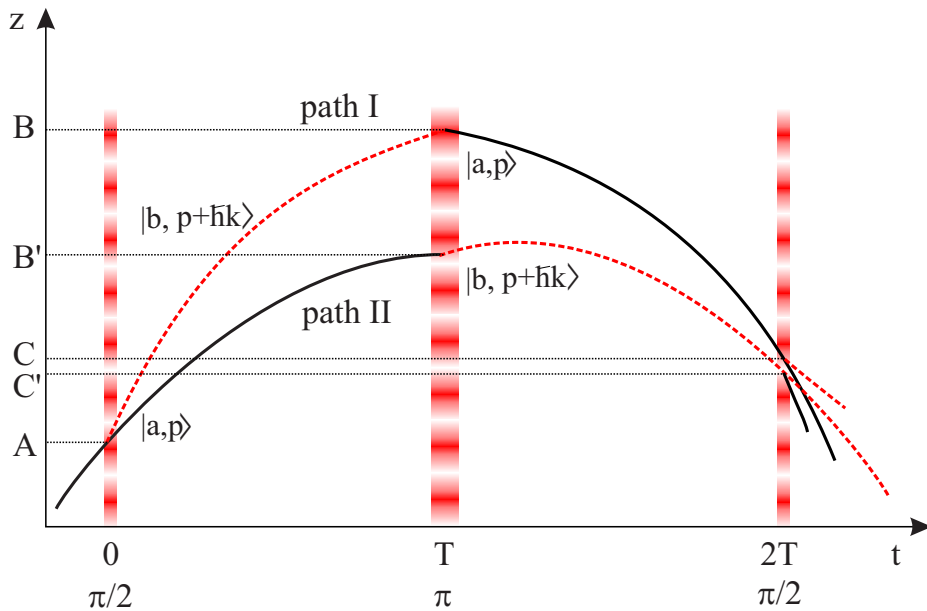


Figure 2.3: Schematic illustration of a vertical, symmetrical light pulse interferometer. The atom cloud originally in state $|a\rangle$ is split, reflected and recombined by three Raman light pulses. Atoms either pass through path I (ABC) or path II (AB'C').

We will analyze in the following the special case of a symmetric, vertical Raman light pulse interferometer (see Fig. 2.3). Atoms are interrogated by Raman pulses at three different times $t = 0, T, 2T$ to split, reflect and recombine the atomic wave-function. The phase difference $\Delta\phi$ between the two paths of an atom interferometer can be decomposed into two main parts:

$$\Delta\phi = \Delta\phi_{\text{laser}} + \Delta\phi_{\text{evolution}} \quad (2.54)$$

The first contribution $\Delta\phi_{\text{laser}}$ originates in the phase ϕ_{eff} of the interrogation lasers at the relative position of the atoms, which is imprinted onto the atomic wave-function during the pulses according to (2.46). The second part $\Delta\phi_{\text{evolution}}$ is the dephasing arising from the different evolution of the wave-function travelling along path I or II. If the two paths are exposed to different potentials, a dephasing will be measured at the end of the interferometer.

2.2.2 Phase contribution of Raman pulses

To calculate the occupation probability P_a and P_b at the end of a complete interferometer sequence, we calculate the coefficients c_a and c_b for a sequence of a $\pi/2$, a π and a $\pi/2$ pulse at times $t_1 = 0$, $t_2 = T$ and $t_3 = 2T$, respectively. According to (2.50), the important phase terms, imprinted onto the wave-function during the i-th pulse are

$$\phi_{\text{eff}}(t_i) = \phi_{\text{eff}}(z(t_i), t_i) = \omega_{\text{eff}} t_i - k_{\text{eff}} z(t_i) + \phi_{\text{eff},0}(t_i). \quad (2.55)$$

We abbreviate the phase at the space-time point A (see Fig.2.3) with $\phi_A = \phi_{\text{eff}}(z_I(0), 0)$, $\phi_B = \phi_{\text{eff}}(z_I(T), T)$, and so forth. To calculate the phase output of the whole sequence of $\pi/2$, π and $\pi/2$ pulses, we perform three iterations using the equations (2.48) and starting with the atom in state $|a\rangle$, zero detuning δ_{12} and light shift compensation (see section 2.1.3) $\delta_{AC} = 0 \leftrightarrow \Omega_R = \Omega_{\text{eff}}$. The pulse length τ for a π pulse is $\tau = \pi/\Omega_R$. The coefficients at the various times are:

$$\begin{aligned} c_a(t < 0) &= 1 \\ c_b(t < 0) &= 0 \\ c_a(0 < t < T) &= \frac{1}{\sqrt{2}} \\ c_b(0 < t < T) &= -\frac{i}{\sqrt{2}} e^{-i(\pi/2+\phi_{\text{eff}}^A)} \\ c_a(T < t < 2T) &= -\frac{1}{\sqrt{2}} e^{-i(\pi+\phi_{\text{eff}}^A-\phi_{\text{eff}}^{B'})} \\ c_b(T < t < 2T) &= -\frac{i}{\sqrt{2}} e^{-i(\pi/2+\phi_{\text{eff}}^B)} \\ c_a(t > 2T) &= -\frac{1}{2} e^{-i(\pi+\phi_{\text{eff}}^A-\phi_{\text{eff}}^{B'})} - \frac{1}{2} e^{-i(\pi+\phi_{\text{eff}}^B-\phi_{\text{eff}}^{C'})} \\ c_b(t > 2T) &= \frac{i}{2} e^{-i(3\pi/2+\phi_{\text{eff}}^A-\phi_{\text{eff}}^{B'}+\phi_{\text{eff}}^C)} + \frac{i}{2} e^{-i(\pi/2+\phi_{\text{eff}}^B)}. \end{aligned} \quad (2.56)$$

We derive the following probabilities of finding the atom in state $|a\rangle$ and $|b\rangle$:

$$\begin{aligned} |c_a(t > 2T)|^2 &= \frac{1}{2} (1 + \cos(\Delta\phi_a)) \\ \text{with } \Delta\phi_a &= \underbrace{(\phi_A - \phi_B)}_{\text{pathI}} - \underbrace{(\phi_{B'} - \phi_{C'})}_{\text{pathII}} \quad \text{and} \\ |c_b(t > 2T)|^2 &= \frac{1}{2} (1 - \cos(\Delta\phi_b)) \\ \text{with } \Delta\phi_b &= \underbrace{(\phi_A - \phi_B + \phi_C)}_{\text{pathI}} - \underbrace{(\phi_{B'})}_{\text{pathII}}. \end{aligned} \quad (2.57)$$

The end-points z_C and $z_{C'}$ of the interferometer might be spatially separated in the presence of an inhomogeneous potential. We will define a phase $\phi_{\bar{C}}$ at the mean point $z_{\bar{C}} = \frac{z_C + z_{C'}}{2}$ and a separation phase ϕ_{sep} as

$$\phi_{\bar{C}} = \frac{p(z_C + z_{C'})}{2\hbar} = \frac{\phi_C + \phi_{C'}}{2} \quad (2.58)$$

$$\phi_{\text{sep}} = \frac{p(z_C - z_{C'})}{2\hbar} = \frac{\phi_C - \phi_{C'}}{2}, \quad (2.59)$$

where $p = \hbar k_{\text{eff}}$ is the momentum of the plane wave, so that we can write

$$\begin{aligned} P_a &= \frac{1}{2} (1 + \cos(\Delta\phi - \phi_{\text{sep}})) \\ P_b &= \frac{1}{2} (1 - \cos(\Delta\phi + \phi_{\text{sep}})) \\ \text{with } \Delta\phi &= \phi_A - \phi_B - \phi_{B'} + \phi_{\bar{C}}. \end{aligned} \quad (2.60)$$

The phase shift ϕ_{sep} can be understood as the phase-change of a plane wave over the distance $\frac{z_C + z_{C'}}{2}$. What we cannot see in the plane wave approximation, is the loss of contrast of the interferometer, because of less overlap of the waves. We can introduce the contrast factor A:

$$P_a = 1/2A(1 + \cos \Delta\phi). \quad (2.61)$$

To explicitly calculate this phase contribution, the equations of motion for the applied potential must be solved to know the position of the atoms at the times of interaction.

Conclusion: The phase contribution of the Raman lasers to the interferometer is the sum of the phase contributions of the laser pulses (see section 2.1.3) of path one minus the sum of those on path two. In an inhomogeneous potential, the end points of the interferometer are not the same and we observe an additional phase term, which is of opposite sign for state $|a\rangle$ and state $|b\rangle$ and is equal to the phase shift of a plane wave over the shift of the end point:

$$\left\| \Delta\phi_{\text{laser}} = (\phi_A - \phi_B) - (\phi_{B'} - \phi_{\bar{C}}) + \frac{p(z_{C'} - z_C)}{2\hbar}. \right. \quad (2.62)$$

For constant laser phase offset and constant frequency, this simplifies to

$$\Delta\phi_{\text{laser}} = k_{\text{eff}}(z_A - z_B - z_{B'} + z_{C'}) + \frac{p(z_{C'} - z_C)}{2\hbar}. \quad (2.63)$$

All the other phase terms, imprinted on the wave-function during the pulses cancel out. In the case of uniform gravity $z(t) = v_0 T - \frac{1}{2}gT^2$ and $\Delta\phi_{\text{laser}} = k_{\text{eff}}gT^2$.

2.2.3 Free evolution

We will now face the problem of how to calculate the dephasing between the two paths *I* and *II* of the atom interferometer. To determine the evolution of the atomic wavefunction during the passage of one path, we will use the convenient approach of the *Feynman path integrals*, valid for at most quadratic Lagrangians. In this paragraph, we will provide the tools for calculating the dephasing, but will not derive everything; it can be found in [33]. The problem we have to solve is the calculation of the wavefunction $\psi(z_b, t_b) = \psi(b)$ at a certain position z_b and time t_b . The evolution in the given potential starts at a time $t_a < t_b$ at the unknown position z_a with $\psi(z_a, t_a) = \psi(a)$. To solve this problem of evolution, we first give a short explanation of the Feynman method:

Feynman path integral: The quantum evolution operator $K(z_b, t_b; z_a, t_a) = K(b, a)$ determines the evolution of a wave-function between time t_a and time t_b .

There is an infinite number of possibilities or paths Γ for an atomic wave packet to evolve from (z_a, t_a) to (z_b, t_b) . Feynman postulated that K can be expressed as a sum over all possible paths Γ , where every path contributes the same amplitude and where the phase of each contribution is the classical action S_{cl} divided by \hbar :

$$K(b, a) = \sum_{\text{all } \Gamma} e^{iS_{cl}(\Gamma)/\hbar} \quad (2.64)$$

In the *classical limit* of $S_{cl}(\Gamma) \gg \hbar$, a small variation of the path $\Delta\Gamma$ will change the phase by a big amount and different paths will interfere destructively. In the vicinity of the classical path, the action has an extremum and very close paths have similar phases and interfere constructively, thus leading to the classical solution.

Let us assume a particle at time t_a , whose amplitude $\psi(a)$ indicates the probability with which it can be found at z_a . To know the probability amplitude $\psi(b)$ of finding this particle at z_b at time t_b , wherever it has been at time a , we need to integrate $K(b, a)\psi(a)$ over all z_a :

$$\psi(b) = \int K(b, a) \psi(a) dz_a \quad (2.65)$$

The sum in (2.64) can be written as an integral and simplified for the case of quadratic Lagrangians [33] to take the following form:

$$K(b, a) = e^{\frac{i}{\hbar} S_{cl}(b, a)} F(t_b, t_a), \quad (2.66)$$

where the integral has been solved partially and the remaining integral F only depends on time and no more on position.

If we insert (2.66) into (2.65), we still have an inconvenient integral in the evolution term. To simplify the integral, it would be nice to know, if some z_a contribute to the integral more than others. There is an infinite number of possible real paths from all z_a finishing in z_b , but if we use the knowledge of the initial momentum p_0 , we will find only one path, which, for a certain Lagrangian, leads to z_b, t_b . We call the initial position (time t_a) of this path z_0 and develop the action S_{cl} around $(z - z_0)$, keeping in mind the quadratic nature of the action:

$$\begin{aligned} S_{cl}(z_b, t_b; z_a, t_a) &= S_{cl}(z_b, t_b; z_0, t_a) \\ &\quad + \underbrace{\frac{\partial S_{cl}(z_b, t_b; z_0, t_a)}{\partial z_0}}_{=-p_0} (z_a - z_0) + \underbrace{\frac{1}{2} \frac{\partial^2 S_{cl}(z_b, t_b; z_0, t_a)}{\partial z_0^2}}_{=C(t_b, t_a)} (z_a - z_0)^2 \end{aligned} \quad (2.67)$$

If we insert (2.67) into (2.65) we see that in the case of *plane waves* $\psi(z_a, t_a) = e^{\frac{i}{\hbar} p_0 z_a}$, the term with z_a cancels out and only points near the classical position z_0 contribute to the integral, which can now be solved leading to

$$\psi(z_b, t_b) = F(t_b, t_a) \sqrt{\frac{i\pi\hbar}{C(t_b, t_a)}} \cdot e^{\frac{i}{\hbar} S_{cl}(z_b, t_b; z_0, t_a)} \psi(z_0, t_a). \quad (2.68)$$

In the case of a particle of mass m in a pure gravitational field we get

$$C(t_b, t_a) = \frac{m}{(2(t_b - t_a))} \quad \text{and} \quad F(t_b, t_a) = \sqrt{\frac{m}{2i\pi\hbar(t_b - t_a)}} \quad (2.69)$$

what corresponds to

$$\psi(z_b, t_b) = \psi(z_0, t_a) e^{\frac{i}{\hbar} S_{cl}(z_b, t_b; z_0, t_a)}. \quad (2.70)$$

The validity of the *plane wave approximation* applied right above can be once more justified by the low temperature in the order of μK of the atoms in the fountain (see section 2.1.5): A Raman pulse of $\tau = 50 \mu\text{s}$ corresponds to a velocity selection with width $\Delta v = \Delta\omega/k_{\text{eff}}$, leading to $\Delta v = 8.3 \times 10^{-3} \text{ m/s}$ (vertical temperature of 720 nK).

The wave-function can be written as a superposition on plane waves $\psi = \int a_p e^{\frac{i}{\hbar} p_z} dp$, where only waves within a $\Delta p = m_{Rb87}\Delta v$ contribute significantly. An evaluation of the phase contribution $\Delta\phi = S_{cl}/\hbar$ (in a potential with gravity and gravity gradient) for those plane waves within Δp will show the error of the approximation, which lies in the range of $< 10^{-15} \text{ g}$ in a typical gravimeter, which is far below our aimed precision.

Conclusion: The phase evolution between point a and b in a quadratic potential is

$$\left\| \Delta\phi_{\text{evolution } a \text{ to } b} = \frac{1}{\hbar} S_{cl}(b, a). \right. \quad (2.71)$$

It is sufficient to calculate the classical action along paths I(ABC) and II(AB'C) and take the difference between both: $\Delta\phi = \phi_{ABC} - \phi_{AB'C}$. In the case of spatially separated

beam paths and a spatially inhomogeneous potential, the phase shift on both paths can be different and the result non-zero. In contrary, the phase contribution is zero in the case of uniform gravity.

Exemplary calculation of the phase due to free evolution: We use the result (2.68) expressed in terms of classical action to solve the exemplary case of an evolution in a gravity field:

We start with the plane wave at time t_a , from which we only know the initial momentum p_0 . We first need to find out the position $z_0(t_a)$, so that the wave with p_0 passes z_b at time t_b . The solution is found by solving the Lagrange equation.

For a particle in a gravitational potential the Lagrangian is:

$$L(z, \dot{z}) = \frac{1}{2}m\dot{z}^2 - mgz \quad (2.72)$$

Solving the Lagrange equation

$$\frac{d}{dt} \frac{\delta L}{\delta \dot{z}} = \frac{\delta L}{\delta z} \quad (2.73)$$

and using the solutions

$$\dot{z}(t) = \dot{z}(t_a) - g \cdot (t - t_a) \quad z(t) = z(t_a) + \dot{z}(t_a) \cdot (t - t_a) - \frac{1}{2}g \cdot (t - t_a)^2 \quad (2.74)$$

to determine the necessary parameters, one can calculate the classical action

$$\begin{aligned} S_{cl}(b, a) &= S_{cl}(z_b, t_b; z_a, t_a) \\ &= \int_{t_a}^{t_b} [L(z, \dot{z})] dt = \int_{t_a}^{t_b} \left[\frac{1}{2}m\dot{z}^2(t) - mgz(t) \right] dt \\ &= \frac{m(z_b - z_a)^2}{2(t_b - t_a)} - \frac{mg}{2}(z_b + z_a)(t_b - t_a) - \frac{mg^2}{24}(t_b - t_a)^3. \end{aligned} \quad (2.75)$$

To obtain the total dephasing $\Delta\phi_{\text{evolution}}$ of our interferometer (see Fig. 2.3), we need to take the difference between the phase evolution of path I and path II:

$$\Delta\phi_{\text{evolution}} = \Delta\phi_I - \Delta\phi_{II} = (\Delta\phi_{AB} + \Delta\phi_{BC}) - (\Delta\phi_{AB'} + \Delta\phi_{B'C}). \quad (2.76)$$

According to (2.68), the phase evolution on path $a \rightarrow b$ is $\Delta\phi = S_{cl}(b, a)/\hbar$. We therefore use (2.75), whose last term does not depend on position and falls out, and insert the remaining two terms into equation (2.76); resulting in:

$$\Delta\phi_{\text{evolution}} = \frac{1}{\hbar T} (z_B - z_{B'}) (z_B + z_{B'} - z_A - z_C - gT^2). \quad (2.77)$$

By setting $t_A = 0$, $z_A = 0$ and $v_0 = 0$ as it cancels out anyway, (2.74) gives us:

$$\begin{aligned} z_B &= -\frac{1}{2}gT^2 \\ z_{B'} &= -\frac{1}{2}gT^2 + \frac{\hbar k_{\text{eff}} T}{m} \\ z_C &= -2gT^2 + \frac{\hbar k_{\text{eff}} T}{m} \end{aligned} \quad (2.78)$$

Inserting these classical positions into (2.77) will give the contribution of the free evolution $\Delta\phi_{\text{evolution}} = 0$, as one would expect for a uniform potential.

2.2.4 The Bordé method

In the last years, an exact treatment for any kind of atom interferometer has been developed by C. Bordé. The Schrödinger equation is solved analytically for a wave-packet in the presence of a time-dependent, quadratic Hamiltonian. The formalism provides quite simple formulas that can be used as a tool to calculate the phase shift of the interferometer to a high precision. We will not go into any detail here, but summarize the most important features of this theory and give the results for the case of our symmetrical three pulse interferometer. A more extensive description of this approach can be found in the thesis of Marco Fattori [52]; detailed calculation in [54] and references therein.

Free evolution: The task is the solution of the quantistic equation of motion for a particle of mass m in a quadratic potential. Bordé used the formal analogy of this problem with the propagation of a laser in a birefringent medium, which can be described with the well known ABCD evolution matrices of Gaussian optics, to develop a similar ABCD law for atom optics. Therefore, the theory had to be expanded to 3 spatial dimensions (ABC and D are now matrices of order 3).

The propagation of a wave-packet is described by the the quantistic evolution operator $K(b, a)$, which can be expressed it in terms of classical action through the Van Vleck's equation:

$$K(t_a, \mathbf{q}_a, t_b, \mathbf{q}_b) = \left(\frac{1}{2\pi i\hbar} \right)^{3/2} \left| \det \frac{\partial^2 S}{\partial q_{i,a} \partial q_{j,b}} \right| e^{\frac{i}{\hbar} s_{cl}}. \quad (2.79)$$

The problem consequently reduces to the calculation of the classical action. We consider a Hamiltonian including gravity waves, rotations, gravity and gravity gradients:

$$\mathcal{H} = \underbrace{\frac{1}{2m} \mathbf{p} \hat{g}(t) \mathbf{p}}_{\text{gravitational waves}} - \underbrace{\boldsymbol{\Omega}(t) (\mathbf{q} \times \mathbf{p})}_{\text{rotation}} - \underbrace{m \mathbf{g}(t) \mathbf{q}}_{\text{gravity}} - \underbrace{\frac{m}{2} \mathbf{q} \hat{\gamma}(t) \mathbf{q}}_{\text{gravity gradient}}. \quad (2.80)$$

³The general case considers relativistic masses m , which might be different on each path. We will just consider equal rest masses.

Some clever transformations and choices of parameters [54] lead to the following ABCD-law for the evolution of the canonical variables q and p :

$$\begin{pmatrix} q_b \\ p_b/m \end{pmatrix} = \begin{pmatrix} U_{b,a} \xi \\ G_b^{-1} U_b \dot{\xi} \end{pmatrix} + \begin{pmatrix} A_{b,a} & B_{b,a} \\ C_{b,a} & D_{b,a} \end{pmatrix} \begin{pmatrix} q_a \\ p_a/M \end{pmatrix} \quad (2.81)$$

where G is the matrix corresponding to the tensor \hat{g} , the vector ξ describes the classical trajectory with the initial conditions $\xi(0) = 0$ and $\dot{\xi}(0) = 0$ of a Hamiltonian, where rotations have been eliminated by a unitary transformation [55] with the operator $U(t_b, t_a)$. The ABCD matrices can be determined by solving an equation array [54]. These ABCD matrices can be used to calculate the classical action. Knowing the classical action allows the determination of the quantum propagator. K results to have a Gaussian form and to solve the Schrödinger equation. A complete set of solutions (Hermite-Gauss functions) can now be derived from K . The Gaussian wave-packet (WP) of lowest order with the form

$$\psi(q, t_a) = \text{WP}(q, t_a, q_a, p_a, X_a, Y_a) = \frac{1}{\det X_a} e^{i \frac{m}{2\hbar} (q - q_a) Y_a X_a^{-1} (q - q_a)} e^{i \frac{m}{\hbar} v_a (q - q_a)} \quad (2.82)$$

is centered in q_0 , has an average velocity v_0 and complex width parameters X and Y . It's evolution

$$\begin{aligned} \psi(q, t_b) &= \int K(q, t_b, q', t_a) \text{WP}(q', t_a, q_a, p_a, X_a, Y_a) \\ &= e^{\frac{i}{\hbar} S_{cl}(t_b, t_a, q_a, p_a)} \text{WP}(q', t_b, q_b, t_b, X_b, Y_b) \end{aligned} \quad (2.83)$$

is governed by the ABCD laws for q and p (2.81) and for X and Y :

$$\begin{pmatrix} X_b \\ Y_b \end{pmatrix} = \begin{pmatrix} A_{b,a} & B_{b,a} \\ C_{b,a} & D_{b,a} \end{pmatrix} \begin{pmatrix} X_a \\ Y_a \end{pmatrix}. \quad (2.84)$$

To summarize: To solve the problem of the quantistic evolution of a Gaussian wave-packet in a quadratic potential, it is sufficient to calculate the matrices ABCD, from which the classical action and the classical equations of motion can be obtained. The phase evolution from time a to b is

$$\Delta\phi_{\text{evolution}} = \frac{1}{\hbar} S_{cl}(t_b, t_a). \quad (2.85)$$

Laser pulses: We have seen in section 2.2.2 how the interaction with the light affects the atomic wave-function in the limit of the plane-wave approximation. An explicit calculation of the evolution of spatial wave packets in the potential of a quadratic Hamiltonian including the electro-magnetic field of a Gaussian beam confirms the plane wave result [56, 54]: The interaction with the light for a certain time τ can be summarized by the multiplication of the wave-function with a phase and an amplitude factor

$$c_{a,b} e^{\omega t_c - \mathbf{k}\mathbf{q}_c + \phi_0}, \quad (2.86)$$

where – in the case of temporal beam splitters – t_c is the *time at the center of the pulse* and $q_c = q_{cl}(t_c)$ the classical position of the center of the wave packet at t_c . The coefficients $c_{a,b}$ depend on the duration of the pulse and on the detuning from resonance and indicate the population probability of state a or b . The phase factor of *one pulse* is the same as in table 2.1.3, which is the effective phase of the laser light at the point of the classical trajectory of the atom at time t_c :

$$\Delta\phi_{\text{laser}} = \omega_{\text{eff}} t_c - k_{\text{eff}} z(t_c) + \phi_{\text{eff},0}. \quad (2.87)$$

The calculation assumed a two-level atom, a weak laser field, non-dispersive⁴ square light-pulses and used the rotating-wave approximation.

Separation: The amplitude of the interferometer signal will decay with an amplitude factor $A \leq 1$, if the center of both wave-packets are spatially separated. The phase shift arising due to the shift is found to be exactly the phase shift of the plane wave from the center of both end-points to the shifted point [55]

$$\Delta\phi_{\text{sep}} = \frac{p(z_{C'} - z_C)}{2\hbar}. \quad (2.88)$$

Interferometer: Let us consider the general case of a symmetrical N-pulse interferometer as shown in Figure 2.4. The interferometer phase output is the differential

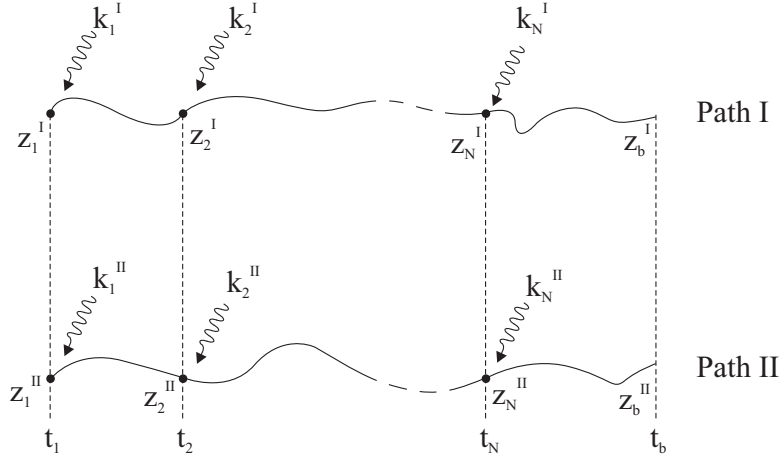


Figure 2.4: *N*-pulse interferometer. The difference in action of both paths only depend on the four end points of the interferometer. Indicated are positions z_i of the interactions with the light pulses with wave-vectors k_i at the times t_i .

⁴A non dispersive pulse does not account for the momentum or energy uncertainty of the atomic wave packet (different detuning δ) and leaves the form of the wave-packet unchanged. This would be equivalent to assuming a plane wave during the interaction.

phase shifts of all phase shifts acquired on path I and path II.

$$\begin{aligned} \Delta\phi &= \underbrace{\sum_{j=1}^N \frac{1}{\hbar} (S_{cl}^{II}(t_{j+1}, t_j) - S_{cl}^I(t_{j+1}, t_j))}_{\text{evolution, (2.85)}} \\ &\quad + \underbrace{\sum_{j=1}^N (k_j^{II} z_j^{II} - k_j^I z_j^I) - (\omega_j^{II} - \omega_j^I) t_j - (\phi_{j,0}^{II} - \phi_{j,0}^I)}_{\text{laser pulses, 2.87}} \\ &\quad - \underbrace{\frac{1}{2\hbar} (p_j^{II} + p_j^I)(z_j^{II} - z_j^I)}_{\text{separation, (2.88)}} . \end{aligned} \quad (2.89)$$

This sum of all phase contributions can even be simplified by the *four points theorem* [53], which connects the difference of classical action between two paths with the four end points of these paths:

$$S_{cl}(t_a, t_b, z_a^I; p_a^I) - S_{cl}(t_a, t_b, z_a^{II}; p_a^{II}) = \quad (2.90)$$

$$\frac{1}{2} (p_b^I + p_b^{II})(z_b^I - z_b^{II}) + \frac{1}{2} (p_a^I + p_a^{II})(z_a^I - z_a^{II}) . \quad (2.91)$$

For the same starting point $z_a^I = z_a^{II}$, the total interferometer phase shift reduces to

$$\Delta\phi = \sum_{j=1}^N (k_j^{II} - k_j^I) \frac{z_j^I + z_j^{II}}{2} . \quad (2.92)$$

Conclusion: With the assumptions of Gaussian wave-packets, a quadratic Hamiltonian, dispersion free light pulses and the same starting point for both interferometer paths, we get the astonishingly simple exact phase shift for a N-pulse interferometer of

$$\left\| \Delta\phi = \sum_{j=1}^N (k_j^I - k_j^{II}) \frac{(z_j^I + z_j^{II})}{2} . \quad (2.93) \right.$$

and in our case of three pulses with constant frequency ω_{eff} , constant phase offset ϕ_0 and constant k_{eff} :

$$\left\| \Delta\phi = k_{\text{eff}} (z_A - z_B - z_{B'} + \frac{z_C + z_{C'}}{2}) . \quad (2.94) \right.$$

The $z(t)$ are the points of the classical trajectories in a quadratic Hamiltonian and can be determined with the matrices ABC and D.

2.2.5 Interferometer phase shift for certain potentials

Evaluating the exact equation (2.94) in the case of *constant gravity* for our interferometer, using (2.78), gives the result

$$\parallel \Delta\phi = k_{\text{eff}} g T^2. \quad (2.95)$$

In the case of *gravity plus gravity gradient* γ , the solution can be either obtained by solving the Euler-Lagrange equation to get the classical path [46] or to use the ABCD matrices [54]. Expanding the result in power series of the gravity gradient γ leads in both cases to:

$$\parallel \Delta\phi = k_{\text{eff}} g T^2 + k\gamma T^2 \left(\frac{7}{12} g T^2 - (v_0 + \frac{\hbar k_{\text{eff}}}{2m}) T - z_0 \right) + O((\gamma T^2)^2). \quad (2.96)$$

The first order term is – for typical experimental conditions – a factor of about 10^{-8} smaller than the zero order term whereas the second order term is smaller by about 10^{-16} and can be safely neglected.

Rotations will introduce additional phase terms, the two most important of which are:

$$\parallel \Delta\phi_{\text{rotation}} = \underbrace{2 \mathbf{k}_{\text{eff}} (\mathbf{v} \times \boldsymbol{\Omega}) T^2}_{\text{Coriolis}} + \underbrace{\mathbf{k}_{\text{eff}} (\boldsymbol{\Omega} \times (\boldsymbol{\Omega} \times \mathbf{r})) T^2 R}_{\text{Centrifugal}} \quad (2.97)$$

$$\text{for Earth rotation} = 2 k_{\text{eff},x} T^2 \Omega_z v_y + k_{\text{eff},z} T^2 \Omega_y^2 R \quad (2.98)$$

where v is the velocity of the atoms, R is the Earth radius, Ω the Earth rotation rate in the laboratory frame (x,y,z). In [34], the most significant correction terms for interferometers are given and evaluated for typical experimental values.

The phase shift is related to the state-population of state $|a\rangle$ via

$$P_a = \frac{1}{2}(1 + \cos \Delta\phi). \quad (2.99)$$

2.3 Sensitivity to noise

Noise is a natural enemy of precision measurements and the knowledge about an enemy is fundamental for a contest. We therefore will first introduce some basic tools for the description of noise [48], followed by a treatment of the special problem of phase noise on the Raman lasers. The phase fronts of the Raman lasers provide a ruler for the acceleration measurement and any phase noise on the lasers will transfer onto the interferometer phase noise with a certain weight, which images the response of the phase of the atomic wave-function on the laser phase. To get an idea of the quality of the necessary phase stability, we assume a typical interferometer time $T = 150$ ms, yielding a phase shift due to the Earth's acceleration g of $\Delta\phi = k_{\text{eff}}gT^2 \approx 3.6 \cdot 10^{-6}$ rad. A measurement accuracy of $\Delta g/g = 10^{-9}$ signifies a maximum phase noise on the order of 1 mrad. In the second part of this chapter, we will derive the above mentioned weight function for a gravimeter. It needs to be said that we will assume plane wave fronts of the Raman beams as well as of the atomic wave-function in this section.

2.3.1 Definitions

Let us consider a laser with electric field

$$E(t) = (E_0 + \epsilon(t)) \sin(2\pi f_0 t + \phi_N(t) + \phi_0), \quad (2.100)$$

which shows frequency, phase and amplitude noise and where the instantaneous frequency and phase noise are related by $f(t) = f_0 + \dot{\phi}_N(t)/2\pi$. In the following, we omit the index N of the phase noise for convenience, but it will reappear in chapter 4. It is useful to define the instantaneous fractional frequency deviation y from the center frequency f_0 as

$$y(t) = \frac{f(t) - f_0}{f_0} = \frac{1}{2\pi f_0} \frac{d\phi(t)}{dt}. \quad (2.101)$$

The spectral Fourier analysis of the phase or frequency noise is often expressed in terms of the *spectral density of phase or frequency fluctuations* in radians square per Hz bandwidth:

$$S_\phi(f) \left[\frac{\text{rad}^2}{\text{Hz}} \right] = \frac{1}{f^2} S_f(f) \left[\frac{\text{Hz}^2}{\text{Hz}} \right] = \frac{f_0^2}{f^2} S_y(f) \left[\frac{1}{\text{Hz}} \right]. \quad (2.102)$$

For $\int_f^\infty S_\phi(f') df' \ll 1 \text{ rad}^2$, one can define the Single Sideband Phase Noise $L(f)$ as $L(f) = 1/2 S_\phi(f)$ ⁵.

For a time-domain characterization of the noise around $\phi = 0$, the one-sample variance $\sigma_{\phi,1}(\tau)$ (mean square phase modulation) can be employed, where we use $\bar{\phi}$ as the

⁵The SSB phase noise in [dBc/Hz]: $L[\text{dBc}/\text{Hz}] = 10 \log_{10} \frac{S_\phi/2}{\text{1 rad}^2}$.

average of the signal $\phi(t)$ over a time τ :

$$\begin{aligned}\sigma_{\phi,1}^2(\tau) &= \left\langle \bar{\phi}(t_i)^2 \right\rangle_{t_i} = \left\langle \left| \frac{1}{\tau} \int_{t_i}^{t_i+\tau} \phi(t') dt' \right|^2 \right\rangle_{t_i} = \left\langle \left| \int_{-\infty}^{\infty} \phi(t') h_1(t_i - t') dt' \right|^2 \right\rangle_{t_i} \\ &= \lim_{T \rightarrow \infty} \frac{1}{2T} \int_{-T}^T |(\phi \otimes h_1)(t)|^2 dt = \lim_{T \rightarrow \infty} \frac{1}{2T} \int_{-\infty}^{\infty} |\Phi_T(f)|^2 \cdot |H_1(f)|^2 df \\ &= \int_0^{\infty} S_\phi(f) |H_1(f)|^2 df = 2 \int_0^{\infty} S_\phi(f) \frac{\sin^2(\pi f \tau)}{(\pi f \tau)^2} df\end{aligned}\quad (2.103)$$

We wrote the Fourier transforms in capital letters, where $\Phi_T(f)$ is the Fourier transform of $\phi(t)$ and the subscript T emphasizes that $\phi(t)$ is defined only in the interval $-T < t < T$. The subscript is not used on the so-called transfer function $H_1(f)$, since $h_1(t)$ is per se only defined within this interval: it reaches the constant value $h_1(t) = 1/\tau$ between $t=0$ and τ and zero else and therewith images a sample of duration τ . For infinite sampling time $\tau \rightarrow \infty$, the variance is just $\sigma_\phi^2 = \int_0^{\infty} S_\phi(f) df$.

One will find that this variance does not converge for certain types of noise (Random walk and flicker frequency-noise; see below) and long measurement times. For this reason the two sample variance without dead time, called *Allan Variance* $\sigma_{\phi,2}$, has been introduced. It takes the average over all times t_i of the difference between *two consecutive mean values* $\bar{\phi}$ with sample time τ , and has the transfer function $|H_2(f)|$:

$$\begin{aligned}\sigma_{\phi,2}^2(\tau) &= \left\langle \frac{(\bar{\phi}(t_i + \tau) - \bar{\phi}(t_i))^2}{2} \right\rangle_{t_i} = \frac{1}{2} \left\langle \left[\frac{1}{\tau} \int_{t_i}^{t_i+\tau} \phi(t') dt' - \frac{1}{\tau} \int_{t_i-\tau}^{t_i} \phi(t') dt' \right]^2 \right\rangle_{t_i} \\ &= \frac{1}{2} \left\langle \left[\int_{-\infty}^{\infty} \phi(t') h_2(t_i - t') dt' \right]^2 \right\rangle_{t_i} = \int_0^{\infty} S_\phi(f) |H_2(f)|^2 df \\ &= 2 \int_0^{\infty} S_\phi(f) \frac{\sin^4(\pi f \tau)}{(\pi f \tau)^2} df.\end{aligned}\quad (2.104)$$

The transfer function $|H_2(f)|$ is the Fourier transform of the function $h_2(t)$, which cuts out the two consecutive samples of the function $\phi(t)$ and takes their difference:

$$h_2(t) = \begin{cases} 1/\tau & , -\tau \leq t < 0 \\ -1/\tau & , 0 \leq t < \tau \\ 0 & , t > |\tau| \end{cases}\quad (2.105)$$

Types of noise: The spectral density plot of any real oscillator noise is a combination of different noise processes. There is the *discrete frequency noise*, which might for example originate in mechanical resonances, and there is the *power-law noise*. The power-law model assumes the spectral density of phase (frequency) fluctuations to be equal to a sum of terms, each of which varies with an integer power of frequency. There will thus be two quantities, which completely specify the spectral noise density: the slope α on a log-log plot over frequency and the amplitude h_α :

$$S_{\phi \text{ or } y}(f) = \sum_{\alpha=-\infty}^{\alpha=\infty} h_\alpha f^\alpha.$$

For power-law types of noise, the variance can be written as

$$\sigma_\phi^2(\tau) = 2 \sum_{\alpha=-\infty}^{\alpha=\infty} h_\alpha \int_0^\infty f^\alpha |H(f)|^2 df = \sum_{\alpha=-4}^{\alpha=0} h_\alpha a_\alpha \tau^\mu. \quad (2.106)$$

where we performed a power expansion of $\sigma_{\phi,2}^2$ in τ to reveal the characteristic exponent μ of τ for each type of noise. Expression (2.106) does not converge for the transfer function of the one-sample variance H_1 for $\alpha_\phi = -4, -3$ and $\tau \rightarrow \infty$, whereas it does converge for the transfer function H_2 of the Allan variance.

Comment: The Allan variance shows the same dependence on Flicker and White phase noise, what makes it useless for a careful analysis of limiting noise types. For this reason, a *modified Allan variance* has been introduced, which can also be found in [48].

There exist five common noise processes with the following exponents α for the spectral densities – or μ in case of the Allan variance. The following table contains these exponents and Figure 2.5 shows the corresponding slopes of the spectral densities and the Allan variance:

Noise type	α for S_ϕ	α for S_y	μ for $\sigma_{\phi,2}^2$
Random walk frequency	-4	-2	1
Flicker frequency modulation	-3	-1	0
White frequency modulation	-2	0	-1
Flicker phase modulation	-1	1	-2
White phase modulation	0	2	-2

2.3.2 Weighting function

The phase noise of the laser will transmit via discriminators onto the interferometer phase noise. In the Fourier space, the discriminators will apply some frequency dependent weight onto the noise. We will assume a stable amplitude of the Raman lasers and can state that also relative frequency fluctuations between the Raman lasers will remain small because of the phase-lock. Absolute frequency variations will be the same for both lasers and will not change the Raman transition rate as long as the deviation stays small relative to the detuning from resonance.

The Raman lasers are first of all discriminated by a shutter, which cuts three rectangular pulses of lengths $\tau, 2\tau$ and τ out of the continuous light. Let's call this discrimination function $h(t)$. The output of the discriminator is the convolution of $\phi(t)$ with $h(t)$ (for h consisting of rectangular pulses the convolution is equal to the product).

Here, we will make the assumption that during these pulses the laser phase noise is directly transmitted onto the atomic wave-function, which means, the interferometer

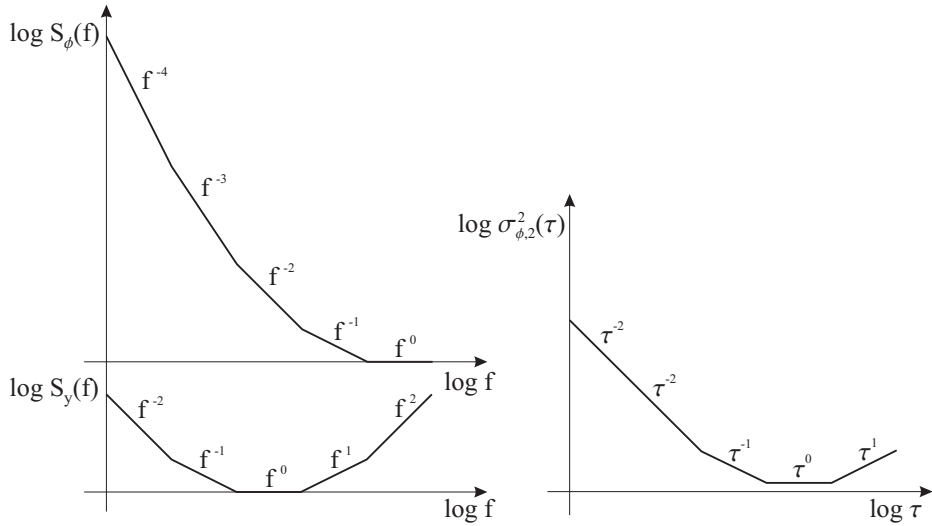


Figure 2.5: Double-logarithmic plots of the spectral noise densities for common power law noise sources. On the left the spectral phase noise density on top of the spectral (normalized) frequency noise density and on the right the Allan Variance over sample time.

performs phase measurements of the laser and combines them to the output (see section 2.2.2)

$$\Delta\phi = \bar{\phi}_A - 2\bar{\phi}_B + \bar{\phi}_C, \quad (2.107)$$

which in turn is linked to the measured relative state population by

$$\frac{N_a}{N} = \frac{1}{2}A(1 + \cos(\Delta\phi)), \quad (2.108)$$

where A is a contrast factor. We call $\bar{\phi}_K$ the average phase $\bar{\phi}_K = 1/\tau \int_{-\tau/2}^{\tau/2} \phi(t)dt$ during the pulse $K = A, B$ or C . Section 2.3.4 will explain the difference between this approximate- and the exact calculation of section 2.3.3, which includes the interaction of light and atoms during the pulse.

The link between $\Delta\phi$ and $\bar{\phi}_K$ signifies a further weighting of the phase noise by the pulses with 1, -2 and 1, respectively, and h thus gets $\bar{h}(t)$ which is shown in Fig. 2.6⁶.

⁶The integral of each pulse is initially normalized. First and last pulse of length τ to $1/\tau$ and the second pulse of length 2τ to $1/2\tau$. The weight of $\phi_A - 2\phi_B + \phi_C$ leads to Fig. 2.6

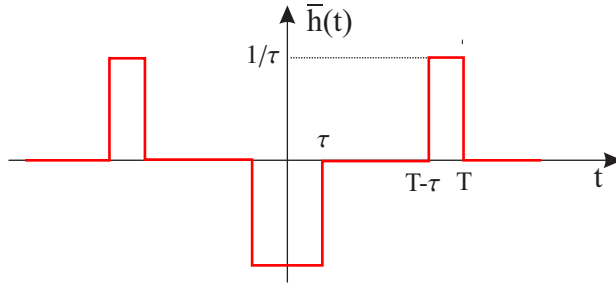


Figure 2.6: The weighting function $\bar{h}(t)$. The atoms will be opposed to the convolution of the phase noise of the Raman lasers $\phi(t)$ with $\bar{h}(t)$. We center the function in $t=0$ for symmetry reasons. The whole length of the interferometer sequence is $2T$, including the pulses.

We calculate the variance σ_ϕ^2 of $\Delta\phi$ (2.107) according to (2.103):

$$\begin{aligned}
 \sigma_\phi^2 &= \left\langle \left| \frac{1}{\tau} \int_{t_i-T}^{t_i-T+\tau} \phi(t') dt' - 2 \frac{1}{2\tau} \int_{t_i-\tau}^{t_i+\tau} \phi(t') dt' + \frac{1}{\tau} \int_{t_i+T-\tau}^{t_i+T} \phi(t') dt' \right|^2 \right\rangle_{t_i} \\
 &= \left\langle \left| \int_{-\infty}^{\infty} \phi(t') \otimes \bar{h}(t_i - t') dt' \right|^2 \right\rangle_{t_i} \\
 &= \lim_{T \rightarrow \infty} \int_0^{\infty} \frac{2|\Phi(f)|^2}{T} |\bar{H}(f)|^2 df \\
 &= \int_0^{\infty} S_\phi(f) |\bar{H}(f)|^2 df , \tag{2.109}
 \end{aligned}$$

where $\bar{H}(f)$ is the Fourier Transform of $\bar{h}(t)$ and takes the form

$$\begin{array}{lcl}
 \bar{H}(f) &=& -\frac{4}{\pi f \tau} \sin(\pi f \tau) \sin(\pi f(T - \tau)) \sin(\pi f T) \\
 &=& -\frac{4}{f/f_0} \sin(\pi f \tau) \sin(\pi f(T - \tau)) \sin(\pi f T) \tag{2.110}
 \end{array}$$

$|\bar{H}(f)|^2$ is called the weighting function (or transfer function as in (2.103) and in control theory), since it indicates the weight of the phase noise density $S_\phi(f)$ at a certain frequency. This function has a low frequency cutoff below $f = 1/(\pi T)$ and a high frequencies filtering above $f_0 = 1/(\pi\tau)$.

2.3.3 Exact calculation of the weighting function

We will now consider the the change of the atomic wave-function during the Raman pulses (see equations (2.46)) to get a more accurate estimation of the weighting function. The whole formalism has been introduced to characterize atomic clocks, which are driven by microwave pulses. Recently, these results have been applied to optically driven atom-interferometers in [51] and [50].

According to [130], we introduce the sensitivity function $g(t)$ as the relative variation of the transition probability δP due to a phase step $\delta\phi$ occurring at time t :

$$g(t) = 2 \lim_{\delta\phi \rightarrow 0} \frac{\delta P(\delta\phi, t)}{\delta\phi}. \quad (2.111)$$

We will determine $g(t)$ around $P = 1/2$, where the interferometer is most sensitive to phase noise and where P_a depends linearly on $\Delta\phi$:

$$\begin{aligned} P_a &= \frac{1}{2} (1 + \cos(\Delta\phi)) = \frac{1}{2} (1 + \cos(\pi/2 + \epsilon)) \\ &= \frac{1}{2} (1 + \sin(\epsilon)) \approx \frac{1}{2} (1 + \epsilon). \end{aligned} \quad (2.112)$$

To determine $g(t)$, we have to calculate P or $\Delta\phi$ for a phase jump at time t . We use the equations (2.48) for zero detuning and compensated light shift. For optimum fringe contrast, we assume $\Omega_{\text{eff}} = \pi/2\tau$. We can proceed according to the calculation of the interferometer phase shift (2.56), but need to add an additional iteration in the following manner: If the phase jump happens during a pulse, we split the pulse into two consecutive pulses with different phase offset. For illustration, we will do the example of a phase jump from $\phi = 0$ to $\phi = \delta\phi$ at time t during the first pulse, $-T < t < -T + \tau$, which we split into two pulses of duration $T + t$ and $-T + \tau - t$. We again start with all atoms in state $|a\rangle$:

$$\begin{aligned} c_a(-T) &= 1 \\ c_b(-T) &= 0 \\ c_a(t) &= \cos\left(\frac{\Omega_{\text{eff}}(T+t)}{2}\right) \\ c_b(t) &= -i \sin\left(\frac{\Omega_{\text{eff}}(T+t)}{2}\right) \\ c_a(-T + \tau) &= \cos\left(\frac{\Omega_{\text{eff}}(T+t)}{2}\right) \cos\left(\frac{\Omega_{\text{eff}}(-T+\tau-t)}{2}\right) \\ &\quad + e^{i\delta\phi} \sin\left(\frac{\Omega_{\text{eff}}(T+t)}{2}\right) \sin\left(\frac{\Omega_{\text{eff}}(-T+\tau-t)}{2}\right) \\ c_b(-T + \tau) &= ie^{-i\delta\phi} \cos\left(\frac{\Omega_{\text{eff}}(T+t)}{2}\right) \sin\left(\frac{\Omega_{\text{eff}}(-T+\tau-t)}{2}\right) \\ &\quad - i \sin\left(\frac{\Omega_{\text{eff}}(T+t)}{2}\right) \cos\left(\frac{\Omega_{\text{eff}}(-T+\tau-t)}{2}\right). \end{aligned}$$

The iteration continues to derive the coefficients after the second and third pulse, keeping the phase offset $\delta\phi$. From the final probability amplitude of finding the atom in state $|a\rangle$:

$$P_a = \frac{1}{2} (1 + \sin(\delta\phi) \sin(\Omega_{\text{eff}}(T + t))) \quad (2.113)$$

follows the sensitivity-function in the time interval $-T < t < -T + \tau$ as

$$g(t) = 2 \lim_{\delta\phi \rightarrow 0} \frac{\delta P(\delta\phi, t)}{\delta\phi} = \sin(\Omega_{\text{eff}}(T + t)). \quad (2.114)$$

We proceed in a similar way by introducing the phase step during the other two pulses to find the sensitivity function for those time intervals.

It is easier to derive the sensitivity function for the times between the pulses. We already found out that $P_a = \frac{1}{2}(1 + \cos \Delta\phi)$ with $\Delta\phi = \phi_A - 2\phi_B - \phi_C$. To ensure

$P_a = \frac{1}{2} \pm \epsilon$, we set $\phi_C = \pi/2$. A phase jump between the first and second pulse signifies $\phi_A = 0$, $\phi_B = \delta\phi$ and $\phi_C = \pi/2 + \delta\phi$, what leads to

$$P_a = \frac{1}{2}(1 + \sin \delta\phi) \quad \text{and} \quad (2.115)$$

$$g(t) = 2 \lim_{\delta\phi \rightarrow 0} \frac{1}{2} \cos \delta\phi = 1 \quad (2.116)$$

within this time interval.

We find the total sensitivity function to be (see Fig. 2.7):

$$g(t) = \begin{cases} 0 & , -T_{\text{rep}}/2 < t < -T \\ \sin(\Omega(t+T)) & , -T \leq t < -T + \tau \\ 1 & , -T + \tau \leq t < -\tau \\ -\sin(\Omega t) & , -\tau \leq t < \tau \\ -1 & , \tau \leq t < T - \tau \\ \sin(\Omega(t-T)) & , T - \tau \leq t < T \\ 0 & , T < t < T_{\text{rep}}/2 \end{cases} \quad (2.117)$$

We defined g only between $-T_{\text{rep}}/2$ and $T_{\text{rep}}/2$ since the interferometer sequence will

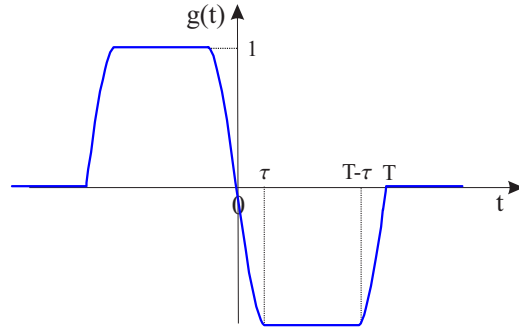


Figure 2.7: The sensitivity function $g(t)$ describes the sensitivity of the interferometer phase on a small phase step of the Raman lasers.

be repeated with frequency $1/T_{\text{rep}}$.

To find the link between $g(t)$ and σ_ϕ^2 , we will write the continuous phase noise $\phi(t)$ as a sum over many phase steps:

$$\phi(t) = \lim_{\Delta t \rightarrow 0} \sum_{N=1}^{T_{\text{rep}}/\Delta t} \delta\phi(N\Delta t) . \quad (2.118)$$

From the definition of the sensitivity function (2.111) and by using (2.112) follows

$$\begin{aligned}
 \delta P &= \frac{1}{2} \delta(\Delta\phi) = \frac{1}{2} \lim_{\Delta t \rightarrow 0} \delta\phi g(t) \\
 &= \frac{1}{2} \lim_{\Delta t \rightarrow 0} \sum_{N=1}^{T_{\text{rep}}/\Delta t} g(-T_{\text{rep}}/2 + N\Delta t) \delta\phi(-T_{\text{rep}}/2 + N\Delta t) \\
 &= \frac{1}{2} \int_{-T_{\text{rep}}/2}^{T_{\text{rep}}/2} g(t) \frac{\delta\phi}{dt} dt = \frac{1}{2} \int_{-\infty}^{\infty} g(t) \frac{\delta\phi}{dt} dt \Big|_{\substack{\text{if } g=0 \text{ for } \\ |t|>T_{\text{rep}}/2}} . \quad (2.119)
 \end{aligned}$$

It gets clear that our previous $h(t)$ is the derivative of $g(t)$: $h(t) = \partial g(t)/\partial t$. We thus get the weighting function as the Fourier transform of $g(t)$ times $2\pi f$, or as the Fourier transform of $h(t)$, what is somehow easier to calculate:

$$\begin{aligned}
 \left\| H(f) \right. &= \omega G(f) \quad (2.120) \\
 &= \frac{2\Omega_{\text{eff}}^2}{\Omega_{\text{eff}}^2 - \omega^2} \left(\cos(\omega(T - \tau)) - \cos(\omega\tau) - \frac{\omega}{\Omega_{\text{eff}}} \sin(\omega T) \right) \\
 &= -\frac{4\Omega_{\text{eff}}^2}{\Omega_{\text{eff}}^2 - \omega^2} \sin(\omega T/2) \left(\sin(\omega(T - 2\tau)/2) + \frac{\omega}{\Omega_{\text{eff}}} \cos(\omega T/2) \right) \\
 &\left. = -\frac{4}{1 - f^2/f_0^2} \sin(\pi f T) \left(\sin(\pi f(T - 2\tau)) + f/f_0 \cos(\pi f T) \right), \right.
 \end{aligned}$$

using $\Omega_{\text{eff}} = \pi/(2\tau)$ so that $f_0 = 1/(4\tau)$. The second order pole in the denominator is counterbalanced by the term in the big brackets. The relation between $h(t)$ and $g(t)$ is also obvious if one calculates the one sample variance of the phase fluctuations using equation (2.119) according to (2.103):

$$\begin{aligned}
 \sigma_{\phi}^2 &= \langle |\delta(\Delta\phi)|^2 \rangle_{t_i} = \langle |2\delta P|^2 \rangle_{t_i} \\
 &= 2 \left\langle \left| \frac{1}{2} \int_{-\infty}^{\infty} g(t - t_i) \frac{\delta\phi(t)}{dt} dt \right|^2 \right\rangle_{t_i} \\
 &= \lim_{T \rightarrow \infty} 2 \int_0^{\infty} \frac{1}{T} |G(f)|^2 |(2i\pi f)\Phi(f)|^2 df \\
 &= \int_0^{\infty} S_{\phi}(f) \underbrace{(2\pi f)^2 |G(f)|^2}_{|H(f)|^2} df. \quad (2.121)
 \end{aligned}$$

2.3.4 Comparison of rough and exact result for the weighting function

Let us compare the results for the weight-function (2.110) and (2.120) of the previous sections. Figure 2.8 shows g - and h -functions for the rough and accurate calculation.

The smoother (sine) h -function in the accurate calculation can be understood intuitively well in the Bloch picture: Imagine the atom being in state $|a\rangle$ and the atomic wave-vector starting to rotate around the electric field vector. A phase fluctuation of

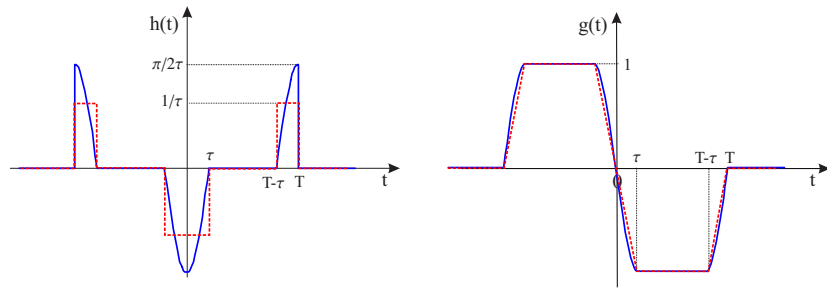


Figure 2.8: g - and h - sensitivity functions for the rough (dashed) and accurate (solid) noise calculation.

the electric field will change the rotation axis, what results in a different population probability at the end of the pulse. Obviously, a phase fluctuation at the beginning of the pulse will have little effect, whereas the effect is maximum when the atom is in a symmetric superposition of $|a\rangle$ and $|b\rangle$ ($P \sim \cos(\delta\phi)$) and the Bloch vector lies in the x-y plane.

This smooth reaction to the square pulses has as a consequence that the weighting function (2.120) shows a higher contribution at middle frequencies and lower contributions at very high frequencies if compared to the weighting function (2.110), as can be seen in Figure 2.9. The cutoff at high frequencies due to the finite duration of the interferometer pulses lies in the square case at $f_0 = 1/(\pi\tau)$, whereas in the exact case the cutoff is earlier, at $f_0 = 1/(4\tau)$. The higher contribution to the phase noise at frequencies around 10 kHz of the weighting function (2.120) causes an increase of the overall integrated phase noise (assuming white noise) by 25% relatively to the weighting function (2.110). On the other hand, the low frequency part of both transfer functions shows exactly the same behavior as a frequency filter below $f = 1/(\pi T)$, determined only by the duration of the interferometer sequence.

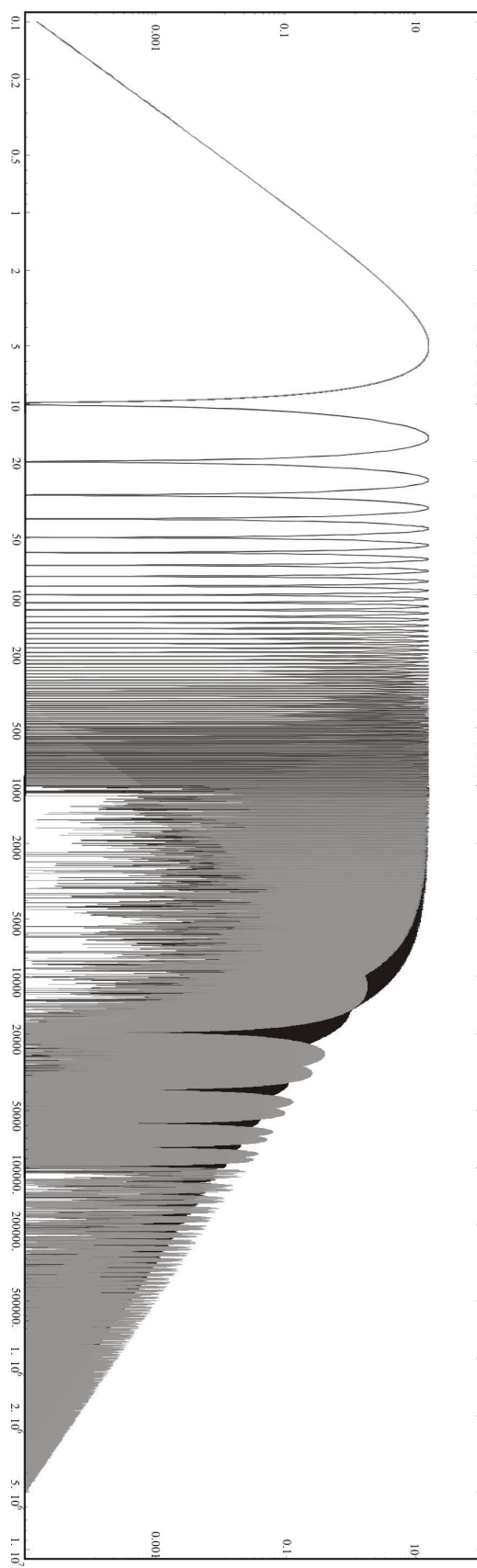


Figure 2.9: Double logarithmic plot of the rough and exact calculation of the weight functions for typical values of $T=100$ ms and $\tau=50$ μ s. The simple model (red curve in front) underestimates the noise by 25% at frequencies around 10kHz relative to the more accurate model (blue).

2.3.5 Dick effect

Our measurement will consist of a long sequence of measurement cycles to average out noise. About $m = 10000$ measurements will be taken with a fix repetition rate of T_{rep} , what gives rise to an aliasing phenomenon well known for atomic clocks, called *Dick effect* [130], which will down-convert multiples of the frequency $1/T_{\text{rep}}$ to low frequencies and increase the sensitivity of the interferometer on these frequencies.

As we have seen in section 2.3.1, the one sample variance (2.121) is no appropriate description for long average times. We will thus calculate the Allan variance as the variance of the difference between the average phase-noise of two consecutive measurement cycles, each containing a certain number $N = \bar{\tau}/T_{\text{rep}}$ of single measurements (see Figure 2.10).

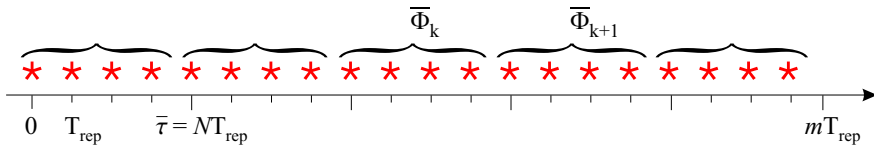


Figure 2.10: A sequence of interferometer measurements (stars), repeated m -times with repetition rate $1/T_{\text{rep}}$. Each point is a variation of the interferometer phase $\delta(\Delta\phi) = 2\delta P$ as a response on the phase fluctuations on the Raman laser $\phi(t)$. To calculate the Allan variance $\sigma_{\phi,2}(\bar{\tau})$, one groups the measurements in time $\bar{\tau}$ to a cycle of $N = \bar{\tau}/T_{\text{rep}}$ single measurements and takes the difference between two consecutive average-values of one cycle $\bar{\phi}_k$.

With the average noise of N interferometer measurements at time t_k

$$\bar{\phi}_k = \frac{1}{N} \sum_{l=0}^N \delta(\Delta\phi(t - lT_{\text{rep}})) = \frac{1}{N} \sum_{l=0}^N \int_{t_k + lT_{\text{rep}}}^{t_k + (l+1)T_{\text{rep}}} g(t - t_k - (l + 1/2)T_{\text{rep}}) \frac{d\phi}{dt} dt, \quad (2.122)$$

the Allan Variance can be written as

$$\sigma_{\phi,2}^2(\bar{\tau}) = \frac{1}{2} \left\langle (\bar{\phi}_{k+1} - \bar{\phi}_k)^2 \right\rangle_{t_k} = \frac{1}{2} \lim_{m/N \rightarrow \infty} \frac{1}{m/N} \sum_{k=1}^{m/N} (\bar{\phi}_{k+1} - \bar{\phi}_k)^2, \quad (2.123)$$

where $\bar{\tau} = N \cdot T_{\text{rep}}$, $t_k = k \cdot \bar{\tau}$, $k = 0, \dots, \frac{m}{N}$.

For convenience, we shift the g -function, which is centered in $t = 0$ according to (2.117), by $T_{\text{rep}}/2$ to begin in $t = 0$, what can be done without loosing generality. We define the function $g_{N,k}(t)$ as the sum of all g -functions in one measurement cycle:

$$g_{N,k}(t) = \sum_{l=0}^N g(t - k\bar{\tau} - lT_{\text{rep}}) \quad (2.124)$$

so that we can write

$$\bar{\phi}_k = \frac{1}{N} \int_{t_k}^{t_k + \bar{\tau}} g_{N,k}(t) \frac{d\phi}{dt} dt \quad \text{and} \quad (2.125)$$

$$\bar{\phi}_{k+1} - \bar{\phi}_k = \frac{1}{N} \int_{t_k}^{t_k + \bar{\tau}} \underbrace{(g_{N,k+1}(t) - g_{N,k}(t))}_{\tilde{g}_k(t)} \frac{d\phi}{dt} dt. \quad (2.126)$$

The new function $\tilde{g}_k(t)$ represents the difference between two consecutive $g_{N,k}$ -functions. For long enough averaging times $\bar{\tau}$, there will be no correlation between the noise on $(\bar{\phi}_k - \bar{\phi}_{k-1})$ and $(\bar{\phi}_{k+1} - \bar{\phi}_k)$ and we can assume $\tilde{g}_k \equiv \tilde{g}_0$:

$$g_{N,k+1}(t) - g_{N,k}(t) = \tilde{g}_k(t) \stackrel{!}{=} \tilde{g}_0(t) = \sum_{l=0}^{N-1} (g(t - \bar{\tau} - lT_{\text{rep}}) - g(t - lT_{\text{rep}})). \quad (2.127)$$

For clarity, the functions that are used here are shown in Figure 2.11.

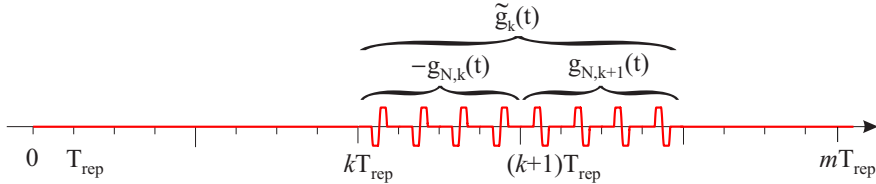


Figure 2.11: To calculate the Allan variance of the noise on the output phase signal of an interferometer, we defined the functions $g_{N,k}(t)$ and $\tilde{g}_k(t)$. The first is just the sum over the g -functions in one measurement cycle of N single measurements and the latter is the difference between two successive $g_{N,k}$ -functions.

We immediately calculate the Fourier transform $\tilde{G}(f)$ of $\tilde{g}_0(t)$, which will serve us later on for the calculation of the Allan variance. We make use of $N = \bar{\tau}/T_{\text{rep}}$, the property of the Fourier transform that a shift in time by t_0 corresponds to a multiplication with $e^{i\omega t_0}$ of the Fourier transform and some algebraic transformations⁷:

$$\begin{aligned} |\tilde{G}(f)|^2 &= \left| \sum_{l=0}^{N-1} (G(f) \cdot e^{2i\pi f(\bar{\tau} + lT_{\text{rep}})} - G(f) \cdot e^{2i\pi f l T_{\text{rep}}}) \right|^2 \\ &= 4|G(f)|^2 \cdot \frac{\sin^4(\pi f \bar{\tau})}{\sin^2(\pi f T_{\text{rep}})}. \end{aligned} \quad (2.128)$$

Here, $G(f)$ is the Fourier transform of the g -function (2.117) of the previous chapter.

The transfer function can be expressed according to the relation $\tilde{H}(f) = 2\pi f \tilde{G}(f)$:

$$|\tilde{H}(f)|^2 = 4 \frac{\sin^4(\pi f \bar{\tau})}{\sin^2(\pi f T_{\text{rep}})} |H(f)|^2, \quad (2.129)$$

where $H(f)$ is the weighting function of the one-sample variance (2.120).

⁷ $\sum_{l=0}^{N-1} e^{\alpha l} = \frac{-1 + e^{\alpha N}}{-1 + e^{\alpha}}$

Now we insert the difference (2.126) into the expression for the Allan variance (2.123), which yields

$$\left\| \sigma_{\phi,2}^2(\bar{\tau}) = \frac{1}{N^2} \int_0^\infty \underbrace{|\tilde{G}(f)|^2 (2\pi f)^2 S_\phi(f)}_{=|\tilde{H}(f)|^2} df . \right. \quad (2.130)$$

In the limit of *long averaging times* $\bar{\tau}$, we can write $\tilde{H}(f)$ as a sum

$$|\tilde{H}(f)|^2 \xrightarrow{\bar{\tau} \rightarrow \infty} \frac{2\bar{\tau}}{T_{\text{rep}}^2} \sum_{n=-\infty}^{\infty} \delta(2\pi(f - n/T_{\text{rep}})) |H(f)|^2 , \quad (2.131)$$

and the Allan variance (2.130) simplifies to:

$$\left\| \sigma_{\phi,2}^2(\bar{\tau}) = \frac{1}{\bar{\tau}} \sum_{n=1}^{\infty} \left| H\left(\frac{2\pi n}{T_{\text{rep}}}\right) \right|^2 S_\phi\left(\frac{2\pi n}{T_{\text{rep}}}\right) . \right. \quad (2.132)$$

Noise at multiples of the repetition frequency $1/T_{\text{rep}}$ will limit the sensitivity of a long interferometer measurement.

One can now examine the contribution of various types of noises. The easiest is to watch the case of white phase noise, which has no frequency dependence (see section 2.3.1). One will find a linear dependence of the Allan variance on the inverse Raman pulse length. But the longer the pulse, the stronger the velocity selection and the less atoms will participate in the interferometer, what degrades the signal to noise ratio. For the Paris gyroscope, the optimum pulse length was found to be $20\ \mu\text{s}$ [49, 50].

Chapter 3

Experimental setup

This chapter is divided into four sections. The first section describes the experiment chamber of the gradiometer, motivates the choice of materials for the ultra-high vacuum (UHV) system and introduces the sealing techniques with lead and glue, we used for this system. A short second section describes, how we ensure the proper magnetic field configuration in the various parts of the apparatus. This description is followed by a section that deals with the laser system for the gradiometer and the gravimeter. We introduce the lasers on which the system is based and sketch the beam path, including the fiber system that delivers the light to the experiment. An important aspect of the MAGIA experiment are the source masses used for the determination of G . We will explain in the fourth section of this chapter first, how the double-differential G -measurement will be performed and how we optimize the atomic trajectories to reduce sensitivity on launch imperfections. Then, we describe the source masses themselves together with their support.

3.1 Vacuum System

In this section, we will mainly describe the vacuum system of the MAGIA experiment (gradiometer for the determination of G), since it was constructed during this thesis. The vacuum system for this atom interferometer had to fulfill several conditions:

- *Vacuum:* The experiment requires a vacuum that is good enough to prevent collisions of the atoms with the background vapor to disturb the measurement. The pressure p should be in the order of 10^{-9} mbar = 10^{-7} Pa, which corresponds to ($pV = NkT$) 25 million particles per centimeter cube and a mean free path (for N_2) of around 70 km.
- *Material:* Necessary properties of the material used in the construction of the vacuum system are: A low outgassing, a high resistance to prevent the formation

of Eddy currents and a low permanent magnetization to prevent Zeeman shifts during the interferometer. The whole apparatus should be heatable to at least 150 °C to clean the inner surfaces.

- *Windows:* For the manipulation of the atoms, the apparatus should offer good optical access for laser beams without disturbing their wavefront curvature or producing strong reflections.
- *Spatial restrictions:* For a G measurement, heavy source masses have to be placed very close to the atoms to produce a reasonably high signal and therefore the interferometer region needs to be kept thin.
- *Alignment:* The launch of the atom must be exactly vertical and the apparatus should allow an easy alignment of the launch direction.

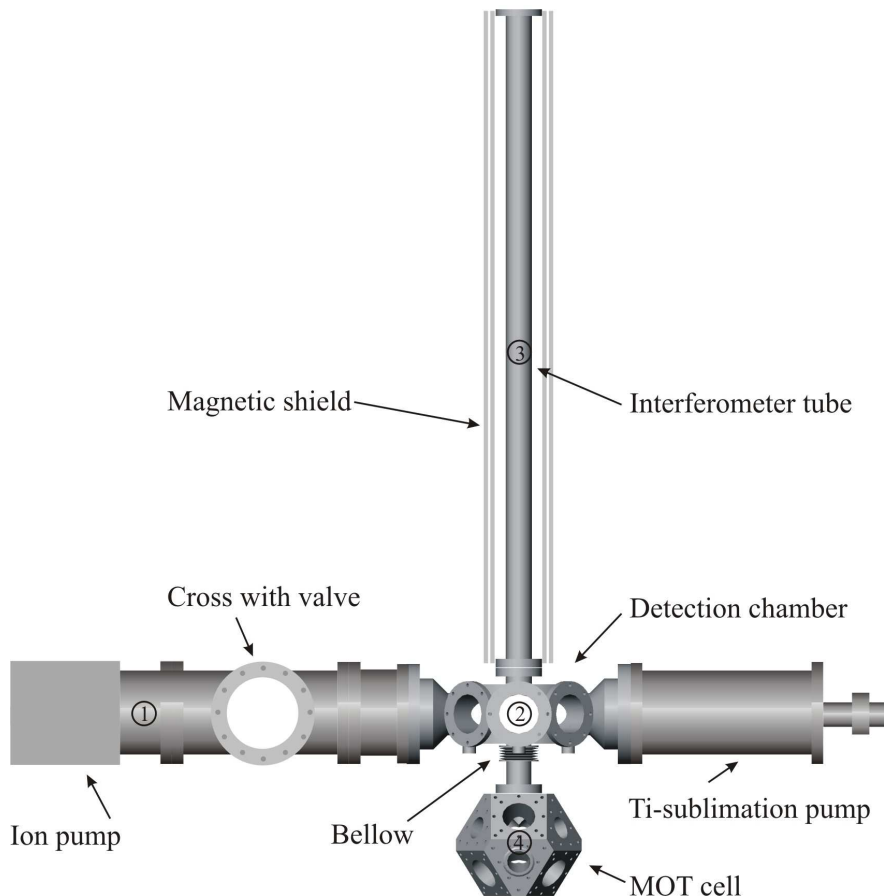


Figure 3.1: The MAGIA apparatus. The experiment is performed in the central part where the atoms are cooled (MOT cell), manipulated and detected (Detection chamber) and opposed to interferometer pulses (Interferometer tube). Vacuum pumps are attached on the left and right of the detection chamber. The height of the whole apparatus is about 1.5 m.

3.1.1 Description of MAGIA apparatus

All the above considerations lead to the apparatus, which will be described in the following paragraphs and which shown in Fig. 3.1 schematically and in Fig. 3.3 as it is in reality. Manufacturing was done by HIGH VACUUM PROCESS, Parma.

MOT cell: The cell for the magneto-optical trap (MOT) is machined from titanium and has the geometry of a cube with 15 cm side length, whose eight edges are cut orthogonally to the principal diagonals to get 14 surfaces: 6 quadratic and 8 triangular ones with holes for optical access of 50 mm and 35 mm diameter, respectively. The cube is oriented with one principle diagonal along the vertical axis. The MOT beams enter the cube by the holes in the 6 quadratic surfaces under an angle of $\alpha \approx 54.7^\circ (\cos \alpha = 1/\sqrt{3})$ to the vertical (1-1-1 MOT configuration).

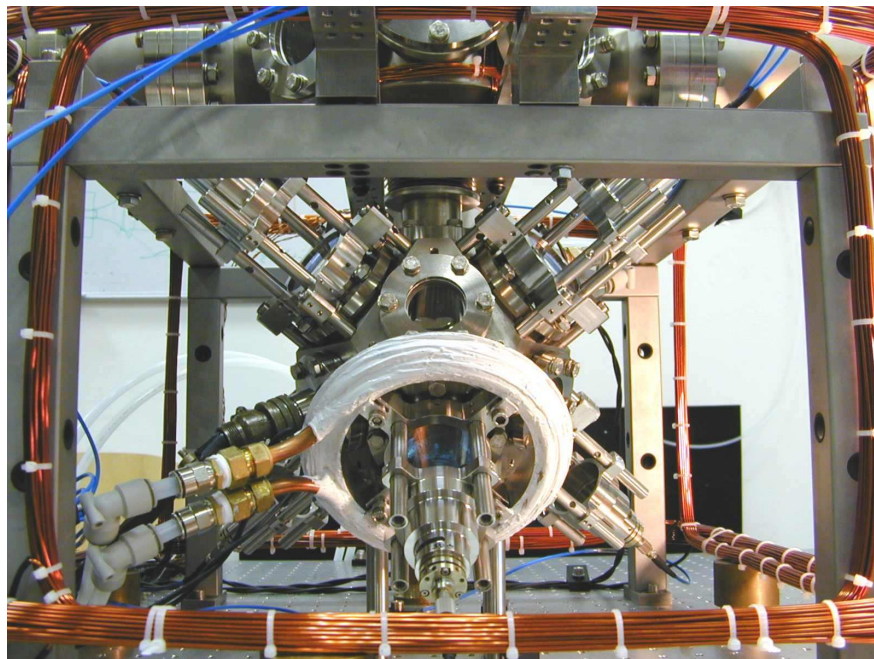


Figure 3.2: Cell for magneto-optical trapping of the atoms. Visible are the collimators for the cooling beams, fixed rigidly to the square surfaces, the water-cooled MOT coils and one free window. At the border of the image one can identify some compensation coils.

The beams serve for trapping and cooling the atoms and a frequency detuning of the 3 beams entering the cell from below relative to the beams entering from above will cause a vertical launch of the atoms. The vertical axis itself is left free for the Raman beams, which enter through the bottom window, pass the whole apparatus, escape through the top window and are reflected back by a mirror above the interferometer tube.

We installed rubidium dispensers in one access flange to create a rubidium background pressure high enough to ensure an effective loading of the MOT. The fluorescence of the trapped atoms is monitored through a further window and a last flange is left free for the future connection of a 2 dimensional MOT.

Detection chamber: To ease the alignment of the launch, a flexible bellow connects the MOT cell to the detection chamber, which is made of non-magnetic stainless steel 316LN. It provides 6 AR coated windows of 60 mm diameter for optical access and is connected by two CF100 flanges to a titanium sublimation pump and an ion pump. The detection chamber is used for state preparation, state-sensitive detection and in future for a further cooling of the atoms.

Interferometer tube: The interferometer region consists of a 1 m long titanium tube (Ti90Al6V4) with a window at the top through which the Raman beams escape. The tube has an external diameter of only 4 cm (internal: 3.5 cm) to permit a close positioning of the source masses. A coil is wrapped around the tube to apply a magnetic field along the vertical axis that defines a quantization axis for the atoms. External fields are shielded by a double layer magnetic shield (see section 3.2.2).

Pumps: We use a 75 l/s *ion pump* (VARIAN VacIon 75 Plus Star Cell, driver MidiVac) connected by large CF100 tubes to the detection chamber to ensure a high pumping rate. It is placed far from the experiment (55 cm) to allow the strong magnetic fields to decay sufficiently to below 0.5 Gauss. Nevertheless, a shielding of the pump is projected.

We mounted a *titanium sublimation pump* (THERMIONICS SB-1020 with driver VARIAN 9290023) for effective pumping of gases like H₂ and N₂. The combination with an ion pump is important for the non-gettable gases like Ar or CH₄. The pump consists of 3 titanium filaments (85% Ti, 15% Mo to prevent burnout). When sending current through the filaments, the titanium evaporates and forms a thin layer on the wall of the vacuum chamber, which can adsorb gas. The pumping speed varies from 9 l/s/cm² for CO over 3 l/s/cm² for H₂ to 0 l/s/cm² for CH₄. Assuming a dominant pressure of N₂ (4 l/s/cm²) and the total coverage of the surface around the cell with titanium (1240 cm²), pumping speed is only limited by the conductance to the pump; e.g. 120 l/s in the detection chamber. The Ti-layer saturates after a while and a new cover has to be made. The cycles of operation depend on pressure and are typically 1 hour at 10⁻⁹ Torr and 8h at 10⁻¹⁰ Torr. Currently, the sublimation pump is not used, since the ion pump alone already maintains a sufficiently low pressure.

Rubidium dispenser: Five rubidium-dispensers (SAES getters 5G0807) supply the MOT with atoms. Each dispenser is a 12 mm long container which enclose a reser-

voir of rubidium-chromate (Rb_2CrO_4) that contains 4.5 mg of rubidium. A current between 3 and 7 Ampere through the dispenser heats up the container to a maximum temperature of 800°C. The Rb starts to evaporate at 500°C and escapes its container through a slit. The atoms immediately scatter at the wall of the MOT cell and thermalize to ambient temperature. Those atoms with velocities lower than 30-40 m/s can be trapped by the MOT. We usually work with a constant dispenser current between 3 and 4 Ampere. In the past one and a half years, we always used the same (and only one) dispenser.

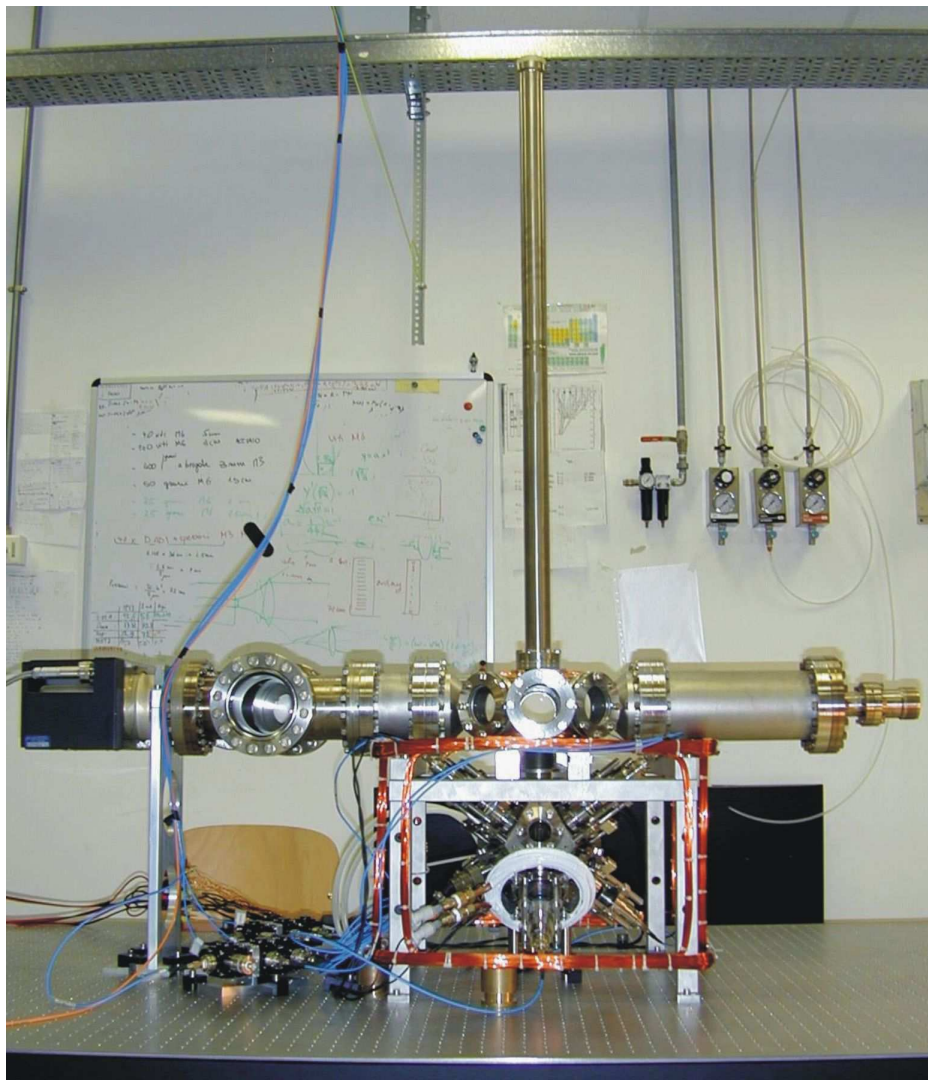


Figure 3.3: The MAGIA apparatus. We show a photo of the naked system in may 2003 to recognize all elements discussed in this section. In the present status they would no longer be clearly visible.

Bake-out of system: We baked our whole system for 5 weeks to evaporate all impureness from the surfaces. The steel parts were heated to 200°C and the more delicate parts with lead and glue up to 140°C, although higher temperatures had been tested before. Our final pressure in the MOT chamber is of the order of 10^{-10} Torr, the major gas load consists of CO, N₂ and H₂. The lower the pressure, the more dominant gets the fraction of Hydrogen.

Properties of Vacuum materials: Ultra-high vacuum chambers require the use of low outgassing materials and good sealing techniques. The system needs to be baked to clean the surfaces and therefore requires a good matching of the thermal expansion coefficient at delicate junctions like metal-glass. Materials with low magnetic susceptibility are important to exclude magnetic field contributions that would disturb the measurement. What cannot be avoided are the magnetic fields of the MOT-coils, which are switched off during the critical part of the experiment, but whose switching can induce Eddy currents in materials with low electric resistivity, what makes also this parameter important in the choice of materials. Table 3.1 presents some important properties of the materials we use in our vacuum systems:

Material	CTE μm/ m/ K	OG baked Torr l/ s/ cm ²	unbaked l/ s/ cm ²	Resistivity nΩ· m	Magn Susc $\chi \times 10^{-3}$
<i>M</i> TiAl6V4	7.6	$2 \cdot 10^{-12}$	$5 \cdot 10^{-10}$	1700	<1
<i>e</i> 316LN	16.2	$3 \cdot 10^{-13}$	$1 \cdot 10^{-10}$	740	<5
<i>t</i> 304	17.8	$3 \cdot 10^{-13}$	$1 \cdot 10^{-10}$	720	<10
<i>a</i> Al	23.6	$5 \cdot 10^{-13}$	$1 \cdot 10^{-10}$	26.5	+0.022
<i>l</i> Cu	16.2	$1 \cdot 10^{-12}$	$1 \cdot 10^{-10}$	17	-0.010
Pb	28.9	$1 \cdot 10^{-9}$	$4 \cdot 10^{-9}$	210	-0.018
<hr/>					
BK7	7.5	$5 \cdot 10^{-12}$	$1 \cdot 10^{-10}$	$\gg 10^{10}$	$< - 0.01 $
Graphite	3.8	$5 \cdot 10^{-12}$	$1 \cdot 10^{-10}$	14000	-0.021
<hr/>					
Hardness Shore D					
<i>G</i> Aremco 526	33	$8 \cdot 10^{-10}$	$8 \cdot 10^{-6}$	89	300
<i>l</i> Aremco 631	49	$1 \cdot 10^{-9}$	$1 \cdot 10^{-7}$	75	204
<i>u</i> Epo-Tek H72	42			81	>300
<i>e</i> Epo-Tek 310	soft			22	>250
Epo-Tek 353	54			87	>250

Table 3.1: Properties of all materials of our vacuum system. Values are taken from various references [106]. Outgassing values OG are assumed –not measured– values we used to estimate the pressure. The thermal expansion of the glues can more than double above the glass transition temperature, which is usually between 100 and 150°C.

The main experiment chambers are made of TiAl6V4¹ and stainless steel 316LN, parts leading to the pumps of stainless steel 304; copper is used for sealing the CF-flanges, lead and glue is used to connect the windows made of BK7, purified graphite is used as a passive getter pump, whereas aluminium is just indicated for comparison.

3.1.2 Pressure estimation

One can model the gas flow in high vacuum with laws equivalent to current flow in electronics. The outgassing OG is the equivalent to a current source generating the current I , the gas conductance C through a tube or around a corner like the conductance $1/R$ for a current through a resistance R , where the pressure p is the equivalent to the electronic voltage U and the equivalent to Ohm's law $U = RI$ can be written as $p = OG/C$. Various books contain tables with conductances of holes and tubes of all forms and sizes [99]. The conductance of a long tube of diameter d and length l (in cm) for example is $C = 12D^3/L$ l/s. When designing the apparatus, we assumed the approximative outgassing rates of table 3.1, which in reality depend a lot on the condition of the surface, the previous cleaning and the baking temperature and duration. The equivalent to an electric circuit diagram for the gas flow and pressure of our apparatus is shown in Fig. 3.4. Outgassing OG (in Torr l/s/cm²) of the various materials of

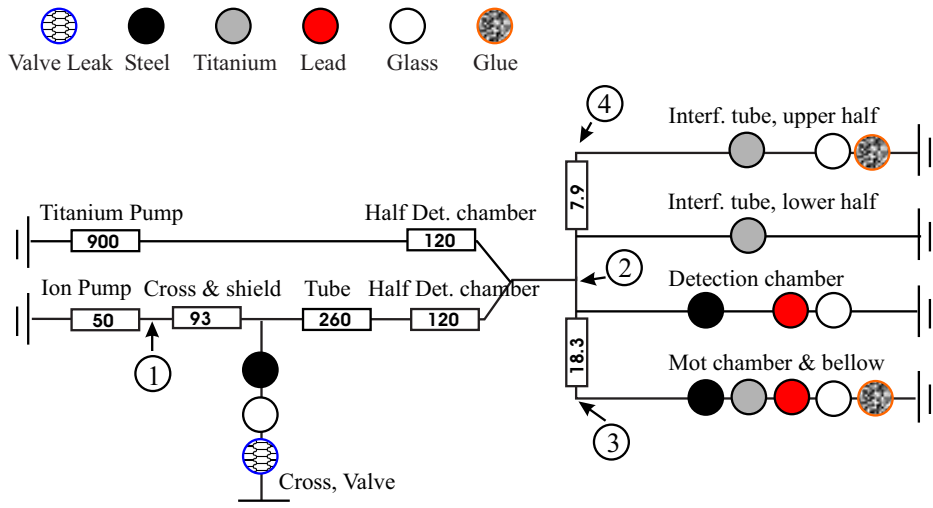


Figure 3.4: Circuit diagram of the vacuum apparatus. Outgassing of various materials are indicated as parallel current sources, conductances of tubes are given in l/s with the pumps indicated as conductances to ground. The numbers 1 to 4 refer to the positions of the pressure values given in the following table: 1: in front of ion pump, 2: in detection chamber, 3: in MOT cell, 4: at top of tube; see numbers in Fig. 3.1.

¹In contrary to the assumed value in table 3.1, TiAl6V4 seems to show an outgassing 10 times lower than 361LN and does not degas hydrogen according to [127].

the chamber are sketched with filled circles, the conductances in liters per second (l/s) are shown with resistance symbols and can be put in series in the same way as electrical resistances. The pumps are indicated as a certain conductance (l/s) to ground. The outgassing of the apparatus can be calculated by multiplying the outgassing values of table 3.1 with the surfaces of the apparatus which are exposed to vacuum:

Surfaces of vacuum apparatus

Segment of apparatus	Surface cm ²				Volume cm ³
	316LN	Ti	BK7	Pb	
Detection chamber	1660		250	3.4	3420
MOT chamber	165	1000	170	4.1	2067
Interferometer tube		1100	9.6	1.0	962
Cross pumps	1480		79		3850
Shield ion pump	40				
Valve turbo pump	80			leakage 5×10^{-10} l/s	
Ti-pump*	1240	235			2904
Tube	314				785
Total:	0.5 m ²	0.23 m ²	508 cm ²	7.5 cm ²	2 cm ²
					14 l

*: Surfaces of Ti-pump count only if the pump is inactive.

These values multiplied with the assumed outgassing rates of the various materials (table 3.1) allow the estimation of the pressure at various places of the system:

Pressure in vacuum chamber

Position 1 Ion Pump	Position 2 Detection	Position 3 MOT cell	Position 4 Interf. tube
p (N ₂) × 10 ⁻¹⁰ Torr 5.3 / 1.0		7.4 / 1.3	11.7 / 6.0

The above table gives two pressure values calculated for N₂: the first one (bold) in the case that only the ion pump is used and the Ti-sublimation pump is considered as an outgassing surface, and second if both pumps are active. The desired pressure of 10⁻⁹ Torr should be reachable even with our conservative outgassing assumptions. The H₂ pressures are lower by a factor dependent on the mass ratios $\sqrt{M_{N_2}/M_{H_2}} \approx 3.7$ for equal pumping speeds.

When designing the system, we always tried to use tubes with a diameter as big as possible. We attached the ion pump and titanium sublimation pump at two different flanges of the detection chamber to increase pumping speed. In the end, we measured a pressure of the order of 3×10^{-10} Torr in the MOT cell, pumping only with the ion-

pump, which shows that we overestimated the outgassing. It had been a long story of leak searching and re-assembling before we reached this pressure.

We can give an *upper limit for the outgassing* of the glue, if we assume that all outgassing originates only from the glue with its 2 cm^2 total surface. We find the upper limit for the outgassing rate to be

$$OG_{\text{Glue, max}} = 1 \cdot 10^{-9} \text{ Torr l/s/cm}^2. \quad (3.1)$$

The same estimation for lead leads to an upper limit of

$$OG_{\text{Pb, max}} = 6 \cdot 10^{-10} \text{ Torr l/s/cm}^2. \quad (3.2)$$

3.1.3 Sealing with lead and glue

The lack of commercial flanges with good quality AR coated windows, the special demands on small wavefront distortion and the reduced space of our vacuum chamber made it necessary to use non-commercial sealing techniques. There are a few techniques around, as for example copper sealing with a sharp edge (Stanford, Florence), indium sealing – very popular but not bakeable at high temperatures – or glue (Paris). When using standard flanges, the tight fixing of the screws transmit pressure onto the window, which in turn might deform and lose its optical qualities. This drawback is the main reason for using glue to attach windows. Gluing windows onto UHV chambers is a topic, where few people have little experience. Also the replacement of indium with lead to attach glass directly to steel or titanium on a UHV chamber seems to be used scarcely if at all. This is the reason why we will describe our experience with this technique in detail.

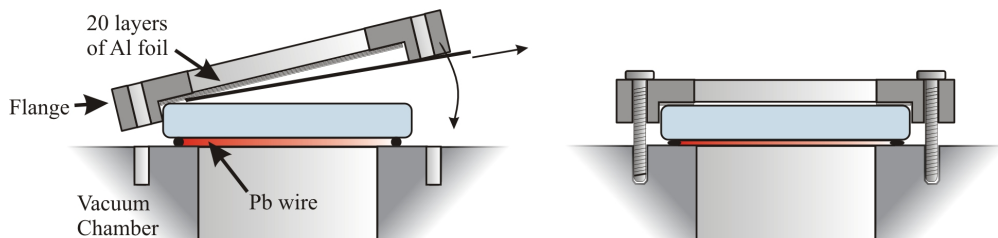


Figure 3.5: Lead sealing: The window is placed on a ring of lead wire. Left: 20 layers of Al-foil are placed between the flange and the window to distribute the pressure. A piece of paper (black) prevents them from falling out during the positioning. Right: The screws of the flange are fixed with 3-4 Nm. After the baking, the aluminium foil is cut out from above the window.

Lead-sealing: BK7 windows of 50 to 70 mm diameter, 10 mm thickness and AR coating on both sides were attached onto a smooth surface of stainless steel (316LN)

or titanium (TiAl_6V_4). The procedure was done in the following way:

- All surfaces including the wire of pure lead (ADVENT, 99.99% purity, 0.5 mm diameter) were cleaned with Acetone.
- We shaped the wire to a circle with overlapping ends, with a diameter about 1 cm smaller than the window; placed this ring onto the surface of the apparatus and slightly fixed the overlapping ends.
- The glass window was placed on top of the lead ring.
- Now the flange needed to be positioned on top of the window. Of course, there must be some soft material between the flange and the window. We first tried a second lead ring, but as it is never exactly above the one below the window, there might arise pressure gradients inside the window when tightening the flange. We therefore cut 20 discs of aluminium foil and put them between flange and window.
- Now we fixed the screws over cross, in steps of 0.5 Nm until the final value of 3 Nm. In fact, we had good results for pressures between 2.5 Nm and 5 Nm. (We broke a test window at 8 Nm but in a silly way, applying single-edged pressure.) After tightening the flange, the lead ring is squeezed to a width of about 2 to 3 mm.
- Bake-out of the system. Lead melts at 327°C , a much higher temperature than the well known sealing material indium (157°C). We heated the system up to a maximum temperature of 170°C during a test and left it at 140°C for five weeks.
- After the baking, the tightness of the screws was found to be reduced by 1 Nm and we re-tightened them to the previous value.
- Finally, the aluminium foil, which still covered the window was cut out from above the window with a scalpel.

Sealing with glue: The use of glue is a trade between the disadvantages of an unknown outgassing rate, an unknown sealing quality and difficulties in exchanging the window, against the hope for a small tension in the window and small required space. In an atom interferometer, an undisturbed Gaussian wavefront of the Raman lasers is very important (we need a surface quality of $\lambda/20$) and windows fixed with standard flanges have distorted surfaces that in turn distort the wavefronts. Gluing windows implies the following problems:

The harder a glue, the less outgassing it has, but the more tension it puts on a window if its own thermal expansion coefficient (TEC) is very different from glass. In contrary, a soft glue mediates tensions resulting from different expansion of glass and metal. If the

glue is hardened at high temperatures, what principally lowers its outgassing rates, one must consider the expansion effects when cooling down to room temperature. There exist glues especially designed for UHV applications like Torr Seal (VARIAN) or H77 and H27D (CABURN), but they cannot be heated above 125 and 150°C, respectively, and therefore we decided to look for an alternative solution.

Our first test was done with the glue AREMCO 526N (see table 3.1). We glued 6 windows (25.2 mm diameter, 3.3 mm thickness) onto a tube of stainless steel 316LN. The gluing was done at 160°C, but the windows almost all broke after 2 weeks because of the permanent stress provoked by the different thermal shrinking during cooling to room temperature. We made another try with thicker windows (1 cm), a softer glue (AREMCO 631), titanium instead of steel (better match of TEC, see table 3.1) and a lower gluing temperature. Here a short summary of the gluing procedure, which finally proved to work well:

- The two components of the epoxy-glue were mixed with a special mixing adaptor for a syringe and we made sure that there were no air inclosures in the glue. For the mixing, glue and surface were heated to 40 to 50°C to reduce the viscosity of the glue and to simplify the mixing and distribution.
- A thin (<1 mm) end-to-end ring of warm glue (checked for air inclosures) was poured onto the surface and the window put onto the glue inside a mould to prevent the window from sliding all over the surface.
- The windows were pressed onto the glue inside their mould and put into an oven to heat everything up to 80°C for 2 hours to harden the glue. The higher the temperature during the hardening, the better the later outgassing of the glue, but the higher the tensions at room temperature.
- After one and a half years, the windows did show no problem. The outgassing of the glue is $< 10^{-9}$ Torr l/s/cm² (see section 3.1.2). The properties of some glues, tested for UHV are listed in table 3.1².
- The windows can be easily removed with a small knock after heating the glue up to 350 - 400 °C.

²A vacuum test by Annie Gerard in Paris compared the relative outgassing of various glues under the same conditions. The measured parameter was the pressure which was reached after the baking of a system with one glued window. Some results are (in Torr): EPO-TEK H72: $6 \cdot 10^{-10}$, AREMCO 631: $9 \cdot 10^{-10}$, EPO-TEK 310 (flexible): $4.5 \cdot 10^{-9}$. Generally the harder the glue, the lower the outgassing.

3.2 Magnetic fields

Magnetic fields are necessary to trap atoms in a MOT, to compensate external fields and to define a quantization-axis for the atoms. A wrong field-component in the interferometer region would allow unwanted Raman transitions (see section 5.2.4), what is the reason why we need to shield this region well.

3.2.1 Coils

To achieve the proper magnetic configuration for the MAGIA experiment we implemented various coils, which will be described here:

- *MOT coils*: A magneto optical trap for rubidium demands a magnetic field gradient of a few Gauss per cm at its center. Two coils in anti-Helmholtz configuration create the following magnetic field along their symmetry axis (x -axis):

$$B(x) = \frac{\mu_0 N I R^2}{2} \left[\left(\frac{1}{(R^2 + (x-d)^2)^{\frac{3}{2}}} \right) - \left(\frac{1}{(R^2 + (x+d)^2)^{\frac{3}{2}}} \right) \right] \quad (3.3)$$

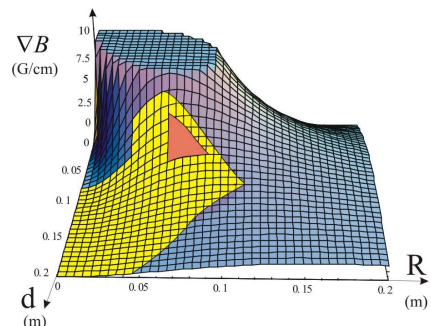
with the gradient at the center

$$\frac{\partial B(x)}{\partial x} \Big|_{x=0} = \mu_0 N I R^2 \frac{-3d}{(R^2 + d^2)^{\frac{5}{2}}} \quad (3.4)$$

N is the number of windings, I the current in the coil, R the coil-radius and d the distance between the coils.

The geometrical constraints – allowed is only the light (yellow) region on the figure below, made by Giacomo Lamporesi [100] – lead to following design of the coils whose triangular cross section is highlighted in the figure:

- Number of windings of each coil is $N=50$.
- Diameter of the copper wire of 2 mm yields a total resistance for one coil of $R \approx 12.5 \text{ m}\Omega$.
- Inner diameter of coil: 12 cm, relative distance d between coils: 18 cm;
- Triangular cross-section of coil; aluminium mount is cut to prevent current induction.
- A current of $I = 30$ Ampere creates gradient of 10 G/cm in the center (see Figure above, calculated for 20 A).

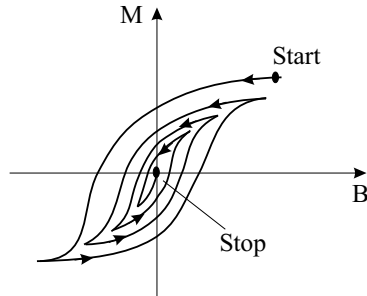


- Water cooling prevents heating to far above 100°C. The wire is covered with thermally conductive and electrically isolating paste (LOCTITE 5404) for efficient thermalization.
- *MOT compensation coils*: An offset field like e.g. the Earth's magnetic field will spatially shift the center of the magnetic field zero of the MOT coils. Any shift can be compensated with three pairs of Helmholtz coils around the cell, which should be able to produce a stable field up to 3 Gauss in a region of $1 \times 1 \times 2$ cm. Our vertically oriented coils (horizontal field compensation) are rectangular with 29×38 cm side-length at a distance of $d = 44$ cm with $N = 25$ windings. The horizontal coils are squares with 48 cm side-length at a distance of $d = 28$ cm and $N=50$ windings.
- *Detection compensation coils*: Again, the field in the detection region is shielded by three pairs of compensation coils, which at the same time serve to define the axis of quantization during another state of the experiment, and whose current thus changes between two different values. The coils are wrapped around the detection chamber with $N = 30$ for the coils creating the field along the axis of the detection beam, and $N = 20$ for the other ones. The dimensions of the vertical coils are 10×8 cm at a distance of $d = 8$ cm, the horizontal ones are round with diameter 18 cm and $d = 8$ cm.
- *Offset coil*: We wrapped a coil with $N = 687$ windings around the interferometer tube, to ensure a well defined quantization in vertical direction. The coil is connected to a stable current source (laser driver), whose current I creates a field $B = \mu_0 NI/l$, which, for the length $l = 55$ cm gives a dependence of 15 G/Ampere.

3.2.2 Magnetic shielding

Magnetic fields can cause Zeeman shifts of first and second order in the atomic transition frequencies, what would introduce a systematic effect in interferometer signal. To exclude all fields, both DC and AC, from the interferometer region, we mounted a double layer magnetic shield around the tube. The diameters of the two cylindrical μ -shields of 1028 mm length are 74 and 95 mm. We left open the option of inserting a third shield of 54 mm diameter into the existing mount. A magnetic shield consists of a high magnetic permeability material, in which the microscopic magnetic dipoles (atomic magnetic moments) can move freely. They will consequently follow the outer field and compensate for it. The easier the magnetic moments can move, the more will follow the outer field and the better the outer field is compensated for; but on the other hand a saturation effect will happen earlier, leaving the magnetic moments fixed in a certain orientation.

Once the shield is saturated, it can be degaussed by forcing the magnetic moments to follow a very strong outer AC-field. The AC field forces the magnetization to follow the hysteresis curve and ramping down the field lets the magnetization return to zero as sketched in the righthand figure.



Experimental degaussing procedure: The usual degaussing is done by lengthwise wrapping of a coil around the cylindrical shield. The field produced by the coil is $H = \frac{NI}{2\pi R}$. To degauss mumetal, H must be bigger than 1 A/cm. One ramps up an AC current (e.g. of a Variac) for 15 seconds, holds it for 15 s and ramps it down exponentially for at least 15 s. Repeating the procedure three times degausses the shield.

Material: The magnetic shield is made of 0.76 mm thick Amumetal (from AMUNEAL), a special Nickel-iron alloy (80% Ni) with a very high permeability, which can reach a value of 400 000 for optimum field strength inside the material of around $B_{int} = 2500$ Gauss. The high permeability signifies a low saturation point of 8000 Gauss of the field $B_{sat, int}$ inside the material. To calculate the maximum outer field $B_{sat, out}$, one can use the following approximative formula:

$$B_{sat, out} = \frac{B_{sat, int} d}{2R} \quad (3.5)$$

with d the material thickness and R the shield radius. In our case, the maximum outer field is 60 Gauss, above which saturation occurs.

Attenuation: The attenuation A of a single layer (SL) and double layer (DL) shield for $\mu \gg 1$ can be written as:

$$A_{SL} = \frac{B_{out}}{B_{in}} = \frac{\mu}{4} \left(1 - \frac{R_i^2}{R_o^2} \right) \quad (3.6)$$

$$A_{DL} = 1 + A_{SL,1} + A_{SL,2} + A_{SL,1} A_{SL,2} \left(1 - \frac{R_{o,1}^2}{R_{i,2}^2} \right) \quad (3.7)$$

where index 1 denotes the inner shield and 2 the outer shield, R_o the outer radius and R_i the inner radius. In our case the DC attenuations were calculated by the software of the manufacturer (AMUNEAL) to be 6740:1 (76 dB) for radial fields over most of cylinder length, with reduced shielding within 74 mm of either open end and 2854:1 (69 dB) for the axial field over extended central portion of cylinders, with greatly reduced attenuation at ends (for calculation of shielding see [145]). Above values are calculated based on conservative assumed relative permeability of 15000, and provided only as an estimate of expected performance. Measurements of the B-field with the atoms were not yet performed.

Annealing Once all fabrication of the shield has been completed, materials like Amumetal require hydrogen annealing to effect optimum shielding characteristics since this process usually increase the material's permeability by 40 times. The standard annealing is done in dry hydrogen atmosphere by heating up to 1177°C for four hours. This procedure removes the carbon and other trace elements from the material and relieves the mechanical stresses due to processing and fabrication. This allows the grain boundaries of nickel's crystalline structure to expand. This newly formed nickel structure creates a low reluctance path for magnetic fields to follow, thus increasing the material's permeability. After the annealing cycle it is critical to avoid any rough handling of the material as it is extremely sensitive to shock and vibration. The newly formed crystalline grain structure of nickel is relatively fragile and any disturbance will begin to destroy the material's effective permeability.

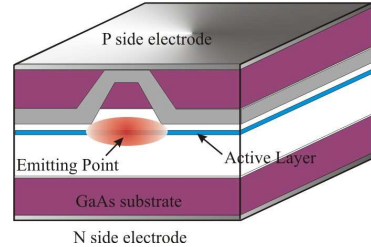
3.3 Laser System

We use the D₂ transition between the 5²S_{1/2} to 5²P_{3/2} states of ⁸⁷Rb to trap, cool and manipulate the atoms. Particularly suited is the closed $F = 2 \rightarrow F' = 3$ transition, if at the same time the lost atoms are recycled by a repumper between the $F = 1 \rightarrow F' = 2$ levels (see Appendix A for the Rb level-scheme). These transitions lie around 780 nm, which is easily accessible by laser diodes. After describing a few options to produce this wavelength, we will present the workhorse of atomic physics, the extended cavity diode laser. The laser system for both gradiometer and gravimeter are based on this kind of laser and both systems will be described in the following sections. Finally, we will present the fiber system, which delivers the laser light to the experiment.

Diode-laser sources at 780 nm: Light at the wavelength of 780 nm is usually generated by either high power and very expensive Titan-Sapphire lasers or by AlGaAs laser diodes, taking benefit from the fast development of diodes for compact-disc writers at 785 nm. Here we give a selection of the most common diode-laser sources at 780nm:

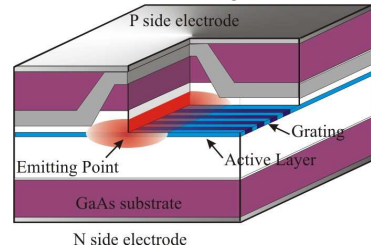
- *Fabry-Perot Diode lasers* use the front faces of the semi-conductor material as a Fabry-Perot resonator. At 780 nm, diodes can emit up to 150 mW power and cost between 20 Euro (commercial CD writing diodes) and 1000 Euro.

They show a very large gain profile of several nanometers and linewidths of several hundred MHz (length of internal resonator ≈ 1 mm), which can be reduced by a long external cavity. To achieve single mode operation, the light is guided within the chip in a rectangular region of 3 to 7 μm confined by wells of either lower refractive index material (index guided) or material with optical loss (gain guided).



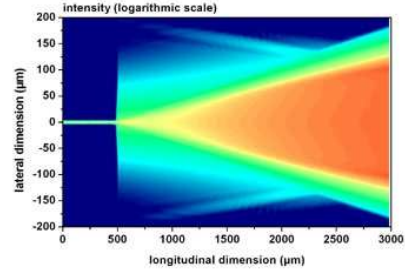
- *Distributed Feedback (DFB) lasers* are fixed wavelength single mode diode lasers. The single mode emission is enforced by a Bragg grating within the semiconductor material of the laser chip, defining the emitted wavelength.

DFB lasers can be frequency-tuned by temperature because thermal expansion changes the spacing of the grating. Recent DFB diodes deliver 80 mW at 780 nm and cost around 1000 – 3000 Euro. Their linewidth is around 3 MHz as was measured by [108].



- Diodes can be produced with a broader emitter region of up to 50 μm , which means multiple mode operation, but a high power of up to several Watt (broad area diodes).

A *tapered diode* consists of a single mode Fabry-Perot diode with small emitter region of 3 to 7 μm at one end, a broad area diode at the other end and a tapered region between both for mode matching. The intensity distribution in the chip is shown in figure, which is taken from [125]. If the broad-area region is injected by the single mode region, the whole chip emits single mode up to 1.5 W power. The tapered chips usually have anti-reflection coated surfaces and need to be injected by an external laser or an external feedback cavity. The costs are between 1500 to 3000 Euro. A problem can be the relatively intense spontaneous emission.



3.3.1 Extended cavity diode lasers

An extended cavity provides optical feedback to the laser, reducing the threshold current, narrowing the linewidth and providing broad tunability. The linewidth of a diode laser $\Delta\nu$ in a cavity of length l with small spontaneous emission and at room temperature can be written with the Schawlow-Townes formula [101]

$$\Delta\nu_L = \frac{\pi h \nu_L \Delta\nu_c^2}{P_L} \quad (3.8)$$

with the laser frequency ν_L , the cavity linewidth $\Delta\nu_c$ and the laser output power P_L ³. To calculate the cavity linewidth, we start by writing down the power losses of k round trips through the cavity, each of duration $t = 2nl/c$, as the product of absorption losses e^{-az} with absorption parameter a and transmittance of the two surfaces with reflectivity R :

$$P(k \cdot 2nl/c) = P(0) \cdot (R_1 R_2 e^{a2l})^k. \quad (3.9)$$

With $P(\tau) = e^{-1}$ follows for the mean lifetime τ of a photon in the cavity

$$\tau = \frac{nl/c}{al - 1/2 \ln(R_1 R_2)}. \quad (3.10)$$

Typical values are for a laser diode are $l = 250 \mu\text{m}$, $n = 3$, $R_1 = 0.95$ and $R_2 = 0.3$, which lead to a lifetime of $\tau = 4 \text{ ps}$ for $a = 0 \text{ m}^{-1}$.

When adding an external mirror with reflectivity R_3 at distance L from the diode surface, the new lifetime τ_{EC} is enhanced to

$$\tau_{EC} = \frac{(n l + L)/c}{a l - 1/2 \ln(R_1(1 - R_2)^4) R_3}, \quad (3.11)$$

which, in the typical case of $L = 2 \text{ cm}$ and $R_3 = 0.2$ leads to the mean lifetime of $\tau_{EC} \approx 40 \text{ ps}$, which is ten times bigger than without extended cavity. This signifies that the addition of an external cavity reduces the linewidth by a factor of 100.

³There is an additional factor of 2 for the operation below threshold.

The emitting wavelength of the ECDL is determined by the interplay of gain profile, internal cavity modes and external cavity modes. If the gain profile of the laser is very broad like in the case of diode lasers, several modes might experience similar gain and multi-mode emission occurs. Introducing a frequency selective element into the cavity will give different weight to adjacent internal cavity modes and there will usually be one mode, which is the most favored. An internal cavity of maximum 1 mm length corresponds to $c/2L = 150$ GHz (≈ 0.33 nm) mode spacing at 780 nm, what requires a frequency selective element that shows considerable dispersion over this range. The extended cavity offers the possibility of accurate frequency control by adjusting the cavity length with a piezo-electric crystal (PZT) with frequencies up to a few kHz. Faster frequency changes can be done by modulating the laser current.

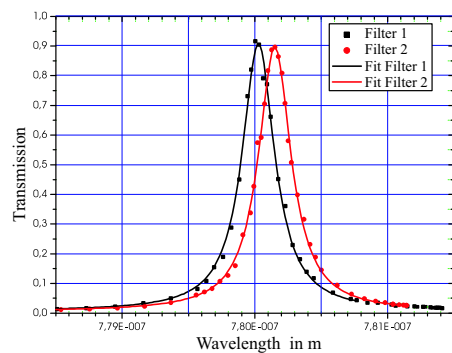
Grating as frequency discriminator: A grating is the most common frequency discriminator and it is placed behind the diode to feed back the first diffraction order into the laser and to couple out the reflected light. The selected wavelength $\lambda = 2d \cdot \sin \alpha$ is determined by the line spacing d of the grating and the incident angle α , equal to the angle of the first order diffraction.

Since the intra-cavity power of the laser is limited, high feedback of the grating goes with more frequency stability, but lowers the output power. A good compromise seems to be a diffraction efficiency of 15 to 20%. We had some lasers running with only 3% refraction efficiency and higher output power, but the single-mode operation was more difficult.

The wavelength-selectivity depends on the distance of the grating from the diode and the line spacing (angle of first order) but is definitely better than the required 0.3 nm. Any wavelength within most of the several nm broad gain profile can be selected. This configuration with the first order of a grating directly fed back into the laser is called *Littrow configuration*. Its design often goes back to the design of Ricci et al. [102].

Remarks on grating efficiency: Gratings coated for visible light still achieve diffraction efficiencies of the order of 70% for p-polarized light. Using the grating with s-polarized light results in efficiencies around 20 %. This can become a problem for AR-coated diodes that tend to emit in both polarizations, as the unwanted and small p-polarization component is reflected with higher efficiency into the diode.

Etalon as frequency discriminator: Until recently, etalons couldn't reach the required frequency selectivity and at the same time did absorb too much light. At the gravimeter, we recently received Fabry-Perot etalons from RESEARCH ELECTRO-OPTICS showing a linewidth of 0.3 nm, what qualifies them to replace a grating as frequency discriminator. The wavelength of 780 nm is in resonance at an angle of 8°. The transmission curves on



the right have been measured by turning the angle of the etalon and converting it to wavelength. Frequency selection of the laser is done by inserting the etalon into the extended cavity and adjusting the angle for transmission at the desired wavelength. The extended cavity consists of a semi-reflective mirror behind the etalon. In difference to gratings, wavelength tuning will not change the beam pointing.

Anti-reflection coated diodes: The competition between different modes for dominance in the laser can cause instabilities if two of them experience similar gain. It would be desirable, if only the external cavity together with the grating or etalon would determine the emission frequency. This can be realized by anti-reflection coating of one diode surface, which usually has a reflectance of about 30% ($n(\text{AlGaAs})=3.3\text{-}3.6$). Various companies like EAGLEYARD, SACHER or TOPTICA offer AR coated diodes with a reflectivity to below $5 \cdot 10^{-4}$, which exhibit the following particularities [103, 104]:

- Threshold current increases such that the operational current remains below the internal threshold current for extremely good gratings.
- A higher threshold current causes a higher carrier density inside the active region of the diode, leading to a bigger splitting of the band gap, which in turn results in a shift of the gain profile by about 20 nm towards the blue, increasing the overall tunability of the frequency.
- Without the concurrence of the internal modes, the laser couples a lot better to the external cavity and the mode-hop free tuning range is enhanced significantly up to 30 GHz from the usual 1.5 to 4 GHz of an uncoated ECDL. Of course, the tuning range cannot be bigger than the free spectral range of the external cavity, in our case 5 to 10 GHz.
- In the vicinity of a mode hop, the laser changes its characteristic phase delay, because the mean lifetime of a photon in the cavity τ changes. This poses problems, when the laser is used in a phase-lock. With the AR coating, the unstable regimes can be far away and we have a flatter phase response.

3.3.2 Laser setup of gradiometer

The weight of this section will lie on the laser system for the gradiometer, because a lot of time has been invested in its setup. The frequency control of the lasers will be described in the separate chapter 4. The transition frequencies of ^{87}Rb can be found in Appendix A.

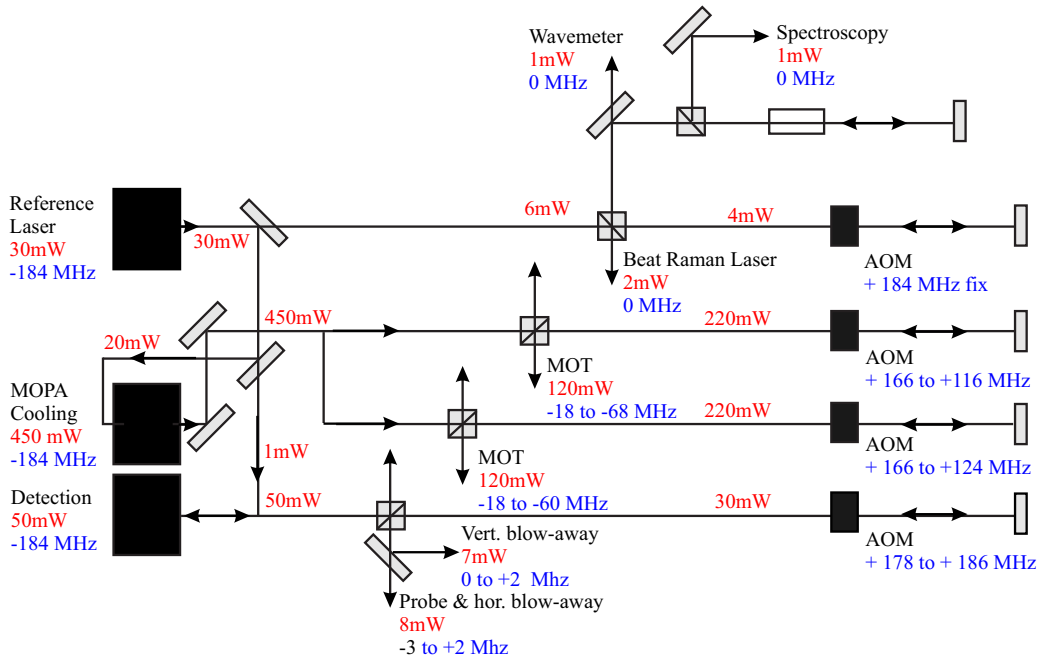


Figure 3.6: Schematic view of reference, cooling and detection laser of the gradiometer. The reference laser is stabilized on a Rb transition and injects a tapered amplifier (cooling laser) and a detection laser. The beams are all coupled into optical fibers, which deliver the light to the experiment.

Reference, cooling and detection laser: We use an ECDL with a SHARP diode (GH0781JA2C) as reference laser. A lens of focal length $f=4.5$ mm (THORLABS C230TM-B) collimates the beam to about 2 mm $1/e^2$ diameter. The frequency discriminator is a holographic grating (EDMUND SCIENTIFIC NT-43 775) with 1800 lines per mm at a distance of 2 cm from the diode (FSR= 0 GHz). This laser reaches an output power of 30 mW from which we separate a small part for spectroscopy and frequency stabilize the laser at -184 MHz distance from the $F = 2 \rightarrow F' = 3$ transition of the ^{87}Rb D₂ line (see Appendix A). A double pass acousto-optic modulator (AOM) shifts the laser in frequency and at the same time modulates the light with 70 kHz to enable the frequency lock (see chapter 4.4). Another small part of the laser power is used for a beat with the master Raman laser, a further part for injecting the detection laser and the biggest part for the injection of a tapered amplifier (TOPTICA TA 100). The light of the tapered amplifier (450 mW) is split into two paths, each one controlled in frequency and amplitude by its own double pass AOM and driver. Both beams are finally injected into fibers, split into three parts (fiber splitter see section 3.3.5) and lead to the MOT chamber, where they serve as upper and lower cooling beams. To launch the atoms, the upper laser is detuned relative to the lower one by the AOMs.

The detection laser is mounted similar to the cooling laser but without grating. Its wavelength is defined by the injected light of the master. A double pass AOM shifts

the frequency of the detection laser to either near resonance ($F = 2 \rightarrow F' = 3$) when used to blow away wrong atoms during the state selection, or slightly red detuned during the detection of the interferometer signal in a standing wave.

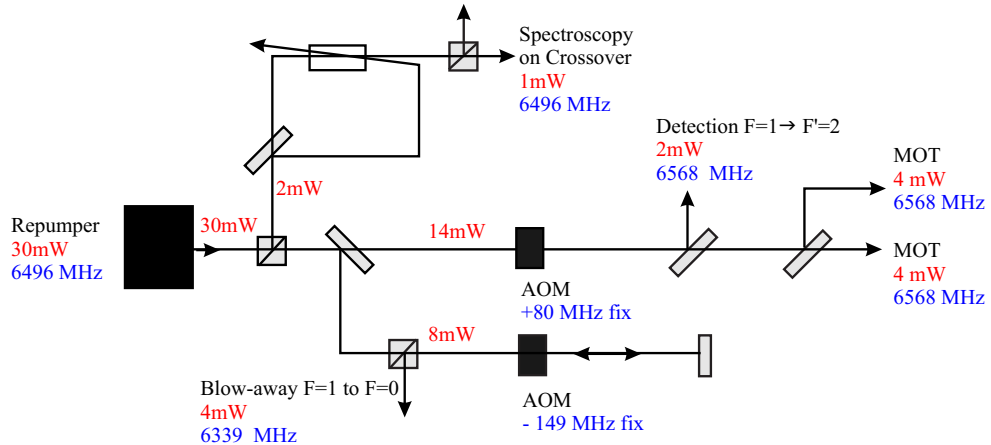


Figure 3.7: The repumper is locked on a Rb transition and split into four different beams leading via optical fibers to the experiment.

Repumper: The repumper has to repump those atoms, which got lost during the cooling cycle between $F = 2$ and $F' = 3$ to the other hyperfine ground state $F = 1$. The repumper pumps from $F = 1$ to $F' = 2$, from where they can fall back into $F = 2$. The laser is mounted in the same way as the cooling laser, the frequency is locked with the Doppler free DAVLL method (see section 4.1.3) to the intercombination line $F = 1 \rightarrow F' = 1, 2$. The frequency of this laser is shifted with a single pass AOM by +78 MHz to the $F = 1 \rightarrow F' = 2$ transition to recycle the lost atoms in the MOT and the detection region and with a double pass AOM by -150 MHz to the $F = 1 \rightarrow F' = 0$ transition to blow away atoms in $F = 1$ during the state preparation for the interferometer.

Raman lasers: The master Raman laser includes a Sanyo diode (DL7140-201-785) and a grating for the extended cavity at a distance of 1 cm. Its output power is 25 mW. The old slave laser (Sharp) has recently been replaced with a new AR coated diode (SACHER SAL-0780-040) working extremely well for currents up to 66 mA. The grating has an efficiency of 18% and the back reflection seems to be too strong for higher currents, for which the laser becomes unstable. Below this value, we achieve a mode-hop free tuning range of the piezo scan, which is only limited by the FSR of the cavity to 9 GHz; a significant improvement compared to the 1 to 3 GHz of our diodes without coating. The laser does not change mode when tuning the current by more than 15 mA. The optical output power is 35 mW.

A loose phase-lock keeps the frequency of the Master laser at a difference of 3.3 GHz

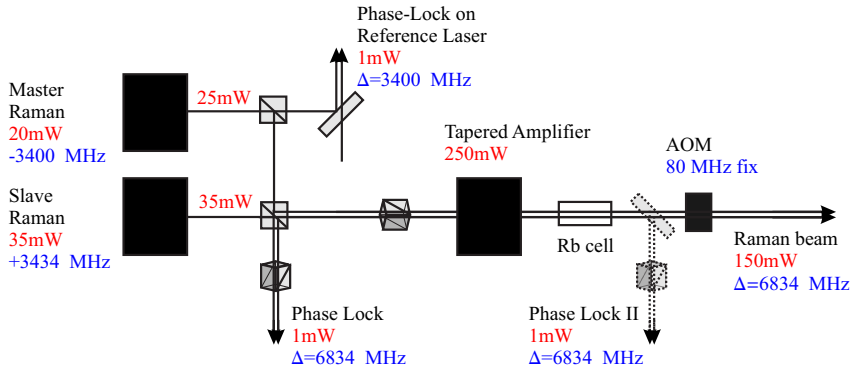


Figure 3.8: Two phase-locked lasers inject a tapered amplifier, whose light is cleaned from spontaneous emission in a heated Rb cell, before it is lead via an optical fiber to the interferometer. Cubes oriented at 45° overlap two orthogonal beams. The second phase lock will in future correct for the low frequency noise of the MOPA.

to the reference laser. The slave in turn is phase-locked tightly (see section 4.4.4) to the Master laser with a difference frequency of 6.8 GHz (Rb hyperfine splitting), which during the experiment needs to be swept. The biggest part of the overlapped beams injects a tapered amplifier (EAGLEYARD EYP-TPA-0785-00000-3006), who, at the moment, delivers no more than 250 mW due to thermal problems. To clean the light from eventual spontaneous emission near resonance, we send the beam through a heated vapor cell before injecting it into an optical polarization maintaining, single-mode fiber. To switch the light on and off, we placed an AOM in front of the fiber and inject the first diffracted order into the fiber.

3.3.3 Laser setup of gravimeter

The laser system for the Watt-balance gravimeter should enable transportation and is designed for a high compactness. A breadboard of 60x60 cm contains the entire setup but will be replaced by a 80x80 cm board since it got too full recently. For this very reason of compactness, the number of laser sources is reduced as far as possible. Bringing to mind that the cooling laser and the Raman lasers are never used contemporaneously, directs the thoughts to the idea of using the cooling laser and the repumper to drive the Raman transitions, too. In this case a huge frequency shift of 2 GHz is required between the two experimental stages. This tuning is realized by locking the lasers with a frequency or phase-lock onto a stable reference laser and controlling the offset frequency by electronics (see section 4.3).

The lasers are ECDL in Littrow configuration with TOPTICA diodes (LD-0785-0080-1) and a grating at 4 cm distance, resulting in a smaller linewidth than the lasers for the gradiometer of measured 270-500 kHz. The new laser with etalon and AR coated

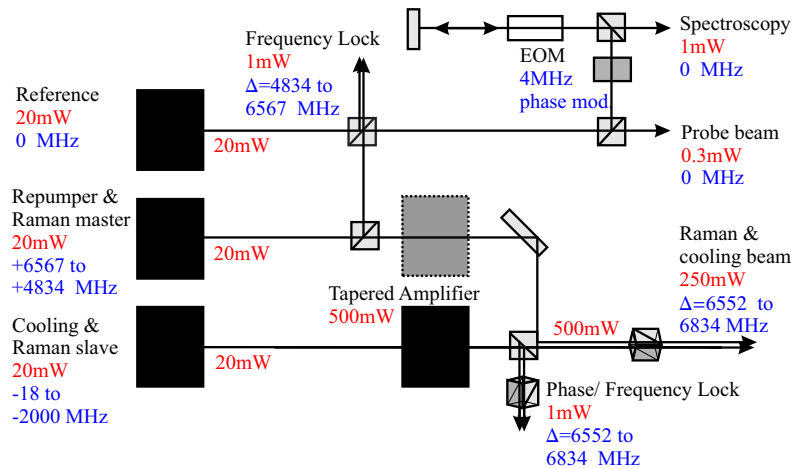


Figure 3.9: The laser system of the Watt-balance gravimeter uses one reference laser locked on a Rb transition and two further lasers, which are frequency and phase locked to the reference laser. These two lasers are used both for cooling and as Raman lasers and are amplified by tapered amplifiers; one not yet mounted.

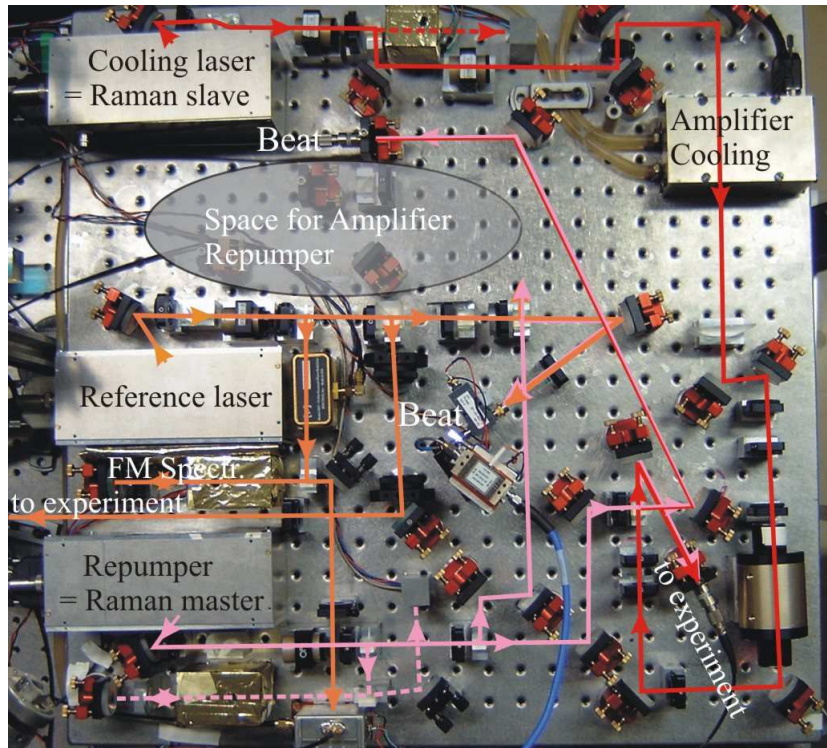


Figure 3.10: Photo of the breadboard of 60x60 cm side-length containing the laser system for the gravimeter. The only missing element is a second tapered amplifier.

diode (SACHER EYP-RWE-0805-03000-0750) gives 40 mW output power but has a bad mode structure.

3.3.4 Summary and new laser system gradiometer:

Summary: Laser technology is developing rapidly and new commercial diodes and laser systems emerge quickly. We had the opportunity of testing a new New Focus Littman laser (TLB-7000; 60mW) with very sophisticated mechanics and comparing it to the new SACHER Littman laser (TEC-520-780-100; 120 mW), which has a coating on both sides of the diode and couples out the light on the opposite side of the grating to avoid the conflict between high power or high feedback. We also received a new 1.5 W tapered chip, a new DFB 80 mW diode (EAGLEYARD), a test version of the 1 W SACHER Tiger laser and the TOPTICA 1 W DLX110. All these new lasers make work a lot easier and allow to reduce the number of lasers and problems. We will give here a table with the different lasers currently in use at the two experiments and also about the ones already bought and ready to be mounted.

Diode	P_{max} mW	P_{EC} mW	I_{max} mA	I_{Th} mA	AR	Use as	Where
Sharp GH0781JA2C	120	35	167	30	No	R, MC, D	F
Sanyo DL7140-201-785	80	27	140	30	No	MR,	F, P
Rohm RLD78PZW1	80	30	150	30	No	(1)	F
EYP-RWE-0805-03000-0750	80	40	200	24	Yes	-	P
Sacher SAL-0780-040		40	(2)120	27	Yes	SR	F
Toptica TA 100 MOPA	500		1400		Yes	MC	F
EYP-TPA-0785-00000-3006	400		2000		Yes	R	F, P
NewFocus TLB-7000-P-13		60	150		No	(3)MR	F
Sacher TEC050-0780-080 DFB	80		200	50	Yes	(4)R	F
Toptica LD-0785-0080-1	100	25	120	28	No	R	P

Legend: *EY= Eagleyard, R= Repumper, MC= Master laser Cooling, D= Detection laser, MR= Master Raman laser, SR= Slave Raman laser, P_{max} = maximum output power, P_{EC} = power out-coupling of extended cavity, I_{Th} = Threshold current, I_{max} = maximum current, AR= at least one diode surface Anti-Reflex coated, P= Paris, F= Florence, (1)= all four broken after 1 year latest, (2)= over 67 mA multi-mode with 20% feedback, (3)= future master Raman, (4)= future repumper*

New laser system: The MAGIA experiment is not yet mounted totally; in 2005 we will install a 2D MOT for efficient loading of the trap and a new cooling system – Raman sideband cooling in a lattice – to achieve lower temperatures of the cloud and use more atoms for the interferometer. These extensions require more laser power and we thought of a new setup relying on few but powerful lasers. Since the existent setup

does not allow a big detuning of the cooling laser and we lose a lot of power with double pass AOMs, we can correct for these points, too. We will summarize the main features of the new setup, which also goes along with a new electronic control system:

- We will set up 1 stable reference laser, locked to the $F = 2 \rightarrow F' = 3$ transition with frequency modulation spectroscopy.
- The reference laser will inject a tapered amplifier to create the light for the 2D MOT. Its full power will be used without any AOM in between, resulting in a lot shorter beam paths, which is important for stable fiber coupling.
- Instead of injecting the cooling laser with the fix frequency of the master laser and doing all the necessary detuning during the cooling with AOMs, we will lock the beat signal of a new high power laser with the reference laser to a signal generator. In this case, bigger detunings will be possible without power losses.
- We will mount a high power DFB laser (80 mW) as new repumper.
- A new tapered amplifier will deliver higher power of the Raman lasers, allowing for shorter pulses.

3.3.5 Fiber system

The use of optical fibers has several advantages:

- They physically decouple optics. Once the incoupling of a fiber is aligned, the beam after the fiber is always the same and does not have to be realigned.
- The lasers can be mounted on a different table, which remains accessible for work, while the sensitive parts of the experiment can be covered with the light being delivered there by optical fibers.
- Single mode fibers clean the spacial mode of the laser beam. The higher order Hermite-Gaussian modes need to propagate in the cladding of the single-mode fiber because of their broader intensity distribution and are damped out totally after a few meters of propagation.

We use single mode polarization maintaining Panda-core fibers from SCHÄFTER & KIRCHHOFF. All fibers are angle polished at 8° to prevent reflections and etalon effects. These fibers have low coupling between the two orthogonal modes; in the worst case, we observe the coupling of half a percent of the intensity in one mode into the other mode after 7 meters of propagation in the fibre. The beams leading to the optical trap are split and combined with the repumper by *integrated fiber splitters* (SCHÄFTER & KIRCHHOFF), used both for the gradiometer and the Watt-balance gravimeter. The

splitters are mounted in a very compact and hermetically closed way such that temperature fluctuations have little effect on the coupling efficiencies. Polarization is cleaned inside the splitters (1:10 000) and the relation of the light entering the splitter to the light, coupled out of the escaping fibers is better than 60%. The splitting ratios can be changed by half-wave plates in front of polarizing beam-splitter cubes.

At the gradiometer, the upper and lower cooling beams need to be detuned relative to each other during the launch of the atoms. This requires two independent beam paths and splitters. The intensity relation between both needs to be controlled constantly to ensure an efficient launch. For this purpose, a photo-diode is included in the splitter, monitoring a small part of the incoming light. The splitters split the upper or lower cooling beam each into three parts of equal power, all of them cleaned in polarization. The repumper is overlapped with one of the three outgoing beams.

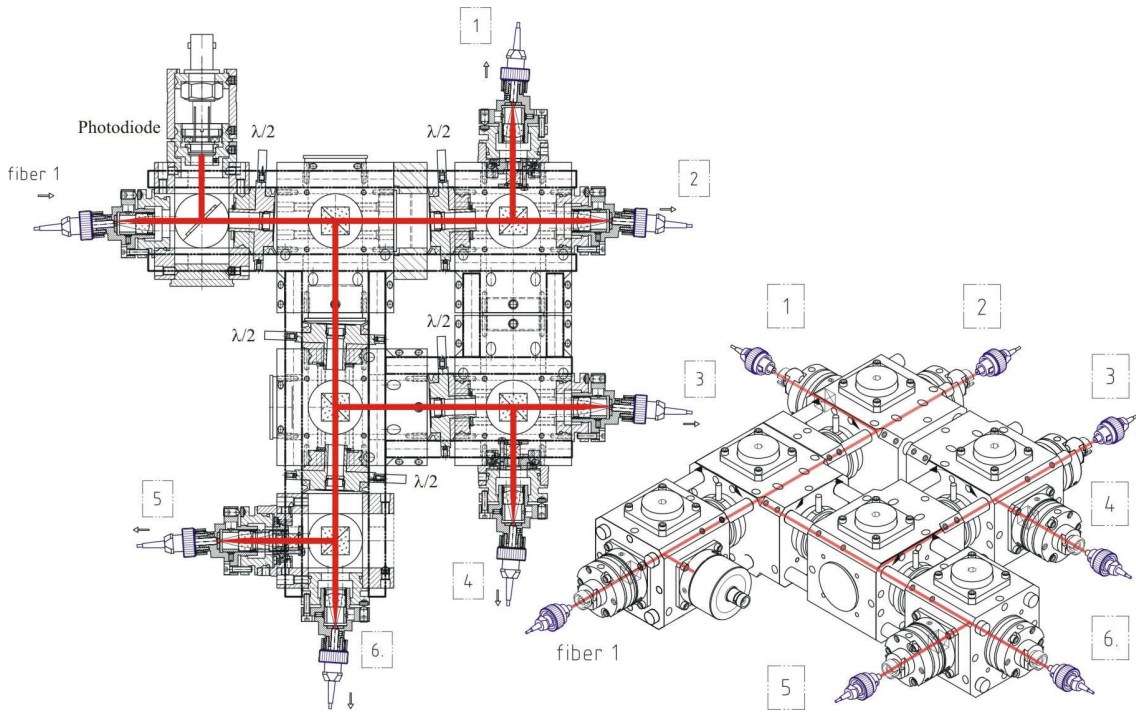
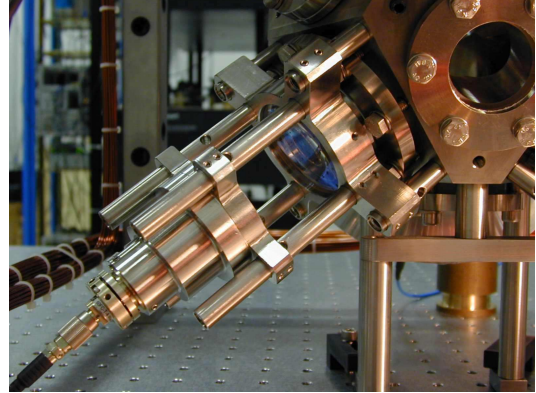


Figure 3.11: The one-to-six splitter from SCHÄFTER & KIRCHHOFF used for the MOT of the gravimeter. The intensity of the incoming laser beam is monitored on a photodiode (1% beam splitter) and is then divided into six beams with half-wave plates and polarizing beam-splitters. Similar splitters are used at the gradiometer.

At the gravimeter, the atom cloud is just released and not launched, which allows the splitting of one beam into six cooling beams, all with the same frequency. Fig. 3.11 shows as an example the one-to-six splitter. The incoming beam consists of both the cooling laser and the repumper with orthogonal polarizations. Consequently, the splitting ratio inside the splitter is different for the cooling beam and for the repumper

but is of no importance for the latter. A second one-to-three splitter is used for the 2 dimensional MOT. We observe a stability of the splitting ration in the order of few per mill on the scale of hours and of few percent a month. We realign the power ration slightly about once in two months, whenever the relation changed by more than a few percent.

The fibres leaving the splitters are mounted into *collimators* made of 316LN, which are fixed to the MOT cell. The mount allows a change of the collimation lens for beam diameters between 17 and 31 mm. In the present configuration we inserted achromatic doublet lenses with focal length $f=120$ mm. The fiber with numerical aperture $NA=0.11$ is collimated to a $1/e^2$ beam diameter of 22 mm.



⁴ We also have the freedom of small alignments of the beam angle and position to optimize the cooling. In the initial situation, each beam is coupled into the fiber at the opposite end of the cube.

⁴The numerical aperture of the fiber 0.11 corresponds to the half angle radiation cone $\sin \alpha = NA$. Since the numerical aperture is related to the 5% intensity level, we have to multiply by the factor 0.82 to obtain the $1/e^2$ intensity level of 13.5 %: $\alpha_{13.5} \approx 0.82 \cdot 2NA180^\circ/\pi = 5.18^\circ$.

3.4 Masses

The principle of a G-measurement seems to be simple: A source masse M induces an acceleration α on rubidium atoms at a distance r according to $\alpha = G \frac{M}{r^2}$ and the interferometer measures the displacement due to the acceleration in the interferometer time $2T$ (see interferometer phase shift (2.94)) as a variation of g . As we expect, a closer look will uncover some difficulties:

1. *Small signal on noisy background:* A source mass of 1 ton, placed as close to the interferometer as possible for our geometry will create a maximum vertical acceleration of $\alpha = 10^{-6} \text{ ms}^{-2} = 10^{-7} \text{ g}$, added to Earth gravity acceleration g . Our targeted accuracy of $\Delta G/G = 10^{-4}$ implies an absolute determination of acceleration to 10^{-11} g . In practice, a determination of g is limited to an accuracy of about 10^{-9} due to the noise on the frequency reference, of varying electric or magnetic fields and of Earth gravity noise itself. To nevertheless reach the desired accuracy on α , noise sources will be eliminated by a double differential measurement, described in section 3.4.1.
2. *Gravity gradient:* The Earth's gravity gradient γ is about $3 \cdot 10^{-6} \text{ s}^{-2}$. A position variation of $\Delta s = 30 \mu\text{m}$ would therefore signify an error in the measured acceleration of $\gamma \cdot \Delta s = 10^{-10} \text{ ms}^{-2} = 10^{-11} \text{ g}$. Such a small position uncertainty cannot be reached by our interferometer. A solution to this problem will be a compensation of γ by the source mass at the position of the measurement as described in section 3.4.2.
3. *Trajectories:* The non-uniform gravity field of the source masses will provide an exact compensation of γ only in two points in space. The sensitivity on atomic position or velocity variations will depend a lot on the atomic trajectory. Consequently, we numerically search the "best" trajectories, which are the least sensitive on fluctuations on the atomic position and velocity. A realistic value for the launch precision is about 1 mm and we will see that there exist trajectories, which allow for uncertainties of this order: see section 3.4.3.
4. *Source Masses:* The source mass needs to posses a high enough density to compensate Earth gradient γ , it must be well machinable, it should be of moderate cost and exhibit good homogeneity. Our choice has been a Tungsten alloy, described, together with its support, in section 3.4.4.
5. *Simulation of the signal:* To get an analytic solution for the interferometer signal (2.94), a quadratic potential is a necessary condition as we have seen in section 2.2. Unfortunately, the gravitational field of the source masses is not quadratic; – but can be approximated with a linear and a quadratic time-dependent term within the dimensions of the atomic wave-packet ($\approx 100 \text{ nm}$) with a sufficiently small error.

The following description of the source masses is kept short and for a detailed treatment in particular of the numerical simulations refer to the thesis of Marco Fattori [52].

3.4.1 Double differential measurement

A double differential measurement eliminates a big number of systematic errors and this enables a high accuracy measurement of the acceleration induced by the source masses (SM). The first differential measurement is carried out between two atom clouds, one above the other. The source masses are in configuration I (see Figure 3.12) and such accelerate the upper cloud 1 downwards and the lower cloud 2 upwards. For the second difference, the masses are moved to configuration II, where the attraction on the atoms is directed in opposite directions. The position of the atom clouds remain the same during the first and second differential measurement.

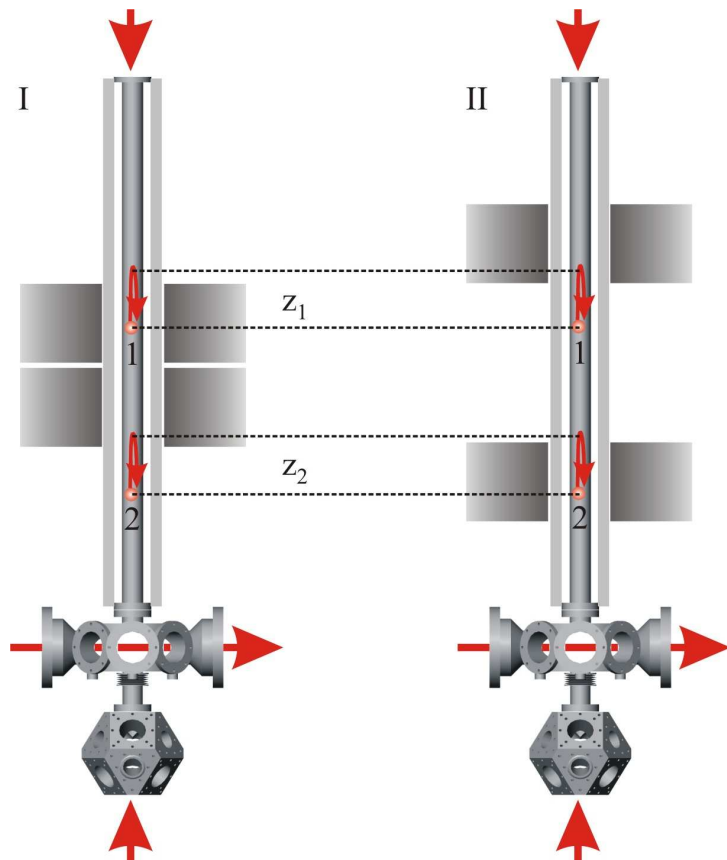


Figure 3.12: Gradiometer with two atom clouds in configuration I (left) and II (right). The atomic trajectories remain fix and only the masses are moved such that the source mass' induced acceleration points into opposite direction in the two positions. Indicated are in addition interferometer beams and detection beam.

We decompose the phase-shift signal of one interferometer $\Delta\phi$ into one position dependent term originating from gravity $\phi_g(z)$, one term determined by the source masses acceleration $\phi_{SM}(z)$ and one time and position dependent term containing systematic effects $\phi_{Syst}(z, t)$. In this section, the parameters (z, t) serve only as an indication of the cloud position z at the initial time t of the interferometer. We can thus write the phase shift of the two interferometers indicated in Figure 3.12 in position 1 and 2, respectively, as follows:

$$\begin{aligned}\Delta\phi_1^I &= \phi_g(z_1) + \phi_{SM}^I(z_1) + \phi_{Syst}(z_1, t_1) \\ \Delta\phi_2^I &= \phi_g(z_2) + \phi_{SM}^I(z_2) + \phi_{Syst}(z_2, t_1) \\ &= \phi_g(z_1 - \Delta z) - \phi_{SM}^I(z_1) + \phi_{Syst}(z_1 - \Delta z, t_1) \\ \Delta\phi_1^{II} &= \phi_g(z_1) + \phi_{SM}^{II}(z_1) + \phi_{Syst}(z_1, t_2) \\ &\approx \phi_g(z_1) - \phi_{SM}^I(z_1) + \phi_{Syst}(z_1, t_2) \\ \Delta\phi_2^{II} &= \phi_g(z_1 - \Delta z) - \phi_{SM}^{II}(z_1) + \phi_{Syst}(z_1 - \Delta z, t_2) \\ &\approx \phi_g(z_1 - \Delta z) + \phi_{SM}^I(z_1) + \phi_{Syst}(z_1 - \Delta z, t_2)\end{aligned}$$

A difference will eliminate gravity and spatially constant systematic errors:

$$\begin{aligned}(\Delta\phi_1^I - \Delta\phi_2^I) &= \phi_g(\Delta z) + 2\phi_{SM}^I(z_1) + \phi_{Syst}(\Delta z, t_1) \\ (\Delta\phi_1^{II} - \Delta\phi_2^{II}) &= \phi_g(\Delta z) - 2\phi_{SM}^I(z_1) + \phi_{Syst}(\Delta z, t_2)\end{aligned}$$

A second difference will eliminate gravity gradient and temporally constant errors:

$$\left\| \begin{aligned}(\Delta\phi_1^I - \Delta\phi_2^I) - (\Delta\phi_1^{II} - \Delta\phi_2^{II}) &= 4\phi_{SM}^I(z_1) + \phi_{Syst}(\Delta z, \Delta t)\end{aligned} \right. \quad (3.12)$$

We wrote $\Delta z = z_1 - z_2$ for the distance between both clouds, we made use of the equality of the signals $\phi^I(z_2) = -\phi^I(z_1)$ and approximated $\phi^{II}(z_1) \approx -\phi^I(z_1)$.

Apparently, the double difference eliminates effects of gravity, gravity gradients and further effects like laser phase noise, which do not vary in time $\Delta t = t_2 - t_1$ over the distance $\Delta z = z_1 - z_2$. The time Δt is in the order of 10 minutes.

This means that we are only affected by systematic effects that are spatially inhomogeneous and change in time Δt .

3.4.2 Gravity gradient

To measure a signal of $\alpha = 10^{-6} \text{ m/s}^2$ with an accuracy of 10^{-4} , the error needs to stay below 10^{-10} m/s^2 . In a gravity gradient of $\gamma = 3 \cdot 10^{-6} \text{ m/s}^2$, an error of this order is provoked by a variation in position of only $30 \mu\text{m}$, and it would therefore be extremely helpful to compensate the gradient γ over the whole area of the interferometer. The compensation with electric or magnetic fields is not precise enough and would just introduce further errors; instead, it seems to be a better idea to use the already well characterized gravitational field of the source masses for compensation. Under which circumstances will this be possible?

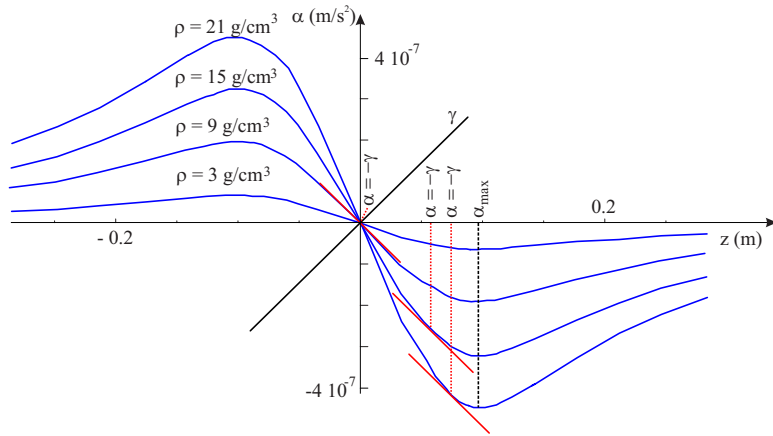


Figure 3.13: Acceleration signal α of one of our source masses consistent of 12 cylinders of 15 cm height and 10 cm diameter in hexagonal configuration. For densities ρ below 9 g/cm^3 , compensation of the Earth's gradient γ is impossible; for increasing density, the 2 points of compensation with $\alpha = \gamma$ above and below the center ($z = 0$) approach the point of maximum acceleration α_{\max} .

For fixed dimensions, the absolute signal of the mass as well as its gradient increase with increasing density until for a certain critical density around $\rho = 9 \text{ g cm}^{-3}$ a compensation of the Earth's gradient will happen at the center of the SM, where the SM induced acceleration has a zero crossing and inflexion point. With a further increase of the density, two points of stationary acceleration will move away from the center of the SM towards the points of maximum acceleration as indicated in Figure 3.13. Obviously, we are interested in both a big signal and in a good compensation of the gradient, what can be achieved with high density materials, which have their stationary points very close to the points of maximum SM acceleration. Increasing the mass and not the density will not let the signal scale in the same way, because in this case also the distance to the center of the mass increases.

Each SM offers such two points of compensated gradient and reversed acceleration α . Between configuration I and II, the two SM move in such a way that the stationary gravity point will come to lie at exactly the same positions – and the atom position will stay the same in both configurations; an important issue for the elimination of systematic effects. Figure 3.14 shows the acceleration of our source masses (see section 3.4.4), each with a mass of 240 kg. The masses are separated by 4 cm in configuration I to leave space for their support, a 4 cm thick plate of titanium.

The knowledge of G and γ to 10^{-2} will permit us to designate two regions of about 1 mm^3 each, where gravity does not change by more than 10^{-11} .

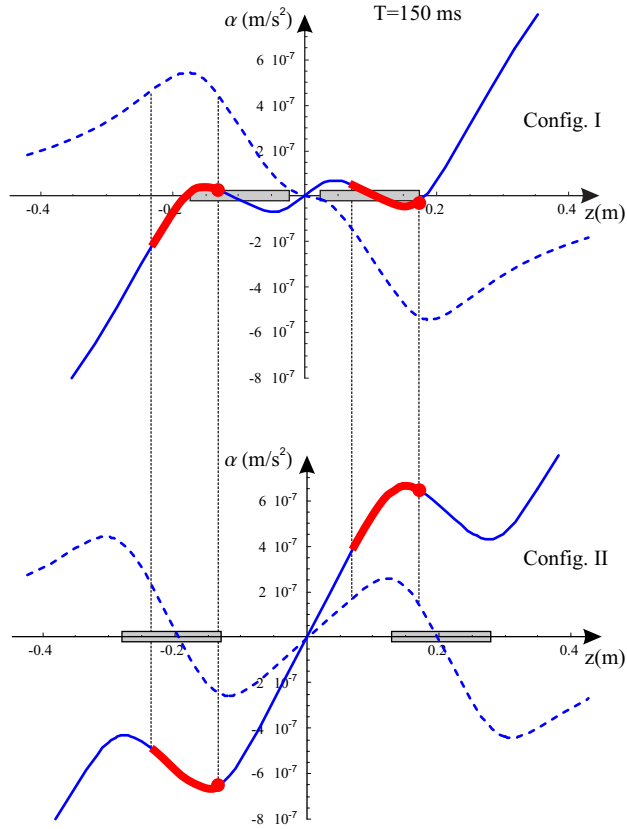


Figure 3.14: Dashed: Acceleration along vertical axis induced by our source masses alone in configuration I (upper curve) and II (lower curve). The position of the source masses is indicated with grey boxes. Solid Line: Acceleration of source masses plus gravity gradient. The atomic trajectories are highlighted, the turning point marked with a dot. The trajectories lie around the maxima of the total acceleration to reduce sensitivity on atomic position. Thanks to the high density of the SM, these stationary points lie near the maxima of the SM induced acceleration.

3.4.3 Best Trajectories

Our atoms do not remain permanently in the compensated region described in the previous section, but are falling. We underline that we will perform the interferometer around the the turning point of the free-flight parabola of the atoms because in this way the atoms can stay longer in the strongest field of the source masses. If now this trajectory includes a (local) maximum of the overall acceleration, including the gravity gradient (see Fig. 3.14), an advantage will show up, described in the caption of Figure 3.15: the dependence of the interferometer phase on the initial positions of the atoms is significantly reduced.

To evaluate the dependence on initial position and velocity of the atoms and to find the trajectory which is less sensitive, numerical calculations of the phase shift have been

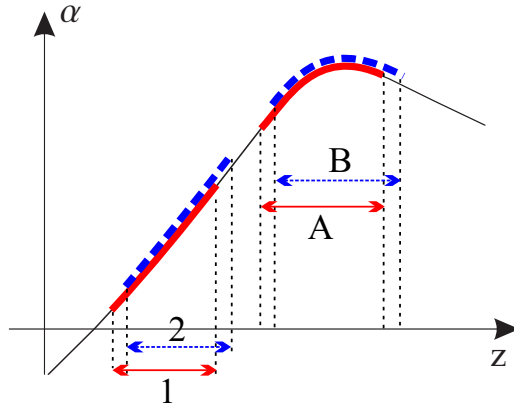


Figure 3.15: Close-up of acceleration $\alpha(z)$. Atoms starting from different positions z will experience different acceleration α . Without a stationary point within the trajectory (left curves 1,2), the different acceleration will sum up over the whole path and the measured acceleration on trajectory 2 will be higher than the one on trajectory 1. With an extremum included in the trajectories (right curves, A,B) the atom following the trajectory B will experience higher acceleration than A at the beginning and lower acceleration towards the end and the overall acceleration on both trajectories is very similar and depends a lot less on the initial position.

performed, described in detail in [52] and to some extend in [96]. The simulations have been performed for an interferometer spacing of $T = 150$ ms in the following order: First of all the points of stationary acceleration for mass configuration I are determined. Once known, we find configuration II with coinciding stationary point of oppositely directed acceleration. By varying the parameters of initial position and velocity, we find those trajectories, which are least sensitive on the variation of the initial parameters (indicated in Figure 3.14).

Parameter	Expected Uncertainty	$\Delta G/G \cdot 10^{-5}$
Vertical position of atoms	< 1.5 mm	< 10
Vertical velocity of atoms	< 5 mm/s	< 10
Radial position of atoms	< 1.5 mm	< 10
Absolute distance between SM	$10 \mu\text{m}$	2
Knowledge of distance between SM	$5 \mu\text{m}$	2
Verticity of system	< 2'	< 2
Mass of single cylinder	< 20 mg	< 0.1
Dimension of single cylinder	$1 \mu\text{m}$	1
Radial positioning of cylinders	$5 \mu\text{m}$	2

The above table shows the maximum expected variations of the initial velocity and position of one atom and the corresponding error on G for the optimized trajectories. For a whole cloud of atoms, we take a weighted (Gauss) average. The table additionally shows further uncertainties related to the masses and support with their corresponding errors on the G -measurement.

Including the points of stationary acceleration in the interferometer permits the identification of trajectories, which allow position uncertainties of the atoms of more than 1 mm in all directions.

3.4.4 Characteristics of Masses

Material: We decided for a material called INERMET 180, produced by the company PLANSEE. It is sintered from a powder composed of 95% Tungsten, 3,5% Nickel and 1,5% Copper with grain sizes of $10\text{-}50\ \mu\text{m}$. The reasons for the choice were mainly its high density of $18\ \text{g}/\text{cm}^3$ (lead has $9\ \text{g}/\text{cm}^3$) and its good machinability. It further shows a resistivity of $1.2\cdot10^{-7}\ \text{Wm}$, a low thermal expansion of $5\cdot10^{-6}\ \text{m}/\text{m/K}$ and also low magnetic susceptibility.

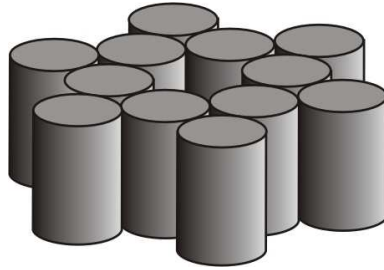


Figure 3.16: One of the two test masses, composed of 12 single cylinders each.

Shape: Each of the two source masses consists of 12 cylinders in hexagonal arrangement illustrated in Fig. 3.16. One cylinder is 15 cm high, has a diameter of 10 cm, weights around 20 kg and is machined with an accuracy of a few micron. The twelve cylinders create a gravitational field with axial symmetry such that the resulting force on the atom is vertical (plotted in Fig. 3.14). The distance of the masses from the center of the interferometer tube is 5 cm; large enough to allow for a broad Raman beam and to be less sensitive on small scale density fluctuation on the material, but also small enough to induce a sufficiently strong acceleration. The expected signal of these masses in terms of interferometer phase is 0.4 rad.

Homogeneity: The sintering of the material is performed at temperatures of 1500°C . Ni and Cu melt and occupy the holes between the grains of W. An inhomogeneous

cooling of the material might cause a migration of the Ni and Cu due to a volume shrinking during solidification, leading to the creation of *holes* in the material, as for example on the microscopic image of Figure 3.17. A further treatment called *Hot*

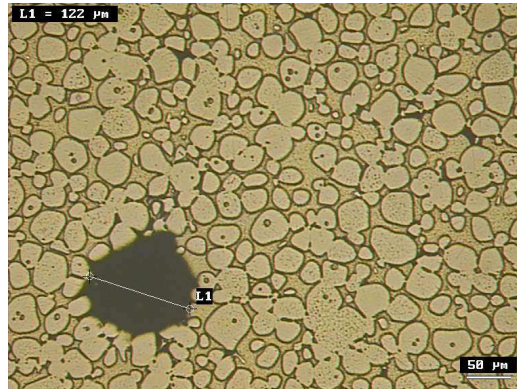


Figure 3.17: Microscopic image of holes as they can arise in the center of big blocks of the sintered tungsten alloy INTERMET 180.

Isostatic Pressing (HIP) under high temperature (1200°C) and pressure (1500 atm) helps to reduce the holes. The density of a test cylinder increased by one part per thousand (17.766 g/cm^3 to 17.789 g/cm^3) during the HIP treatment. An ultrasonic test still indicates some kind of inhomogeneities, but the signal is not yet well understood.

Tests of homogeneity: We fabricated an aluminium mould, which basically is a block of aluminium with a U-formed groove, whose diameter is just $200 \mu\text{m}$ bigger than the one of the cylinders (see Figure 3.18). Compressed air is delivered to three

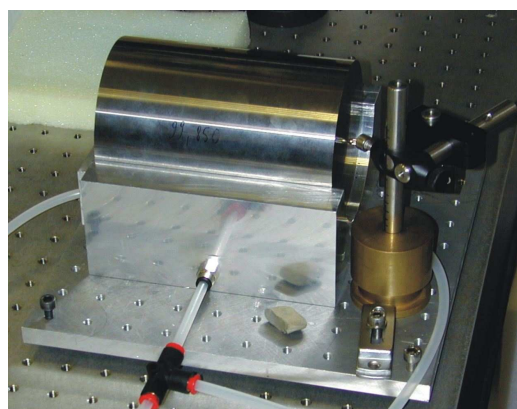


Figure 3.18: Air-cushion test: Masses are floating on an air cushion in a mould. Their oscillation behavior indicates radial inhomogeneities in the material.

tiny holes at the bottom of the groove such that the cylinder within the groove will

be elevated and floats freely. We observe a radial oscillation of the cylinder around a certain zero-point. The air flow induces a pressure dependent torque on the cylinder, why the zero-point of the oscillation changes with pressure. To find the true center of the oscillation we do an extrapolation of the pressure dependent center-points to zero pressure. If we assume that there is just one inhomogeneity at half radius responsible for the oscillation, we can state that in contrary to the unHIPed cylinder, the HIPed one indicates sufficiently low inhomogeneities on the order of 10^{-4} – causing variations of the acceleration in the order of 10^{-5} . In collaboration with the MGC in Torino (Istituto di Metrologia "G. Colonnetti"), we are currently performing destructive tests on a test cylinder by cutting it into small pieces and comparing their density to obtain further information about eventual spacial fluctuations.

Positioning: To ensure a reproducible exact positioning of the cylinders, three conical holes are drilled into the bottom surface of each cylinder and three triangular grooves in the titanium plate on which the cylinders are placed. Balls inside the conical holes will enable a positioning of the masses within a few micron accuracy. A control of the positioning will be done by a 3D-measurement at University of Padova in January 2005. During the experiment, the 24 masses can be interchanged to check eventual systematic errors arising from density fluctuations or positioning uncertainties. Deformations of the 4 cm thick titanium support plate have been studied by

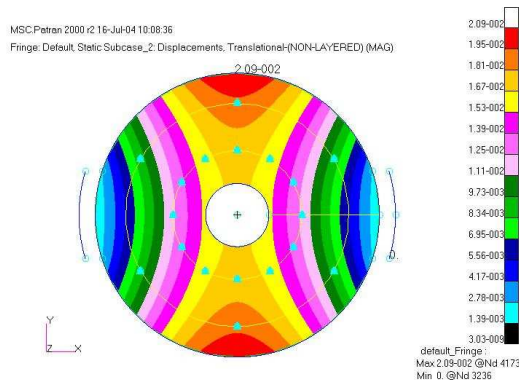


Figure 3.19: Simulation of deformations of the Ti-support, which carries the 12 cylindrical source masses. The biggest deformations os about $20 \mu\text{m}$ occur at the outer edges of the plate orthogonal to the points of suspension.

finite-element analysis and Figure 3.19 illustrates the deformation of this plate under the weight of 12 cylinders. The simulation indicates a deformation of up to $20 \mu\text{m}$ that made us design a 10 cm high reinforcing aluminium ring, which can be seen in Figure 3.20. To model the gravitational field of the masses (and other moving elements of the support) in three dimensions, we use the method of multipole expansion.

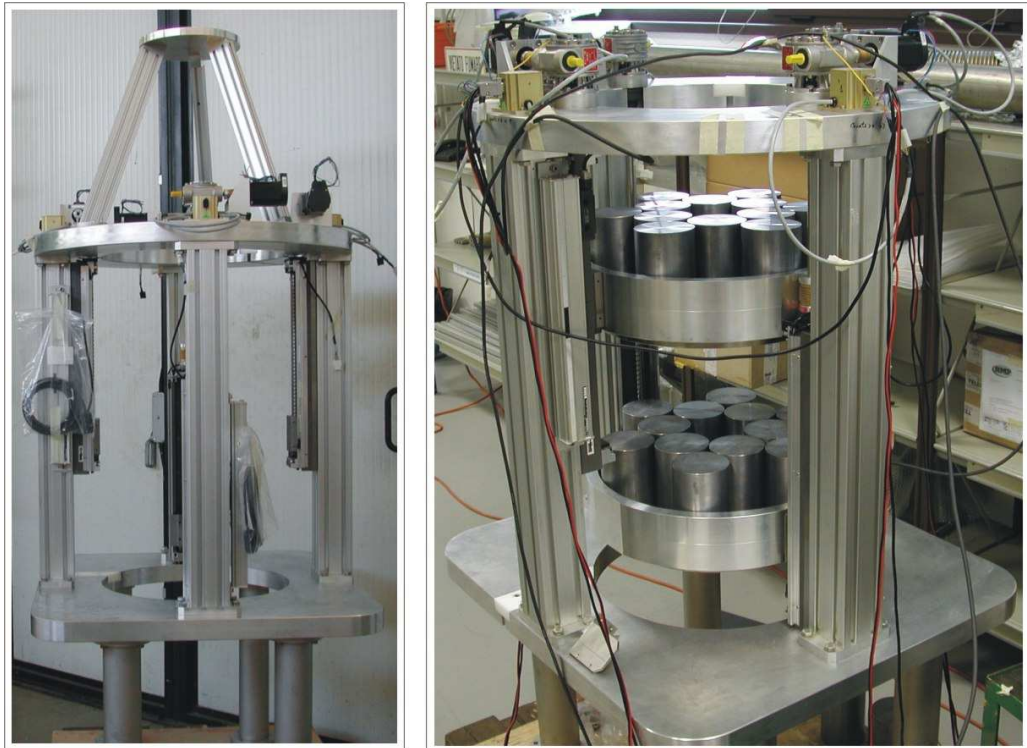


Figure 3.20: *Support for MAGIA source masses. Left: whole support without masses, right: equipped with 24 lead masses. The vertical movement of the masses with four step-motors is accurate to few micrometers and is controlled by a calibrated optical ruler. The cylinders are placed 12 each on a 4 cm thick titanium plate, reinforced with an outer aluminium ring.*

Support: The development of the support to carry and move the SMs (see Fig. 3.20) has been carried out in collaboration with the Laboratori Nazionali di Frascati, LNF and the company R.M.P. in Rome. The positioning of the two SMs can be controlled to $10 \mu\text{m}$ and their distance determined with an optical ruler to $1 \mu\text{m}$; whereas the verticality is guaranteed to at least 2 arc minutes. The functioning of the optical ruler has been checked on small distances and will be checked on big distance with a laser tracker. Each of the two Ti-plates, which support the altogether 24 cylindrical masses, is attached to two slides, which are moved by two electric step-motors coupled in velocity. To stabilize possible oscillations of the table due to its high center of mass, the hole optical table is held by two floating U-shaped mounts.

Temperature stabilization: Thermal expansion of the support and the source masses will change the mass distribution and therefore the expected gravitational potential. This can lead to drastic errors in the determination of G . To stay within the aimed accuracy, the temperature must be controlled to a tenth of a degree. We will therefore

stabilize the environment of the whole apparatus inside an independent chamber. At the moment, we have to deal with temperature fluctuations of another magnitude and we managed to push the temperature fluctuations from up to 8 degrees per day down to ± 1.5 degrees. Construction work to better isolate the walls of the room from the tremendous summer-temperatures of the outer walls and the unconditioned corridor are presently under way.

Chapter 4

Laser frequency and phase control

A free running ECDL will jump or drift by up to a few GHz per day, far too much to stay in resonance with the rubidium transitions with their natural linewidth of about 6 MHz. It is thus indispensable to stabilize the laser frequency to either an atomic resonance or to an already stabilized laser, may it be in frequency or in phase, like in case of the interferometer lasers that drive Raman transitions. A big variety of techniques for frequency and phase control have been developed in parallel to use of lasers in laboratory, many of which can be found in [109].

This chapter will present some methods that we implemented at the gravimeter and gradiometer experiment. Some more space is dedicated to a new method, developed at the MAGIA experiment in Florence, called Doppler-free DAVLL [116]. After the introduction to these techniques, the experimental realization of frequency and phase control for the Watt-balance gravimeter and the gradiometer will be described in detail, since it has been one of the main topics of the work during the past three years.

4.1 Frequency stabilization

To stabilize a laser frequency to a reference, one needs *information about the frequency difference* between both. Therefore, the frequency must somehow be *converted into a voltage* with a zero-crossing at the lock point, such that it can be used to give a *feedback* to the laser. The reference frequency must be of the order of the laser frequency and can be either an *atomic transition* or *another laser*.

The conversion of the frequency difference to a voltage can be done by:

1. the absorption or dispersion of an atomic transition or
2. a Frequency-to-Voltage converter.

When using an atomic sample for spectroscopy, we distinguish between two different classes of spectroscopic methods that differ in the generation of the dispersive signal from atomic spectra:

1. The first class uses modulation and demodulation of light, such as Frequency-Modulation (FM) spectroscopy [110, 111] or modulation-transfer spectroscopy [112], to derive a dispersive signal from either absorption or dispersion induced by the atoms. These techniques are very powerful and provide high signal-to-noise ratios at the price of expensive optic modulators and electronic components.
2. The methods of the second class do not include modulation and generally imply less optical and electronic components, which makes them easier to implement. Still, they are often able to fulfil the demands in atomic and laser physics. Polarization spectroscopy [114], Dichroic Atomic Vapor Laser Lock (DAVLL) [115] and side-locking on saturated absorption spectroscopy signals [120] (and more general [117] and [119]) belong to this class.

4.1.1 Frequency modulation spectroscopy

Modulation of the spectroscopy-laser and the demodulation of the spectroscopy signal with the same frequency ω_m is a trick to get around the big flicker noise at low frequencies disturbing the signal. At the same time, this method delivers a dispersive signal with a zero-crossing at the line-center, which is well suited for locking. In the following, the field of the spectroscopy laser is

$$E(t) = E_0 \cos(\omega_L t + \phi_0) = E_0 \cos \phi(t), \quad (4.1)$$

with phase offset zero $\phi_0 = 0$.

Frequency and Phase modulation: Let us first compare a phase-modulated signal

$$E_{PM}(t) = E_0 \cos(\omega_L t + m \cos \omega_m t) = E_0 \cos \phi_{PM}(t) \quad (4.2)$$

and a frequency-modulated one:

$$E_{FM}(t) = E_0 \cos[(\underbrace{\omega_L + m' \cos \omega_m t}_{\bar{\omega}})t]. \quad (4.3)$$

We define the instantaneous frequency as

$$\omega(t) = \frac{d\phi(t)}{dt} \leftrightarrow \phi(t) = \int_0^t \omega(t') dt' + \phi_0. \quad (4.4)$$

For the phase of a frequency modulated signal (4.3) with the modulated frequency $\bar{\omega}$ follows with (4.4) and $\phi_0 = 0$:

$$\phi_{FM}(t) = \int_0^t \bar{\omega}(t') dt' = \omega_L t + \frac{m'}{\omega_m} \sin \omega_m t + \phi_0 = \omega_L t + m \sin \omega_m t = \phi_{PM}(t) \quad (4.5)$$

which shows the equivalence of frequency modulation with phase modulation of modulation index $m = \frac{m'}{\omega_m} = \frac{\Delta\omega_{max}}{\omega_m}$.

We can write the modulated light field E_M as

$$E_M(t) = E_0 \cos[(\omega_L t + m \sin \omega_m t)t] = E_0 [\cos \omega_L t \cos(m \sin \omega_m t) - \sin \omega_L t \sin(m \sin \omega_m t)] \quad (4.6)$$

A Fourier expansion of $\sin(m \sin \omega_m t)$ and $\cos(m \sin \omega_m t)$ in terms of Bessel-functions of first kind ¹ yields

$$\begin{aligned} E_M(t) = E_0 [& J_0(m) \cos \omega_L t - J_1(m) (\cos(\omega_L - \omega_m)t - \cos(\omega_L + \omega_m)t) \\ & + J_2(m) (\cos(\omega_L - 2\omega_m)t + \cos(\omega_L + 2\omega_m)t) \\ & - J_3(m) (\cos(\omega_L - 3\omega_m)t - \cos(\omega_L + 3\omega_m)t) \\ & + \dots]. \end{aligned} \quad (4.7)$$

After the modulation, the laser beam passes a spectroscopy cell, in our case a rubidium vapor cell of length L and absorption coefficient α . We define the attenuation $a_j = \alpha_j L/2$ and the phase shift $\phi_j = n_j L(\omega_L - j\omega_m)/c$, where $j = 0, \pm 1, \pm 2, \dots$, denote the frequency components as $\omega_L, \omega_L \pm \omega_m, \omega_L \pm 2\omega_m, \dots$, respectively, with the frequency dependent refractive indices n_j . The transmitted field E_T is therefore:

$$\begin{aligned} E_T(t) = & E_0 \{ J_0(m) e^{-a_0} \cos(\omega_L t + \phi_0) \\ & - J_1(m) (e^{-a_{-1}} \cos[(\omega_L - \omega_m)t + \phi_{-1}] - e^{-a_{+1}} \cos[(\omega_L + \omega_m)t + \phi_{+1}]) \\ & + \dots \}. \end{aligned} \quad (4.8)$$

In the following, we will only consider the case of small modulation index $m \ll 1$, neglect higher order sidebands than the first ones and drop terms with order m^2 and higher. The slowly varying (average over terms oscillating with $\omega \gg \omega_m$) intensity envelope $I(t)$ of the light on the detector is then given by

$$\begin{aligned} I(t) = & \frac{1}{2} c \epsilon_0 E_T(t)^2 \\ = & \frac{1}{2} c \epsilon_0 E_0^2 e^{-2a_0} \left[J_0^2(m) + J_0(m) J_1(m) (a_{-1} - a_1) \cos \omega_m t \right. \\ & \left. + (\phi_1 + \phi_{-1} - 2\phi_0) \sin \omega_m t \right]. \end{aligned} \quad (4.9)$$

We assumed that $|a_0 - a_{\pm 1}| \ll 1$ and $|\phi_0 - \phi_{\pm 1}| \ll 1$ to approximate the exponential with the first order expansion term. For $m \ll 1$, $J_0(m) \approx 1$ and $J_{\pm 1}(m) \approx m/2$.

The detector voltage signal is proportional to $I(t)$ and contains a beat signal at ω_m , if

¹ $\cos(x \sin s) = J_0(x) + 2 \sum_{n=1}^{\infty} J_{2n}(x) \cos(2ns)$ and $\sin(x \sin s) = 2 \sum_{n=1}^{\infty} J_{2n-1}(x) \sin((2n-1)s)$

one of the two last terms of expression (4.9) is not zero. This signal can be detected by demodulating it on a mixer with ω_m and filtering out higher frequencies.

The $\cos \omega_m t$ -term of (4.9) is proportional to the difference in *amplitude* loss of both first order sidebands whereas the $\sin \omega_m t$ -term is proportional to the *phase* difference experienced by the carrier and the average phase shift of the side-bands.

- In case that ω_m is smaller than the investigated transition, the $\cos \omega_m t$ -component is proportional to the *derivative of the absorption* and the $\sin \omega_m t$ -component to the *second derivative of the dispersion*. If we do not want to superimpose these signals, the relative phase of the demodulation frequency needs to be adjusted before the mixer to either get a pure absorptive or a pure dispersive signal. One can use both signals for spectroscopy. The absorptive signal is bigger for very small frequencies ($\omega_m < 0.1 \times \text{FWHM}$ of spectroscopic line) and in this case one often speaks of *Lock-In technique*. On the contrary, when using the dispersive signal, which gets stronger for higher frequencies, one often speaks of *FM spectroscopy*, even though the distinction is not clear.
- If ω_m is bigger than the spectral feature (ω_m up to $50 \times \text{FWHM}$), just one sideband will probe it and the cosine and sine components are directly proportional to absorption and dispersion. In this regime, only the dispersive signal shows a sharp zero crossing and can be used for locking [111].

When demodulating with the third harmonic, the signal is proportional to the third derivative of the absorption and not only the flat but also slightly curved background of the spectroscopy signal is suppressed.

For Doppler free spectroscopy on a vapor cell, one uses a pump-probe setup, where either the pump beam, the probe beam or both can be modulated. In the case of pump beam modulation, the modulation is transferred onto the probe beam by four-wave mixing. We use the FM-spectroscopy with a modulation frequency of $\omega_m = 5 \text{ MHz}$ at the gravimeter (see section 4.3.1) and the Lock-In technique with a modulation at $\omega_m = 70 \text{ kHz}$ at the gradiometer (see section 4.4.2).

4.1.2 DAVLL

The Dichroic Atomic Vapor Laser Lock (DAVLL) was used at the gradiometer during the first year to lock the cooling laser. The underlying idea of DAVLL is illustrated in Fig. 4.1a). Two Doppler broadened Gaussian line profiles are shifted in frequency relatively to each other. The difference A-B between the two signals results in a dispersive curve. The slope at the zero-crossing reaches its maximum at a relative shift of half the Doppler broadened linewidth.

The DAVLL scheme [115] has got a large capture range of the size of the Doppler-broadened linewidth and a slope comparable to that of saturated absorption spectroscopy. The locking point can be chosen anywhere within the Doppler-broadened profile. However, if not locking on the exact zero-crossing, the method is very sensitive on power fluctuations and drifts. This results in a change of the lock point that can exceed several MHz for ordinary diode-lasers. Furthermore, it is hard to determine the actual frequency.

4.1.3 Doppler free DAVLL lock

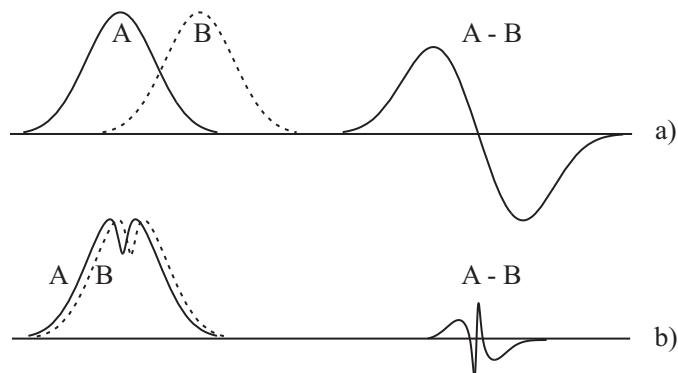


Figure 4.1: a): The subtraction of two relatively shifted Doppler-broadened Gaussian line profiles generates a DAVLL signal. b): The subtraction of two relatively shifted saturated absorption lines generates a Doppler-free DAVLL signal.

We encountered the necessity of locking a laser to an atomic transition without modulating the beam. The DAVLL method resulted to be too noisy, because the desired locking point was not located at the center of the Doppler broadened line, which implies a big offset and therefore noise in the locking signal. Polarization spectroscopy was not sensitive to the desired transition and this lead us to the development of a Doppler-free spectroscopic method, which can be described as a *combination of saturated absorption spectroscopy and DAVLL*. Compared to the DAVLL, Doppler-free DAVLL ([116], [122]) offers higher frequency accuracy and a bigger slope of the signal but enables locking only at certain frequencies.

Idea: Doppler free DAVLL relies on the same idea as the DAVLL, but uses two relatively shifted Lorentzian dips in the Doppler profile. The difference signal will be a narrow dispersive signal on top of a very low and broad DAVLL background as illustrated in Fig. 4.1b). To get a difference signal with maximum slope, both Doppler-free lines should be shifted one against the other by 0.58 times their linewidth². At zero crossing, the difference signal hence has got a slope twice as big as the slope of the absorption dip and a magnitude of 1.6 times the magnitude of the Doppler-free dip. To generate such a relative shift in frequency between two saturated absorption signals, we use *magnetically induced dichroism*. A vapor cell is exposed to a magnetic field along the propagation axis of two counter-propagating pump- and probe beams. The σ^+ and σ^- components of the linearly polarized probe beam are both generating a saturated absorption profile, each Zeeman-shifted by the same amount but in different directions from the center frequency. By separately detecting the two components and subtracting their signals from each other, a Doppler-free DAVLL signal is created.

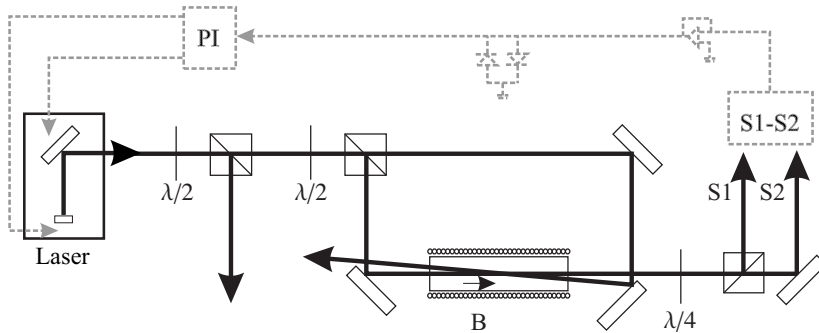


Figure 4.2: Setup of the Doppler-free DAVLL. The laser is split into pump and probe beam and the σ^+ and σ^- components of the probe beam are detected independently after the passage through a rubidium vapor cell. They are subtracted from each other and the resulting signal is used to lock the laser frequency. The spectroscopy signal is amplified and cut at voltages bigger ± 0.7 Volts to protect the laser.

Description of the setup: Our setup for the Doppler-free DAVLL is shown in Figure 4.2. A variable part of our laser power is taken off for spectroscopy, split into counter-propagating pump and probe beam and sent through a 70 mm long cell of rubidium vapor (see photo 4.3).

The cell is slightly tilted relative to the beam propagation to avoid reflections of the pump going to the detectors. Around the cell, we fixed a coil with $N=144$ windings, diameter 24 mm and 90 mm length (see Fig. 4.2) to be able to apply a magnetic field up to 40 Gauss along the propagation axis of the beams. We additionally wrapped a heating foil around the cell to heat the vapor to about 40°C, which increases the pressure and therefore the absorption signal.

²The maximum slope of a Lorentzian is found at $1/\sqrt{3} \approx 0.58$ times its linewidth.

We consider the linear polarized probe beam as a superposition of clockwise and counter-clockwise circularly polarized light. Inside the vapor cell, these two components are affected by magnetically induced dichroism. The passage through a quarterwave-plate behind the vapor cell transforms the two circular polarized components into two orthogonal linear polarized beams, which are separated by a polarizing beam-splitter and detected independently with two detectors. The difference between these two signals forms a dispersive Doppler-free DAVLL signal. The detection and subtraction is done within a single unit. We experimentally optimize the total power used for spectroscopy and the power ratio between pump and probe beam on a maximum size of the signal. We find the following values: pump power $480 \mu\text{W}$, probe power $220 \mu\text{W}$ (beam diameter of 2.5 mm). The magnetic field has been optimized to a value of 11 Gauss in order to obtain a maximum slope of the dispersive signal.

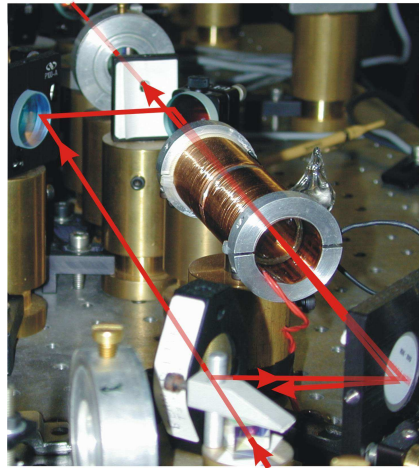


Figure 4.3: Photo of saturated absorption spectroscopy with counter-propagating pump- and probe-beam on a Rb vapor cell. A coil and a heating foil are wrapped around the cell.

Results on the rubidium D₂ line: To study Doppler-free DAVLL on the ^{87}Rb D₂ line, we will use the notation of Fig. A.1 in Appendix A for the rubidium transitions and cross-over (CO) transitions. The natural linewidth of the D₂ transition is 6 MHz and the power of $480 \mu\text{W}$ in the pump beam of 2.2 mm diameter is equivalent to a saturation parameter $S=7.9$, corresponding to a power broadened linewidth ($\Delta\nu_{PB} = \Delta\nu_{nat} \sqrt{1 + S}$) of 18 MHz.

We apply a magnetic field such that the Zeeman-splitting remains smaller than the power-broadened linewidth. The magnetic field defines the quantization axis, which is slightly tilted respect to the beam propagation by the Earth magnetic field (≈ 0.5 Gauss). Dividing the component of the Earth magnetic field orthogonal to the propagation axis by the total magnetic component parallel to it, one obtains the reduction factor of the signal.

With perfectly balanced offset, the zero-crossing of the spectroscopic signal corresponds to the unperturbed transition-frequency and is neither altered by stray magnetic fields nor by power fluctuations, which both only vary the size of the signal ³.

Fig. 4.4 shows, how the spectroscopic signal is generated on the ^{87}Rb D₂ transition.

³Fields parallel to the propagation axis will shift the two signals into opposite directions leaving the zero crossing unaffected, whereas fields perpendicular to the propagation axis will reduce both signals and just change the size of the signal.

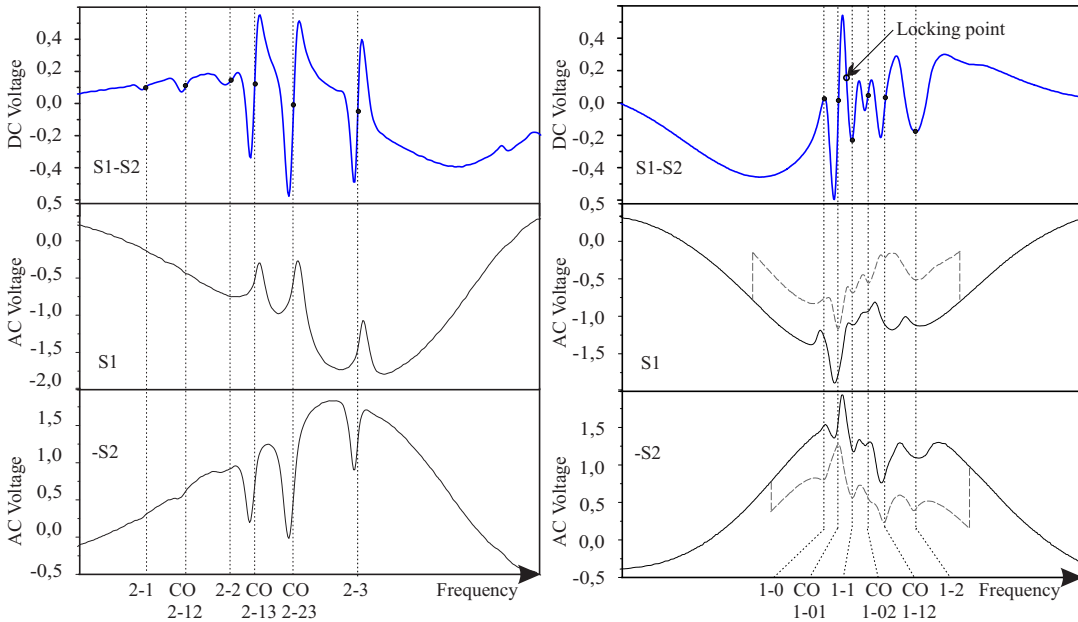


Figure 4.4: Spectroscopic signal of the upper (left) and lower (right) hyperfine transition of ^{87}Rb . The signals S_1 and $-S_2$ are shifted in opposite directions and the subtractions delivers a dispersive spectroscopic signal with low background. Notations are according to Fig. A.1. We used the lock first on the cooling transition 2-3. Presently, we lock the repumper laser on a slope near the transition CO1-01, indicated as locking point. The dotted lines and black dots correspond to the center of the transitions. In the right picture, we added the dashed lines of the spectroscopy without magnetic field.

The two symmetrically shifted saturated absorption signals S_1 and $-S_2$ add to give a dispersive spectroscopic signal S_1-S_2 .

- *Cooling transition:* Initially, we used the Doppler-free DAVLL to lock on the cooling transition $F=2$ to $F'=3$, in our notation the transition 2-3, left on Figure 4.4. We have a locking bandwidth of only few kHz and within this bandwidth the error signal indicates frequency fluctuations of around 120 kHz. An estimation from frequency-jitter on the spectroscopy signal indicates noise smaller than 100 kHz, so that the value of the error signal is a good estimation within its bandwidth.
- *Repumper transition:* At present, we use our method to lock the repumper with an offset on the transition CO1-01, as indicated in Fig. 4.4, right. With the 80 MHz shift of an AOM, the laser frequency arrives near the repump-transition 1-2 (see Fig. 3.7). Since the absorption signal of this line shows not only dips but also peaks, the difference signal either has a zero crossing or an extremum at the position of the resonance; but shows a nice slope with zero crossing at the frequency we need. The lock error signal as well as the estimation from the

jitter on the spectroscopy signal indicate frequency fluctuations less than 350 kHz, what is perfectly all right for the repumper, where fluctuations up to 1 MHz would be within the requirements.

Closer look on the line shape: The formation of a peak or dip in the spectroscopic signal depends on various competing effects: 1: The depopulation of the resonant level by the pump beam leads to less absorption of the probe, resulting in a dip. 2: With a loss channel in the transition to the other hyperfine state, depopulation is increased and the dip deepens (e.g. transition CO2-23). 3: If the pump is in resonance with a transition of $\Delta F = +1$, atoms are pumped to the extreme m_F -states, from where the transition probability is higher. This effect increases absorption. 4: A dark state like the $m_F = 0$ in the 1-0 transition, which in addition is closed (atoms cannot escape into F=2), accumulates atoms by redistribution effects between the m_F during the excitation with the pump beam and a probe beam with access to the dark state (1-2 or 1-3) will experience increased absorption. This means a greatly increased absorption for transitions like the CO1-01. Result of these effects is a more or less pronounced dip or peak.

Background: The difference $S_1 - S_2$ does not totally cancel out the background, because also the Doppler-broadened profiles are slightly shifted in opposite directions. This will underlay the signal with a broad and flat dispersive signal of the same origin (see Fig. 4.1b)). *Heating* the cell will not only increase the number of atoms but also broaden the Doppler-profile and flatten the background. To evaluate the maximum background, we assume the Doppler broadening to be Gaussian with a width of 570 MHz (corresponding to 30°C). Taking the difference between two Gaussian profiles, each shifted by half the Doppler-free linewidth of 18 MHz, we find the maxima to be reduced by a factor of 60 compared to the height of the Doppler broadened profile.

Noise: Assuming the power fluctuations of the laser to be the dominating noise, we can state that the noise is proportional to the background and also greatly reduced by taking the difference. A further source of background is the slight rotation of the probe beam by the Faraday effect. By adequately rotating also the last quarterwave-plate and polarizing beam-splitter (see Fig. 4.2), this effect can be compensated.

4.1.4 Further modulation-free locking techniques

We will shortly mention two alternative techniques for locking to an atomic transition without modulation and compare them to the Doppler free DAVLL:

Side-locking of saturated absorption signals: Side-locking on a spectroscopy signal has the intrinsic disadvantage of being sensitive on effects that change the size of the signal like varying stray magnetic fields. To evaluate the noise on a lock signal, we consider the Doppler-background to be subtracted from the Doppler-free signal and we assume the power-fluctuations of the laser to be the limiting noise source. Then, the noise is directly proportional to the size of the signal at the lock point. This point

is at half height of the absorption dip, whereas with Doppler-free DAVLL the signal at the lock-point is determined by the background. For absorption dips bigger than the thirtieth part of the size of the Doppler line, Doppler-free DAVLL offers lower noise and in addition a steeper slope, a bigger signal and a larger capture range of the lock.

Polarization spectroscopy: Instead of using absorption, polarization spectroscopy ([114, 121]) makes use of dispersion to generate spectroscopic signals, which can reach high signal-to-noise values. Generally, one can remark that polarization spectroscopy exhibits its full potential and superiority for small peaks on a big background and for thin or low-pressure samples.

In spite of this fact, we set up a simple polarization spectroscopy apparatus using the same large vapor cell and standard optical components as in DAVLL, in order to compare the methods under the same conditions. For a better understanding, we first give a small review on polarization spectroscopy:

The classical pump-probe configuration is used, the pump being circularly polarized. The circular polarization pumps the atoms into an extreme magnetic hyperfine sub-level, what results in a macroscopic polarization of the sample, causing an optically induced dichroism. The σ^+ and σ^- components of the linear polarized probe beam experience different amounts of absorption and dispersion around a transition frequency; in contrast to a relative shift of the transition frequencies as it is generated by the magnetically induced dichroism in Doppler-free DAVLL. The difference in dispersion of the two components results in a rotation of the linear polarization of the probe beam. On each side of the transition, the rotation has got a different sign and the detection of the rotation gives a dispersive-like spectroscopic signal. The difference in dispersion depends a lot on the amount of polarization the pump is able to induce, what again depends on the particular transition.

If atoms are pumped into an atomic state, which allows a decay into a different ground state, like e.g. transition 1-2, the probe beam reveals a smaller polarization of the sample. The resulting signal is smaller than that of a pure two-level system. In ^{87}Rb , the only pure two level systems are 2-3 and 1-0 and our experiments showed that these transitions produces by far the strongest spectroscopic signal. The crossover resonances CO2-23 and CO2-13, which show the biggest absorption dips in saturation spectroscopy, are very small using polarization spectroscopy and of predominantly absorptive character. In our 7 cm long vapor cell, big differences in absorption between the σ^+ and σ^- components can arise, giving a symmetric contribution to the dispersive signal, thus adding an offset to the lock point and shifting the zero crossing. Stray magnetic fields reduce the polarization of the sample and the signal is reduced.

The detection of transitions with small difference in dispersion and small rotation of the polarization requires good quality polarizers and beam-splitters. Their imperfections contribute to a flat background, which also exists for Doppler-free DAVLL, where it is adding to the small characteristic curved background.

Again assuming the power fluctuations on the laser light to be the limiting noise, the

noise of the zero-crossing of the signal depends only on the size of the background. Considering this, we conclude that in a setup with standard, economical optical components and for the same absolute size of the signal, the noise of Doppler-free DAVLL is comparable to that of polarization spectroscopy, but the first method offers good signals for more transitions and shows a bigger slope of the dispersive signal.

4.1.5 Frequency Lock with f-to-V converter

When we do not use the natural frequency to amplitude or phase conversion of an atomic sample, but compare a laser frequency to the frequency of a reference laser, the difference can be directly converted into a voltage signal by a frequency-to-voltage (f-to-V) converter. The converter compares the incoming frequency-difference signal with an internal voltage and triggers a current pulse whenever the input voltage exceeds the threshold of the comparator. The length of this pulse can be adjusted and the current is injected into an integrator (see Fig.4.5). A periodic triggering will charge the capacitance to a relatively steady mean value, – the output voltage – which shows a ripple at the input frequency. The shorter the current pulses, the higher the possible input frequency, but the bigger also the ripple. An increase of the integrator capacitance will better smooth the output signal, but at the same time it slows down the reaction speed. A f-to-V converter is used in the frequency control system of the gravimeter (see section 4.3).

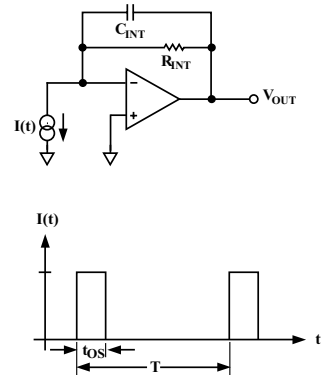


Figure 4.5: Simplified scheme of f-to-V converter (top) and current injected into integrator (bottom).

4.2 Phase Stabilization

To perform Raman transitions between the two fundamental hyperfine levels of ^{87}Rb (F=1↔F=2), the beat signal between the two lasers must be locked to the hyperfine transition frequency of 6.834 GHz. For the interferometer, the relative phase of the Raman lasers is an extremely important variable, since it determines the interferometer signal (see chapter 2.2) and a phase-lock between both is a basic necessity⁴. Again, like in the case of frequency, we have several possibilities to convert a phase into a voltage signal for the feedback:

1. by an analog Mixer,

⁴Small frequency offsets in contrary will be off no importance, as long as they do not change the transition probability.

2. by a digital phase and frequency detector or
3. by a phase difference counter.

Before describing these three phase detectors, which are actually used in the experiments, we will give a very brief introduction to phase-locked loops.

4.2.1 Phase-locked-loop

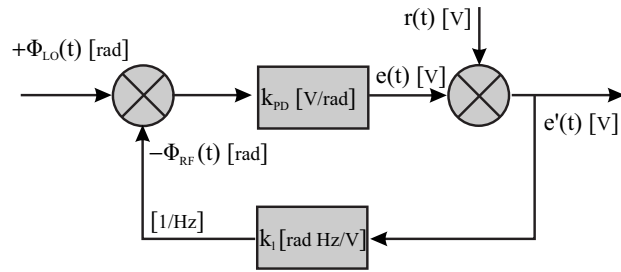


Figure 4.6: *Phase-locked-loop*: The phase difference between a LO and an RF signal ($\phi_{LO} - \phi_{RF}$) is converted into an error signal $e(t)$ with gain k_{PD} on a phase detector (PD). The loop adds noise $r(t)$ and the feedback signal $e'(t)$ is converted into a frequency with gain k_I to correct the phase error.

The goal of a phase-locked loop (PLL) is the stabilization of the phase of a noisy radio-frequency (RF) source onto a clean local oscillator (LO) signal with the following instantaneous frequencies and phases:

$$\omega_{LO} = 2\pi f_0; \quad \phi_{LO}(t) = 2\pi f_0 t + \phi_{LO,0} \quad (4.10)$$

$$\omega_{RF}(t) = 2\pi f_0 + 2\pi f_N(t); \quad \phi_{RF}(t) = 2\pi f_0 t + 2\pi \int_0^t f_N(t') dt' + \phi_{RF,0}. \quad (4.11)$$

The RF-signal shows the frequency noise $f_N(t)$ and we define the resulting phase noise⁵ as

$$\phi_N(t) = 2\pi \int_0^t f_N(t') dt'. \quad (4.12)$$

A phase-locked-loop (PLL) consists of a Phase Detector (PD), who converts the detected phase difference ($\phi_{LO}(t) - \phi_{RF}(t)$) into a voltage with a certain gain k_{PD} [V/rad]. We assume here an ideal PD with linear gain. We call the voltage signal at the PD output error signal $e(t)$:

$$e(t) = k_{PD}(\phi_{LO}(t) - \phi_{RF}(t)). \quad (4.13)$$

A noise $r(t)$ is added by the loop, e.g. by the laser driver, to the error signal $e(t)$:

$$e'(t) = e(t) + r(t). \quad (4.14)$$

⁵We omitted the index N labelling the noise in chapter 2.3, but will keep it here for clarity.

This error signal is used as a feedback to correct for the noise of the RF signal. In our case, the feedback is directed to a laser driver, who converts the voltage signal with a gain k_l [rad Hz/V] into a frequency change $\delta f(t)$

$$\delta f(t) = \frac{k_l}{2\pi} e'(t) \quad (4.15)$$

within time τ , where the time τ depends on the locking bandwidth. By inserting (4.15) into (4.11) we can write the RF-phase at time $t + \tau$ as

$$\phi_{RF}(t + \tau) = 2\pi f_0(t + \tau) + k_l \int_t^{t+\tau} e'(t) dt + \phi_{RF,0} . \quad (4.16)$$

It is important to note that the loop includes a natural integrator, due to the fact that a phase change is corrected with a feedback on frequency.

After the time τ , the error signal $e'(t)$ will include the reaction to the noise at time $t = 0$ and – using (4.13) and (4.16) – will change by:

$$\begin{aligned} e'(\tau) - e'(0) &= (e(\tau) + r(\tau)) - (e(0) + r(0)) \\ &= k_{PD} (\phi_{LO}(\tau) - \phi_{RF}(\tau)) - k_{PD} (\phi_{LO,0} - \phi_{RF,0}) + r(\tau) - r(0) \\ &= \dots = -k_{PD} k_l \int_0^\tau e'(t) dt + r(\tau) - r(0) . \end{aligned} \quad (4.17)$$

To pull the phase error efficiently to zero, both gains need to be as high as possible. We can switch to *frequency space* by a Laplace transform of (4.17). After four steps of basic calculation we find the following relation between error signal and noise:

$$E'(f) = \frac{R(f)}{1 + k_{PD} k_l / i f} \quad (4.18)$$

for $f \neq f_0$ and where the Laplace-transforms are indicated by capital letters. The unity gain frequency of the loop is $f_1 = k_{PD} k_l$. The loop behaves like a first order filter. In reality, we add integration stages to increase the low frequency gain.

4.2.2 Analog Phase Detector

An analog phase detector consists of a mixer, which multiplies the RF signal $s_{RF}(t) = A_{RF} \cos \phi_{RF}(t)$ with the LO signal $s_{LO}(t) = A_{LO} \sin \phi_{LO}(t)$ with a certain gain k_m [1/Volt]. With the phases (4.10) & (4.11) and by setting $\phi_{LO,0} = 0$ and $\phi_{RF,0} = \pi/2$ we can write the signal $m(t)$ after the multiplication as:

$$\begin{aligned} m(t) &= k_m A_{RF} A_{LO} \sin(\phi_{LO}(t)) \cos(\phi_{RF}(t)) \\ &= \frac{1}{2} k_m A_{RF} A_{LO} \left(\sin \phi_{LO} \cos \phi_{RF} + \sin \phi_{LO} \cos \phi_{RF} + \sin \phi_{RF} \cos \phi_{LO} - \sin \phi_{RF} \cos \phi_{LO} \right) \\ &= \frac{1}{2} k_m A_{RF} A_{LO} \left(\sin(\phi_{LO}(t) - \phi_{RF}(t)) + \sin(\phi_{LO}(t) + \phi_{RF}(t)) \right) \\ &= \frac{1}{2} k_m A_{RF} A_{LO} \left(\sin \phi_N(t) + \sin(2\omega_0 + \phi_N(t)) \right), \end{aligned} \quad (4.19)$$

where we substituted the phase noise according to its definition (4.12) into $\phi_{RF}(t)$ of (4.11).

A low pass filter with gain k_{LP} [V/V] will filter out the second term, which oscillates with $2\omega_0$ and the remaining first term of (4.19) is proportional to the phase difference between RF- and LO signal, the latter of which we set to zero in the last step of 4.19.

For *small phase differences* (actually small deviations from $\pi/2$), the sine can be linearized yielding:

$$e(t) = k_{PD} (\phi_{RF}(t) - \phi_{LO}(t)) . \quad (4.20)$$

We introduced the phase detector gain [Volt/rad] as $k_{PD} = \frac{k_m k_{LP} A_{RF} A_{LO}}{2} \frac{1}{\text{rad}}$ to have the same notation as in section 4.2.1.

For *big phase fluctuations* ($|\Delta\phi| > \pi$), the sinusoidal error signal inverts its sign and the feedback will increase the phase difference to relock again at 2π distance. The locking point thus jumps whenever the phase difference exceeds π (phase slip), limiting the total locking range to $\pm\pi$.

The advantage of an analog mixer is its fast response and its low noise.

4.2.3 Digital Phase and Frequency Detector

For the gravimeter, the phase lock relies on a digital Phase and Frequency Detector (PFD) integrated in a single chip (ON SEMICONDUCTOR MCH12140). This chip compares the digitalized RF and LO signals and generates an output signal on its two output channels UP and DOWN, if the phase or frequency of both signals differs. The pulse difference of the rising edges of both signals is directed to channel UP, if the LO phase is leading and to channel DOWN, if the RF phase is leading. In this way, the smoothed (low pass filter) difference between both channels is positive in one case, negative in the other and zero for zero phase difference (for details see [126]). Obviously, the proportional dependence on the phase difference of the output voltage holds only in the range $|\Delta\phi| < 2\pi$, where we can again write

$$e(t) = k_{PD} (\phi_{LO}(t) - \phi_{RF}(t)) . \quad (4.21)$$

For differences in frequency, the chip again puts the signal on either UP or DOWN channel, depending on which frequency is higher to be able to correct also for frequency deviations and to ensure a big capture range. The digitalization brings about certain introduction of noise (aliasing effect, AD converter), which though is below our requirements.

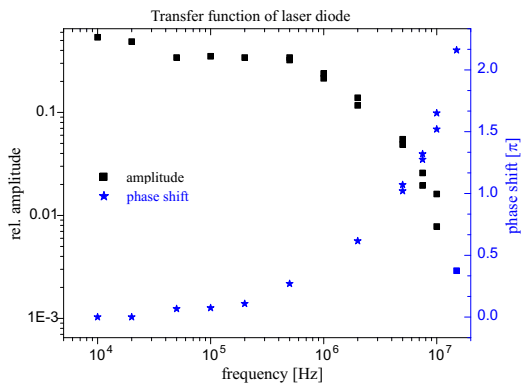
4.2.4 Digital Phase Difference Counter

The heart of the digital PD at the gradiometer is a Phase Difference Counter (PDC), included together with other logic on a programmable chip (ALTERA EPM7064-J44).

The initial position of the counter is in the center of its range. It will count upwards with every RF pulse and downwards with every LO pulse and goes into saturation, once reached its limits. Its output voltage is proportional to the difference to the initial value. We use an 8 bit counter (counts from 0 to 256 with initial position 128). the filtered output signal will have a linear slope over a phase difference of $\pm 128 \cdot 2\pi$; which in our case is reduced to $\pm 112 \cdot 2\pi$ for technical reasons. The PDC thus keeps the phase lock for fluctuations up to $\pm 112 \cdot 2\pi$ and then goes into saturation, where it is still able to recapture the lock. The gravimeter uses a combination of an analog and digital phase detector (see section 4.4.4).

4.2.5 Locking bandwidth and capture range

The locking bandwidth f_{BW} of a phase-lock is limited by the time delay τ , which the signal acquires during one loop: $f_{BW,\max} < \frac{1}{2\tau}$. A major part of the delay is caused by the laser diode. The picture on the right shows a typical measurement of the phase delay of a diode⁶. The locking bandwidth should be more or less 3-5 times the RF linewidth to be able to lock a large fraction of the total power.



If the lasers show a frequency difference Δf , a phase difference of 2π is acquired in a time $T = 1/\Delta f$. In the case of an *analog PD* with its sinusoidal response, the error signal will average to zero during this time. If we want to catch the lock, our loop needs to recapture the frequency to stop the phase deviation before it arrives at 2π . This means that we need a locking bandwidth (unity gain frequency) of $f_{BW} \approx \Delta f_{max}$, or, the other way round, our *capture range* Δf_{max} is no bigger than the locking bandwidth f_{BW} .

The capture range of the saturating *digital PD* is limited on one side by the LO frequency and on the other side by the working range of the PD.

⁶The measurement has been done by recording the transmitted light when the laser is locked onto the slope of a Fabry-Perot line. A fast oscillation imposed on the laser frequency will express as a modulation of the transmitted light, whose delay can be compared to the original oscillator signal. For equal path lengths before the mixer, the delay will be the one of the laser current driver plus diode.

4.3 Frequency control for gravimeter

The setup of the frequency control system was one of the main topics during of the work on the gravimeter. The ambition to use no more than two lasers for cooling, repumping and to drive Raman transitions makes it necessary to develop a reliable electronic control system to ensure the necessary detuning [124]. The scheme we realized is sketched in Fig. 4.7. Many of the components are assembled in a box, shown in Fig. 4.8.

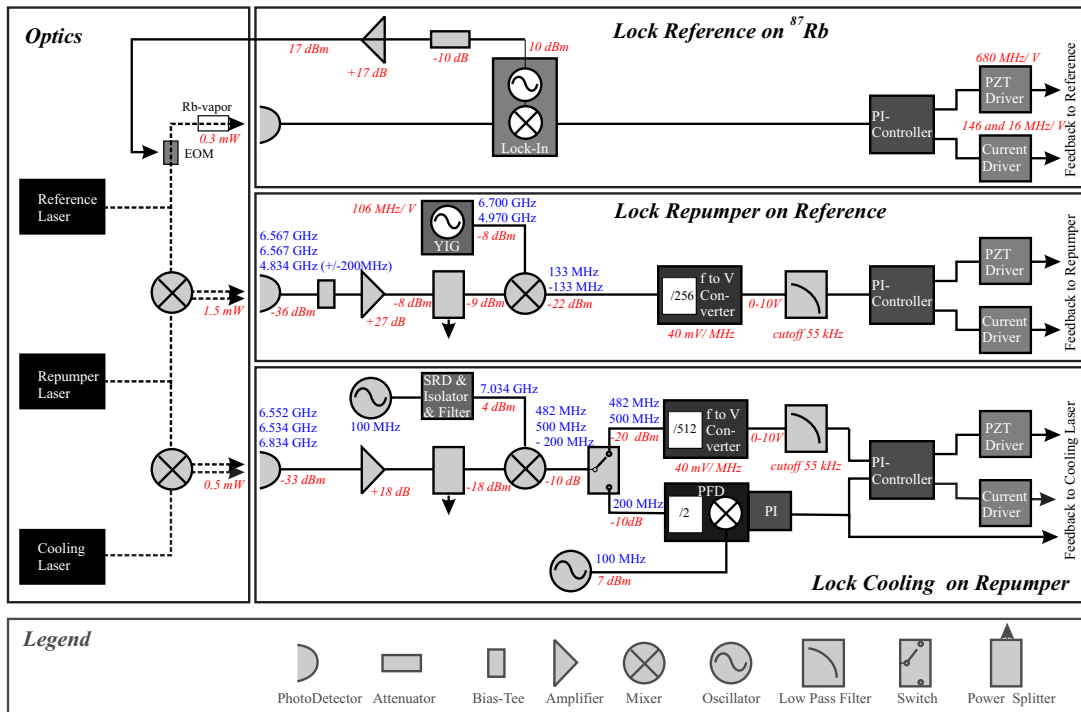


Figure 4.7: Electronic scheme of the three frequency locks for the gravimeter. The reference laser is locked on Rb vapor with FM-spectroscopy, the repumper is frequency-locked onto the reference laser and the cooling laser is frequency- or phase-locked on the repumper. Repumper and Cooling laser also serve as Raman lasers in the phase-locked mode.

4.3.1 Lock Reference Laser on rubidium transition

The reference laser is locked to the $^{87}\text{Rb} |5S_{1/2}, F = 2\rangle \rightarrow |5P_{3/2}, F' = 3\rangle$ hyperfine transition. The spectroscopy cell is magnetically shielded to prevent Zeeman-shifts and broadening of the line. All further lasers are locked relative to this well defined frequency by beat signals.

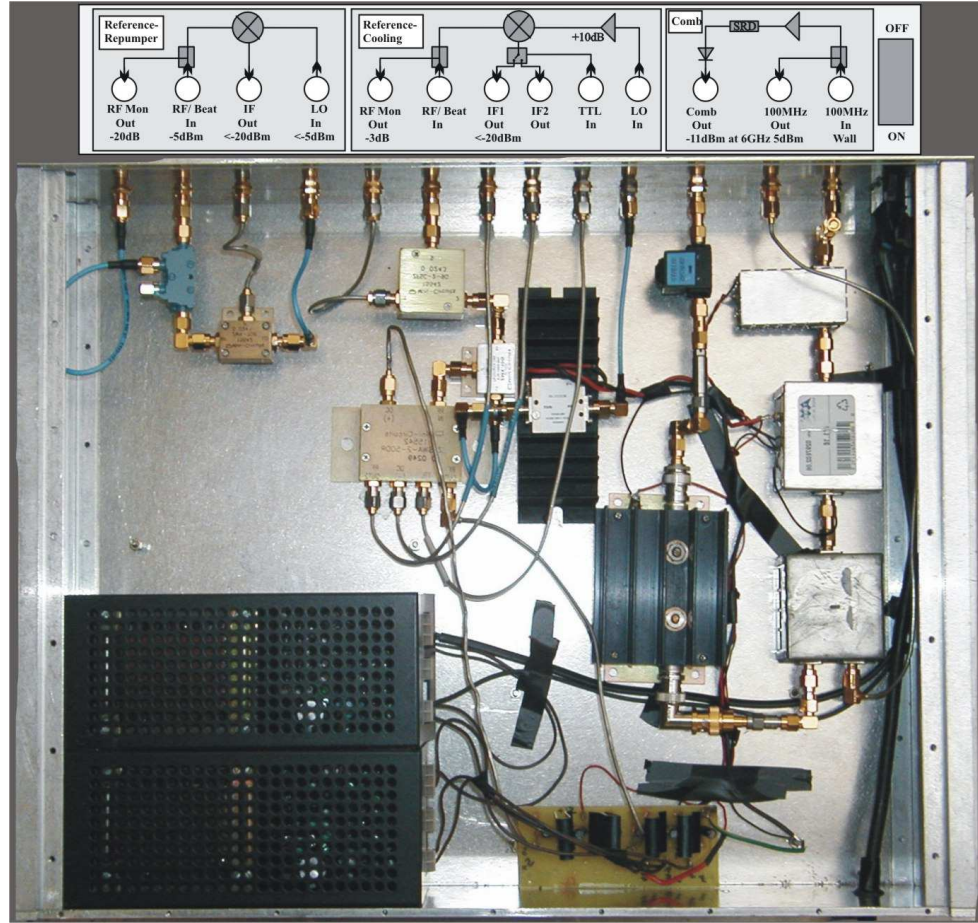


Figure 4.8: Box including electronic components for frequency locks at the Watt-balance gravimeter.

FM-spectroscopy: An electro optical modulator (EOM, New Focus 4001) modulates the phase of the reference beam with $\omega_m = 5$ MHz before entering the vapor cell. The signal of the saturated absorption spectroscopy (see section 4.1.1) is detected by a polarized passive photo-detector (photo-diode: HAMAMATSU 5973). Its AC-output is filtered with a first order high pass filter with cutoff frequency of 330 kHz. The signal is fed into a Lock-In amplifier, where it is amplified and demodulated by the same 5 MHz oscillator, which is also used to supply the EOM. The signal, which supplies the EOM is amplified to reach the desired modulation depth (EOM: 0.15 rad/V) of around 0.5 rad ($\approx 90\%$ of power in carrier, 10% in 1st order sidebands).

Feedback: The demodulated signal is delivered to a PI-controller, which sends the integrated and amplified signal to the current-driver of the laser (conversion of 146 MHz/V, optional 16 MHz/V) and the doubly integrated and amplified signal to the PZT-driver (conversion of 680 MHz/V). The locking bandwidth of the reference laser is 160 kHz, limited by the filtering of the $2\omega_{\text{LO}} = 10$ MHz component, but could

principally be extended some more by optimizing the filters of the loop.

4.3.2 Lock Repumper on Reference

Since the repumper will serve not only as repumper but also as Raman laser, it will have to be detuned by about 2 GHz between the release of the atoms and the first Raman pulse within a time of about 20 ms. The beat signal at the difference frequency between reference laser and repumper needs to be locked to an oscillator, which must be tunable by 2 GHz. To prevent the laser from mode-hopping during the frequency change, the laser current must be corrected during the sweep to remain in the middle of the laser's mode-hop free tuning range.

Detection: The beat signal between the repumper and the reference laser of either 6.567 GHz (cooling and repumping) or around 4.834 GHz (Raman pulses) is detected by a fast photodiode (HAMAMATSU G4176), which is polarized with 9 V from a battery via a Bias-Tee (PULSAR BT-26-463115). After amplification (AML 48L2701), a small part of the beam is split for monitoring by a directional coupler (BROADWAVE TECH. 251-014-020), and the rest is mixed (MINI-CIRCUITS ZMX-7GR) with a signal from a tunable microwave oscillator.

YIG: The tunable microwave oscillator is based on a YIG (Yttrium iron garnet) sphere, which shows low phase noise (<-100 dBc/Hz at 10 kHz), linear tuning and low frequency drift (3 MHz over 70°C). However, the YIG will in future be locked on a stable absolute reference. Our YIG (MICROWAVE Inc. MSO-0307-1) is tuned by a current, which is provided by a modified laser current driver. The laser current driver either delivers a fixed, very stable current equivalent to a YIG frequency of 6.7 GHz plus an optional (less stable) offset controlled by a computer voltage (equivalent to about 4.97 GHz) or – with minor changes of the controller – can be switched between two stable current values by a TTL signal. In the first case, the tuning by a computer-controlled voltage (0-10 V) has a conversion factor of 106 MHz/V.

Frequency to Voltage converter: After the mixing with the YIG, the signal either has a frequency of (6.7-6.567 GHz)=133 MHz or of (4.97-4.834 GHz)=133 MHz. This frequency is divided by a factor of 256 down to 520 kHz, which comes to lie in the middle of the frequency range of 0 to 1 MHz of a frequency to voltage converter (ANALOG DEVICES AD650) with a conversion factor of 10 V/MHz.

In section 4.1.5, we have seen that the output signal of a f-to-V converter will show a ripple at the frequency of the input signal. The faster the desired reaction of the converter, the bigger the ripple will grow. Our requirements of first, a capture range of at least 100 MHz, second, a resolution of at least 100 kHz and third, a locking bandwidth of at least 10 kHz to compensate for acoustics, lead to a design of the converter that results in a cutoff frequency at 23 kHz and a ripple bigger than 500 mV at the signal frequency around 500 kHz. This ripple is equivalent to a frequency

fluctuation of $(0.5 \text{ V} \times 100 \text{ kHz/V} \times 256 =) 12.8 \text{ MHz}$ at 500 kHz.

Bessel-Filter: To cut the ripple above 300 KHz efficiently without changing the amplitude or phase of the signal within the locking bandwidth too much, we designed a 4th order Bessel filter [123] with cutoff frequency at 55 kHz. In this design a ripple at 300 kHz is already suppressed by 45 dB. This reduces its amplitude from 500 mV to 2.8 mV, which is equivalent to a sufficiently low residual frequency fluctuation of 72 kHz. At the same time, the phase shift of this filter at 10 kHz is only 23 degrees.

Feedback: The signal from the converter is compared to an offset voltage around 5 V from the computer and the laser will catch the lock anywhere within the capture range of $1 \text{ MHz} \times 256 = 256 \text{ MHz}$. We reach a locking bandwidth of 16 kHz⁷. The beat signal between the reference laser and the repumper shows a FWHM of 270 kHz when locked.

4.3.3 Lock Cooling Laser on Repumper

The cooling laser is locked onto the repumper with a frequency offset between 6.534 and 6.834 GHz. During the cooling, the laser is stabilized by a frequency lock with tunable offset using a frequency-to-voltage converter similar to the one described in the previous section. After the cooling, the frequency lock is converted into a phase lock.

Detection: The detection is done with a high speed detector (NEW FOCUS 1431), the signal is amplified (NEW Focus 1422), split (MINI-CIRCUITS ZFS-2-9G) and sent to a mixer (MINI-CIRCUITS ZMX-10G). The local oscillator signal at 7.034 GHz is generated by a DRO (Dielectric Resonance Oscillator), locked to a stable 100 MHz signal. A switch (MINI-CIRCUITS ZASWA-2-50DR), controlled by a TTL signal directs the signal to either the frequency-to-voltage converter or to the phase and frequency detector, which will be described in section 4.2.3.

Frequency Lock: During the cooling process, the beat frequencies lie between 480 and 500 MHz, which after a division by 512 result in frequencies between 900 and 1000 kHz. These frequencies are converted into a voltage by a f-to-V converter, whose ripple is filtered with a 4th order Bessel filter (see Lock Repumper on Reference). The signal is compared to a variable offset voltage to control the lock frequency.

Phase-Lock: During the frequency scan, the cooling laser stays frequency-locked to the repumper, and when we actually switch from frequency- to phase-lock, the frequency is already at exactly the hyperfine transition frequency of 6.834 GHz and the phase-lock catches rapidly. The switching is done with a TTL signal by directing the mixer output signal - in this case 200 MHz - to the PFD (see section 4.2.3) instead of to

⁷At 16 kHz, phase shift of 1st order filter in converter is -27° , of 4th order Bessel filter -43° and of PI-controller -90° , which makes -160° .

the f-to-V converter. The local oscillator of the PFD will in future be a Direct Digital Synthesis oscillator (DDS, ANALOG DEVICES, AD 9852). The phase-lock has not been fully implemented during my stay in France but has meanwhile been installed, tested and optimized. The error signal indicates a noise contribution of less than 1 mrad to the interferometer phase.

Feedback: The current feedback of the phase-lock is added to the supply current directly at the laser, whereas the frequency lock adds the feedback to the current-controller unit. In contrast, both locks have a common PZT-line. The feedback signals are added in the PI-controller of the frequency lock before the last integrator. During the short switching process, the charge of the integrator remains and ensures a smooth switching without any frequency hop. In frequency-locking mode, we achieve a locking bandwidth of 18 kHz and the beat signal has a FWHM of 460 kHz.

Frequency scan: The desired frequency sweep between the cooling stage and interferometer stage is determined by a programmable computer output voltage. To avoid abrupt frequency changes, the voltage has the form of a smooth sinusoidal ramp. The YIG will follow this ramp with its frequency that in turn determines the difference between reference- and cooling laser, since this difference is locked onto the YIG frequency. If the lock tries to stay behind the frequency change of 2 GHz, it is probable that the laser will mode-jump. What we do to prevent this jump is to change the current and PZT offset during the scan in a controlled way, such that the laser already follows the YIG frequency quite well even without activated lock. Figure 4.9 shows the effect of this offset by demonstrating the small error signal in spite of the big detuning of the YIG. The remaining frequency error is mainly due to a slow thermal response of the laser to a current change. When switching the lock on, the error signal is added to the offset voltage and the electronics just has to compensate for small frequency

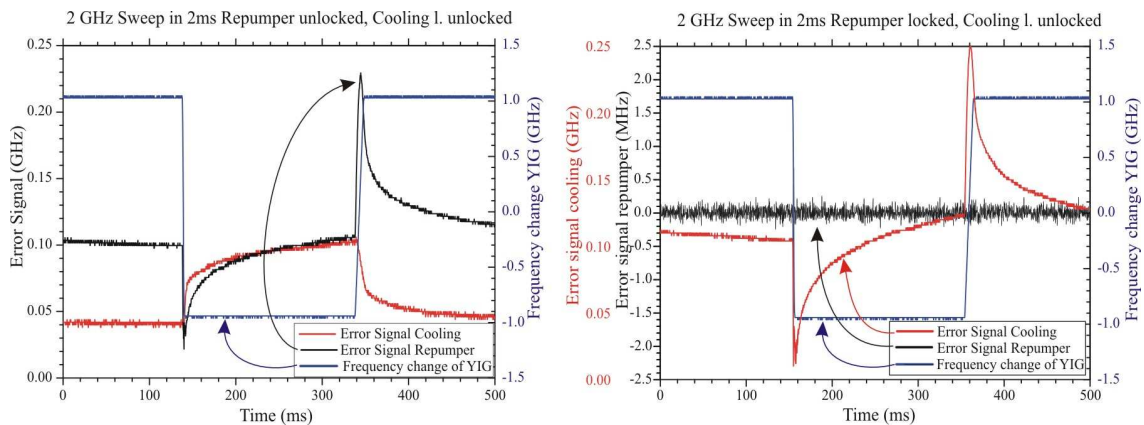


Figure 4.9: Frequency deviation of lasers from the YIG frequency during a sweep of 2 GHz in 2 ms. Left: both lasers are unlocked, frequency is regulated by a signal to current and PZT. Right: Repumper is locked and cooling laser unlocked.

deviations. The repumper is stabilized onto the cooling-laser, it also has to follow the ramp and obviously it will receive similar current and PZT-offsets to stay far from any mode-hops. In the left picture of Figure 4.9, both lasers are unlocked and one can see the slightly different sweep behavior of the YIG and the laser, whereas in the right picture the repumper is already locked to the YIG and only the cooling laser follows without active feedback.

In Figure 4.10 (left), the feedback was added also to the cooling laser and one observes a small spike on the error signal of ± 1 MHz during the scan. This spike grows to ± 2.5 MHz, when the scan is accelerated from 2 ms to 0.8 ms duration (see Fig. 4.10, bottom). The rms frequency noise of the error signal is 150 kHz for the repumper and 210 kHz for the cooling laser. The swinging of the Piezo crystal emerges from the noise when averaging the signal, as can be seen in Fig. 4.10. The PZT resonance frequencies are 1.8 kHz for the repumper and 1.3 kHz for the cooling laser. The lasers stay locked very reliably for long periods of fast frequency sweeps. A typical picture is shown in Fig. 4.10, bottom.

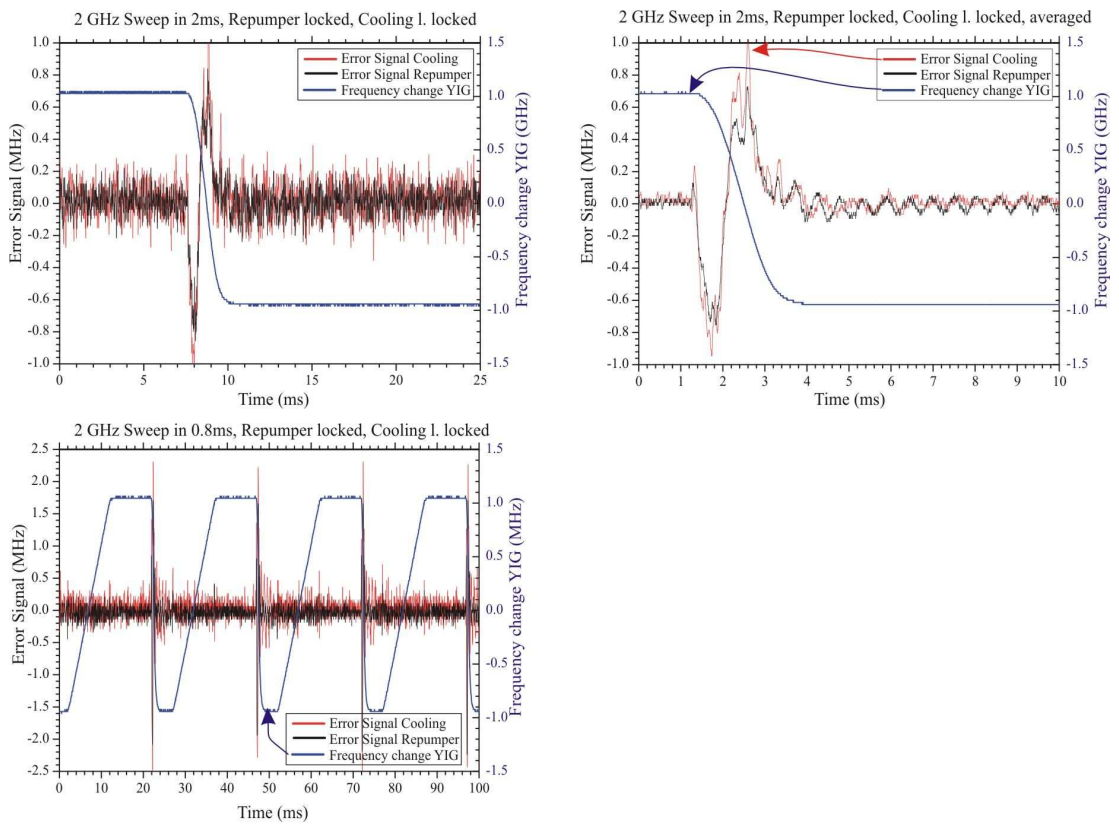


Figure 4.10: *Top: Frequency deviation during sweep of 2 GHz in 2 ms, both lasers with active feedback. Left: Frequency noise during sweep, right: averaging the signal 64 times let Piezo-oscillations emerge from noise. Bottom: Frequency error during repeated 2 GHz sweeps in 0.8 ms.*

4.4 Frequency control for gradiometer

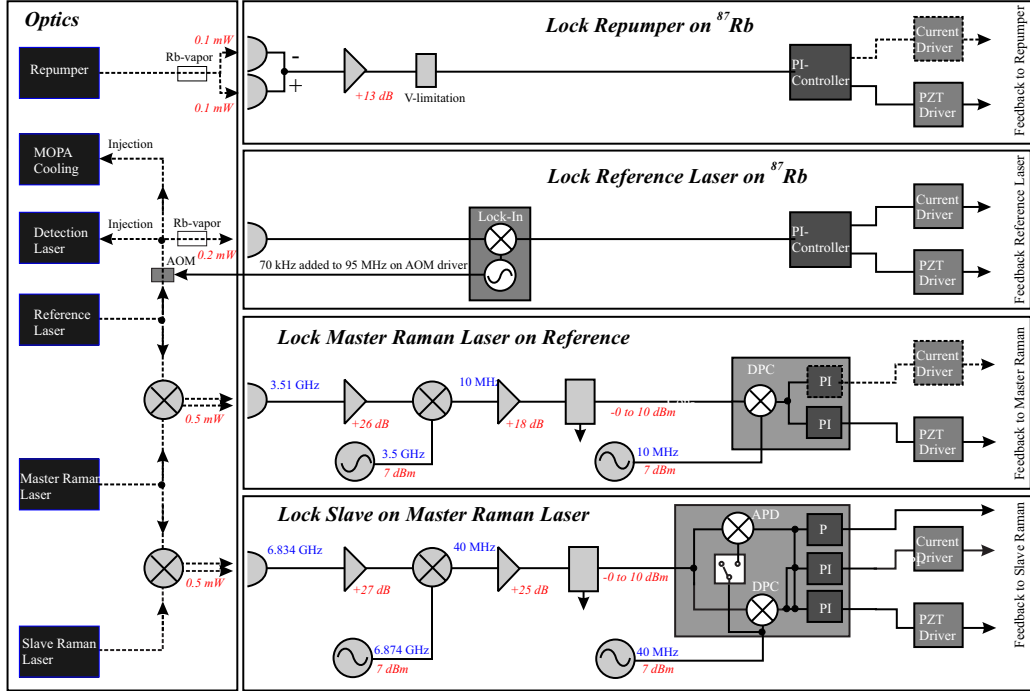


Figure 4.11: Electronic scheme of the frequency stabilization for the gradiometer lasers. The repumper and the reference laser are locked on Rb transitions; the cooling and detection lasers are injected by the reference laser. The Master Raman laser is loosely phase-locked to the reference laser with a difference of 3.5 GHz and the Slave Raman laser is phase-locked onto the Master with a difference frequency of 6.8 GHz. Symbols are identical to Fig. 4.7.

4.4.1 Lock Repumper on rubidium transition

The repumper laser is locked with an offset onto the crossover-transition CO 1-01 with the Doppler free DAVLL (see section 4.1.3). Two photodiodes register the two relatively shifted spectroscopy signals and subtract them. The voltage limited signal is fed into a PI-controller and gives feedback to the PZT with a locking bandwidth (BW) of 1 kHz and optionally to the current controller (BW around 10 kHz). The absolute frequency stability is better than 500 kHz.

4.4.2 Lock Reference Laser on rubidium transition

The reference laser is locked to the rubidium $F = 2 \rightarrow F' = 3$ transition with the Lock-In technique (see section 4.1.1). A modulation of 70 kHz is imposed onto the

pump and probe beam of a saturated absorption setup by an AOM in double pass, who, at the same time, shifts the light by -184 MHz (see section 3.3.2). The locking bandwidth of the PZT feedback is 1 kHz and of the current loop around 12 kHz, which stabilizes the laser frequency to around 150 kHz.

The reference laser injects the cooling laser (MOPA), which is split into two parts, each independently controlled in frequency by an AOM. Each part is split into three beams (see section 3.3.5), which serve as upper and lower trapping and cooling beams. During the MOT, both AOMs shift the light by the same frequency, which is given by one single voltage controlled oscillator (VCO). With the start of the launch, a switch assigns the frequency control to two phase-locked frequency generators (AGILENT 33120A). The difference between both frequencies determines the launch velocity of the cloud and their common center frequency the detuning from resonance. A trigger (FSK) can switch both frequencies to a second value to increase the detuning during the cooling.

The detection laser is locked by injection to the frequency of the reference laser.

4.4.3 Lock Master Raman laser

A fast NEW Focus 1580 12 GHz photo-detector registers the beat signal between the reference laser and the master Raman laser, which is then mixed (MITEQ DM0104LA1) with a LO (MARCONI 2024) at 3.3 GHz (1.1 GHz in third harmonic) down to an intermediate frequency of 10 MHz. After amplification (MINI-CIRCUITS ZFL 1000LN), this signal enters a PDC (see section 4.2.4), where it is compared to a 10 MHz signal and converted into a correction voltage. The phase-lock is very loose and gives feedback only to the PZT within a band of 1 kHz.

4.4.4 Phase-Lock Slave Raman laser

We detect the beat signal between master $A_{L1} \cos(\omega_{L1}t - \phi_{N,L1}(t))$ and slave $A_{L2} \cos(\omega_{L2}t - \phi_{N,L2}(t))$ laser. We use the notation introduced in (4.11) and (4.12), set the offset $\phi_{L1,0} = \phi_{L2,0} = 0$ but consider the noise terms $\phi_{N,L1}$ and $\phi_{N,L2}$ so that the beat signal is:

$$\frac{A_{L1}A_{L2}}{2} \left(\underbrace{\cos((\omega_{L1} - \omega_{L2})t + (\phi_{N,L1} - \phi_{N,L2}))}_{=\Delta\omega_L} + \underbrace{\cos((\omega_{L1} + \omega_{L2})t + (\phi_{N,L1} + \phi_{N,L2}))}_{=\Delta\phi} \right) \text{ filtered out} \quad (4.22)$$

This beat has a frequency of $\Delta\omega_L = 6.834$ GHz and is recorded with a photo-detector (NEW Focus 1002, 60 GHz). The signal is amplified (JCA 48-301) and mixed (mixer MITEQ M0408) with a signal generator (ANRITSU MG3692A, ultra low phase noise option) down to an intermediate frequency of $\Delta\omega_L - \omega_{LO} = 40$ MHz according to

(4.19)⁸ what results in:

$$A \cos((\Delta\omega_L - \omega_{LO})t + (\Delta\phi - \phi_{LO})). \quad (4.23)$$

We already cut out the filtered term at frequency $\Delta\omega_L + \omega_{LO}$.

After splitting (MINI-CIRCUITS ZFDC-10-2) and a further amplification (MINI-CIRCUITS ZFL-500LN) the signal is registered by a combined analog and digital phase detector. An AGILENT 33250A 80 MHz arbitrary waveform generator, whose internal quartz oscillator is phase-locked to the ANRITSU oscillator, provides the LO signal at about 40 MHz.

Combination of analog and digital phase detector: For the gradiometer, a joint digital and analog phase detector has been designed by Marco Prevedelli [128]. It has the ambition of combining the advantage of velocity and low noise of an analog mixer on the one hand with the big capture range for phase and frequency of a digital system on the other hand. The PDC described in section 4.2.4 is used in parallel to an analog mixer. As long as the phase difference $\Delta\phi$ is bigger than π , the PDC is active and generates an error signal. In this stage, the LO signal leading to the analog mixer is switched off by the PDC chip. As soon as the phase difference $\Delta\phi - \phi_{LO}$ is equal or smaller to π , the PDC itself delivers signal zero and switches on the LO for the analog mixer, adding the 90° phase shift this mixed requires. In this case, only the analog part is active and delivers an error signal to the feedback electronics.

Feedback to laser: The error signal of the PD is split into three different paths. The first path delivers low frequency feedback ($f < 1$ kHz) onto the Piezo-crystal (PZT) with a conversion of around 400 MHz/V. The signal is integrated twice and the gain matched. The second path (gain and integration) leads to the current driver and covers the mid-frequency feedback between approximately 1 and 800 kHz. The conversion is around 10 mA/V \times 100 MHz/mA. The third part is delivered only by the analog phase detector and is added directly to the laser current for a feedback up to a few MHz. To compensate for delay, a phase advance is introduced in this branch.

⁸The reasons for using an intermediate frequency are the following: 1) Our DPC works only for input signals between 20 and 90 MHz, 2) the Anritsu is not capable of phase continuous sweeps, which will be necessary, 3) the generation of exactly the resonance frequency will emit radiation and might drive unwanted hyperfine transitions between the ground-states.

4.4.5 Noise on phase-lock

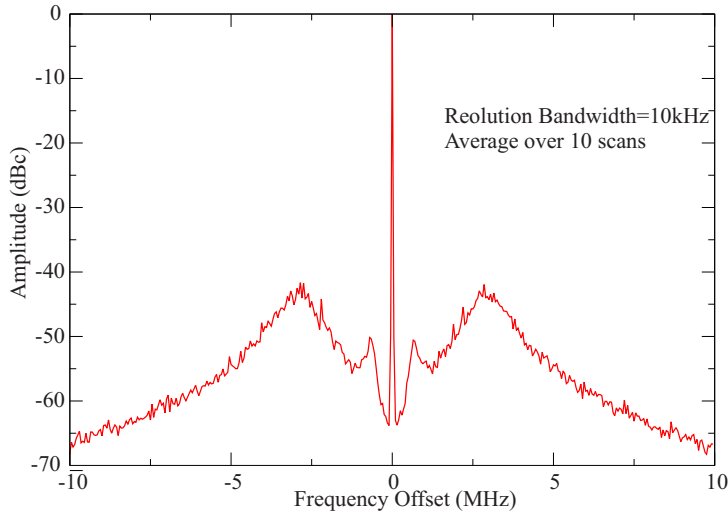


Figure 4.12: Beat signal of the Raman lasers, recorded by a spectrum analyzer. Clearly visible is the strong noise suppression of the mid-frequency current feedback up to the servo bump at 800 kHz. The high frequency loop determines the total bandwidth, which is of 3 MHz during this particular measurement. The amplitude suppression at a certain frequency f relative to the carrier must be divided by the resolution BW (here 10 kHz) and multiplied by 1 rad^2 to obtain the phase noise in rad^2/Hz .

The phase noise on the laser beat note transfers to the interferometer signal with a certain weight according to the description in section 2.3.2 and 2.3.3. Phase noise on the Raman lasers can not be distinguished from accelerations of the atoms and therefore leads to a systematic error of a gravimeter. In contrary, the *difference signal in a gradiometer measurement with two clouds suppresses laser phase noise*. However, considering the possible use of the gradiometer also as a gravimeter, we put severe restrictions on the phase noise, which should not exceed few mrad integrated over the relevant frequencies. Figure 4.12 shows the power spectrum of our phase lock, and the corresponding spectral density of the phase noise is found in Fig. 4.13. One recognizes the bumps at the bandwidth of the mid- and high frequency branch of the PLL.

The most important contributions to the noise on the Raman lasers originate in:

- *Local oscillator:* Local oscillator noise transfers 1:1 onto the laser signal within the locking bandwidth, because there is no way of compensating for it without a comparison to a better oscillator. The high-frequency LO of the gradiometer is an ANRITSU MG3690B, its SSB phase noise is measured by comparison with two equal units (see Fig. 4.13, right).

The measurement shows big noise at low frequencies due to a bad internal oscillator. In our case, we lock the Anritsu onto an external 10 MHz oscillator but

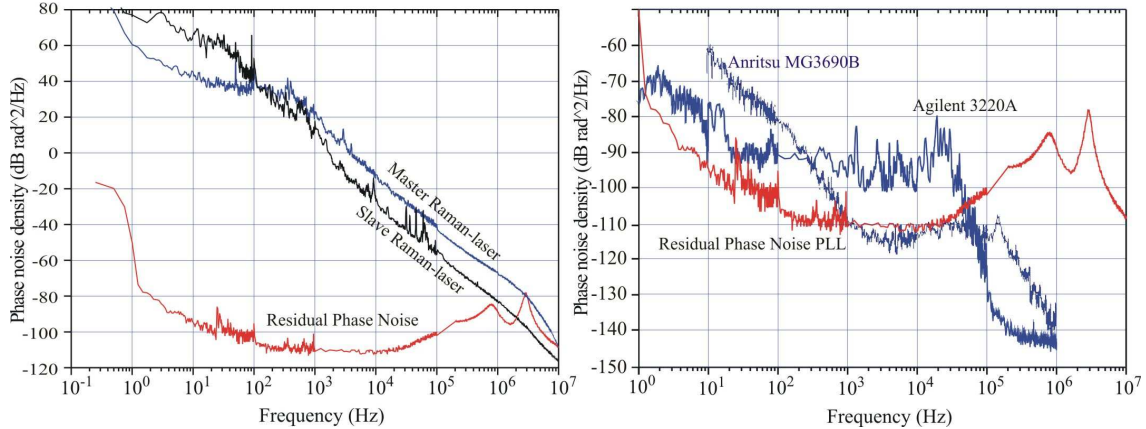


Figure 4.13: Left: Free running phase noise density of the two Raman lasers (extended cavity length: 1 and 2 cm, respectively). The lasers were loosely locked onto the side of a fringe of a Fabry-Perot cavity and the noise on the transmitted signal was converted into first frequency noise and then phase-noise. The lower curve is the residual phase-noise on the lock signal and one can see the strong suppression of the initial noise. The plateau at around -110 dB rad²/Hz is limited by amplitude fluctuations of the light and above 10 kHz by insufficient loop gain. Right: Phase noise of either LO Anritsu MG3690B and LO AGILENT 33250 exceed the residual phase noise of the PLL.

did not measure its noise. For better stability, the Anritsu will in future be substituted by a frequency chain based on one (10 MHz) or two (10 & 100 MHz) quartz oscillators. This HF-source mixes down the beat signal to an intermediate frequency, which is then mixed with the second LO, an AGILENT 33250A, which unfortunately has extremely bad noise characteristics (see Fig. 4.13, right) even at higher frequencies. We will either substitute the bad internal PLL, which locks its 800 MHz oscillator onto a (in this case external) 10 MHz signal or will be substituted in future by a DDS (AD 9854, setup by M. Prevedelli).

- *Phase-locked-loop:* Noise sources within the loop are suppressed with the closed loop gain $k_{PD}k_l$ (see section 4.2.1 and Fig. 4.13). Since this gain is finite, all noise sources like e.g. laser current noise, intrinsic laser phase-noise, amplifier noise or Johnson noise should be reduced as far as possible. Following advices from the Paris gravimeter group, low frequency noise could be further reduced by a higher LO level on the PLL, mid frequency noise by a higher light-power level on the PD and high frequency noise by introducing a further (third) integrator into the feedback-loop.
- *Tapered Amplifier:* The tapered amplifier in the beam path (see Fig. 3.8) is injected by both lasers. Amplitude fluctuations as well as mechanical or thermal noise can translate into phase noise to a certain amount. We measured a

noise contribution at frequencies around 100 Hz. We will in future add a low frequency feedback to the Piezo to correct for those fluctuations.

- *Beam path:* The displacement of a mirror by a distance Δs results in a phase change of the beat signal between laser 1 and laser 2 by $\Delta\phi = (k_{L1} - k_{L2})\Delta s$. With our effective wave-vector for co-propagating beams $k_{\text{eff}} = k_{L1} - k_{L2} = 142 \text{ rad/m}$, a displacement of $7 \mu\text{m}$ signifies a phase-change of 1 mrad. We can convert acceleration noise (S_a in $[m^2/s^4/\text{Hz}]$) into phase noise with the relation S_ϕ in $[\text{rad}^2/\text{Hz}]$: $S_\phi = k_{\text{eff}}^2/\omega^4 S_a$. We did not yet measure horizontal accelerations as we did for vertical ones; but if we assume same amplitudes, the effect of mirror vibrations can have a big effect – without vibration isolation of the optical table. Also air fluctuations caused by the air-conditioning will have similar effect (see Figure 4.15).

Further disturbances could originate in dispersive elements in the beam-path like the rubidium vapor cell and the optical fiber. We could not measure any significant contribution to the phase-noise, which would be visible on the big background.

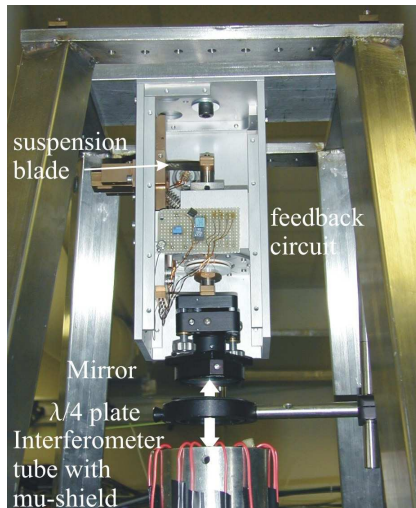


Figure 4.14: Vibration isolated upper mirror to reflect the Raman beams. The mirror is suspended by a curved metal-blade and a feedback loop can be closed by sending current through coils whose magnetic field induces a displacement of the mirror. At the moment, the feedback is deactivated.

- *Upper Mirror:* If both lasers are superimposed, all fluctuations are converted into phase with $\Delta\phi = (|k_{L1}| - |k_{L2}|)\Delta s$. If the paths are separated, the fluctuations convert into phase with $k_{\text{eff}}\Delta s = k_{L1,L2}\Delta s$, which is a factor of 10^5 bigger. Unfortunately, the beam paths have to be separated at a certain moment, because, as we have seen in previous chapters, the atoms need to absorb one photon from below and one from above, what implies a separation of both beams. In our case, the only element which affects just one beam is the mirror above the interferometer region. We received an isolation platform from the VIRGO project in Pisa that we adopted to hold our mirror, who is suspended by a blade with a resonance frequency of 2 Hz. In a later stage, an accelerometer can be fixed

to the mirror and the feedback loop of the platform can be activated to actively suppress vibrations.

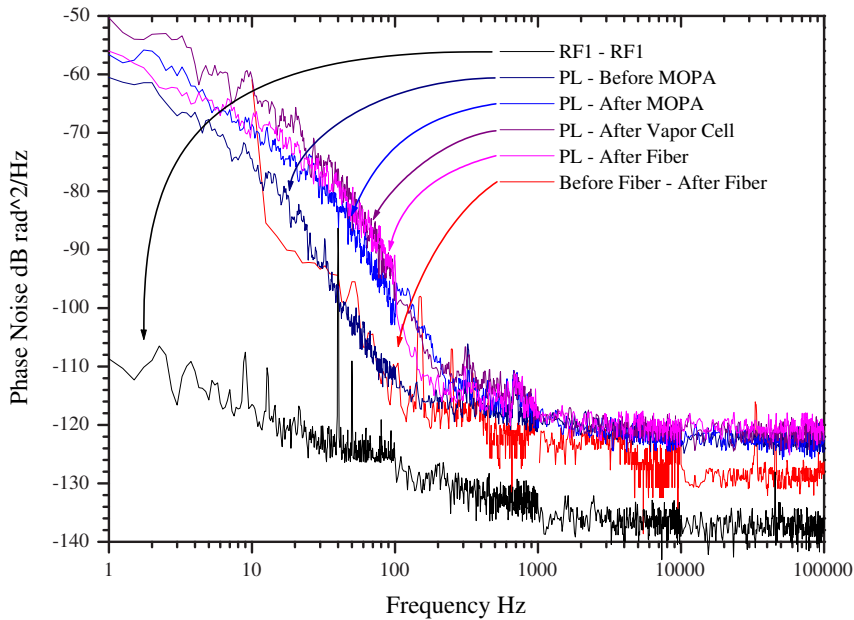


Figure 4.15: Measurement of relative phase noise introduced on the Raman laser beam path at various places. The MOPA introduces noise at low frequencies. At high frequencies we reach the plateau of the white noise of the detection system. The huge noise at frequencies below 300 Hz is not fully understood and is investigated further.

Figure 4.15 shows a measurement of the phase noise, introduced on the beam path. Figure 4.16 demonstrates the setup for the measurement showing the components used. The spectra were recorded by a Fast-Fourier Transform Analyzer (HP 3561A) in dB V/ $\sqrt{\text{Hz}}$ and are converted into dB rad²/Hz each with its according conversion factor C ($S_\phi[\text{dB rad}^2/\text{Hz}] = S_V[\text{dB V}/\sqrt{\text{Hz}}] - 20 \cdot \log C [\text{V}/\text{rad}]$).

The lowest curve in Fig. 4.15 (RF1-RF2) is obtained by mixing a RF signal of 6.8 GHz with itself and shows basically the noise of the mixer (see Fig. 4.16). The curve (PL-Before MOPA) is the beat of the Raman lasers we use for the lock (PL) with the same signal recorded with another photodiode about 1 m away from the first one. It shows the noise of both detection systems (detector, amplifier, mixer) at high frequencies but is largely dominated by the vibration-noise of the optical elements at low frequencies as well as by air fluctuations. For the next measurement (PL-After MOPA), the second photodiode is placed behind the MOPA and one notices again a significant increase of the noise between 3 and 300 Hz. After the vapor cell (PL - After Vapor Cell) and after

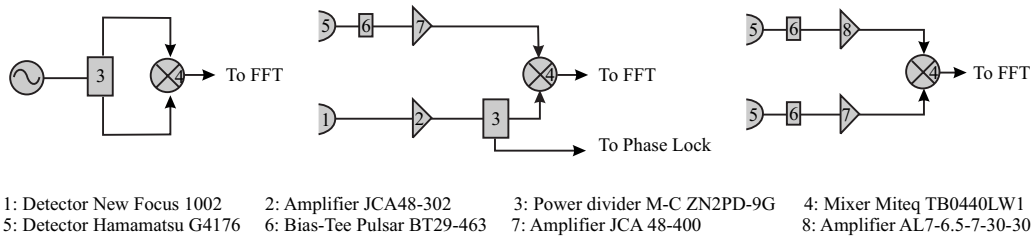


Figure 4.16: Setup for noise measurement of mixer (left), of noise introduced by detection electronics on the beam path (center) and of the noise introduced by the fiber (right).

a 0.5 m long polarization maintaining single-mode fiber (*PL - After Fiber*) no further increase could be measured. To measure the noise of only the fiber, we recorded the difference between one photodiode before and one after the fiber (curve *Before Fiber - After Fiber*). No noise contribution of the fiber could be measured⁹

Conclusion: The contribution of the different noise sources with their spectral phase noise densities S_ϕ (in rad^2/Hz) to the interferometer phase noise is calculated according to (2.121) as

$$\sigma_\phi^2 = \int_0^\infty S_\phi(f) |H(f)|^2 \, df, \quad (4.24)$$

where $H(f)$ is the weighting function of our experiment (2.120) plotted in Figure 2.9. Its weight lies between 10 Hz and 10 KHz.

The measurement curves presented in this section yield the following phase noise $\bar{\sigma}_\phi^2$ between 10 Hz and 10 MHz and its contribution to the interferometer phase noise, weighted with $H(f)^2$, σ_ϕ^2 , all in mrad:

Noise Source	$\bar{\sigma}_\phi^2$	σ_ϕ^2	Comment
Lock	105	1.1	$H(f)$ cuts high noise contrib. above 100 kHz
LO Anritsu HF	4	9	Main contrib. 1Hz-1kHz due to bad internal quartz
LO Agilent RF	2	6	Main contrib. around 10 kHz, amplified by $H(f)$
Beam Path	2.2	4.5	Noise almost all below 300 Hz

The phase-lock itself could still be improved but is already sufficiently good as it is now for the targeted 1 mrad phase noise. The Anritsu oscillator, which supplies the 6.8 GHz, would be fine when locked to a low noise quartz because its noise is mainly at low frequencies; above 1 kHz it would give a contribution around 1 mrad to the interferometer noise. The Agilent local oscillator, which provides the 40 MHz signal,

⁹In this measurement, one observes a lower white phase-noise, which indicates that the photodiodes used in this measurement (Hamamatsu) show less noise than the New Focus detector of our phase-lock signal.

will be changed soon and the noise introduced on the beam path, including vibrations, MOPA, fibre and the upper mirror, is still under investigation.

Chapter 5

Experimental procedure and first results

During the stay at the gravimeter experiment, we set up a 2D-MOT and its characterization will be presented in the first section of this chapter. With the intention to present the 2D-MOT as a closed unit, also its setup and some theoretical tools are part of the description although this might not properly fit into this chapter. The MAGIA experiment (gradiometer) allowed some preliminary measurements and the observation of interference fringes in summer 2004. The single elements of the experiment will be described in the order of their complexity starting from the three-dimensional MOT, mentioning the velocity selection and state preparation and finishing with the observation of Rabi oscillations and interferometer fringes.

5.1 2D-MOT

Both experiments, gravimeter and gradiometer require a *high loading rate* of the MOT:

- *Gravimeter*: The higher the repetition rate of a gravimeter, the faster the integration towards a high precision g -value can proceed. The integration velocity is important to resolve temporal varying accelerations originating for example from tides, air pressure changes or movement of nearby masses. A high repetition rate of > 3 Hz with a nevertheless high initial number of $N = 10^8$ atoms in the cloud requires an effective loading of the MOT.
- *Gradiometer*: The gradiometer relies on a simultaneous measurement on two atom-clouds at different positions. The time between the two launches is of the order of 100 ms or less, which leaves little time for trapping the atoms of the second cloud. Because the desired resolution per shot requires an initial number

of 10^8 to 10^9 atoms in each cloud. Again, an effective loading of the MOT is a crucial experimental requirement.

In an interferometer, *ultra-high vacuum conditions* are required to minimize deleterious interactions with the background vapor, which additionally can cause phase fluctuations of the Raman laser beams. This requirement is opposed to a fast loading of the MOT, where a high background pressure is advantageous below the limit where collisions dominate. As a consequence, it is desirable to have a region dedicated to the production of a beam of cold atoms, which will feed the MOT. These requirements are met by the following techniques:

1. *Zeeman-Slower*: A Zeeman slower decelerates a beam of thermal atoms along the propagation axis by radiation pressure, while spontaneous emission processes give rise to a transverse heating of the atoms. This results in a strongly diverging beam with a flux of up to 10^{11} atoms/s with a mean velocity down to 20 m/s. In our case, the geometrical size of this slower does not fit into the gravimeter experiment and would confine the transportability of the gravimeter. In addition, the strong magnetic fields and the broad beam on axis are disadvantageous.
2. *3D-MOT Sources*: MOT sources provide better collimation of the beam, are smaller and have a lower background of thermal atoms. Atoms can be extracted either pulsed with an integrated flux of up to a few times 10^9 atoms/s or continuous with a dark channel in one of the laser beams. A flux of $5 \cdot 10^9$ atoms/s has been reached with the latter method, called LVIS (Low Velocity Intense Source) [134].
3. *2D-MOT sources*: The approach of using two-dimensional cooling is relatively new [131]. It has the advantage of a simple and compact setup, a high flux of collimated atoms ($\approx 10^{10}$ atoms/s) and the liberty to leave the propagation axis free from light. One can distinguish three variations:
 - (a) *Ordinary 2D-MOT*: The basic setup of a 2D-MOT implies two orthogonal pairs of laser beams to transversally cool atoms in a vapor cell (see Figure 5.1). Four elongated coils provide a quadrupole magnetic field for the MOT with zero field along the z-axis, on which the atoms are confined. They will escape the trap at both sides quickly, since they are not cooled in longitudinal direction; therefore collisions will not limit the flux up to high background pressures. A flux of up to $6 \cdot 10^{10}$ atoms/s has been achieved [133] and geometrical filtering can limit the mean longitudinal velocities to below 30 m/s.
 - (b) *2D-MOT+*: The 'plus' stands for an additional beam pair along the z-axis to cool the atoms also longitudinally. The mean velocity along this axis

decreases to below 10 m/s, which means that more atoms can be captured. But since on the other hand the longer stay in the trap will increase the collision probability, the optimum pressure will be lower than in an ordinary 2D-MOT. This kind of atom source is chosen, when the longitudinal velocity of the atoms is of importance [132]; the flux has been found to be on the order of $\lesssim 10^{10}$ atoms/s.

- (c) *2D-MOT with pusher:* A thin red-detuned pushing beam along the z-axis added to the 2D-MOT will accelerate the atoms towards the hole, particularly those with negative or small longitudinal velocity components. This beam can increase the atomic flux by a factor of 2 to 5 and it is this configuration that we use at the gravimeter and are presently mounting for the gradiometer.

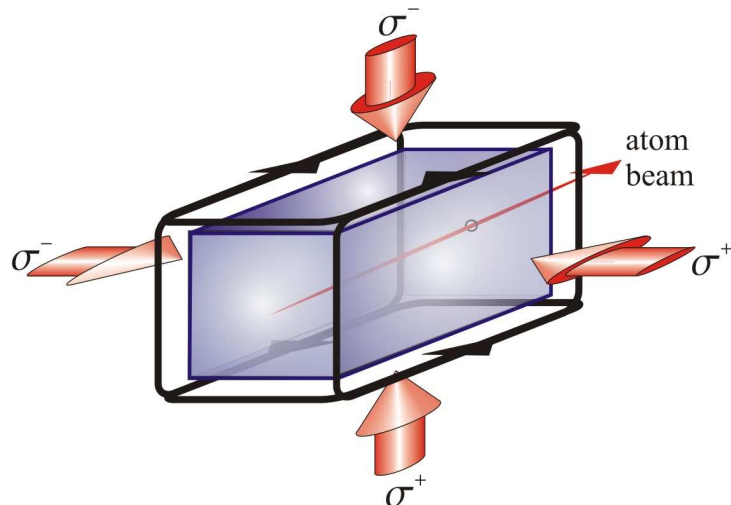


Figure 5.1: Scheme of a 2D-MOT. Atoms in an elongated vacuum cell with a high rubidium background pressure are transversally cooled by 4 laser beams, indicated by arrows. A thin collimated beam of atoms will escape the 2D-MOT on both sides, on one side onto the window and on the back side through a small hole towards the UHV region. The 2D magnetic quadrupole field is provided by 4 coils outside the cell.

5.1.1 Experimental setup

Atoms evaporate from a heated rubidium reservoir and, through a 15 mm diameter tube, access a vapor cell with dimensions of 25x25x90 mm (see Figure 5.2). The cell is machined from titanium and 4 rectangular windows (15x80x3 mm) are glued to its sides for optical access. Two sets of coils are attached to the cell to provide the desired magnetic gradients of about 20 Gauss/cm. Two orthogonal beam pairs of the cooling laser – with the repumper overlapped – enter the vapor cell through the rectangular windows and radially cool the atoms. For the sake of compactness of the optical setup,

each beam is split into three circularly polarized parts with 24.5 mm beam-diameter. An atom beam of about 40 mrad divergence is coupled out through a 2 mm long hole of 1.5 mm diameter at the back surface of the cell.

After the out-coupling, the atom beam passes through a tube of purified graphite with a conical hole for differential pumping, before entering the UHV chamber, whose center is at 38 cm distance from the 2D-MOT.

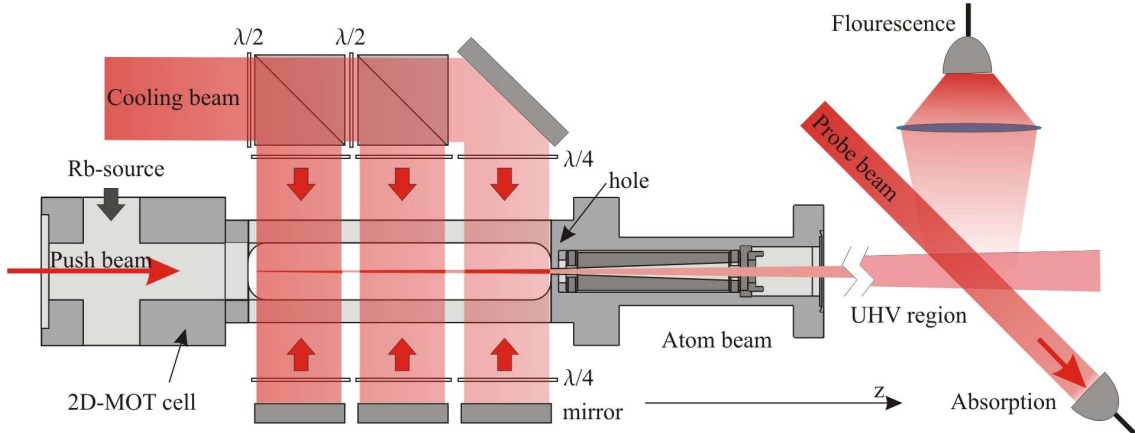


Figure 5.2: Lengthwise cut through the 2D-MOT for the gravimeter. Each of the two cooling laser beams, superimposed with the repumper, is split into three retro-reflected beam pairs to save space-consuming optics for elliptical beams. A push beam augments the atom flux through a hole, which is followed by a conical graphite tube to assure differential pumping between the 2D-MOT cell and the UHV region. After 38 cm of flight, the atom beam is interrogated by a probe beam and analyzed by fluorescence and absorption measurements.

A pushing beam with the same frequency as the MOT beams (red detuned from resonance $F=2 \leftrightarrow F'=3$) enters the cell along the z -axis. It is in resonance with atoms with a certain negative z -velocity component v_z and pushes them back into the opposite direction towards the outcoupling hole. By adding the pushing laser, a notable increase of the flux is achieved, last but not least, because accelerating the slow atoms reduces the possibility that a scattering event will throw them out of the beam. We will see in the following discussion that scattering will be important at the high pressures of the 2D-MOT. The pushing beam is experimentally optimized to a power of $350 \mu\text{W}$ and a diameter equal to the hole diameter. To address efficiently all atoms in the beam, the zero of the magnetic field must be well aligned with the pushing beam.

5.1.2 Tools to describe a 2D-MOT

Capture velocity: The capture radius r_c is usually defined as the position, where the detuning δ of the laser from the atomic resonance is similar to the Zeeman shifted

transition frequency:

$$\delta = \frac{1}{\hbar} \mu_B g r_c \text{ grad}B. \quad (5.1)$$

Our cell allows for a maximum capture radius r_c of about 10 mm.

With a constant cycling rate on resonance $\Gamma = 2\pi \cdot 6$ MHz, an atom with radial velocity component v_r needs the time

$$\tau = \frac{2mv_r}{\hbar k\Gamma} \quad (5.2)$$

to be slowed down to zero velocity by the absorption of $\tau \cdot \Gamma / 4\pi$ photons with momentum $\hbar k$. The fastest atoms to be captured will come to rest only after the transit of the whole capture area $2r_c$ in a time $\tau_{max} = 2r_c/v_c$. With (5.2) follows a maximum capture velocity v_c in our cell of

$$v_c = \sqrt{r_c \frac{\hbar k\Gamma}{m}} \approx 47 \text{ m/s} \equiv v_{c0}. \quad (5.3)$$

Above a critical longitudinal velocity v_z , which we call $v_{z,crit}$, the longitudinal propagation transition time $\tau_z = z/v_z$ will be shorter than the radial transit time τ_{max} and will limit the capture velocity v_{c0} . For a trap length L , the maximum cooling time is reached for atoms at $z = L$. The critical velocity at each position z in the cell is the one for which $\tau_z = \tau_{max}$:

$$v_{z,crit}(z) = \frac{\hbar k\Gamma}{2m} \frac{z}{v_{c0}}. \quad (5.4)$$

For atoms with $v_z > v_{z,crit}$ the radial capture velocity v_c depends on v_z and we can summarize the following position dependent capture velocity:

$$v_c(z) = \begin{cases} \sqrt{r_c \frac{\hbar k\Gamma}{2m}} &= v_{c0} & \text{for} & v_z < v_{z,crit} \\ \frac{\hbar k\Gamma}{2m} \frac{z}{v_z} &= \frac{v_{z,crit} v_{c0}}{v_z} & \text{for} & v_z > v_{z,crit}. \end{cases} \quad (5.5)$$

To describe the asymptotic behavior of the capture velocity, we can model v_c according to [133] as

$$v_c(v_z) = \frac{v_{c0}}{1 + v_z/v_{z,crit}}. \quad (5.6)$$

Description of cloud: We will in the following consider an atom with one ground state and an excited state, which is split into three magnetic sub-levels $m_F = 0, \pm 1$ to enable σ^+ and σ^- transitions. Multi-photon processes are thus neglected. We will further neglect collisions with the background gas and between trapped atoms (low density limit). Also the decreasing light intensity due to absorption will not be considered (low saturation limit). Although these approximations are not realistic, it is sufficient for a rough description of the system. The force due to the scattering of photons is $\hbar k$ times the cycling rate:

$$F_{sc}(\mathbf{r}) = \hbar k\Gamma \frac{s(\mathbf{r})}{1 + s(\mathbf{r}) + \left(\frac{\delta - \mathbf{k} \cdot \mathbf{v}}{\Gamma}\right)^2} \quad (5.7)$$

where we use the saturation parameter

$$\begin{aligned} s(\mathbf{r}) &= \frac{2\Omega^2(\mathbf{r})}{\Gamma^2} = \frac{1}{2} \left(\frac{d E_0(\mathbf{r})}{\hbar\Gamma} \right)^2 = \frac{I(\mathbf{r})}{I_{sat}} \quad \text{with} \\ I(\mathbf{r}) &= \frac{1}{2} \epsilon_0 E_0^2(\mathbf{r}) \quad \text{and} \quad I_{sat} = \epsilon_0 \left(\frac{\hbar\Gamma}{d} \right)^2 = \frac{\pi\hbar c\Gamma}{3\lambda^3}. \end{aligned} \quad (5.8)$$

d the dipole moment of the transition. As in the previous chapters, δ is the laser detuning from resonance and Γ the natural linewidth of the transition. We examine the one-dimensional case in radial direction, on which we find a magnetic field $B(r) = r \cdot \text{grad}B$. Two counter-propagating, red-detuned and circularly polarized light beams will – in linear approximation of $s(r)$ – exert the average force of

$$F = \frac{1}{2} \hbar k \Gamma s \cdot \left(\frac{1}{1 + 4(\delta - kv_r - \omega_{Lar}(r))^2/\Gamma^2} - \frac{1}{1 + 4(\delta + kv_r + \omega_{Lar}(r))^2/\Gamma^2} \right) \quad (5.9)$$

with the Larmor frequency in the position dependent B-field

$$\omega_{Lar} = \mu_B g_F r \text{grad}B / \hbar \quad (5.10)$$

and the Landé-factor g_F . For slow atoms near the center (small v_r and r), (5.9) reduces to a friction force and a harmonic restoring force

$$F = -m\beta v_{r,0} - m\omega_{trap}^2 r \quad (5.11)$$

with friction coefficient β and oscillation frequency ω_{trap} defined as

$$\beta = 8 s \omega_{rec} \frac{2|\delta|/\Gamma}{(1 + 4\delta^2/\Gamma^2)^2} \quad \text{and} \quad \omega_{trap}^2 = \beta \frac{\mu_B g \text{grad}B}{\hbar k}. \quad (5.12)$$

$\omega_{rec} = \hbar k^2/2m$ is the recoil frequency. An atom inside the trap will perform a damped harmonic oscillation according to

$$\ddot{r} + \beta \dot{r} + \omega_{trap}^2 r = 0. \quad (5.13)$$

For our experimental parameters $\omega_{trap} \approx 1$ kHz and $\beta \approx 6$ kHz. The restoring force, together with a diffusion coefficient (see [136] and references therein for details on the diffusion tensor) fully define the steady state atom velocity and spatial distribution. According to the steady state solution of a one-dimensional Fokker-Planck equation, the atomic transversal distribution is Gaussian

$$w(v, r) = \frac{1}{\sqrt{2\pi} u} e^{-v_r^2/2u_r^2} \cdot \frac{1}{\sqrt{2\pi} s} e^{-r^2/2s^2} \quad (5.14)$$

with the transversal width of velocity and position

$$u_r = \sqrt{\frac{k_B T_r}{m}} \quad \text{and} \quad s = \sqrt{\frac{k_B T_r}{m\omega_{trap}^2}}, \quad (5.15)$$

where the transversal temperature T_r of the trapped atoms is defined as

$$T_r = \frac{1 + \alpha}{8} \frac{\hbar\Gamma}{k_B} \left(\frac{2|\delta|}{\Gamma} + \frac{\Gamma}{2|\delta|} \right). \quad (5.16)$$

α is the diffusion coefficient along the r-axis for circular polarized light and has the value 2/5 (see [136]). The minimum temperature is reached for $\delta = \Gamma/2$ and is in the order of the Doppler temperature $T_{r,min} \approx T_D = \hbar\Gamma/2k_B$, about 140 μK for ^{87}Rb .

Description of Flux The loading rate R of the 2D-MOT can be written as the flux through the surface of the capture volume of atoms with a radial velocity below the capture velocity $v_r < v_c$. We therefore multiply surface (A), density (B) and radial velocity (C) with the Maxwell-Boltzmann distribution as a weight (D), writing the velocity in cylinder coordinates (E):

$$\begin{aligned} R(n, v_z) &= \underbrace{2\pi r_c}_A \underbrace{n}_B \int_0^{v_c(v_z)} \underbrace{v_r}_C \underbrace{((\pi v_{max}^2)^{-3/2} e^{-(v_r^2+v_z^2)/v_{max}^2})}_D \underbrace{v_r 2\pi}_E dv_r \\ &= \frac{4\sqrt{\pi} r_c n}{v_{max}^3} e^{-(v_z^2)/v_{max}^2} \int_0^{v_c(v_z)} dv_r v_r^2 e^{-v_r^2/v_{max}^2}, \end{aligned} \quad (5.17)$$

where $v_{max} = \sqrt{2k_B T/m}$ is the most probable velocity of the Maxwell-Boltzmann distribution¹. R depends on z via v_c .

The total flux at a certain velocity can be written as (see [131])

$$\Phi(n, v_z) = \frac{\int_0^L R(n, v_z) e^{-\Gamma_{coll} z/v_z} dz}{1 + \Gamma_{trap}(n_{tot})/\Gamma_{out}}, \quad (5.18)$$

where we introduced the loss rate of the trapped atoms due to collisions with the background gas Γ_{trap} , the out-coupling rate from the 2D-MOT through the hole Γ_{out} and the exponential loss term due to light assisted collisions of the cold atoms on their way to the hole Γ_{coll} . n is the density of ^{87}Rb and n_{tot} is the density of all rubidium isotopes ($n = 0.28 n_{tot}$). Together with (5.17), we can write for a mean $z = L/2$:

$$\Phi(n, v_z) = \frac{4\sqrt{2\pi} r_c n}{v_{max}^3} \frac{v_z}{\Gamma_{coll}(1 + \Gamma_{trap}/\Gamma_{out})} e^{-(v_z^2)/v_{max}^2} \left(1 - e^{-\Gamma_{coll} L/v_z}\right) \int_0^{v_c} dv_r v_r^2 e^{-v_r^2/v_{max}^2} \quad (5.19)$$

where for simplicity we omitted the dependencies. The whole flux is the integral over all velocities $\Phi_{tot} = \int_0^\infty \Phi(n, v_z) dv_z$

Γ_{trap} is usually of the order of 10 s^{-1} at pressures of 10^{-7} mbar . The typical cooling time is in the order of few ms (we will see later that the mean v_z is below 30 m/s) and therefore $\Gamma_{out} \approx 10^3 \text{ s}^{-1}$. Γ_{coll} is given by

$$\Gamma_{coll} = n_{tot} \bar{v} \sigma_{\text{eff}}, \quad (5.20)$$

¹In a Maxwell-Boltzmann distribution one will find the average velocity $\bar{v} = (8k_B T/\pi m)^{1/2}$, the root mean squared velocity $\sqrt{\bar{v}^2} = v_{rms} = (3k_B T/m)^{1/2}$ and the most probable velocity $v_{max} = \sqrt{2k_B T/m}$.

where σ_{eff} is the effective collision cross section ($\sigma_{\text{eff}} \approx 3 \cdot 10^{-12} \text{ cm}^2$ according to [131, 133]) and \bar{v} the average velocity in the vapor ($\bar{v} = \sqrt{8k_B T / \pi m} = 270 \text{ m/s}$), what leads to $\Gamma_{\text{coll}} \approx 10^2 \text{ s}^{-1}$. The experimental curves can be fitted with (5.19) to receive information about the actual scattering rates.

We conclude that the following atoms contribute to the beam:

- Only those atoms within the capture radius of the MOT, which have a radial velocity component v_r smaller than the maximum capture velocity $v_c(z, v_z)$, can be captured and confined on the z-axis. Since the radial capture velocity is inversely proportional to v_z , atoms with high v_z will not be captured and confined to couple through the hole. The mean velocity of the atoms in the beam is small not because of cooling, but because of this filtering effect. The mean thermal velocity v_{max} is about 270 m/s, whereas the mean velocity in the beam is $\bar{v}_z \approx 30 \text{ m/s}$. We will see later, how this mean velocity scales.
- Fast thermal atoms, which by chance hit the small hole under the right angle, will also arrive at the detection region and provide a thermal background of fast atoms, which however is very small with the severe spatial filtering by the narrow hole and is not even observable in our case. The bigger the background pressure, the higher the number of these atoms.

By playing with the equations of the last paragraphs, one could optimize the setup of the 2D-MOT, which in our case is more based on experiences from previous experiments: match the cloud size $2s$ to the hole diameter $d = 1.5 \text{ mm}$ (it might be useful to define a velocity dependent cloud size s if one wants to chose only the coldest atoms) and find the optimum detuning δ and gradient $\text{grad}B$ for a certain light power. We will see in the following, how the theoretical results of the previous section will help to understand the measurements.

5.1.3 Characterization of 2D-MOT

Cell size: The capture velocity v_c (5.5) increases with the distance of the atoms from the hole. A long cooling region L allows to capture more atoms with higher velocities. The increasing mean v_c will lead to an increased flux Φ , as one can read from equation (5.19). Elongating the cell, more and more atoms will be captured and the flux increases, as well as its mean velocity \bar{v}_z . This effect will invert, when the length L of the cell will become of the order of the mean free path of the atoms, because the distant atoms will be kicked out of the trap before arriving at the hole (factor $e^{-\Gamma_{\text{coll}} L / v_z}$ in equation (5.19)). In addition, light power is usually limited, making a too long cell unfavorable.

A radially larger cell will increase the possible capture volume. For the same detuning,

a lower magnetic gradient is required, which would create a broader flux with hotter atoms.

Hole size: A bigger hole results in a bigger flux (if the hole radius in the order of beam radius s), a bigger beam divergence and a higher mean velocity. In addition, the thermal background will increase. From previous experiences [129, 131, 132, 133], a hole size between 1 and 2 mm seems to be a good compromise between velocity, flux and pressure difference.

Pressure: A high Rb background pressure in the 2D-MOT cell will not only increase the background as mentioned before, but also the number of trapped atoms. As long as the pressure is small and $\Gamma_{trap} < \Gamma_{out}$, the flux increases linear with pressure or density n (see equation (5.19)). The higher the density, the less slow atoms will survive, since those atoms, which stay longer in the trap, have a higher collision probability.

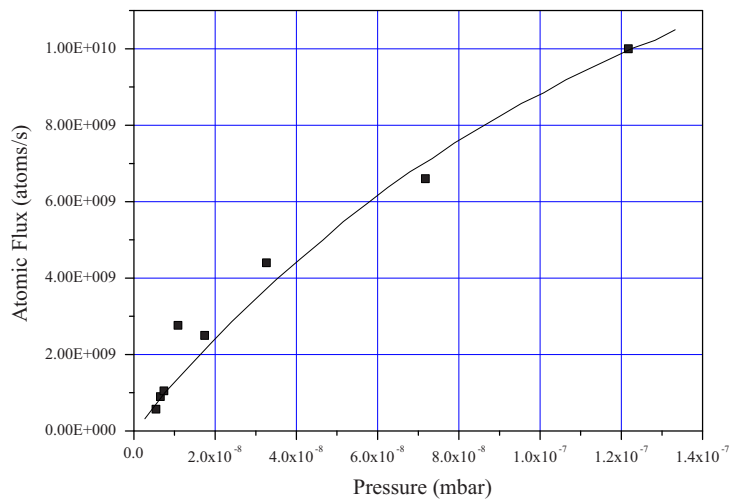


Figure 5.3: Pressure dependence of the flux at our 2D-MOT with the theoretically predicted curve of equation (5.19) corrected in amplitude. Pressure was measured by the absorption of a probe beam, traversing the MOT-cell, and calibrated on a spectroscopy cell. A further increase of the pressure was not possible in our system, but would show a point of maximum flux, which was found to be around $2 \cdot 10^{-6}$ mbar at a comparable system [133], what agrees with the point of saturation of equation (5.19).

With a further increase of the pressure will arrive a situation, where atoms from the border of the capture range will not reach the hole any more because of the high collision rate. Now $\Gamma_{trap} > \Gamma_{out}$ and the flux will start to decrease, since also Γ_{coll} depends on the pressure. This effect is not considered by equation (5.19), which just predicts a saturation, no decline. One will find an optimum pressure when the mean free path is of the order of the size of the cooling region. Since we can not heat the cell itself, our

pressure limit is slightly below the room temperature pressure of $3 \cdot 10^{-7}$ mbar (see Appendix A Figure A.5 for Rb pressure-temperature dependence).

Laser power: Increasing laser power signifies a higher Rabi-frequency, and a faster cycling time means a more efficient confinement (see equation (5.12)). The cloud size s of equation (5.15) will decrease and more and faster atoms will be coupled through the hole. Furthermore, a high intensity power-broadens the transition. The laser can thus be detuned further and by a simultaneous increase of the magnetic gradient a larger transversal capture range and higher (transversal) capture velocities are obtained. Here, the mean longitudinal velocity remains unchanged. Figure 5.4 shows the dependence of the flux on the laser power for fixed parameters of detuning (-7.5 MHz = -1.2Γ), power in pushing beam ($350 \mu\text{W}$) and radial magnetic field gradient (20 G/cm). For a total power of 140 mW and above, what means at least 70 mW for the vertical and 70 mW for the horizontal, retro-reflected beams ($> 3 I_{\text{sat}}$), we reach a flux of about $1 \cdot 10^{10}$ atoms.

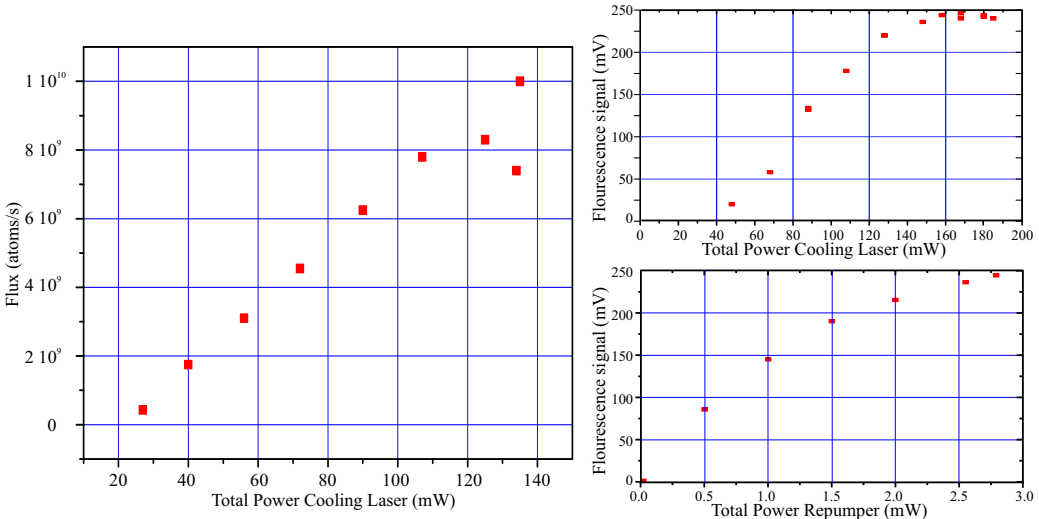


Figure 5.4: Dependence of the flux on the power of the cooling laser (left). Detuning and magnetic field remain unchanged. An uncalibrated measurement with higher power (top right) shows a saturation of the flux above 160 mW total power. The power in the repumper should be at least 3 mW not to limit the flux (bottom right).

Detuning: For a certain fixed laser power, which in our case is about 60 mW per beam (120 mW total power in the beams and 240 mW in the 2D-MOT considering the retro-reflection), one finds the corresponding optimum magnetic field gradient and detuning. A small detuning signifies a small capture radius, which means few atoms but a strong confinement of the atoms near the axis. This favors the capture of atoms

with a high velocity, which at higher detunings are harder to focus onto the z-axis within the available cooling time.

We find an optimum detuning at around -7.5 MHz distance from resonance as can be seen in Figure 5.5, left. A very big detuning will result in a high radial temperature, see (5.16), which increases the extension s of the beam such that a part will not pass the hole any more. Only slow atoms which are cooled sufficiently long will be coupled into the hole, yielding a lower mean velocity. This dependence is illustrated in Figure 5.5, right.

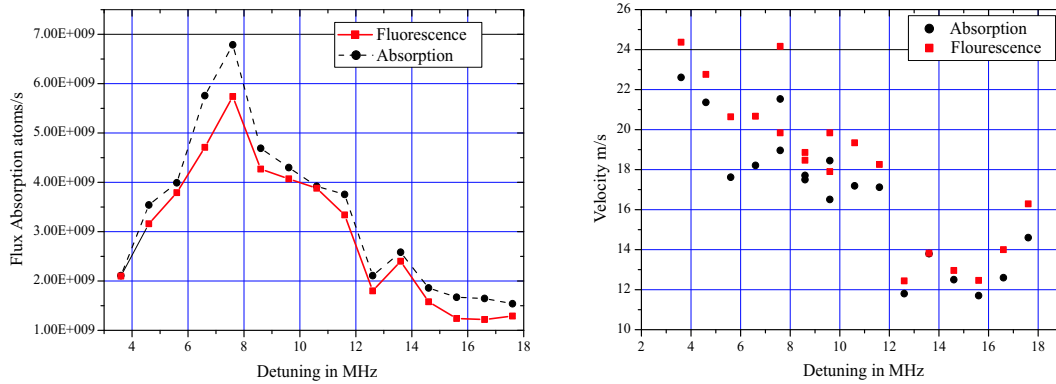


Figure 5.5: Dependence of flux intensity on the detuning of the laser from resonance (left) and the corresponding longitudinal velocity (v_{max} =velocity of biggest flux) in the beam. The spread is due to the sensitivity on the push-beam alignment.

Characterization of atomic flux: For our standard parameters of a light intensity of $2 \times 4 \text{ mW/cm}^2$ (retro-reflection), detuning of -7.5 MHz, field gradient of 20 Gauss/cm, presence of a pushing beam of $350 \mu\text{W}$ power and 1.5 mm diameter and a pressure of around $1 \cdot 10^{-7} \text{ mbar}$, we find a flux of up to 10^{10} atoms/s with a velocity distribution as shown in Figure 5.6. The beam contains few slow atoms first, because they have a higher chance to be scattered out of the beam by the high background pressure, second, because they will be accelerated more than faster atoms by the pushing beam and third, because they will be filtered out spatially by gravitation. Equation (5.19) does not account for the second and third of these effects and a theoretical fit of Figure 5.6 would require a more sophisticated model.

From the measured flux density per velocity class $\Phi(v_z)$ we calculate a mean velocity of the atoms in the beam \bar{v} and a rms velocity variation $v_{z,rms}$ of

$$\bar{v} = \frac{\int dv_z v_z \Phi}{\int dv_z \Phi} = 29.3 \text{ m/s} \quad \text{and} \quad (5.21)$$

$$v_{z,rms} = \langle (v_z - \bar{v}_z)^2 \rangle^{1/2} = \left(\frac{\int dv_z (v_z - \bar{v}_z)^2 \Phi}{\int dv_z \Phi} \right)^{1/2} = 15.08 \text{ m/s.} \quad (5.22)$$

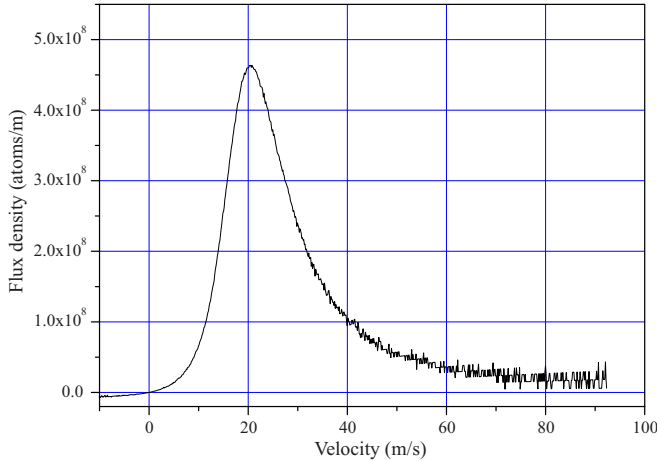


Figure 5.6: A typical velocity distribution in the atom beam. The curve is obtained by scanning the frequency of the probe beam, which hits the atom beam under 45° to the propagation axis. The velocity of maximum flux v_{max} is around 20 m/s. For calibration, the flux at velocity zero is considered zero.

We considered velocities between 0 and 85 m/s. The mean velocity $\bar{v} = 29.3$ m/s is shifted against the velocity of maximum flux $v_{max} = 20$ m/s by 10 m/s because of the long tail of hot atoms. However, we find 75% of the total flux $\Phi_{tot} = \int_0^\infty \Phi dv_z$ of $9.9 \cdot 10^9$ atoms/s below $v_z = 35$ m/s, what is roughly the capture velocity of the 3D-MOT, loaded by the atom beam. Experimentally, one finds a loading rate of the 3D-MOT of $3 \cdot 10^9$ atoms per second (see Figure 5.7), which was recorded after my stay in Paris.

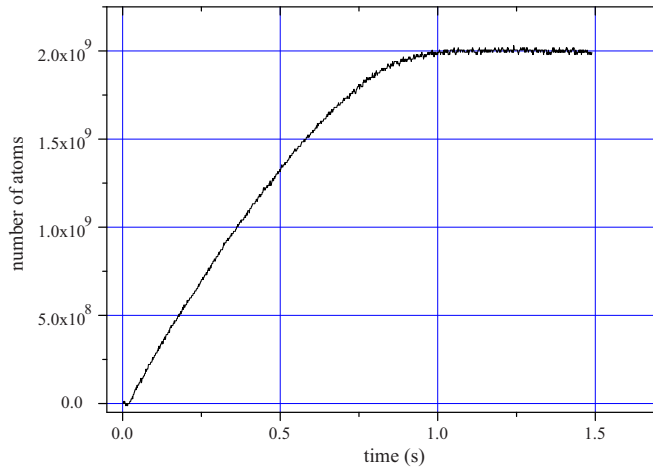


Figure 5.7: Loading of the 3D-MOT from the 2D-MOT. The loading rate is $3 \cdot 10^9$ atoms/s and the number of trapped atoms reaches a steady state value of $2 \cdot 10^9$ atoms.

A radial examination of the flux reveals the dependence of v_{max} on position as the

measurement on Figure 5.8 shows. Assuming the origin of this dependence in the residual radial velocity of the atoms, one can estimate it from the beam size and the distance from the hole to $v_r = 0.4$ m/s.

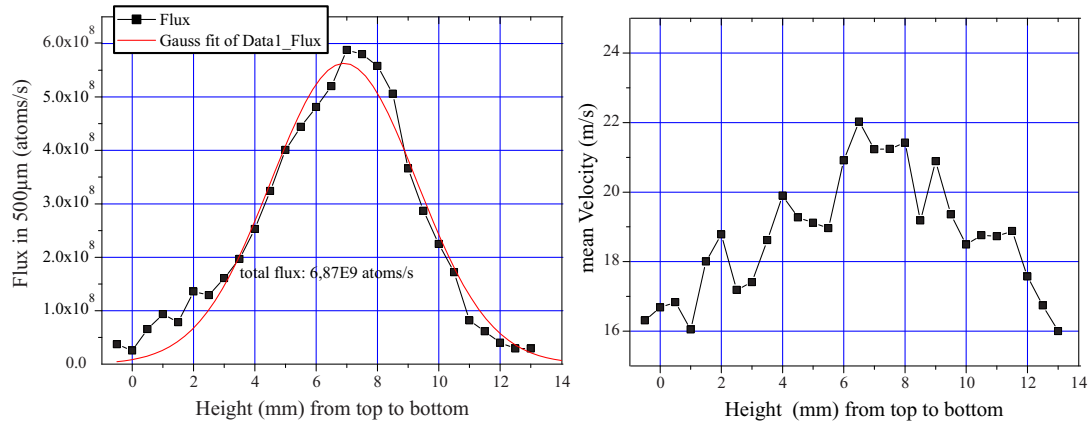


Figure 5.8: Left: Radial dependence of the flux density in the atom beam after 38 cm of propagation in UHV. The FWHM of 16 mm corresponds to a full divergence angle of about 40 mrad. Right: Dependence of v_{max} (velocity class with maximum flux density) on radial position. Slow atoms had more time to diverge from the center.

5.1.4 2D-MOT for gradiometer

We currently assemble the vacuum system for the MAGIA 2D-MOT system. Its design is based on the Paris design and contains minor changes of details that have proven inconvenient. To push the flux up a little higher compared to the gravimeter, we have foreseen a heating of the whole cell to obtain higher Rb pressures and we extended the width of the cell, windows and optics to have a bigger potential capture range. The high flux is necessary, because we only have between 60 and 100 ms of loading time for the second cloud of the interferometer and we would like to load the MOT with 10^9 atoms during this time. The operation of the 2D-MOT will be continuous and with a resonant orthogonal laser beam acting as a shutter right in front of the UHV-cell, which begins at about 30 cm distance from the escape-hole of the 2D-MOT cell. A 1 Watt (Toptica DLX110) laser will supply the 2D-MOT with the necessary laser power.



5.2 Sample preparation and analysis gradiometer

For the proper performance of the gradiometer experiment, we need two samples of 10^9 cold rubidium atoms with a narrow vertical velocity distribution and all in the same $m_F = 0$ sublevel of the ground state. To prepare such samples, the rubidium atoms need to be trapped in a MOT, cooled, velocity selected and prepared in the right state. This section will describe this procedure as well as the final state-sensitive detection of the atoms.

5.2.1 3D MOT

At the beginning of the experiment sequence, the MOT is switched on for a duration between 1 and 2.5 s. It is loaded from the background pressure that is created by the rubidium dispensers. We usually work at relatively low background pressures to have a loading time τ of the MOT of about 2.5 s (4 A current in dispenser), during which we capture about 10^9 atoms. When switching off the dispensers, the pressure in the cell decays exponentially with a τ of 8 s; on the contrary it rises with a time constant of around 40 s after the switching on (measurement curves in [100, 52]). The loading time of the MOT is equal to the mean lifetime of the atoms. For a low dispenser current

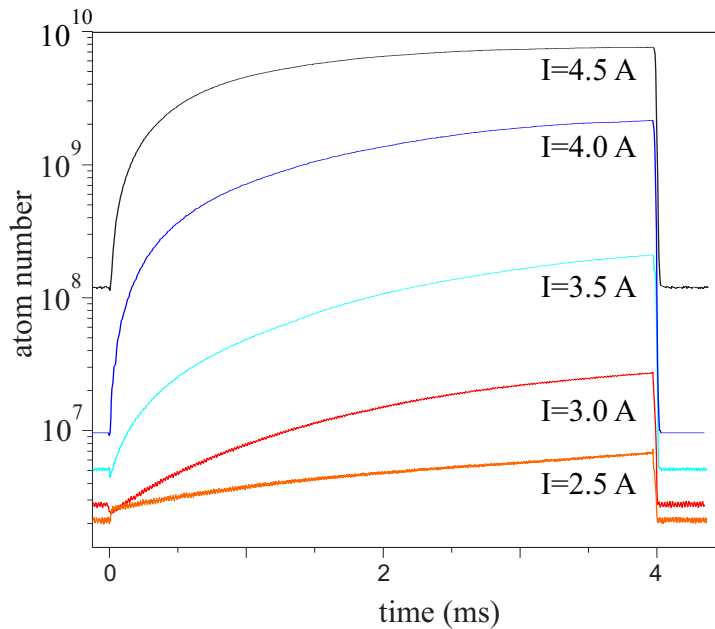


Figure 5.9: Loading curves of the MOT for different currents through the Rb-dispensers (Usually, we use 4 A for the interferometer) in logarithmic scale. The background is due to the fluorescence of the background-gas. This measurement has been done for $\Delta = 3\Gamma$ and $I = 6.4 I_{sat}$.

of 3 A, the MOT has a loading time constant of more than 5 seconds, from which we concluded the background pressure in the MOT-cell to be of the order of 10^{-10} mbar: according to (5.20), $\Gamma_{coll} = n_{tot}\bar{v}\sigma$, where \bar{v} is the mean velocity of the Maxwell-Boltzmann distribution $\bar{v} = \sqrt{8k_B T/\pi m}$, n_{tot} the gas density and σ the collision cross section. With the loading rate R into the volume V

$$R = \frac{1}{2}nV^{2/3} \frac{v_c^4}{v_{max}^3} \quad (5.23)$$

we can fit the exponential loading curve with the solution of the rate equation

$$N(t) = \frac{R}{\Gamma_{coll}}(1 - e^{-\Gamma_{coll}t}) \quad (5.24)$$

to get a pressure estimation $p = nk_B T/V$. Here the capture velocity v_c can be estimated as in section 5.1.2 with the number of scattering events necessary to stop an atom within the beam diameter.

A further characterization of our MOT has been done in the diploma-thesis [100].

5.2.2 Launch

After a sufficiently long loading time, the quadrupole magnetic field is switched off, the cloud is launched and at the same time cooled down further in a moving molasses. The constraints of our present experimental conditions allow for no more than three different laser frequencies and three different intensity levels during one cycle and we optimized our system within these restrictions for an effective launch on the one hand and a low final temperature on the other hand. The switching between different power levels is done smoothly across a low-pass filter. We presently use the following cooling and launching sequence, which is illustrated in Figure 5.10:

Experim. stage	Time after MOT On	Laser Intensity	Detuning Δ from Trans.2-3	MOT Coil	Comp. Coils
<i>MOT</i>	$t_1 = 0$ s	$I = 5I_{sat}$	-3Γ	On	Config. 1
<i>Launch</i>	$t_2 \approx t_1 + 1$ s	$I = 5I_{sat}$	$-4.5\Gamma \pm 2.2\text{MHz}$	Off	Config. 2
<i>Molasses 1</i>	$t_3 = t_2 + 3.7$ ms	$I \approx 2.5I_{sat}$	$-7\Gamma \pm 2.2\text{MHz}$	Off	Config. 2
<i>Molasses 2</i>	$t_4 = t_3 + 2$ ms	$I < 1I_{sat}$	$-7\Gamma \pm 2.2\text{MHz}$	Off	Config. 2
<i>Switch off</i>	$t_5 = t_4 + 0.5$ ms	$I = 0$	—	Off	Config. 2

Since the cooling region is magnetically shielded only by compensation coils, we do not have a uniform field over the whole cooling region, which makes the final temperature very sensitive on changes of the magnetic field. We found it advantageous to load the MOT with a non perfectly compensated magnetic field and to leave an offset, which shifts the position of the MOT downwards (B configuration 1), such the during the molasses, the cloud stays longer in the spatially limited region of a well compensated field (switch to configuration 2).

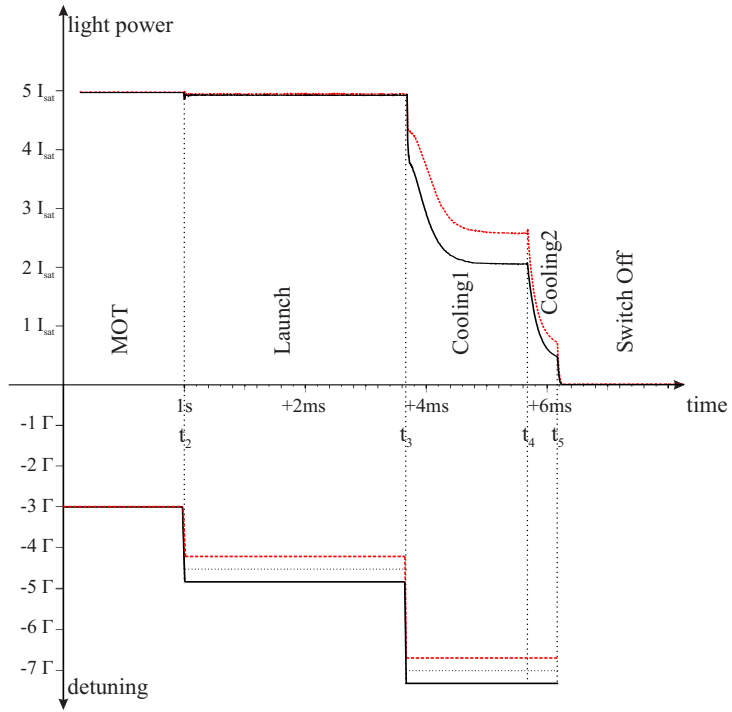


Figure 5.10: *Experimentally optimized cooling and launching sequence indicating the power of the upper (solid) and lower (dashed) cooling lasers and their detuning from the $F = 2 \rightarrow F' = 3$ transition. We find better results for launch efficiency and temperature for a slightly higher power of the lower laser. The switching between the different power levels is smoothed by low-pass filtering the control-voltage signal of the AOM driver.*

Optimization of the temperature is done by observing the spacial spread of the cloud when it returns from its flight through the detection chamber through a Time-of-Flight (TOF) measurement. The temperature of the cloud when it passes a thin sheet of light can be calculated from the fluorescence signal by expressing the cloud as a Gaussian distribution in velocity and position according to (5.15) in three dimensions. With the time and temperature dependent variance of the spatial distribution

$$\sigma_{x,y,z}^2(t, T) \equiv \sigma^2(t, T) = s^2 + u(T)^2 t^2 \quad \text{where} \quad u(T)^2 = \frac{k_B T_{\text{cloud}}}{m}, \quad (5.25)$$

the probability to find an atom at position (x, y, z) at a time t can be written as

$$p(x, y, z, t, T) = \left(\frac{1}{2\pi\sigma(t, T)^2} \right)^{3/2} e^{-\frac{1}{2\sigma(t, T)^2}(x^2+y^2+(z-gt^2/2)^2)}. \quad (5.26)$$

This yields to the following expression for the TOF-signal passing a rectangular sheet of the probe beam along the y -axis of height $2a$ and width $2b$ and uniform light intensity:

$$N(t, T) = \int_{d+a}^{d-a} \int_{-\infty}^{\infty} \int_{-b}^b p(x, y, z, t, T) dx dy dz, \quad (5.27)$$

The integral simplifies for certain probe beam geometries (see [137]) and can be solved numerically else.

The crucial parameters for the experimental optimization of the temperature are:

- alignment of the trapping beams,
- current in compensation coils of trapping and detection region,
- intensities and detuning of cooling beams in various stages of the launch,
- duration of the cooling stages and
- launch direction.

The experimental optimization let us reach a minimum cloud-temperature around 3.5 μK ; however we usually work at temperatures of the cloud between 4 and 5 μK . Our launch efficiency lies between 50 and 100%; a more accurate number cannot be given because of the errors in the estimation of the number of atoms in the MOT (fluorescence) and in the launch (fluorescence time-of-flight signal).

A detuning of both lasers by $\delta\omega$ from the central frequency ω_c will result in a launch velocity v_l given by the Doppler formula $\delta\omega = \mathbf{k} \cdot \mathbf{v}_l$. Taking into account the angle α between \mathbf{k} and \mathbf{v}_l , we can determine the maximum launch height as

$$z_{max} = \frac{v_l}{2g} = \left(\frac{\delta\omega}{k \cos \alpha} \right)^2 \frac{1}{2g}. \quad (5.28)$$

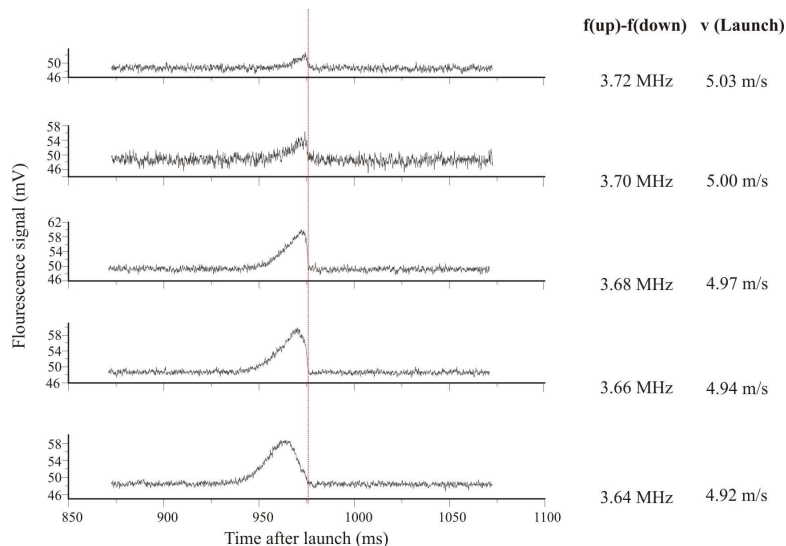


Figure 5.11: Fluorescence signal of the cloud in the detection chamber when returning from a flight up to the upper window at a height of about 1.3 m above the cooling region. The part of the cloud, which hits the window, thermalizes and does not return.

Figure 5.11 shows a launch up to the upper window of the interferometer tube about 1.3 m above the MOT. The upper part of the cloud is cut by the contact with the window.

5.2.3 Juggling

A gradiometric measurement requires two clouds at a distance of about 35 cm, which means that they must be launched with a time difference of 100 ms and less. The number of atoms, which can be loaded in the MOT in this 100 ms is low ($< 10^8$) for reasonable low background pressures. Our 2D-MOT is only in the stage of construction. Therefore, we thought of an intermediate solution, juggling: Since the time between two consecutive measurements is not limited, one could load an important number of atoms into a first cloud, launch it and take advantage of this reprieve of up to one second to load the second cloud, which must be launched right before the arrival

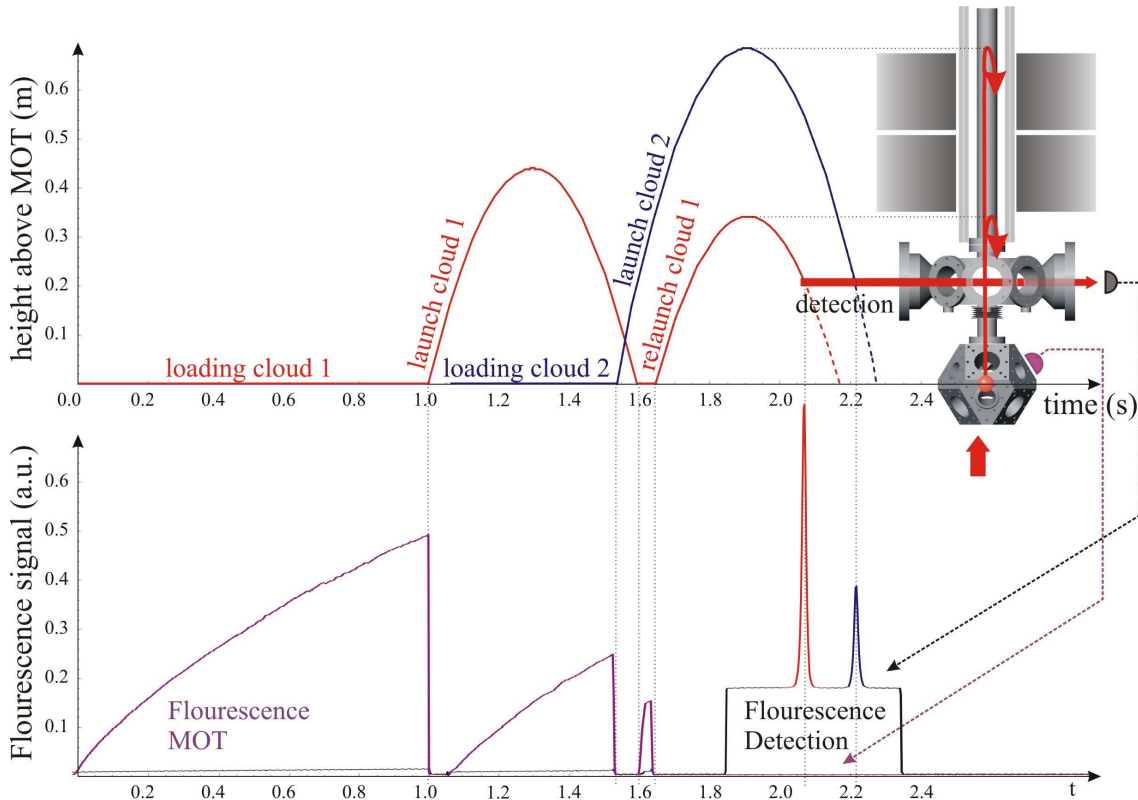


Figure 5.12: *Juggling*: The upper curve indicates the trajectories of the two clouds, the lower curves show the (measured) fluorescence signals of the MOT and detection region. After a long loading time of 1 s, cloud 1 is launched up to 45 cm to gain time to load cloud 2, which is thrown up to a height of 70 cm. Subsequently, cloud 1 is recaptured and launched after only 50 ms loading time. Both clouds now move with the same velocity at a distance of 35 cm until they pass the detection beam.

of the first one in the MOT capture region. The velocity of the first cloud on its arrival is below 10 m/s and the major part of the atoms can be reloaded into the MOT, which therefore fills immediately and can be re-launched shortly after the previous one. Figure 5.12 shows how this juggling of two balls with one hand (MOT) is performed. To provide the right frequencies to the upper and lower cooling beams during the three launches, we need several oscillators: one VCO (Voltage controlled oscillator) which provides the frequency for trapping (in our case 80 MHz), two oscillators (one for upper- one for lower cooling beams) that provide each two frequencies for the cooling during the launch of cloud one and two oscillators for cloud two, since the time between the two last launches is insufficient to reprogram the frequencies. We switch between the frequencies and oscillators with trigger pulses (see Fig. 5.13).

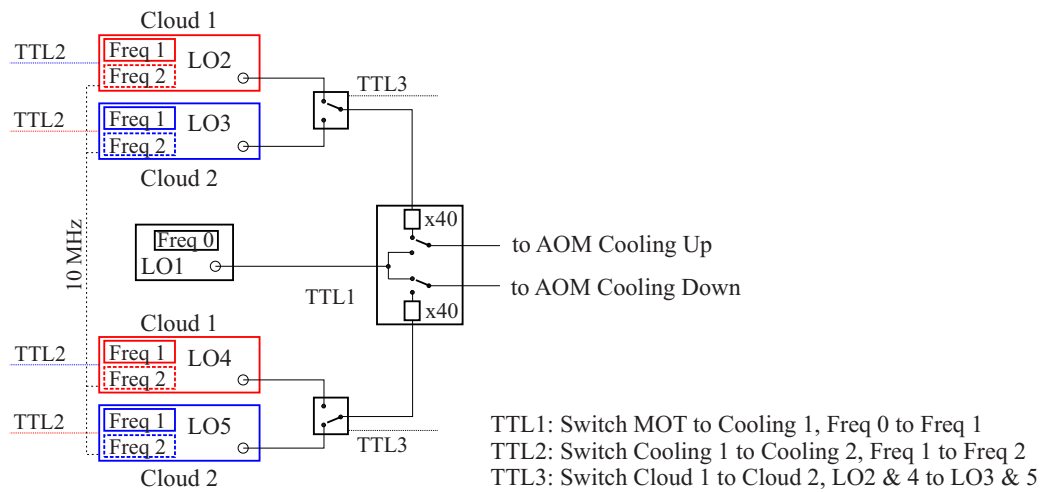


Figure 5.13: Five oscillators provide the necessary frequencies for the juggling sequence. One VCO at 80 MHz and four frequency generators, whose frequencies around 2 MHz are multiplied by 40. Each of these four generators can be rapidly switched between two frequency-values (FSK), which can be reprogrammed within 160 ms.

5.2.4 Velocity selection

To prevent spacial spreading of the atom cloud during the interferometer and to ensure the same transition probability for all atoms during a Raman pulse, we need to perform a velocity selection of the atoms. The selection is performed with a pulse of counter-propagating Raman lasers (see section 2.1.4), and its width is governed by equation (2.44). Figure 5.14 shows a measurement the transition probability versus frequency. Equation (2.44) further shows a dependence on the light shift δ^{AC} and from definitions (2.39), (2.40) and (2.41) follows the linear dependence of the light shift on the intensity

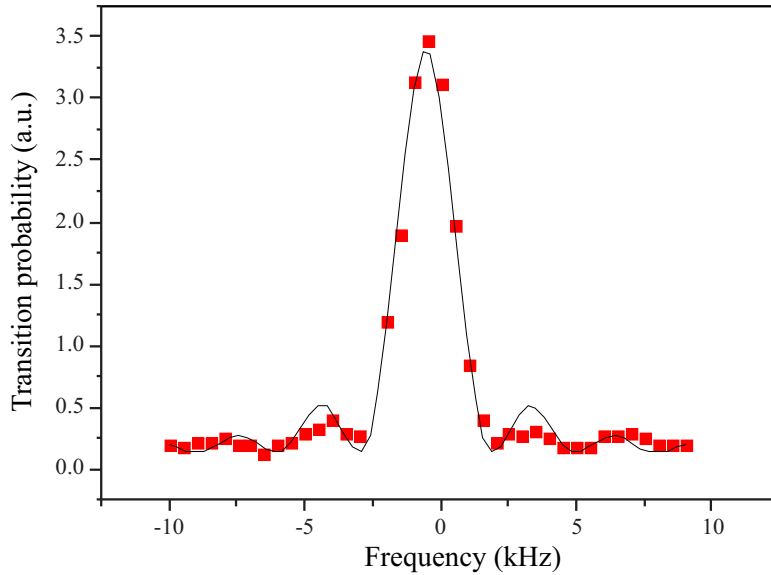


Figure 5.14: Transition probability of a Raman pulse over the detuning of the effective frequency $\omega_{\text{eff}}/2\pi$ using co-propagating Raman beams and a pulse time of 100 μs .

difference between lasers 1 (I_{L1}) and laser 2 (I_{L2}):

$$\delta^{AC} = (\Omega_b^{AC} - \Omega_a^{AC}) \sim (\Omega_{ai1}^2 - \Omega_{bi2}^2) \sim (I_{L1} - I_{L2}) \quad (5.29)$$

Figure 5.15, left, shows a measurement of this dependence, in which the main error comes from the intensity measurement, which is just the readout of the peak transmission through a scanning Fabry-Perot interferometer. The right curve of the same Figure 5.15 has been taken for the transitions between the $m_F = \pm 1$ levels in a varying magnetic field.

Two Raman lasers can in principle drive all transitions with non-zero transition probability indicated in table 5.1. The best choice for the experiment is a Raman transition between the magnetically insensitive levels $|F = 1, m_F = 0\rangle \rightarrow |F = 2, m_F = 0\rangle$ to avoid systematic errors from the first-order Zeeman shift.

Laser 1 with frequency ω_{L1} couples the ground state $F = 1$ to the upper states $F' = 0, 1, 2$ and laser 2 with ω_{L2} the ground state $F = 2$ to $F' = 1, 2, 3$. Only the intermediate states $F' = 1, 2$ are involved in a Raman transition and we consider the detuning Δ of the Raman laser of about 3 GHz as much bigger than the spacing of the hyperfine levels $F' = 1$ and 2 of about 160 MHz. We therefore write the effective Rabi frequencies (2.39) of the transitions between $|F = 1, m_F\rangle$ and $|F = 2, m_F\rangle$ via the intermediate state $|F', m_{F'}\rangle$ all with the same detuning Δ , what makes them easy to sum up:

$$\Omega_{\text{eff};|F=1,m_F\rangle \rightarrow |F=2,m_F\rangle} = \sum_{|F',m_{F'}\rangle} \frac{\Omega_{L1;|F=1,m_F\rangle \rightarrow |F',m_{F'}\rangle}^* \Omega_{L2;|F=2,m_F\rangle \rightarrow |F',m_{F'}\rangle}}{2\Delta}. \quad (5.30)$$

The Rabi-frequencies (2.36) for each transition between the m_F -sublevels can be cal-

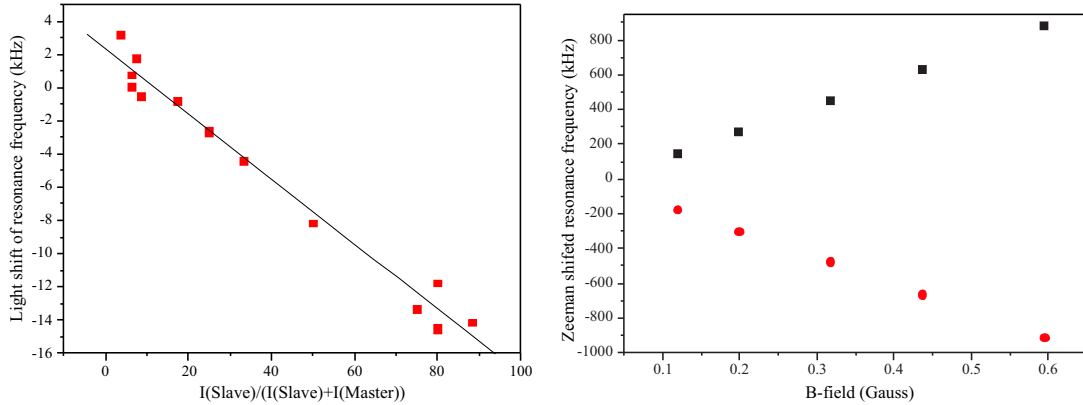


Figure 5.15: *Left:* Relative light shift of resonance frequency versus the relation of power in both Raman-lasers. *Right:* Resonance frequency of transition $|F = 1, m_F = -1\rangle$ to $|F = 2, m_F = -1\rangle$ (circles) and $|F = 1, m_F = +1\rangle$ to $|F = 1, m_F = +1\rangle$ (squares). One finds a dependence of 1.4 MHz per Gauss as one expects from $h\Delta\nu = \mu_B m_F(g_{F=2} - g_{F=1})B$.

culated and written as multiples of certain "reduced matrix elements", which only depend on the quantum number J as explained in Appendix A, Picture A.4.

Table 5.1 gives the multiple of the reduced matrix element for $J=1/2$ and $J'=3/2$ modulo 120.

To calculate the transition probabilities for the three possible transitions $|F = 1, m_F = 0\rangle \rightarrow |F = 2, m_F = 0\rangle$ indicated in table 5.1, one has to do the sum of the transition-probabilities including all possible intermediate states $|F' = 1, 2, m_{F'} = 0, \pm 1\rangle$ accessible by the absorption and stimulated emission of σ^+ , σ^- or π -light. One finds first that the $\pi - \pi$ transition (via $|F' = 1, m_{F'} = 0\rangle$ and $|F' = 2, m_{F'} = 0\rangle$) is forbidden by the selection rules, and second that the probabilities for the transition $\sigma^+ \sigma^+$ and $\sigma^- \sigma^-$ add to zero, if none of the following conditions is fulfilled:

1. Laser 1 and laser 2 are *identically circularly polarized*. To ensure $k_{\text{eff}} = k_{L1} + k_{L2}$, the beams should come from opposite directions.
2. Laser 1 and laser 2 are *linearly polarized and retro-reflected* in orthogonal linear polarization PLUS non-zero atom velocity. In this case, the stimulation of laser 1 and laser 2 from opposite directions is automatically ensured ².

In our experiment, we have chosen the second geometry by introducing a quarter-wave plate in front of the retro-reflecting mirror and for this case we calculated the

²The incident and reflected light can each be decomposed into two contrarily rotating circularly polarized components: $L1 = \sigma_{L1,up}^+ + \sigma_{L1,up}^- + \sigma_{L1,down}^+ - \sigma_{L1,down}^-$ and $L2 = \sigma_{L2,up}^+ + \sigma_{L2,up}^- + \sigma_{L2,down}^+ - \sigma_{L2,down}^-$. The transition probabilities only add up to a value $\neq 0$ by absorption of either $\sigma_{L1,up}^+, \sigma_{L2,down}^+$ and $\sigma_{L1,up}^-, -\sigma_{L2,down}^-$ or by absorption of $\sigma_{L1,down}^+, \sigma_{L2,up}^+$ and $-\sigma_{L1,down}^-, \sigma_{L2,up}^-$, but not both.

	$ F = 1, m_F\rangle$	Abs	Em	$ F = 2, m_F\rangle$	Δm_F	ΔE_{Zeem}	P_{rel}	Comment
+1		σ^-		—	—	—	—	
		σ^+	π	+2	+1	-3	$10\sqrt{6}$	*
		σ^+		+1	0	-2	$10\sqrt{3}$	wrong energy
		σ^-		+2	+1	-3	$-1 \times -10\sqrt{6}$	*
	π	π		+1	0	-2	0	*
		σ^+		0	-1	-1	10	*
		σ^-		+1	0	-2	$-1 \times 10\sqrt{3}$	wrong energy
		σ^-	π	0	-1	-1	-10	*
		σ^+		-1	-2	0	$-10\sqrt{3}$	
0		σ^-		+2	+2	-2	-1×0	
		σ^+	π	+1	+1	-1	$-10\sqrt{3}$	*
		σ^+		0	0	0	-20	desired
		σ^-		+1	+1	-1	$-1 \times -10\sqrt{3}$	*
	π	π		0	0	0	0	*
		σ^+		-1	-1	+1	$10\sqrt{3}$	*
		σ^-		0	0	0	-1×20	desired
		σ^-	π	-1	-1	+1	$10\sqrt{3}$	*
		σ^+		-2	-2	+2	0	
-1		σ^-		+1	+2	0	-1×0	
		σ^+	π	0	+1	+1	-10	*
		σ^+		-1	0	+2	$-10\sqrt{3}$	wrong enery
		σ^-		0	+1	+1	-1×-10	*
	π	π		-1	0	+2	0	*
		σ^+		-2	-1	+3	$10\sqrt{6}$	*
		σ^-		-1	0	+2	$-1 \times -10\sqrt{3}$	wrong energy
		σ^-	π	-2	-1	+3	$-10\sqrt{6}$	*
		σ^+		—	—	—	—	

Table 5.1: Raman-transitions from $F=1$ to $F=2$ of the ${}^{87}\text{Rb}$ ground state $5^2S_{1/2}$. Abs(orption) and Em(ission) indicate the kind of transition stimulated by laser 1 and 2, respectively. ΔE is the Zeeman shift of the transition frequency in multiples of the Zeeman-splitting $\Delta E = N \cdot \mu_B g_F B_z$. Since our beams are parallel to the B -field, the π -transitions marked with * are suppressed. The last column specifies the relative transition probabilities P_{rel} modulo 120 using the values called "Multiple" in (A.4), which are related to the Clebsch-Gordan coefficients (see Appendix A). The probabilities are calculated for Raman beams in a lin-perp-lin configuration, for which the minus-sign of the second σ^- transition is added. To obtain the total probability for a transition $|F = 1, m_F\rangle \rightarrow |F = 2, m_F\rangle$, one has to sum the probabilities of all possible transitions between these two states.

relative transition probabilities in table 5.1. All transitions including π -transitions are suppressed, since the axis of our B-field is parallel to the z-axis and a magnetic shield reduces disturbances. The transitions from the levels $m_F = \pm 1$ with nonzero transition probability can be avoided by the application of a strong enough Zeeman splitting. The relative probability for the transition between the $m_F = 0$ is the sum of all possible transitions from table 5.1:

$$P(m_F = 0 \rightarrow m_F = 0) \sim (-1) \cdot \sigma^+ \sigma^+ + \sigma^- \sigma^- + \pi\pi = (-20 - 20 + 0)/120 = -\frac{1}{3}. \quad (5.31)$$

and one then calculates from (5.30) a Rabi frequency of

$$\begin{aligned} \Omega_R \stackrel{\delta_{12}=0}{=} \Omega_{\text{eff}} &= \sum_{|F',m_{F'}\rangle} \frac{\Omega_{F=1 \rightarrow F'}^* \Omega_{F=2 \rightarrow F'}}{2\Delta} \\ &= \frac{2\sqrt{I_{L1}I_{L2}}}{c\epsilon_0 2\Delta\hbar^2} \sum_{|F',m_{F'}\rangle} \langle F=1, m_F | e\mathbf{r} | F', m_{F'} \rangle \langle F', m_{F'} | e\mathbf{r} | F=2, m_F \rangle \\ &= \frac{2\sqrt{I_{L1}I_{L2}}}{c\epsilon_0 2\Delta\hbar^2 A} \underbrace{\langle J=1/2 | e\mathbf{r} | J=3/2 \rangle^2}_{=(3.58 \cdot 10^{-29} \text{C}\cdot\text{m})^2} \sum_{|F',m_{F'}\rangle} \underbrace{\text{Modulo}(|F', m_{F'}\rangle)}_{\text{see Appendix A, Figure A.4}} \\ &\approx 29 \cdot 1/3 \approx 10 \text{ kHz} \end{aligned} \quad (5.32)$$

for a light power of 10 mW per beam of 25 mm diameter and a detuning Δ of 3 GHz. In the non-shielded region of our apparatus, π -transitions are allowed and we observe the seven different equally spaced transition frequencies $\Delta E = 0, \pm 1, 2, 3$.

5.2.5 State preparation

The interferometer needs to start from a cold sample of atoms, which are all in one state, either $|F=1, m_F=0\rangle$ or $|F=2, m_F=0\rangle$. This situation can be brought about in the following ways:

Old method: Until recently, we were pumping the atoms into the state $F=2$ after the launch by simply switching off the repumper laser 3 ms after the cooling laser. At the moment of the velocity selective Raman π -pulse, which transfers atoms of one velocity class from $|F=2, m_F=0\rangle$ to $|F=1, m_F=0\rangle$, the atoms are in a region with a defined B-field along the z-axis³. Immediately after the selection, a strong B-field is applied along the transversal (!) x-axis with the coils around the detection chamber for an efficient blow-away of the remaining not selected atoms in state $F=2$ by a 5 mm high sheet of circularly polarized, near-resonance light on the closed transition $F=2 \rightarrow F'=3$, which enters the detection chamber along the x-axis (see state-preparation scheme in Fig. 5.16). The atoms will follow the B-field adiabatically from

³In reality also strong transversal B-components are present, what would allow π -transitions between $m_F \neq 0$ -states, but since the field is strong enough, these transitions are Zeeman-shifted out of resonance.

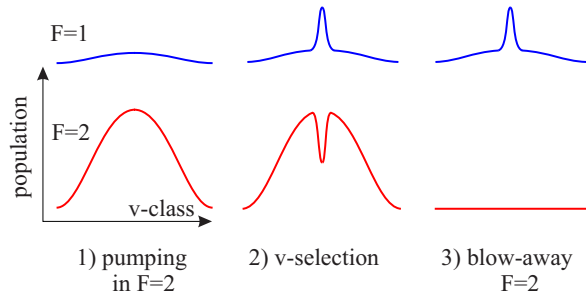


Figure 5.16: State-preparation of Rb atoms for the interferometer. After the cooling, atoms are pumped into the state $F=2$ by the repumper. Then a velocity selection pulse transfers atoms of a narrow velocity class with a Raman transition into $|F = 1, m_F = 0\rangle$. The remaining atoms in $F=2$ are blown away with a vertical on-resonance blow-away beam.

the x-axis to the z-axis (no point of $B=0$ which would allow spin-flips), when they enter the interferometer tube. We find a small background of warm atoms in state $F=1$ because first, the repumper power is very weak and not all atoms are really pumped into $F=2$ and second, because the non-resonant absorption of the far-detuned Raman lasers is non-zero. The fraction of atoms falling into $F=1$ by spontaneous emission is small compared to the total number of atoms in $F=2$, but can be a significant fraction of the number of velocity-selected atoms in $F=1$.

New method: To both eliminate the background and to be able to apply the blow-away on two clouds contemporarily, we set up a new blow-away system along the vertical axis. A linearly polarized beam resonant with the $F = 1 \rightarrow F' = 0$ transition

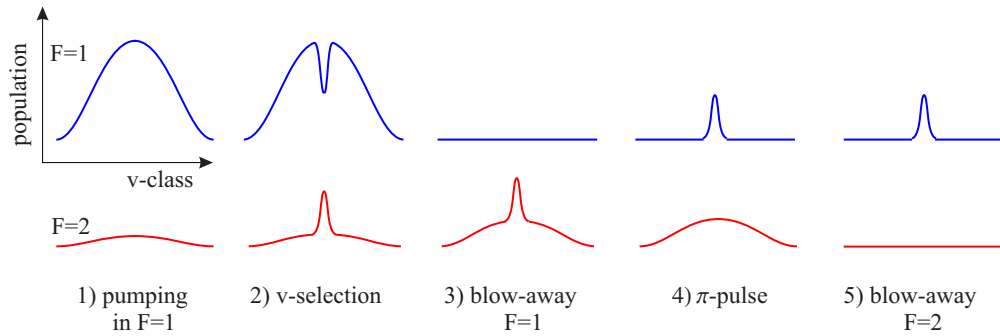


Figure 5.17: Recent scheme of vertical state-preparation. Atoms are first pumped into the state $F=1$ by the cooling lasers, then a velocity selection pulse transfers atoms into $|F = 2, m_F = 0\rangle$, together with a small background of unwanted atoms. The remaining atoms in $F=1$ are blown away, while some will fall into $F=2$ and increase the background. A further velocity selective pulse transfers the already selected atoms into the clean state $F=1$ and a final blow-away removes the background in $F=2$.

and a circularly polarized beam on the $F = 2 \rightarrow F' = 3$ transition enter the beam path of the Raman lasers. Since the $F = 1 \rightarrow F' = 0$ transition exhibits a big loss channel to the $F' = 1$ level, some atoms can fall into the ground state $F=2$. For this reason we need to apply the more effective blow-away $F = 2 \rightarrow F' = 3$ last (see Figure 5.17). With this method of vertical blow-away beams, we can keep the B-field constantly along the z-axis.

5.2.6 Detection

On their way back from the interferometer region, the atoms pass the detection chamber, where two light sheets will reveal their state (see Figure 5.18).

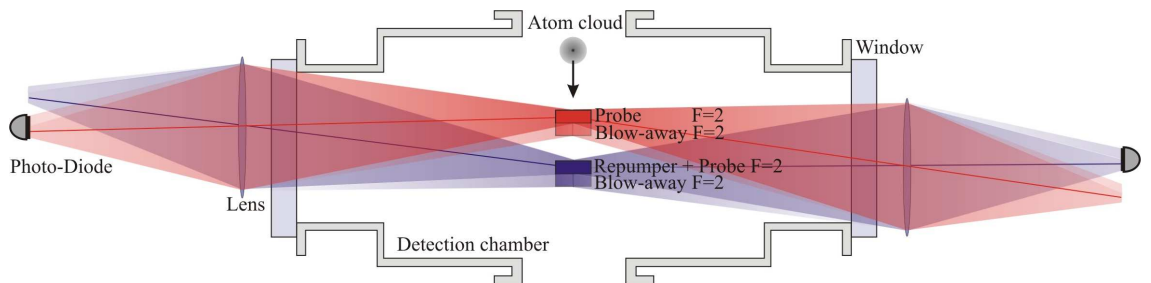


Figure 5.18: *Detection chamber to scale. The atom cloud passes two sheets of light at 2 cm distance to stimulate fluorescence of state $F=2$ and $F=1$. The fluorescence is recorded by two photodiodes. The lenses of aperture 48 mm at a distance of 130 mm from the center image the detection region with a magnification-factor of 0.6 onto the 6 mm high photodiodes. The lowermost blow-away serves only during the state-preparation.*

The atoms first pass a 14 mm broad and 5 mm high retro-reflected circularly polarized beam, slightly red detuned from the $F = 2 \rightarrow F' = 3$ transition to probe the population of state $F = 2$. Immediately after this beam, they encounter a 5 mm high blow-away beam of the same width, which essentially is the same light, but without retro-reflection. Only the atoms in $F = 1$ continue to the next light sheet of same dimensions, which consists of the same beam as the first light sheet, but overlapped with a repumper to transfer the remaining atoms all to the $F = 2$ level. The light sheets are sufficiently far apart (2 cm) to avoid any considerable crosstalk between the two photodiodes, which detect the fluorescence. Figure 5.19 shows a typical fluorescence signal after an interferometer sequence. The signals are automatically analyzed numerically after each shot: the background is subtracted and the remaining peaks are integrated and related to the sum of both integrals to obtain a value for the relative state populations.

We use two Hamamatsu S7510 photodiodes (active area 11 mm width x 6 mm height) for detection, which we protect with interference filters for 780 nm from the back-

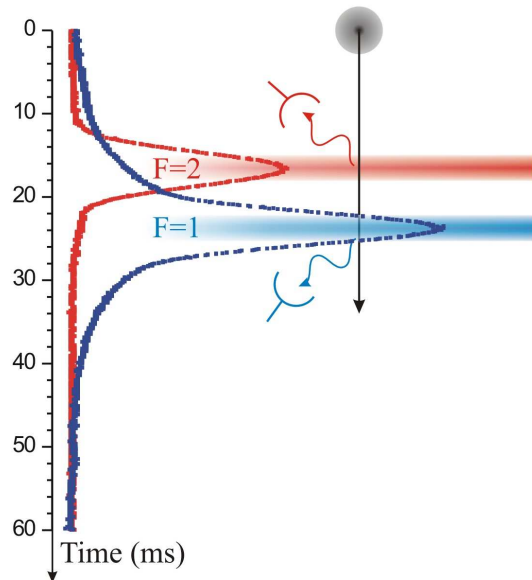


Figure 5.19: *Fluorescence signal of the atom cloud passing the detection region. The two peaks are integrated to determine the relative population of state $F=1$ and $F=2$. The signal $F=1$ is underlaid with a background of warm atoms due to the imperfect state preparation.*

ground light. The photo-current is amplified on an operational amplifier OPA627AP with a transimpedance of $100\text{ M}\Omega$ and the signal cut with a first order low-pass filter at 40 kHz ⁴.

⁴The capacitance across the transimpedance to cut the gain peaking consists of a piece of wire at one end of the resistance, bent closely to the resistance until the right capacitance value in the order of tenths of pico-Farad is reached.

5.3 Interferometry

We applied the interferometer sequence with co- and counter-propagating Raman beams. In the first case, the sensitivity of the interferometer on accelerations is very low but the proper operation of the apparatus can be tested. In the second case, the sensitivity on accelerations is vastly increased but it is more difficult to obtain a good signal because of the velocity selectivity of the Raman-pulses.

5.3.1 Velocity insensitive Interferometer

In the presence of both Raman-lasers and without retro-reflection, the Raman transition between $|F = 1, m_F = 0\rangle$ and $|F = 2, m_F = 0\rangle$ can be driven only, if both lasers are circularly polarized ($\sigma^+ \sigma^+$ or $\sigma^- \sigma^-$ -transition, see table 5.1). In this case of co-propagating Raman lasers, there will be no velocity selection and the effective k -vector is small (see chapter 2.1.4). Since atoms of all velocity classes are addressed, the resulting signal will be big; and this configuration has consequently been the first application of the Raman lasers in our experiment. A Raman-pulse of variable length has been applied to the atoms after the launch and we observed the Rabi-oscillations of Figure 5.20.

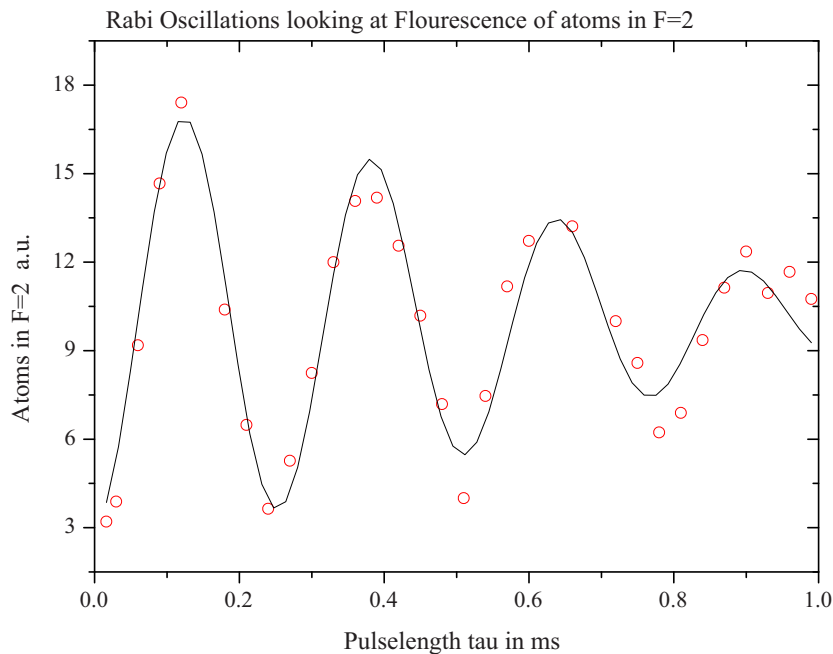


Figure 5.20: Rabi-oscillations for co-propagating Raman beams, red-detuned by $\Delta = 3.3$ GHz from resonance. The curve shows the relative population of state $F=2$ for varying pulse length. The oscillations ($f \approx 4$ kHz) are fitted with a damped sinus.

The application of the total interferometer sequence comprising a $\pi/2$, π and $\pi/2$ pulse – as was explained in chapter 2.2 – leads to a signal which is sensitive on gravitation according to $\Delta\phi = k_{\text{eff}}gT^2$. Scanning the phase of the interferometer makes the fringes visible, shown in Figure 5.21. According to the relation $N_a \sim (1 + \cos \Delta\phi)$, we fitted the fringes with a cosine. With the value of $k = 1.4 \text{ cm}^{-1}$ for the effective k -vector in the co-propagating case, the according resolution of Earth gravity g is embarrassingly low for this measurement:

$$g = (10.3 \pm 0.6) \text{ ms}^{-2}; \quad (5.33)$$

but is at least consistent with the expected value.

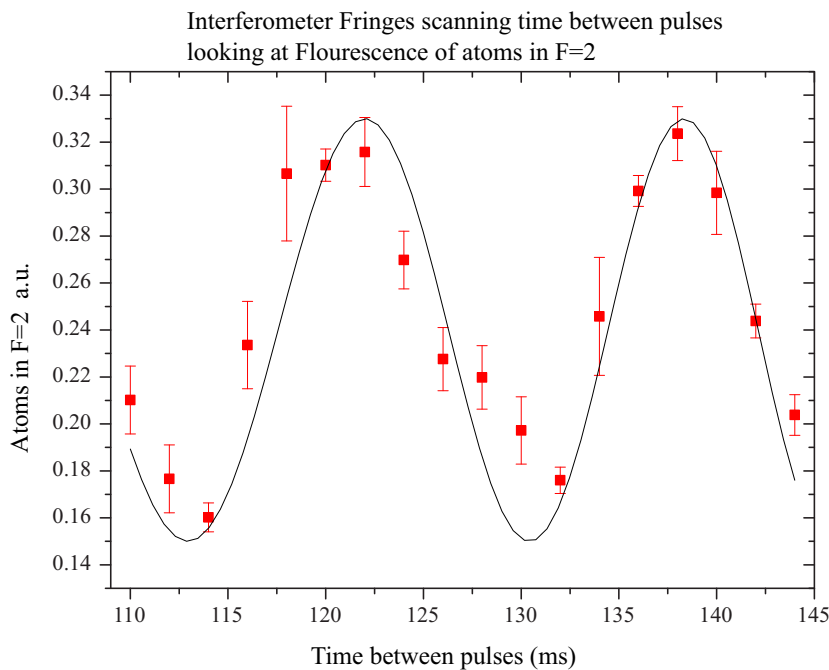


Figure 5.21: *Interferometer fringes for co-propagating Raman beams for a $\pi/2$ -pulse length of $\tau = 50 \mu\text{s}$ and a detuning of $\Delta = 3.3 \text{ GHz}$. The sensitivity is about 10^{-1} g .*

5.3.2 Velocity selective Interferometer

For the velocity selective interferometer we make use of the lin-perp-lin beam-configuration described in section 5.2.4. After the velocity selection and state preparation in the "old" configuration (see section 5.2.5) we apply a further Raman-pulse in the interferometer tube to observe the Rabi oscillations. The longer the pulse, the less atoms will be addressed and the oscillations are damped rapidly as Figure 5.22 shows.

The interferometer pulses are performed in the magnetically shielded tube a few hundred milliseconds after the first selection pulse. To stay in resonance with the hyperfine

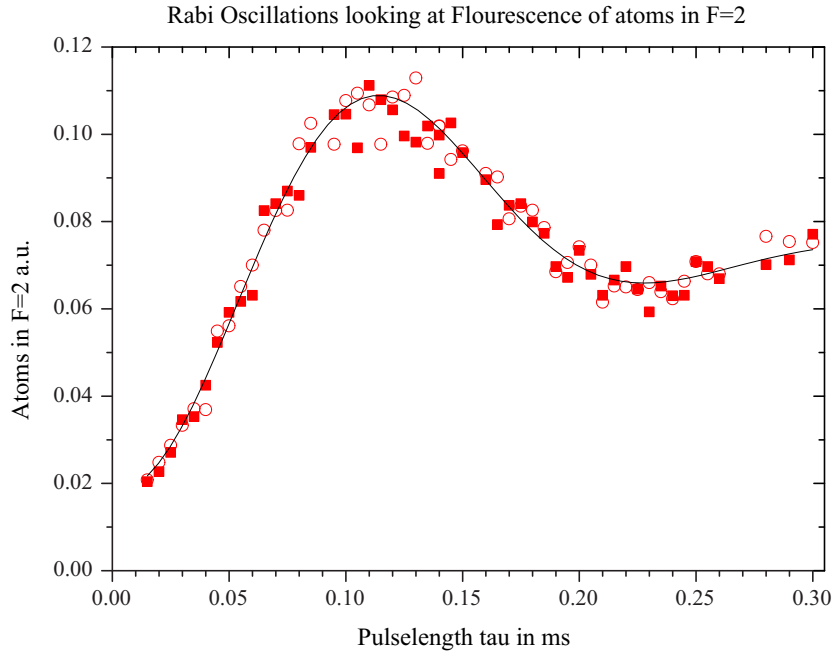


Figure 5.22: Rabi-oscillations for counter-propagating Raman beams with an effective k -vector of $\mathbf{k}_{\text{eff}} = 1.5 \cdot 10^5 \text{ cm}^{-1}$. A fit with a damped cosine leads to a Rabi-frequency around 4 kHz. The measurement was done for a detuning of $\Delta = 3.3 \text{ GHz}$ and around 36 mW total power in both Raman beams, which makes 9 mW in each circularly polarized beam component.

spacing, the Raman lasers need to compensate the Doppler effect during this time interval or will be far out of resonance by the time of the second pulse. A linear frequency ramp is applied to one of the signal generators (Agilent 33250A, see section 4.4.4), which controls the difference of both Raman lasers $\omega_{L1} - \omega_{L2}$ and we adjusted the ramp experimentally to be exactly in resonance at the moment of the velocity selection pulse T_1 and the time of the interferometer $T_2 = T_1 + 200 \text{ ms}$. Obviously this frequency matches exactly the hyperfine transition frequency ω_{HF} between $F = 1$ and $F = 2$ for zero velocity of the atoms.

Just for curiosity we can have a look at the g -value, which results from this frequency matching:

$$2\pi\Delta(t) \equiv \omega'_{L1}(t) - \omega'_{L2}(t) = \omega_{L1,0}\left(1 + \frac{v(t)}{c}\right) - \omega_{L2,0}\left(1 - \frac{v(t)}{c}\right) \quad (5.34)$$

$$= \underbrace{\omega_{L1,0} - \omega_{L2,0}}_{\omega_{HF}} + \frac{v(t)}{c} \underbrace{(\omega_{L1,0} + \omega_{L2,0})}_{\approx 2\omega_L} \quad (5.35)$$

$$= \omega_{HF} + \frac{2\omega_L}{c}(gt + v_0). \quad (5.36)$$

For a conservatively assumed frequency uncertainty of $\Delta f = 15 \text{ kHz}$ and a timing

uncertainty of $\Delta T = 5 \mu\text{s}$ follows

$$g = \frac{(\Delta(T_2) - \Delta(T_1))\lambda}{2(T_2 - T_1)} = 9.802 \pm 0.030 \text{ ms}^{-2}, \quad (5.37)$$

which is consistent with the value measured by a *reversion pendulum* of $(9.807 \pm 0.005) \text{ ms}^{-2}$ and the *calculated value* of $(9.805046 \pm 0.000009) \text{ ms}^{-2}$ (for geophysical calculation see Appendix B).

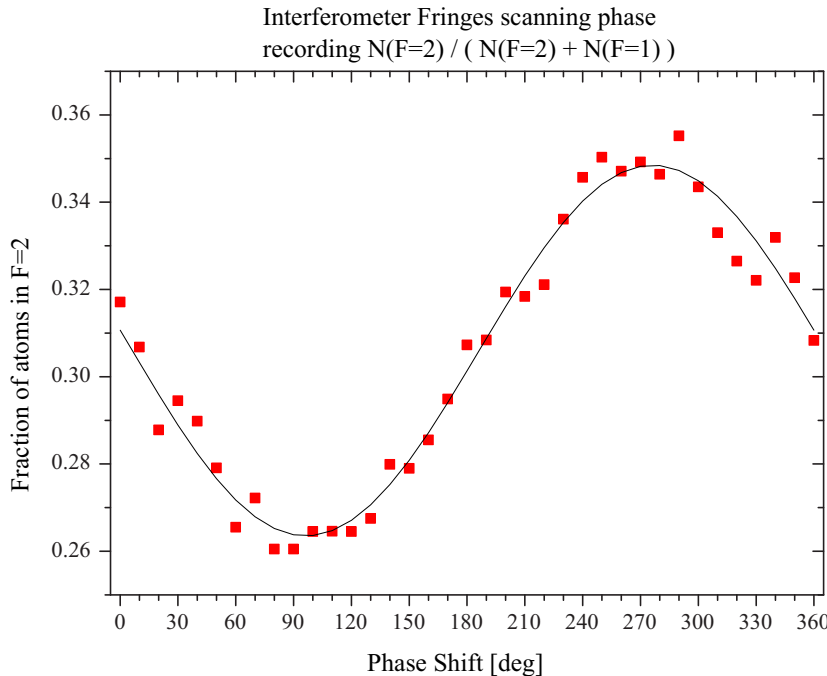


Figure 5.23: *Interferometer fringes for counter-propagating Raman beams for a controlled phase shift of the Raman beams $\phi_{\text{eff},0}$ during the interferometer. The total interferometer time $2T$ is 40 ms; the length of a π -pulse 100 μs . The sensitivity is about $5.46 \cdot 10^{-6} \text{ g}$ per shot.*

The actual interferometer signal for counter-propagating beams is shown in Figure 5.23 for a pulse spacing of 20 ms. Since our effective k -vector is a factor of 10^5 bigger than in the co-propagating case, the resolution of the g -measurement should now be around 10^{-6} g . In fact, a fit of the fringes of Fig. 5.23 with

$$P_{F=2} = A \left(1 + C \cos \left(\phi_{\text{eff},0} + \underbrace{N \cdot 2\pi + \phi_{\text{offs}}}_{=\Delta\phi_I} \right) \right) \quad (5.38)$$

leads to an uncertainty of the interferometer phase $\delta(\Delta\phi_I)$ of 0.0287 rad, which corresponds to an uncertainty in g of

$$\delta g = \frac{\delta(\Delta\phi_I)}{(k_{\text{eff}} T^2)} = 9.1 \cdot 10^{-7} \text{ g}. \quad (5.39)$$

The contrast is 0.14. The whole measurement of 36 shots has been performed in 90 s what means a sensitivity of

$$\frac{\Delta g}{g} = 9.1 \cdot 10^{-7} \cdot \sqrt{90} \frac{1}{\sqrt{\text{Hz}}} = 8.6 \cdot 10^{-6} \frac{1}{\sqrt{\text{Hz}}} \quad (5.40)$$

or $5.46 \cdot 10^{-6} \text{ } 1/\sqrt{\text{Hz}}$ per shot.

To give an absolute value of g , one would have to know the factor N in (5.38): a phase difference of 2π corresponds to $\Delta g = 2 \cdot 10^{-4} g$ ⁵.

An absolute measurement of g can be performed by scanning the interferometer time T and adjusting the frequency ramp of the Raman lasers until one comes to lie in the minimum of the quadratic dependence of $\Delta\phi$ on g , at which point one has reached an exact compensation of the gravitational acceleration with the frequency ramp.

However, also this value would be useless without a careful study of the systematic effects, which has not been performed yet.

For longer pulse spacings than 20 ms, the contrast of the fringes dropped drastically such that for $T = 60$ ms the fringes were already almost invisible. Generally, the conditions of the experiment were very unfavorable for a good sensitivity:

- The optical table neither had neither an activated vibration isolation nor a protection from air fluctuations. Activating the pneumatic stabilization system did not reduce the noise significantly.
- During the measurements, we had to artificially degrade the phase lock by reducing the high frequency gain to avoid a jump out of lock during the frequency scan of the local oscillator. This problem has been fixed now.
- The missing amplitude control of the Raman lasers enables fluctuations in the Rabi frequency and – more important – do not allow to make the velocity selection pulse much longer than the interferometer pulses to first do a strict v-selection and then address all atoms during the interferometer.
- The biggest problem is the strongly fluctuating number of atoms and the temperature from one launch to another. Calculating the relation between two populations does not eliminate all errors introduced by these fluctuations. The problem depends on the beam alignment of the cooling beams, magnetic fields and the power stability of the lasers (we noticed some fibers with badly aligned polarization). We plan a magnetic shielding around the whole apparatus and an amplitude control of all lasers.

⁵For an interferometer time of $T = 20$ ms, gravity g will provoke a phase signal of $\Delta\phi = 6.3 \cdot 10^4 \text{ rad}$. For the final aimed interferometer time of $T = 150$ ms, this signal increases to $\Delta\phi = 3.6 \cdot 10^6 \text{ rad}$.

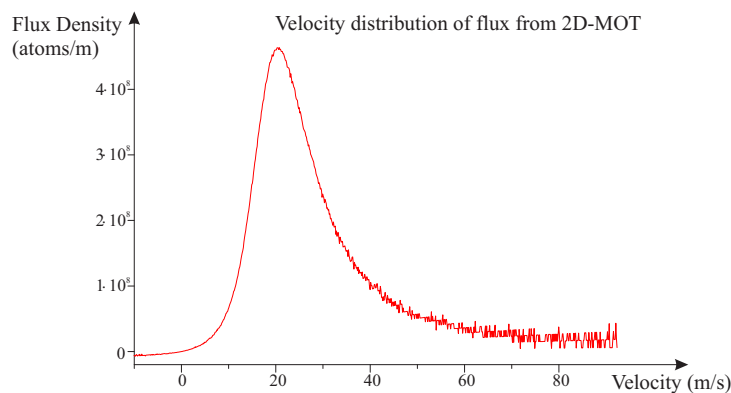
Chapter 6

Conclusion

At this point, we will summarize the work that has been described within this thesis and that has been carried out in the group of the gravimeter for the new BNM Watt-balance during my presence there, and in the group of the MAGIA gradiometer experiment. A small outlook on the milestones of the two experiments will bring this thesis to a termination.

6.1 Summary of work on gravimeter experiment

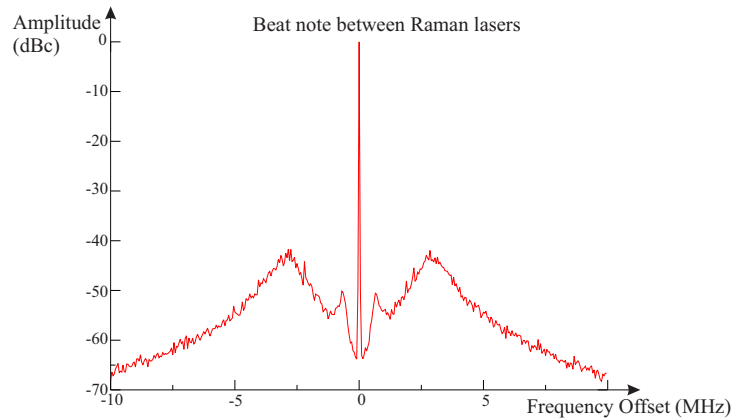
At the gravimeter experiment, we have assembled a *two-dimensional magneto-optical trap* (2D-MOT) to produce a cold beam of transversally cooled atoms. A factor of four in the flux could be gained by the implementation of an on-axis pushing beam. Fluorescence and absorption measurement on the atom beam indicate a flux of up to 10^{10} atoms/s which escape the 2D-MOT cell in a beam of 40 mrad full divergence angle. The atoms travel with a mean longitudinal velocity of 29 m/s, which means that almost all atoms can be trapped by a 3D-MOT. In fact, a loading rate of a 3D-MOT with $3 \cdot 10^9$ atoms/s could be observed.



A first version of a laser system for the gravimeter has been completed on a 60×60 cm breadboard. We stabilized an extended cavity diode laser (ECDL) to an atomic transition frequency and realized *two tunable frequency stabilization systems*, which lock both, the difference frequency between the first and a second ECDL laser in the range of several GHz, and the difference frequency between the second and a third ECDL laser in the same frequency range. A particularity of this system is the ability to perform frequency sweeps of 2 GHz in less than 1 ms without loosing the lock or provoking mode-jumps on the one hand, and the ability to switch between frequency and phase lock on the other hand.

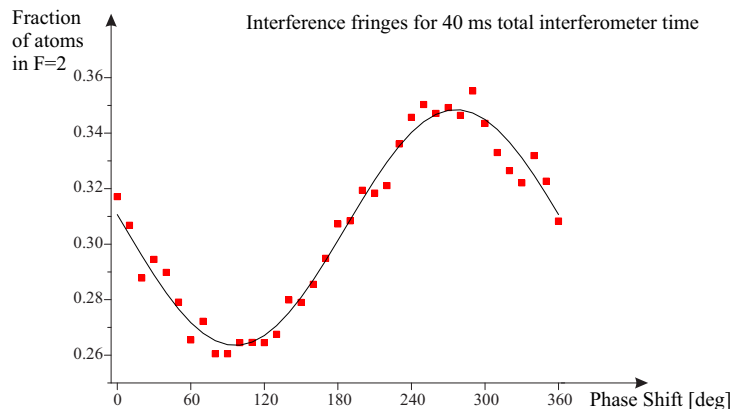
6.2 Summary of work on gradiometer experiment

At the gradiometer experiment, we designed and mounted the UHV apparatus with the experiment chamber by applying new sealing techniques. A system of optical fibres and fiber-splitters delivers the laser light that is required for the manipulation of the atoms and which is produced by a *laser system* an a separate optical table, to the experiment chamber. At the gravimeter as well as on the gradiometer, we made experiences with various ECDL-configurations like the implementation of interference filters in the extended cavity or the use of new anti-reflection coated diodes. For the frequency stabilization of one of the lasers, we developed a new modulation-free spectroscopy method.



Gravimeter and gradiometer both employ the same Raman light-pulse interferometer, which requires the *phase stabilization* of the two lasers that drive the Raman transitions. The reason is the transmission of the laser phase-noise onto the interferometer signal with a certain weight during the interaction of the light with the atoms. This weight-function has been calculated to evaluate the frequency dependent importance of the laser phase-noise, which, for the high resolution that our experiments aim at, must remain on the order of 1 mrad. At the gradiometer, a combination of a digital and analog phase-detector assures low noise and a big capture range of the lock.

Under typical conditions, we loaded 10^9 atoms into a magneto-optical trap (MOT) within one or two seconds and launched the cooled atoms with a temperature of $< 4 \mu\text{K}$ up into the interferometer region. We were able to launch two clouds of $5 \cdot 10^8$ atoms right after another at a temporal distance of 100 ms by *juggling*. After a velocity selection and state preparation on one cloud, we applied a Raman pulse of varying length to observe *Rabi oscillations*. By the application of the whole interferometer sequence we were able to see the *interferometer fringes* for co- and counter-propagating Raman beams. A scan over the fringes was done by changing the phase of the Raman lasers. The phase resolution in the counter-propagating case corresponds to a resolution of accelerations of $5.5 \cdot 10^{-5} \text{ m/s}^2$ per shot.



To proceed versus a measurement of the Newtonian constant of gravitation, we studied the effect of the gravitational acceleration of *masses* of 500 kg tungsten near the atoms. We theoretically optimized the relative positions of source masses and atoms to be the most insensitive on fluctuations of the atomic positions, making use of the compensation of the Earth gravity gradient by the source masses' acceleration. A double differential measurement to eliminate many systematic effects requires a support, which is able to move the heavy source masses with high accuracy. This support is ready to be mounted on the experiment and is equipped with preliminary lead masses until the final masses will be characterized. This projected mounting leads us smoothly to a small outlook on the future milestones of the two experiment.

6.3 Milestones of gravimeter

In the year 2005, the first interference fringes are expected, and a careful study of systematic effects and elimination of noise sources will begin to enable a high accuracy *measurement of g*.

As soon as the accuracy reaches the order of $\Delta g/g = 10^8$, the experiment could principally be transported to the location of the *Watt balance* for preliminary tests of the

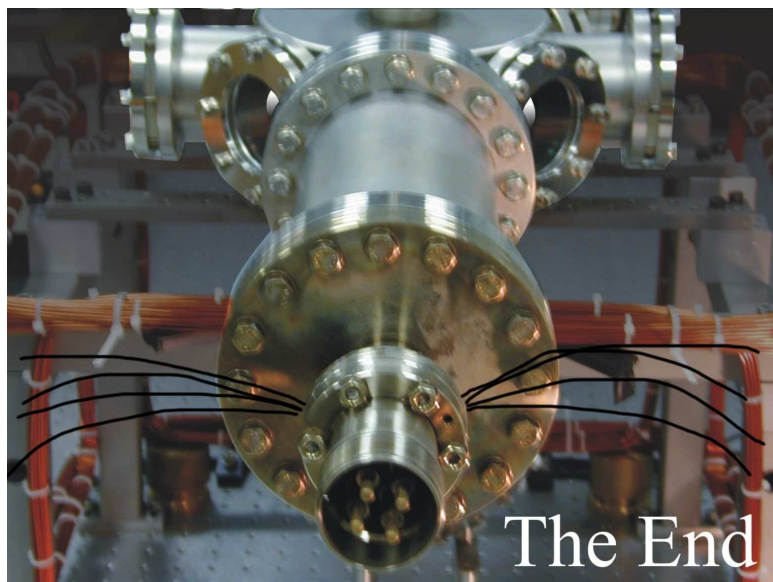
whole ensemble of apparatuses involved in this measurement. *Comparisons* with other absolute gravimeters like the FG5 are projected. To finally arrive at the desired accuracy of $\Delta g/g = 10^{-9}$ will require some more time and effort.

6.4 Milestones of gradiometer

At a certain point, the temperature and corresponding spatial spread will limit the performance of the gradiometer and we already designed the apparatus in view of the future implementation of *Raman sideband cooling* in a moving lattice. This technique has been successfully applied in a Cesium fountain [144] and we expect to reach temperatures well below $1 \mu\text{K}$ also in the case of rubidium [146].

For 2005, we preview the first differential interferometer signals with two clouds. We will mount the source masses and their influence on the signal should be visible. Then the long work of improving the resolution doing systematic studies will begin to obtain *a value for G* within our targeted accuracy of $\Delta G/G = 10^{-4}$.

The differential measurement of the MAGIA apparatus will allow a determination of the *gravity gradient* (see Appendix B). Once reached a sufficiently high accuracy, one could also think of measuring the effect of *curvature of gravitational attraction* (see Appendix B) not of the Earth but of nearby heavy objects like the optical table. Our apparatus offers the advantage of a relative insensitivity to the launch parameters due to the partial compensation of the gradient by the gravitational potential of the source masses at the position of the measurement.



Appendix A

Rubidium Data

This appendix will supply some numbers about the D2-transition that are useful for rubidium-experiments. One will find the line-spacing together with the spectroscopy signals to identify the transitions, the numbers to calculate the transitions probabilities, the temperature-pressure dependence besides some further data. Most information in this section is taken from [118].

A.1 Rubidium spectroscopy signals

Figure A.1 shows the level diagram of ^{85}Rb and ^{87}Rb with information about frequencies, Landé-factors g_F and the Zeeman splitting energy as a multiple of the quantum number m_F . Below we see the corresponding Doppler-free saturated absorption signal with the one-photon transitions allowed by the selection rules.

The spectroscopy setup with counter-propagating pump- and probe beams enables so-called Cross-Over (CO) transitions: atoms that have a certain velocity along the propagation axis of the beams will experience a Doppler shift of the light. If pump- and probe beam are counter-propagating, their frequencies will be Doppler-shifted by the same amount but to opposite directions in the reference system of the atom. If such the laser frequency is centered between two transition frequencies, atoms of the right velocity class may absorb photons of both beams, each on another transition. Our notation is the following: Transition $F = A \leftrightarrow F' = B$ is called A-B and crossover transitions in resonance with $F = A \leftrightarrow F' = B$ and $F = A \leftrightarrow F' = C$ are called CO A-BC.

Figure A.3 shows all ^{87}Rb and ^{85}Rb D2 transitions seen by Doppler-free saturated absorption spectroscopy in absolute frequencies.

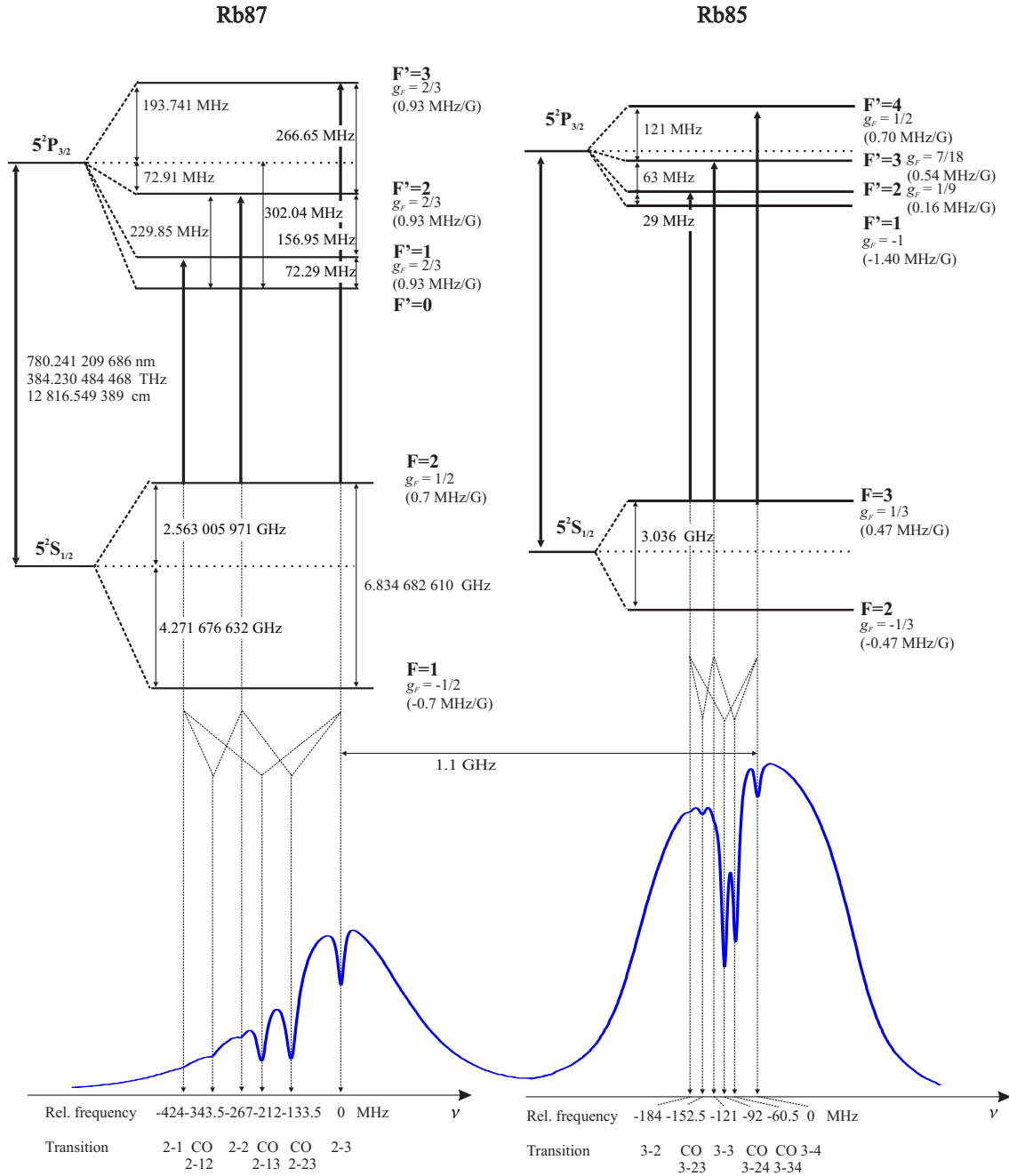


Figure A.1: Rubidium D2 transitions from the upper hyperfine-level of the ground state. Indicated are transition frequencies, information about the levels and below the corresponding saturated absorption spectroscopy signal. The indications for the Zeeman shift need to be multiplied by the m_F quantum number.

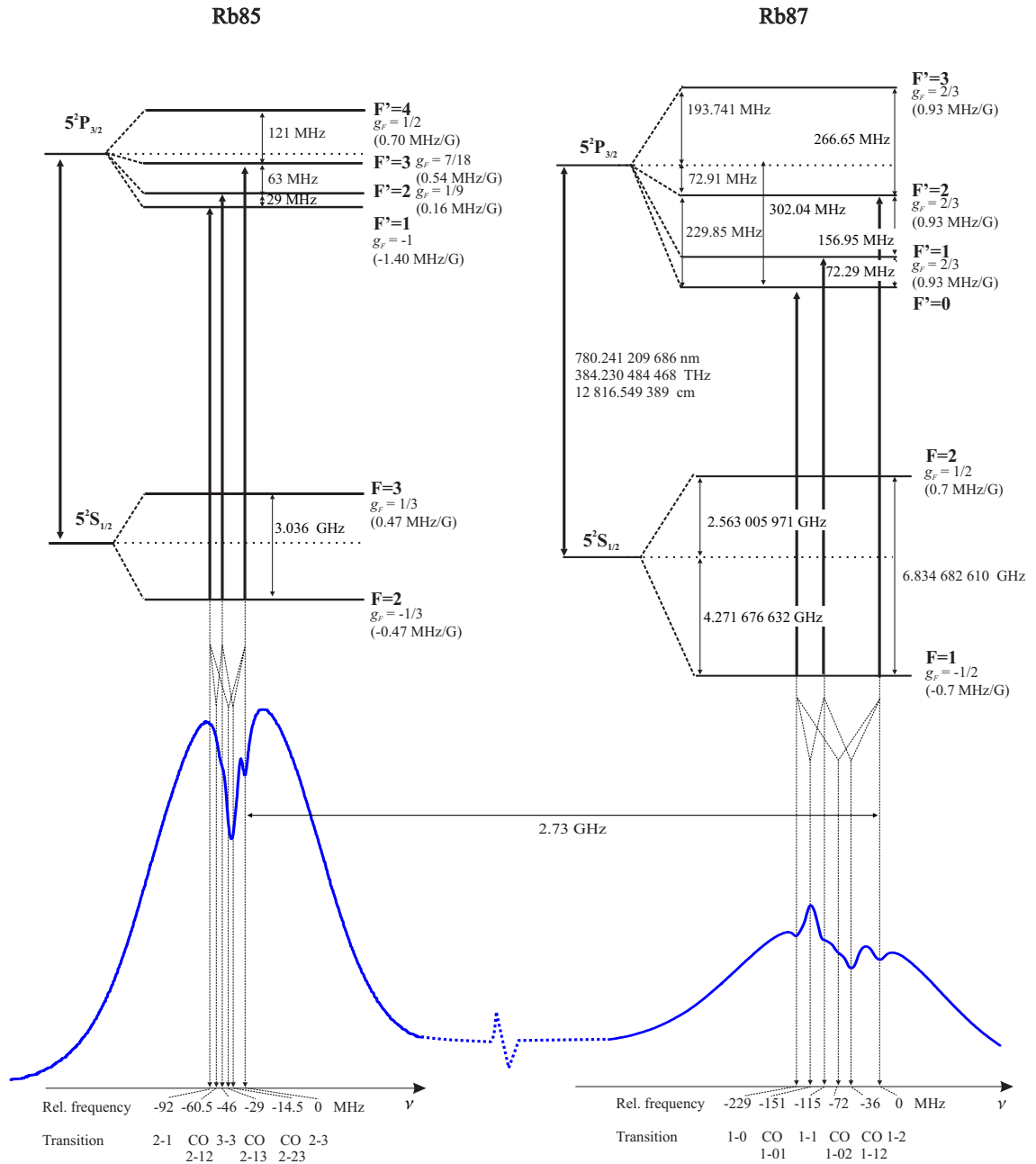


Figure A.2: Rubidium D2 transitions from the lower hyperfine-level of the ground state. Indicated are transition frequencies, information about the levels and below the corresponding saturated absorption spectroscopy signal.

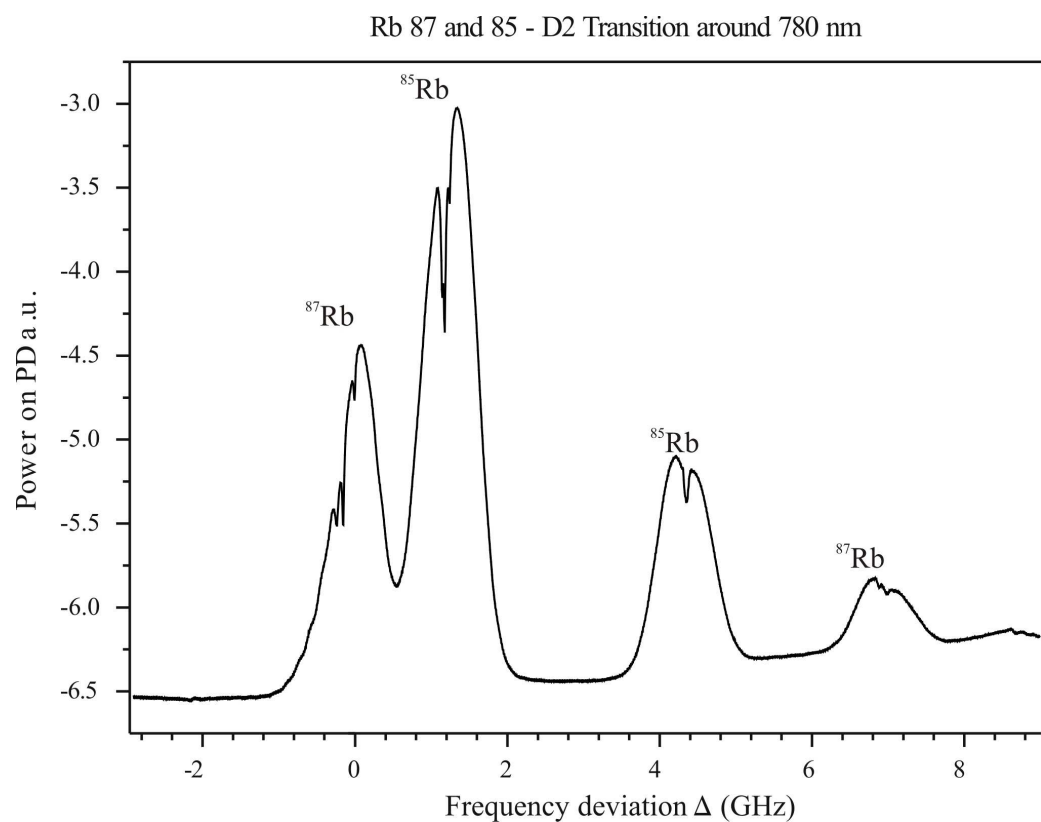


Figure A.3: *Doppler-free saturated absorption spectroscopy signal of rubidium vapor. Frequency deviation from cooling transition 2-3.*

A.2 Transition probabilities

For the calculation of the Rabi-frequency Ω , one needs to know the dipole matrix elements $\langle Fm_F | \mathbf{d} = e\mathbf{r} | F'm'_F \rangle$ coupling two hyperfine sublevels $|Fm_F\rangle$ and $|F'm'_F\rangle$. One usually factors out the angular dependence and writes the matrix element as a product of a Clebsch-Gordan (CG) coefficient and a reduced matrix element (see [138]):

$$\begin{aligned}\langle Fm_F | er_q | F'm'_F \rangle &= \langle F | er | F' \rangle \underbrace{\langle Fm_F | F'm'_F q \rangle}_{\text{CG}} \quad (\text{A.1}) \\ &= \langle F | er | F' \rangle (-1)^{F'-2+m_F} \sqrt{2F+1} \left(\begin{array}{ccc} F' & 1 & F \\ m'_F & q & -m_F \end{array} \right)\end{aligned}$$

Here, r_q denotes the component of \mathbf{r} in a spherical basis and the double bar \parallel indicates that the matrix element is reduced. The CG has been expressed using the Wigner 3-j symbol, which describes the coupled angular momentum of two quantum systems. If we further simplify the matrix element by factoring out the dependence on F , the remaining further reduced matrix element only depends on L, S and J quantum numbers

$$\begin{aligned}\langle F | er | F' \rangle &= \langle JIF | er | J'I'F' \rangle \quad (\text{A.2}) \\ &= \underbrace{\langle J | er | J' \rangle (-1)^{F'+J+1+I} \sqrt{(2F'+1)(2J+1)}}_{\text{Multiple}} \left\{ \begin{array}{ccc} J & J' & 1 \\ F' & F & I \end{array} \right\}\end{aligned}$$

We introduced the Wigner 6-j symbol, which is a generalization of Clebsch-Gordan coefficients and the Wigner 3j-symbol that arise in the coupling of three angular momenta. Its form is of no importance here, it can be found in quantum mechanics textbooks like [147] and can be calculated in Mathematica with the function "SixJSymbol[{J, J', 1}, {F', F, I}]". The numerical value of the reduced matrix element for the ^{87}Rb D₂ transition is

$$\langle J = 1/2 | er | J' = 3/2 \rangle = 3.58 \cdot 10^{-29} \text{ C m.} \quad (\text{A.3})$$

Picture A.4 indicates the multiples of the matrix element (A.3), indicated as "Multiple" in (A.2) according to reference [138].

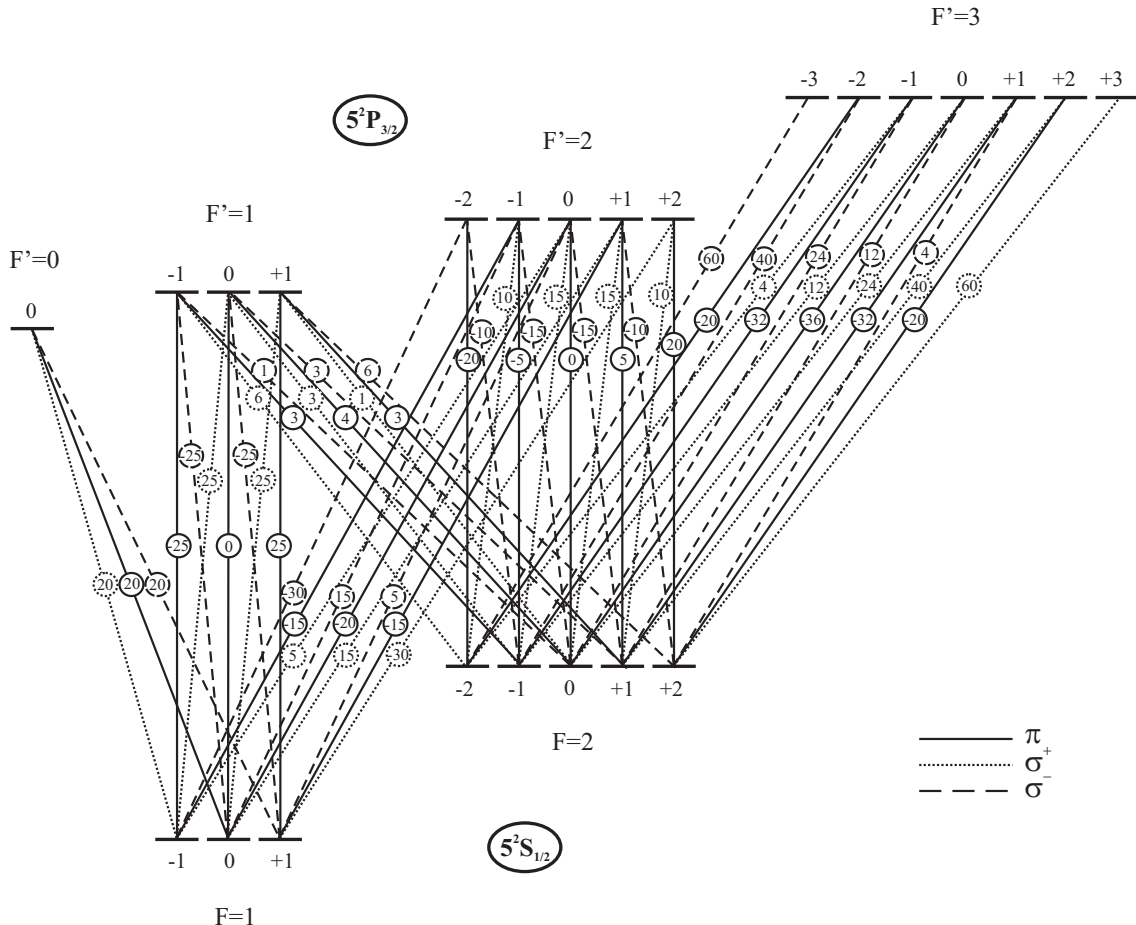


Figure A.4: Multiples of dipole matrix elements $\langle J = 1/2 | \mathbf{e} \mathbf{r} | J' = 3/2 \rangle$ for the ^{87}Rb D_2 transition from $|F m_F\rangle$ to $|F' m_{F'}\rangle$. The indicated values are the squares of the right value "Multiple" modulo 120 with the right sign. One therefore has to divide the indicated value by 120, take the square-root and then apply the indicated sign to get the actual value. Example: $-\sqrt{\frac{20}{120}} = -\sqrt{\frac{1}{6}}$ is indicated in the picture as -20.

A.3 Temperature dependence of pressure

The temperature dependent rubidium pressure in Torr can be estimated sufficiently well by:

$$p_{\text{Rb,vapor}}(T) = 10^{-4208/T+7.331} \text{ Torr} \quad (\text{A.4})$$

with the temperature T in K. The melting point of Rb is at 312,6 K (39.31°C) at a gas-pressure of $p = 1.56 \cdot 10^{-4}$ Pa and the boiling point at 961 K (688 °C).

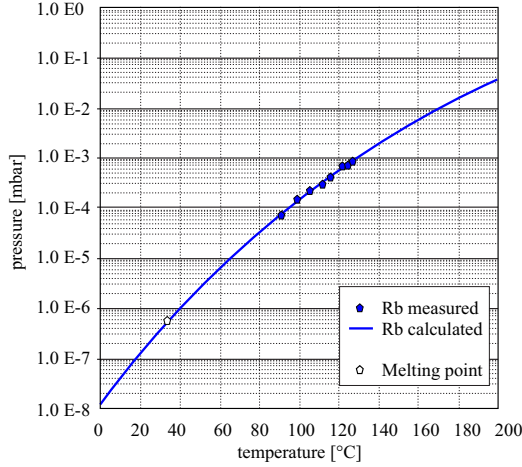


Figure A.5: Vapor pressure of Rb. The picture taken from [135] has been processed for the sake of clarity.

A.4 Further useful numbers on ^{87}Rb

Natural linewidth FWHM	$\Gamma =$	$2\pi \cdot 6.065 \text{ MHz}$
Recoil velocity	$v_{rc} =$	$\frac{\hbar k_L}{m} = 5.88 \text{ mm/s}$
Recoil energy	$\hbar \omega_{rc} =$	$\frac{\hbar^2 k_L^2}{2m} = \hbar \cdot 2\pi \cdot 3.77 \text{ kHz}$
Recoil temperature	$T_{rc} =$	$\frac{\hbar k_B}{m k_B} = 362 \text{ nK}$
Doppler temperature	$T_D =$	$\frac{\hbar \Gamma}{2k_B} = 146 \mu\text{K}$
Effective Saturation Intensities	$I_{\text{sat}, \sigma^\pm} =$	$\frac{c\epsilon_0 \Gamma^2 \hbar^2}{4 \mathbf{e} \cdot \mathbf{d}_{\text{eff}, \text{far}, \pi} ^2} = 1.67 \text{ mW/cm}^2$
	$I_{\text{sat}, \text{iso.}} =$	$\frac{c\epsilon_0 \Gamma^2 \hbar^2}{4 \mathbf{e} \cdot \mathbf{d}_{\text{eff}, \text{iso.}} ^2} = 3.58 \text{ mW/cm}^2$
	$I_{\text{sat}, \text{far}\pi} =$	$\frac{c\epsilon_0 \Gamma^2 \hbar^2}{4 \mathbf{e} \cdot \mathbf{d}_{\text{eff}\sigma^\pm} ^2} = 3.58 \text{ mW/cm}^2$

[118]. Here, k_B is the Boltzmann constant, k_L the wave-vector of the laser light, \mathbf{e} the unit polarization vector of the light field and \mathbf{d}_{eff} the effective dipole operator of all possible transitions in the particular cases of isotropically polarized light field, far detuned, π -polarized light and σ^\pm -polarized light. In these three cases, the sum over all matrix elements (A.1) simplifies and allows an easy calculation of $|\mathbf{d}_{\text{eff}}|^2$. In these cases, the atom behaves like a two-level atom (considering only the D₂-transition) and the saturation intensities can be calculated according to the above expressions or (with $I = 1/2 c\epsilon_0 E_0^2$)

$$\frac{I}{I_{\text{sat}}} = 2 \left(\frac{\Omega}{\Gamma} \right)^2. \quad (\text{A.5})$$

We specified the saturation intensities $I_{\text{sat}, \sigma^\pm}$ for circular polarized light on the cooling transition $|F = 2, m_F = \pm 2\rangle \rightarrow |F' = 3, m_{F'} = 3\rangle$, $I_{\text{sat}, \text{iso.}}$ for an isotropic polarization on the transition $F = 2 \rightarrow F' = 3$ and $I_{\text{sat}, \text{far}}$ for π -polarized light, which is far detuned from the D₂-line. All intensities are given for the steady state condition. In these cases,

we can also calculate the scattering cross-sections from the saturation intensities by the relation

$$\sigma = \frac{\sigma_0}{1 + 4(\Delta/\Gamma)^2 + (I/I_{\text{sat}})} , \quad (\text{A.6})$$

where Δ is the detuning of the laser frequency from resonance, Γ the natural linewidth and σ_0 the on-resonance scattering cross section

$$\sigma_0 = \frac{\hbar\omega\Gamma}{2I_{\text{sat}}} . \quad (\text{A.7})$$

Appendix B

Geophysical determination of gravity

B.1 Predicted value of g

International Gravity Formula: In 1930, the International Union of Geodesy and Geophysics adopted the international gravity formula, which allows to calculate the gravity value on Earth in dependence on the geographical latitude, taking into account an ellipsoid shape of the Earth [139]. The most recent update is the formula of the Geodetic Reference System (GRS) 1980, which leads to the World Geodetic System 1984 (WGS84), the base on which also GPS is working:

$$g_0 = 9.7803267714 \frac{1 + 0.00193185138639 \sin^2 \lambda}{\sqrt{1 - 0.00669437999013 \sin^2 \lambda}} \text{ ms}^{-2} \quad (\text{B.1})$$

where λ is the geographical latitude. The coordinates (coordinate conversion: [142]) for our laboratory are read out from a detailed satellite image with a precision of ± 5 meters [143]:

- *In Universal Transverse Mercator (UTM):*

Easting: (676427 ± 5) m,
Northing: (4854119 ± 5) m

- *In Degrees:*

Latitude λ : $43^\circ 49' (8.7 \pm 0.2)'' = (43.819083 \pm 0.000050)^\circ$,
Longitude: $17^\circ 11' (37.9 \pm 0.2)'' = (17.193861 \pm 0.000050)^\circ$

and it follows with (B.1) a gravity value on the GRS80 ellipsoid of

$$g_0 = (9.805130737 \pm 0.000000050) \text{ ms}^{-2} \quad (\text{B.2})$$



Figure B.1: Satellite image of physics department and LENS in Florence under construction. The web-site indicates the cursor position in the image with a precision of 10 cm when choosing a closer zoom.

Free Air Correction: Since our laboratory floor is located (36.5 ± 2) m above the ellipsoid and the experiment 1.5 m above the floor, we need to apply the free air correction (FAC)[140] for a height of $h = 38$ m above the GRS80 ellipsoid ¹:

$$\begin{aligned}\delta g_{FAC}(h) &= -(0,3087691 - 0,0004398 \sin^2 \lambda)h + 7,2125 \cdot 10^{-8} h^2 \text{ mGal} \\ &\approx (-11.725 \pm 0.61) \cdot 10^{-5} \text{ ms}^{-2}\end{aligned}\quad (\text{B.3})$$

The factors of this equation are calculated from the WGS84 values for the equatorial gravity on the ellipsoid, the Earth's flattening coefficient, the semi-major axis radius of the ellipsoid and the centrifugal force at the equator.

Bouger-correction: Finally, one has to add the so-called Bouger-correction $g_{BC}(H)$, which takes into account that a part of the height above the ellipsoid is filled with solid earth. We had access to the ground data taken during the construction of the department [141], which indicate a mean weight per volume of (20.5 ± 0.6) kN m³ of 119 samples taken between 1.5 and 44.5 meters depth. With the standardized $g = 9.80665 \text{ ms}^{-2}$ for the conversion to mass density $\rho = (2090 \pm 61) \text{ kg/m}^3$, we find a correction for $H = (36.5 \pm 1.5)$ m of

$$\begin{aligned}g_{BC}(H) &= 2\pi G \rho H \\ &\approx (3.20 \pm 5 \cdot 0.13) \cdot 10^{-5} \text{ ms}^{-2}\end{aligned}\quad (\text{B.4})$$

We increased the uncertainty by a factor of 5 to consider varying humidity of the ground.

¹The height above the ellipsoid GRS80, used for example by the GPS system, is not identical to the height above sea-level or geoid. It also is slightly different from the height above the previously used ellipsoid GRS67, still present in many maps.

Theoretical gravity value: Adding up all the above contributions to g

$$\begin{aligned} g &= g_0 + g_{FAC} + g_{BC} \\ &= \underline{(9.805046 \pm 0.000009) \text{ ms}^{-2}} \end{aligned} \quad (\text{B.5})$$

should predict the measured gravity value in our laboratory with an uncertainty of $\Delta g \approx 1 \cdot 10^{-5} \text{ ms}^{-2}$ or $\Delta g/g \approx 10^{-6}$.

Nearby masses will provoke minor changes of the acceleration which have no influence on the given uncertainty; the gravitational acceleration of for example a 200 kg mass at 1 m distance is

$$a_{200 \text{ kg}} = 1.4 \cdot 10^{-8} \text{ ms}^{-2} = 10^{-9} g \quad (\text{B.6})$$

B.2 Predicted value of γ , γ' and γ''

The Earth's *gravity gradient* in free air at $h = (38 \pm 2)$ m height and for our latitude of $\lambda = (43.819083 \pm 0.000050)^\circ$ is

$$\begin{aligned} \gamma(h) &= \frac{\partial g(h)}{\partial h} = \frac{\partial g_{FAC}(h)}{\partial h} \\ &= -(0,3087691 - 0,0004398 \sin^2 \lambda) + 2 \cdot 7,2125 \cdot 10^{-8} h \text{ mGal} \\ &\approx (-3.08555543 \pm 0.00000144) \cdot 10^{-6} \text{ s}^{-2} \\ &= (-3.08555543 \cdot 10^{-6} \pm 1.44 \cdot 10^{-12}) \text{ s}^{-2}. \end{aligned} \quad (\text{B.7})$$

Obviously, the biggest uncertainty will arise from effects, which have not been considered yet like the gradients arising from nearby masses as for example the optical table.

A mass of 200 kg would create a gradient of

$$a'_{200 \text{ kg}} = 2.7 \cdot 10^{-8} \text{ s}^{-2} = 10^{-2} \gamma \text{ per meter} \quad (\text{B.8})$$

at 1 m distance and we therefore should realistically write the theoretical gradient as

$$\underline{\gamma = (-3.09 \pm 0.1) \cdot 10^{-6} \text{ s}^{-2}}. \quad (\text{B.9})$$

The *curvature of the Earth's gravity gradient* is

$$\begin{aligned} \gamma'(h) &= \frac{\partial \gamma(h)}{\partial h} = 2 \cdot 7,2125 \cdot 10^{-8} \text{ mGal} \\ &= 1.44 \cdot 10^{-12} \text{ m}^{-1} \text{s}^{-2} \\ &= \underline{4.66 \cdot 10^{-7} \gamma \text{ m}^{-1}}. \end{aligned} \quad (\text{B.10})$$

Nearby masses like the optical table show much bigger curvatures: the gravity field of a 200 kg mass at 1 m distance has a curvature of

$$a''_{200 \text{ kg}} = 8 \cdot 10^{-8} \text{ m}^{-1} \text{s}^{-2} = 10^5 \gamma', \quad (\text{B.11})$$

which would come into the range of sensitivity of the MAGIA gradiometer.

Bibliography

- [1] Aristotle, *On the Heavens*, Athens (350 B.E.C). Translation by J.L. Stocks in <http://classics.mit.edu/Aristotle/heavens.html> *Page 1*
- [2] Johannes Kepler *Astronomia Nova*, Heidelberg (1609). *Page 2*
- [3] Galileo Galilei *Dialogo dei massimi sistemi*, Florence (1632). *Page 2*
- [4] René Descartes *Principia Philosophiae*, Amsterdam (1644). *Page 2*
- [5] Isaac Newton *Philosophiae Naturalis Principia Mathematica*, London (1687). *Page 2*
- [6] Steven Chu, Interview in *American Scientist*, **86** (1998). *Page 3*
- [7] H. Rauch, W. Treimer, U. Bonse 1974, *Phys. Lett.*, **47A**, 369 (1974). *Page 6*
- [8] K. Moler, D.S. Weiss, M. Kasevich, S. Chu, *Phys. Rev. A*, **45**, 1 (1992). *Page 34, 38*
- [9] S. Fray, C. Alvarez Diez, T.W. Hänsch, M. Weitz, *Phys. Rev. Lett.*, **93**, 240404 (2004). *Page 10*
- [10] L. Feenstra, L.M. Andersson, J. Schmiedayer, *arXiv:cond-mat/0302059 v1* (2003). *Page 7*
- [11] E.M. Rasel, M.K. Oberthaler, H. Batelaan, J. Schmiedmayer, A. Zeilinger, *Phys. Rev. Lett.*, **75**, 2633, (1995). *Page 6*
- [12] D.W. Keith, C.R. Ekstrom, Q.A. Turchette, D.E. Pritchard, *Phys. Rev. Lett.*, **66**, 2693 (1991). *Page 6*
- [13] O. Carnal, J. Mlynek, *Phys. Rev. Lett.*, **66**, 2689 (1991). *Page 6*
- [14] F. Riehle, Th. Kisters, A. Witte, and J. Helmcke, *Phys. Rev. Lett.*, **67**, 177 (1991). *Page 6*
- [15] M. Kasevich, S. Chu, *Appl. Phys. B*, **54**, 321 (1992). *Page 6*

- [16] P.J. Martin, B.G. Oklaker, A.H. Miklich, D.E. Pritchard, *Phys. Rev. Lett.*, **60**, 515 (1988). *Page 6*
- [17] V.I. Balykin, V.S. Letokhov, Y.B. Ovchimnikov, A.I. Sidorov, *Phys. Rev. Lett.*, **60**, 2137 (1988). *Page 6*
- [18] C. Henkel, A.M. Steane, R. Kaiser, J. Dalibard, *J. Phys. II France*, **4**, 1877 (1994). *Page 6*
- [19] T. Pfau, C. Kurtsiefer, C.S. Adams, M. Siegel, J. Mlynek, *Phys. Rev. Lett.*, **71**, 3427 (1993). *Page 6*
- [20] C. Miniatura, J. Robert, O. Goreix, V. Laurent, S. le Boiteux, J. Reinhardt, J. Baudon, *Phys. Rev. Lett.*, **69**, 261 (1992). *Page 6*
- [21] S. Nowak, N. Stuhler, T. Pfau, J. Mlynek, *Phys. Rev. Lett.*, **81**, 5792 (1998). *Page 6*
- [22] Ch. Jentsch, *PhD Thesis, Konzeption und Aufbau ... Inertialsensorik mit lasergekühlten Rubidiumatomen*, Cuvillier Verlag Göttingen (2004). *Page 6*
- [23] F. Yver-Leduc; P. Cheinet; G. Fils; A. Clairon; N. Dimarcq; D. Holleville; P. Bouyer; A. Landragin, *J. Optics B, Quant. Semiclass. Opt.*, **5**, 136 (2003). *Page 6*
- [24] M.W. Zwierlein, Z. Hadzibabic, S. Gupta, W. Ketterle, *Phys. Rev. Lett.*, **91**, 250404 (2003). *Page 7*
- [25] A. Kehagias, K. Sfetsos, *arXiv:hep-ph/9905417 v3* (1999). *Page 8*
- [26] J. Long, J.C. Price, *arXiv:hep-ph/0303057 v2* (2004). *Page 8*
- [27] R. Mathevet, R. Delhuille, C. Rizzo, *Class.Quantum Grav.*, **19**, L37 (2002). *Page 8*
- [28] S. Dimopoulos, A.A. Geraci, *Phys. Rev. D*, **68**, 124021 (2003). *Page 8*
- [29] A.D. Speliotopoulos, R.Y. Chiao, *arXiv:gr-qc/0406096 v1* (2004). *Page 9*
- [30] LISA homepage, <http://lisa.jpl.nasa.gov/> *Page 9*
- [31] S. Gupta, K. Diekmann, Z. Hadzibabic, D.E. Pritchard, *Phys. Rev. Lett.*, **89**, 140401 (2002). *Page 7, 8*
- [32] M. Kasevich, E. Riis, S. Chu, R. DeVoe, *Phys. Rev. Lett.*, **63**, 612 (1989). *Page*
- [33] C. Cohen-Tanoudji, lecture, *Interferometrie atomique* (1992-93). *Page 34, 43*
- [34] K. Bongs, R. Launay, M.A. Kasevich, *eprint arXiv:quant-ph/0204102* (2002). *Page 50*

- [35] A. Wicht, J.M. Hensley, E. Sarajlic, S. Chu, *Phys. Scripta*, **T102**, 82 (2002). *Page 6*
- [36] R. Battesti, *PhD Thesis Université Paris 6*, Accélération d'atomes ultrafroids; mesure de h/M (2003). *Page 6*
- [37] R. Battesti, P. Cladé, S. Guellati-Khélifa, C. Schwob, B. Grémaud, F. Nez, L. Julien, F. Biraben, *Phys. Rev. Lett.*, **92**, 253001 (2004). *Page 6*
- [38] B. Young, M. Kasevich, S. Chu, In: *Atom Interferometry*, edited by P. R. Berman, Academic Press, San Diego (1997). *Page 27, 30*
- [39] Y.-J. Wang, D.Z. Anderson, V.M. Bright, E.A. Cornell, Q. Diot, T. Kishimoto, M. Prentiss, R.A. Saravanan, S.R. Segal, S. Wu, *oai:arXiv.org:cond-mat/0407689* (2004). *Page 7*
- [40] A. Poura, D.R. Brill, B.L. Hu, C.W. Misner, *arXiv:gr-qc/0409002 v1* (2004). *Page 9*
- [41] G. Roati, E. de Mirandes, F. Ferlaino, H. Ott, G. Modugno, M. Inguscio, *Phys. Rev. Lett.*, **92**, 230402 (2004). *Page 7*
- [42] M.J. Snadden, J.M. McGuirk, P. Bouyer, K.G. Haritos, M.A. Kasevich, *Phys. Rev. Lett.*, **81**, 971 (1998). *Page 6*
- [43] J.M. McGuirk, G.T. Foster, J.B. Fixler, M.J. Snadden, M.A. Kasevich, *Phys. Rev. A*, **65**, 033608 (2002). *Page 6, 19*
- [44] T.L. Gustavson, A. Landragin, M.A. Kasevich, *Class. Quantum Grav.*, **17**, 2385 (2000). *Page 6*
- [45] D.S. Weiss, B.C. Young, S. Chu, *Phys. Rev. Lett.*, **70**, 2706 (1993). *Page 6*
- [46] A. Peters, K.Y. Chung, S. Chu, *Metrologia*, **38**, 25 (2001). *Page 6, 13, 50*
- [47] R. Colella, A.W. Overhauser, S.A. Werner, *Phys. Rev. Lett.*, **34**, 1472 (1975). *Page 6*
- [48] D.B. Sullivan, D.A. Allan, D.A. Howe, F.L. Walls, *NIST Technical Note 1337*, Characterization of Clocks and Oscillators (1990). *Page 51, 53*
- [49] I appreciate the assistance of F. Pereira on the Dick effect. *Page 63*
- [50] P. Cheinet, B. Canuel, F. Pereira Dos Santos, A. Gauguet, F. Leduc, A. Landragin, *publication for IEEE in preparation* *Page 55, 63*
- [51] A. Quessada, R.P. Kovacich, I. Courtillot, A. Clairon, G. Santarelli, P. Lemonde, *J. of Optics B*, **5**, 1 (2003). *Page 55*

- [52] M. Fattori, *PhD Thesis, Universita di Firenze*, Sviluppo di un apparato per la misura di G mediante interferometria atomica (2004). *Page* 46, 93, 97, 146
- [53] C. Antoine, C.J. Bordé, *Phys. Lett. A*, **306**, 277 (2003). *Page* 49
- [54] C.J. Bordé, *Lecture, University of Hannover*, Theoretical tools for atom optics and interferometry (2001). *Page* 46, 47, 50
- [55] C.J. Bordé, *Metrologia*, **39**, 435 (2002). *Page* 47, 48
- [56] C.J. Bordé, *Gen. Rel. and Grav.*, **36**, 475 (2004). *Page* 47
- [57] Z.J. Jabbour, S.L. Yaniv, *J. Res. Natl. Inst. Stand. Technol.*, **106**, 25 (2001). *Page* 10
- [58] M. Van Camp, T. Camelbeeck, P. Richard, *Physicalia Magazine, J. of Belg. Soc.*, **25**, 161 (2003). *Page* 13
- [59] Special Issue on Sixth International Comparison of Absolute Gravimeters, *Metrologia*, **39**, 405 (2002). *Page* 13
- [60] A.C. Machacek, *Internal Report, University of Oxford* The Kilogram Definition, Realization and its replacement (1989). *Page* 11
- [61] P.R. Heyl, *J. Res. Natl. Bur. Standards, US*, **5**, 1243 (1930). *Page* 17
- [62] P.R. Heyl, P. Chrzanowski, *J. Res. Natl. Bur. Standards, US*, **29**, 1 (1942). *Page* 17
- [63] L. Facy, C. Pontikis, *C. R. Acad. Sci., Paris*, **272**, 1397 (1971). *Page* 17
- [64] M.U. Sagitov, V.K. Milyukov, Y.A. Monakhov, V.S. Nazarenko, K.G. Tadzhidinov, *Dokl. Akad. Nauk SSSR, Earth Sci.*, **245**, 567 (1979). *Page* 17
- [65] G.G. Luther, W.R. Towler, *Phys. Rev. Lett.*, **48**, 121 (1982). *Page* 17
- [66] H. de Boer, H. Haas, W. Michaelis, *Metrologia*, **24**, 171 (1987). *Page* 17
- [67] H. Walesch, H. Meyer, H. Piel, J. Schurr, *IEEE Trans. Instrum Meas.*, **44**, 491 (1995). *Page* 17
- [68] M.P. Fitzgerald, T.R. Armstrong, *IEEE Trans. Instrum Meas.*, **44**, 494 (1995). *Page* 17
- [69] W. Michaelis, H. Haars, R. Augustin, *Metrologia*, **32**, 267 (1995). *Page* 17
- [70] O.V. Karagoiz, V.P. Izmailov, G.T. Gillies, *Grav. Cosmol.*, **4**, 239 (1998). *Page* 17
- [71] C.H. Bagley, G.G. Luther, *Phys. Rev. Lett.*, **78**, 3047 (1997). *Page* 17

- [72] J.P. Schwarz, D.S. Robertson, T.M. Niebauer, J.E. Faller, *Science*, **282**, 2230 (1998). *Page* 17, 18
- [73] M.P. Fitzgerald, T.R. Armstrong, *Meas. Sci. Techn.*, **10**, 439 (1999). *Page* 17
- [74] F. Nolting, J. Schurr, S. Schlamminger, W. Kuendig, *Phys. Rev. Lett.*, **80**, 1142 (1998). *Page* 17
- [75] J. Luo, Z.K. Hu, X.H. Fu, S.H. Fan, *Phys. Rev. D*, **59**, 42001 (1998). *Page* 17
- [76] J.H. Gundlach, S.M. Merkowitz, *Phys. Rev. Lett.*, **85**, 2869 (2000). *Page* 17, 18
- [77] T.J. Quinn, C.C. Speak, S.J. Richman, R.S. Davies, A. Picard, *Phys. Rev. Lett.*, **87**, 111101 (2001). *Page* 17
- [78] S. Schlamminger, E. Halzschuh, W. Kuendig, *Phys. Rev. Lett.*, **89**, 161102 (2002). *Page* 17
- [79] U. Kleinevoss, *PhD Thesis, University of Wuppertal*, Bestimmung der Newtonschen Gravitationskonstanten (2002). *Page* 17
- [80] T.R. Armstrong, M.P. Fitzgerald, *Phys. Rev. Lett.*, **91**, 201101 (2003). *Page* 17
- [81] T. Damour, *Meas. Sci. Techn.*, **10**, 467 (1999). *Page* 16
- [82] G.T. Gillies, *Rep. Prog. Phys.*, **60**, 151 (1997). *Page* 16
- [83] L. Hodges, http://www.public.iastate.edu/~physics_221/Michell.htm, The Michelson-Cavendish experiment (1998). *Page* 16
- [84] H. Cavendish, *Phil. Trans. R. Soc.*, **83**, 470 (1789). *Page* 16
- [85] <http://www.ptb.de/en/org/I/12/124/ionenex.htm>, Ion Accumulation Experiment (2004). *Page* 11
- [86] B.P. Kibble, I.A. Robinson, J.H. Belliss, *Metrologia*, **27**, 173 (1990). *Page* 11
- [87] J.P. Mbelek, M. Lachièze-Rey, *arXiv:gr-qc/0204064 v1* and *Grav. Cosmol.*, **8**, 331 (2002). *Page* 16, 18
- [88] A. Spallicci, A. Brillet, G. Busca, G. Castatini, I. Pinto, I. Roxburgh, C. Salomon, M. Soffel, C. Veillet, *Class. Quantum Grav.*, **14**, 2971 (1997). *Page* 18
- [89] A.J. Sanders, A.D. Alexeev, S.W. Allison, K.A. Bronnikov, J.W. Campbellk, M.R. Cates, T.A. Corcovilos, D.D. Earl, T. Gadfort, G. T. Gillies, M.J. Harris, N.I. Kolosnitsyn, M. Yu Konstantinov, V. N. Melnikov, R.J. Newby, R. G. Schunkk, L.L. Smalley, *Meas. Sci. Technol.*, **10**, 514 (1999). *Page* 18
- [90] <http://www.esa.int/export/esaLP/goce.html> The Gravity Field and Steady-State Ocean Circulation Explorer mission *Page* 9

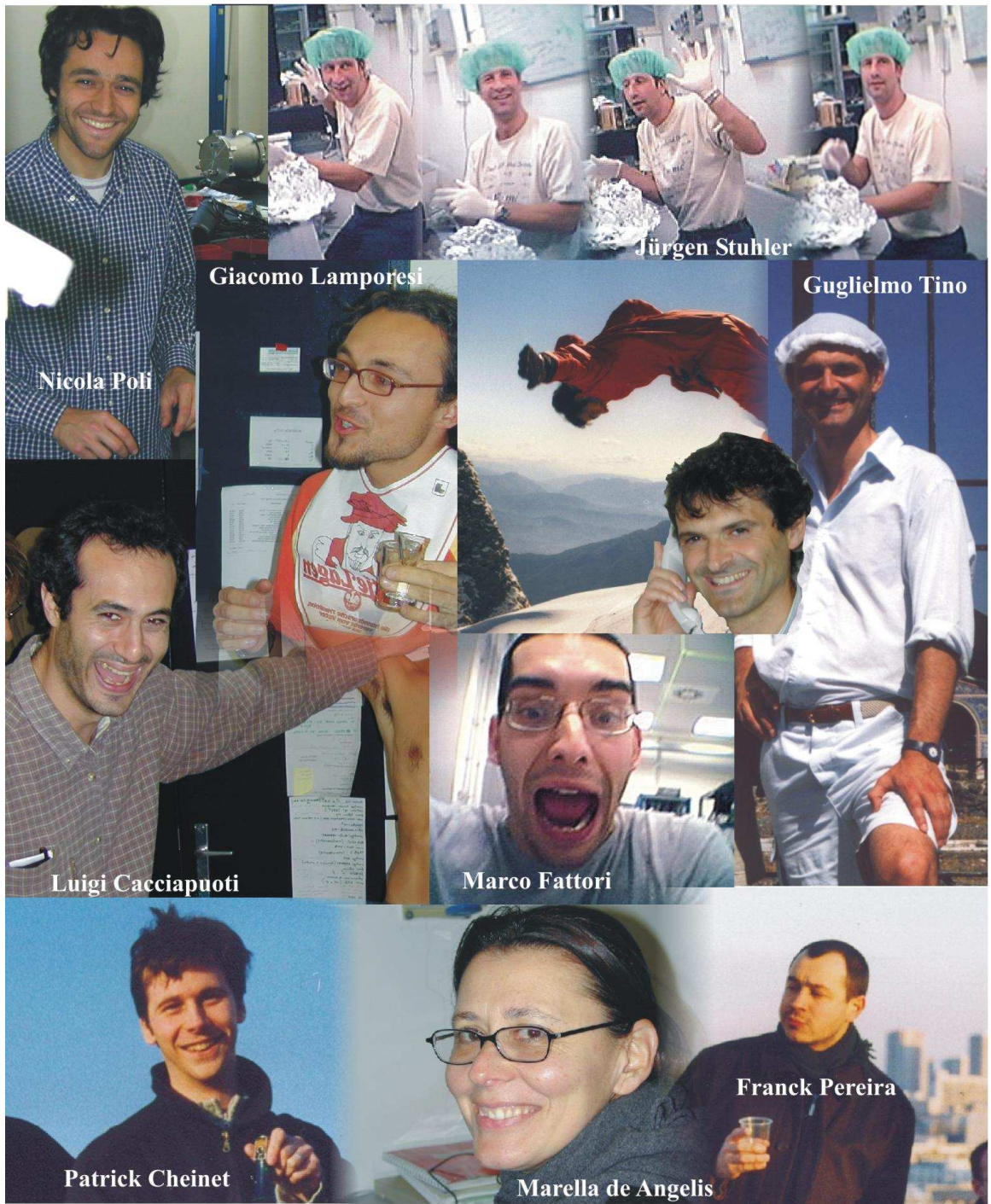
- [91] <http://www.csr.utexas.edu/grace/>, Gravity recovery and climate experiment GRACE *Page 9*
- [92] <http://www1.bipm.org/en/scientific/mass/prototype.html>, International prototype of the kilogram *Page 10*
- [93] Picture taken from homepage Steven Chu group <http://www.stanford.edu/group/chugroup/amo/interferometry.html> *Page 13*
- [94] Picture taken without permission from <http://www.microgsolutions.com/fg5.htm> *Page 13*
- [95] C.J. Bordé, *Gen. Rel. Grav.*, **36**, 475 (2004). *Page 10*
- [96] J. Stuhler, M. Fattori, T. Petelski, G.M. Tino, *J. Opt. B*, **5**, 75 (2003). *Page 6, 97*
- [97] L. Maleki, <http://www.esto.nasa.gov/conferences/estc2004/presentation/B4/b4p1.pdf> (2004). *Page 6, 7, 9*
- [98] M. Kasevich, http://www7.nationalacademies.org/bpa/kasevich_CAMOS_021124.pdf (2002). *Page 6, 7*
- [99] M. Wutz, H. Adam, W. Walcher, *Theorie und Praxis der Vakuumtechnik*, Friedr. Viehweg & Sohn (1988). *Page 71*
- [100] G. Lamporesi, *Master thesis, University of Florence*, Realizzazione di una fontana di atomi di rubidio per un interferometro atomico (2003). *Page 76, 146, 147*
- [101] A.L. Schawlow, C.H. Townes, *Phys. Rev.*, **112**, 1940 (1958). *Page 81*
- [102] L. Ricci, M. Weidenmüller, T. Esslinger, A. Hemmerich, C. Zimmermann, V. Vuletic, W. König and T.W. Hänsch, *Opt. Commun.*, **117**, 541 (1995). *Page 82*
- [103] L. Hildebrandt, R. Knispel, S. Stry, J.R. Sacher, F. Schael, *Appl. Optics A*, **42**, 2110 (2003). *Page 83*
- [104] http://www.sacher-laser.com/AR_Coating.php, application notes *Page 83*
- [105] M. Fattori, G. Lamporesi, T. Petelski, J. Stuhler, G.M. Tino, *Phys. Lett. A*, **318**, 184, (2003). *Page 6*
- [106] Data of glue on company homapages; for steel, Ti and other data was taken from various sources and internet sites like e.g., http://www.io.tudelft.nl/research/dfs/idemat/Onl_db/Id170p.htm for TiAl6V4, <http://www.azom.com/details.asp?ArticleID=965/863> for steel 304/316 *Page 70*
- [107] P. Seyfried, P. Becker, *Metrologia*, **31**, 167 (1994). *Page 11*

- [108] C. Zimmermann, *Private communication*, A beat measurements between two 80 mW DFB lasers indicates a linewidth of 3 MHz, limited by noise on the current supply. *Page 80*
- [109] Demtröder W. *Laser Spectroscopy* 3rd edn. Springer Verlag Berlin (1998). *Page 103*
- [110] G.C. Bjorklund *Opt. Letters*, **5**, 15 (1980). *Page 104*
- [111] G.C. Bjorklund, M.D. Levenson, W. Lenth, C. Ortiz *Appl. Phys. B*, **32**, 145 (1983). *Page 104, 106*
- [112] R.K. Raj, D. Bloch, J.J. Snyder, G. Camy, M. Ducloy, *Phys. Rev. Lett.* **44**, 1251 (1980). *Page 104*
- [113] We are grateful for the help of T. Quinn and R. Davies of the BIPM torsion-pendulum experiment for inspiration and kind advice on the air-cushion technique and cylinder positioning. *Page*
- [114] C. Wieman, T.W. Hänsch, *Phys. Rev. Lett.* **36**, 1170 (1976). *Page 104, 112*
- [115] K.L. Corwin, Z.-T. Lu, C.F. Hand, R.J. Epstein, C.E. Wieman, *Appl. Opt.* **37**, 3295 (1998). *Page 104, 107*
- [116] T. Petelski, M. Fattori, G. Lamporesi, J. Stuhler, G.M. Tino, *Eur. Phys. J. D*, **22**, 279 (2003). *Page 103, 107*
- [117] Letokhov, Chebotayev, *Nonlinear Laser Spectroscopy*, Springer-Verlag Berlin (1977). *Page 104*
- [118] H.S. Lee, S.E. Park, J.D. Park, H. Cho, *J. Opt. Soc. Am. B*, **11**, 558 (1994). *Page 171, 177*
- [119] Meystre P., Sargent M., *Elements of Quantum Optics*, Springer Verlag Berlin (1990). *Page 104*
- [120] P.W. Smith, T.W. Hänsch, *Phys. Rev. Lett.*, **26**, 740 (1971). *Page 104*
- [121] R.E. Teets, F.V. Kowalski, W.T. Hill, N. Carlson, T.W. Hänsch, *Proc. Soc. Phot. Opt. Instr. Eng.*, **113**, 80 (1977). *Page 112*
- [122] G. Wasik, W. Gawlik, J. Zachorowski, W. Zawadzki, *Appl. Phys. B*, **75**, 631 (2002). *Page 107*
- [123] http://www.analog.com/Analog_Root/static/techSupport/designTools/interactive-Tools/filter/filter.html, Interactive Filter design *Page 121*
- [124] Publication of frequency control system of gravimeter in preparation *Page 118*

- [125] Picture taken from homepage of Fraunhofer Institut fuer angewandte Festkoerperphysik. http://www.iaf.fhg.de/ipdetetd/frames_e.htm *Page 81*
- [126] Data sheet of On Semiconductors <http://www.onsemi.com/pub/Collateral/MCH12140-D.PDF> *Page 116*
- [127] Information about degassing of TiAl6V4 from French company SODERN; private communication *Page 71*
- [128] M. Prevedelli et al., *Publication in preparation*, An analog + digital phase and frequency detector for phase-locking of diode lasers *Page 126*
- [129] C.F. Roos, P. Cren, J. Dalibard, D. Guéry-Odelin, *arXiv:cond-mat/0212060 v1* (2002). *Page 141*
- [130] G. Santarelli, C. Audoin, A. Makdissi, P. Laurent, G.J. Dick, A. Clairon, *IEEE Trans. on Ultr., Ferr. and Freq. Contr.*, textbf{45}, 887 (1998). and further articles in this issue *Page 56, 61*
- [131] K. Dieckmann, R.J.C. Spreeuw, M. Weidmüller, J.T.M. Walraven, *Phys. Rev. A*, **58**, 3891 (1998). *Page 134, 139, 140, 141*
- [132] R.S. Conroy, Y. Xiao, M. Vengalattore, W. Rooijakkers, M. Prentiss, *Opt. Comm.*, **226**, 259 (2003). *Page 135, 141*
- [133] J. Schoser, A. Batär, R. Löw, V. Schweikhard, Y.B. Ovchinnikov, T. Pfau, *Phys. Rev A*, **66**, 023410 (2002). *Page 134, 137, 140, 141*
- [134] Z.T. Lu, K.L. Corwin, M.J. Renn, M.H. Anderson, E.A. Cornell, C.E. Wieman, *Phys. Rev. Lett.*, **77**, 3331 (1996). *Page 134*
- [135] <http://www.ldeo.columbia.edu/andreal/AL.Diss/05MetaAtome3.GIF> *Page 177*
- [136] V.I. Balykin, V.G. Minogin, V.S. Letokhov, *Rep. Prog. Phys.*, **63**, 1429 (2000). *Page 138, 139*
- [137] T.M. Brzozowski, M. Mączyńska, M. Zawada, J. Zachorowski, W. Gawlik, *J. Opt. B*, **4**, 62 (2002). *Page 149*
- [138] D.A. Steck, <http://steck.us/alkalidata/>, Rubidium 87 D Line Data, Revision 14.10.2003 *Page 175*
- [139] H. Moritz, http://www.gfy.ku.dk/~ag/HB2000/part4/grs80_corr.htm, Geodetic Reference System 1980; and http://geophysics.ou.edu/solid_earth/notes/potential/igf.htm for the International gravity formula. *Page 179*
- [140] X. Li, H.J. Götze, *Geophys.*, **66**, 1660 (2001). *Page 180*
- [141] Claudia Madiai, Dip. di Ingneria Civile and Gilberto Saccorotti, INGV, Osservatorio Vesuvio, *Private communication* (2004). *Page 180*

- [142] <http://jeeep.com/details/coord/>, Coordinate translation *Page 179*
- [143] <http://ww3.atlanteitaliano.it/atlante/default2.htm>, Ministero dell' Ambiente e della Tutela del Territorio *Page 179*
- [144] P. Treutlein, K.Y. Chung, S. Chu, *Phys. Rev. A*, **63**, 051401 (2001). *Page 168*
- [145] T.J. Summer, J.M. Pendlebury, K.F. Smith, *J. Phys. D. Appl. Phys.*, **20**, 1095 (1987). *Page 78*
- [146] Raman sideband cooling has been tested on ^{87}Rb in the group of S. Chu at Stanford *Private communication &* <http://www.stanford.edu/group/chugroup/amo/BEC.html> and the group of S. Weinfurter in Freiburg *Private cummunication and unpublished Diploma thesis S. Fölling* (2003). *Page 168*
- [147] A. Messiah, *Quantum Mechanics*, North-Holland, Amsterdam (1961). *Page 175*

Men ...



I would like to thank so many kind people I met during my time in Florence and Paris but I don't really know where to start and where to end with my acknowledgements.

That is why I have chosen not to mention all the nice and not so nice people that were around and whose equipment I borrowed and with whom I was discussing physical and other problems, or the whole technical and electronic stuff that helped so much, by name. I rather place a photo of the innermost circle of the two experiments. I could not imagine a better ambiance in (and out of) laboratory than what I encountered with those people:

Marco Fattori (ex-PhD student, will go to Stuttgart now; don't forget your cellular phone, oh, and think of your purse, I think I have seen it on the ion pump...), **Giacomo Lamporesi** (first diploma and now PhD; it's YOUR experiment now) and **Juergen Stuhler** (Post-Doc during first two years) as the hard core of the MAGIA experiment of **Guglielmo Tino**. There are further **Marella de Angelis** (researcher from Naples) and **Marco Prevedelli** (expert for everything, let's say almost everything; without photo) helping the gradiometer to evolve. **Luigi Cacciapuoti** has gone almost before we realized he came - an example of the Italian brain drain and big loss for the MAGIA experiment. Without photo are also the guests we received for a few months from Poland (**Maria Mączyńska**) and France (**Vincent Jacques**).

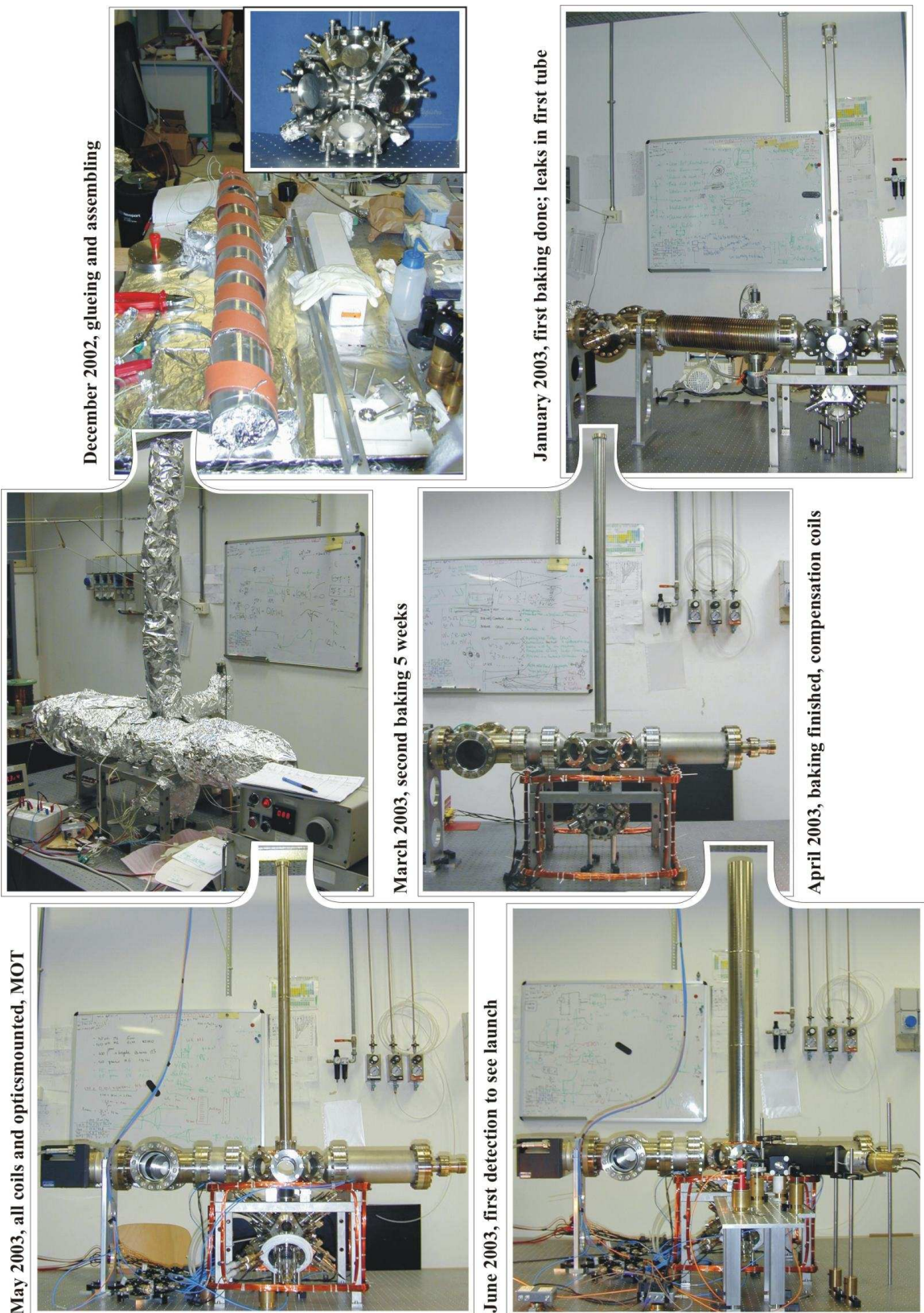
We were very close to the Strontium group (gli stronzi) with **Nicola Poli** (with photo; perhaps this is a good way to tell that we need this f=200 lens back), **Gabriele Ferrari**, **Robert Drullinger**, **Costanza** and **Fiodor**.

Franck Pereira (by now with research position; could by pure words convince a grown up physicist to believe to be a horse - and vice versa...) and **Patrick Cheinet** (PhD student, the horse thing doesn't work on him any more) are the heart of the gravimeter in the group of **Arnaud Landragin** (his manner of speaking is more velocity orientated than Pereira-style gesticulation...) and **André Clairon**, who is the accumulated collective knowledge of the Observatoire.

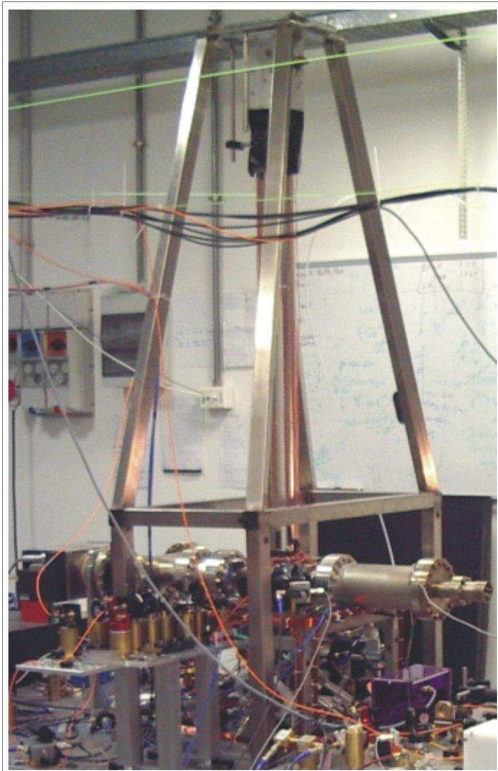
What are the 'stronzi' for the MAGIA group, are the gyroscope people for the gravimeter team: here and there we have two experiments belonging to the same group and having a large flux of equipment in both directions, averaging out over (very) long timescales.

I am also glad that I have found **Christophe Salomon** as a tutor and **Tilman Pfau** and **Ernst Rasel** (who always asks me to send him new PhD students...) as referees; thank you that you do this time-consuming work.

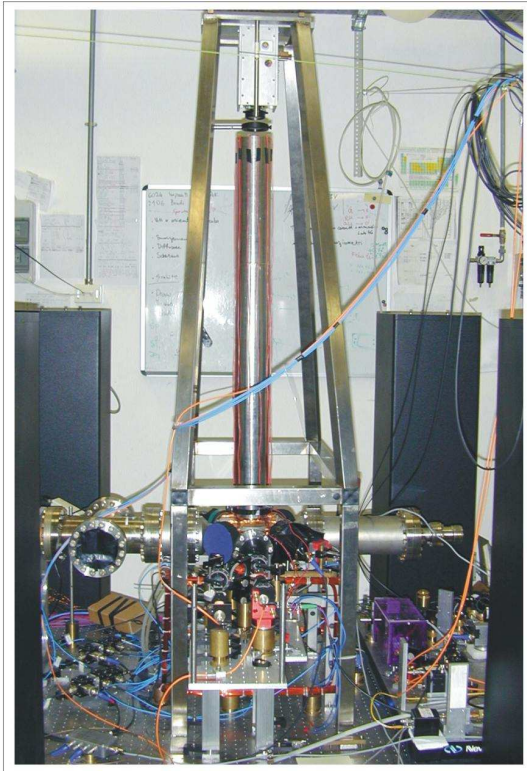
... and Machine



June 2004, upper mirror & detection system, Interferometer



October 2004, legs in U-form mounted, Juggling



I saw two children growing during these three years; one of steel in laboratory and one of flesh and bones at home. That there are differences is not astonishing – and that there are common points, neither.

The machine grew to 1,50 m, a little higher than the real child and the vacuum pumps assure that also here, the stomach always seems to be empty. I try to feed the real one well, whereas the machine is set on a diet with only few µg of rubidium a day, however it tries to suck in some more tasty molecules through every little slit. The most obvious common point is the talent of testing your nerves. Luckily nerves adopt to extreme situations – with a certain delay.

Both children are sensitive on gravity but both are still too young to give any precise, absolute number. When I bring them to bed the evening, I switch out the light, which the machine prefers coherent and – a quite surprising choice for a favorite color – infrared. Both are shy and need some time until they accept strangers to touch them and follow their orders, instead of doing what they want. But, remember: violence is no adequate instrument of education; high voltage or currents must be used very punctual. When children grow older, you realize how many things they need; the whole household is full of puppets, signal generators, cables and laundry.

I finally realized that it is too difficult for me to raise both children and dedicate them only half the time they demand, so I decided to leave our machine in the hands of Giacomo and the new papa Andrea.

